Mechanical and Thermal Properties of SiOC-based Glasses and Glass Ceramics

A dissertation approved by the Department of Materials and Earth Sciences in fulfilment of the requirements for the degree of Doctor Rerum Naturalium (Dr. rer. nat.)

M.Sc. Christina Stabler
Born on 22.04.1987 in München, Germany
17.03.2019 – Darmstadt – D-17

TECHNISCHE
UNIVERSITÄT
DARMSTADT

Mechanical and Thermal Properties of SiOC-based Glasses and Glass Ceramics
Mechanische und Thermische Eigenschaften von SiOC-basierten Gläsern und Glaskeramiken

Genehmigte kumulative Dissertation von M.Sc. Christina Stabler aus München, Deutschland
Fachbereich Material- und Geowissenschaften, Technische Universität Darmstadt

1. Gutachter: PD Dr. Emanuel Ionescu
2. Gutachter: Prof. Dr. Martin Heilmaier

Tag der Einreichung: 02.11.2018
Tag der Prüfung: 11.02.2019

Darmstadt – D 17

Declaration of Authorship

I hereby declare that the thesis submitted is my own unaided work. All direct or indirect sources used are acknowledged as references.

I am aware that the thesis in digital form can be examined for the use of unauthorized aid and in order to determine whether the thesis as a whole or parts incorporated in it may be deemed as plagiarism. For the comparison of my work with existing sources I agree that it shall be entered in a database where it shall also remain after examination, to enable comparison with future theses submitted. Further rights of reproduction and usage, however, are not granted here.

This work was not previously presented to another examination board and has not been published.

Ehrenwörtliche Erklärung

Ich erkläre hiermit ehrenwörtlich, dass ich die vorliegende Arbeit selbständig angefertigt habe. Die aus fremden Quellen direkt und indirekt übernommenen Gedanken sind als solche kenntlich gemacht.

Ich weiß, dass die Arbeit in digitalisierter Form daraufhin überprüft werden kann, ob unerlaubte Hilfsmittel verwendet wurden und ob es sich – insgesamt oder in Teilen – um ein Plagiat handelt. Zum Vergleich meiner Arbeit mit existierenden Quellen darf sie in eine Datenbank eingestellt werden und nach der Überprüfung zum Vergleich mit künftig eingehenden Arbeiten dort verbleiben. Weitere Vervielfältigungs- und Verwertungsrechte werden dadurch nicht eingeräumt.

Die Arbeit wurde weder einer anderen Prüfungsbehörde vorgelegt noch veröffentlicht.

Darmstadt, den 02.11.2019

(Christina Stabler)

The present cumulative dissertation summarizes the essential scientific findings reported to the scientific community in the following peer-reviewed journals. The reports themselves [1] – [6] are enclosed in the Chapter *List of selected reprints* at the end of this work.

[1] **C. Stabler**, E. Ionescu, M. Graczyk-Zajac, I. Gonzalo-Juan, R. Riedel, Silicon oxycarbide glasses and glass-ceramics: "All-Rounder" materials for advanced structural and functional applications, *Journal of the American Ceramic Society*, 101(11) (2018) 4817-4856.

[2] **C. Stabler**, F. Célarié, T. Rouxel, R. Limbach, L. Wondraczek, R. Riedel, E. Ionescu, Effect of composition and high-temperature annealing on the local deformation behavior of silicon oxycarbides, *Journal of the European Ceramic Society,* 39(7) (2019) 2287-2296.

[3] **C. Stabler**, F. Roth, M. Narisawa, D. Schliephake, M. Heilmaier, S. Lauterbach, H.J. Kleebe, R. Riedel, E. Ionescu, High-temperature creep behavior of a SiOC glass ceramic free of segregated carbon, *Journal of the European Ceramic Society,* 36(15) (2016) 3747-3753.

[4] **C. Stabler**, D. Schliephake, M. Heilmaier, T. Rouxel, H.J. Kleebe, M. Narisawa, R. Riedel, E. Ionescu, Influence of SiC/Silica and Carbon/Silica Interfaces on the High-Temperature Creep of Silicon Oxycarbide-Based Glass Ceramics: A Case Study, *Advanced Engineering Materials*, 1800596 (2018) 1-11. Doi: 10.1002/adem.201800596.

[5] **C. Stabler**, C. Seemüller, A. Choudhary, M. Heilmaier, S. Lauterbach, H.J. Kleebe, E. Ionescu, Synthesis and high-temperature creep behavior of a SiLuOC-based glass-ceramic, *Journal of the Ceramic Society of Japan*, 124(10) (2016) 1006-1012.

[6] **C. Stabler**, A. Reitz, B. Albert, P. Stein, R. Riedel, E. Ionescu, Thermal Properties of SiOC Glasses and Glass Ceramics at Elevated Temperatures, *Materials*, 11(279) (2018) 1-18.

Table of Content

Acknowledgments

I thank **Prof. Dr. Ralf Riedel** for the possibility to learn and work in his group and to carry out my PhD research on silicon oxycarbides. I thank him for his constant support and his valuable feedback.

I would like to express my special gratitude to **PD Dr. Emanuel Ionescu** for the first survey of this thesis and his invaluable support during my PhD time. This includes not only numerous scientific discussions and valuable advices, but as well the teaching in scientific writing and working.

Prof. Dr. Martin Heilmaier is gratefully acknowledged for the second survey of this thesis, for the fruitful cooperation in elucidating the high-temperature creep behavior of silicon oxycarbides and for valuable discussions and feedback.

I would like to express my gratitude to our further project partners **Dr. Daniel Schliephake** for support in creep measurements and valuable discussions and **Prof. Karsten Albe, Dr. Jochen Rohrer, Dr. Alexander Stukowski** and **Constanze Kalcher** for the fruitful collaboration and valuable discussions and feedback.

I thank **Prof. Dr. Masaki Narisawa**, **Prof. Dr. Tanguy Rouxel**, **Associate Prof. Fabrice Célarié**, **Prof. Dr. Lothar Wondraczek**, **Dr. René Limbach**, **Prof. Dr. Barbara Albert** and **Adreas Reitz** for fruitful collaborations including the provision of very special SiOC compositions, the support in the assessment of elastic, plastic and thermal properties and valuable discussions and feedback.

I was happy being part of the group of “Disperse Feststoffe”, for the constant support, the friendly atmosphere and company. Especially, I thank **Dr. Felix Rosenburg** who introduced me to the experimental world of SiOCs and for the numerous scientific discussions. I thank **Dr. Dragoljub Vrankovic**, **Dr. Sarabjeet Kaur** and **Dr. Pradeep Vallachira** for sharing their experience in the laboratory and for valuable discussions, **Dario De Carolis** for XRD measurements, **Claudia Fasel** for thermal analysis and constant support in the laboratory and **Dr. Magdalena Graczyk-Zajac** for constant support.

I thank **Dr. Hergen Breitzke** for the assessment and discussion on NMR measurements of SiOCs, **Lothar Bischoff** and **Dr. Maren Lepple** for DSC measurements, **Hans Chen** for the support during last creep measurements and **Prof. Dr. Baixiang Xu** and **Dr. Peter Stein** for computational modeling of the thermal properties.

I gratefully acknowledge the financial support of the Deutsche Forschungsgemeinschaft DFG (IO 64/7-1, “High-Temperature Creep in SiOC-Based Glasses and Glass-Ceramics”).

I wish to express my deepest gratitude to my husband Christopher, for his dedication, continuous support, motivating words and scientific discussions. I would like to express my deepest gratitude to my family, including scientific discussions with my sister Stefanie.

List of Abbreviations

BSU	Basic structure unit
C_{segr}	Segregated carbon phase
CTE	Coefficient of thermal expansion
CTE_{HT}	Coefficient of thermal expansion above glass transition
DSC	Differential scanning calorimetry
ED	Electron diffraction
HRTEM	High-resolution transmission electron microscopy
IR	Infrared (spectroscopy)
MAS	Magic angle spinning
NMR	Nuclear magnetic resonance (spectroscopy)
PAHs	Polycyclic aromatic hydrocarbons
PDC	Polymer-derived ceramic
PIP	Polymer infiltration pyrolysis
RFDA	Resonant frequency damping analyzer
SAXS	Small angle X-ray scattering
SiMOC	Metal-modified SiOC
SiOC	Silicon oxycarbide
SiON	Silicon oxynitride
TEM	Transmission electron microscopy
TGA-EGA	Thermogravimetric analysis with evolved gas analysis
XPS	X-ray photoelectron spectroscopy
XRD	X-ray diffraction
YSZ	Yttria-stabilized zirconia

List of Symbols

A_D	Area underneath the D band in Raman spectroscopy of disordered carbons
A_G	Area underneath the G band in Raman spectroscopy of disordered carbons
α	Thermal diffusivity
B	Material-dependent creep constant
c_p	Specific heat capacity (at constant pressure)
ε	Strain
$\dot{\varepsilon}$	Steady-state strain rate
E	Elastic or Young's modulus
f	Volume fraction of rigid dispersed phase
F	Shape parameter of dispersed particles
G	Shear modulus
H	Hardness
H_V	Vicker's microhardness
K	Bulk modulus
L/L_0	Actual length referred to the starting length (length change)
L_a	Average crystallite size of sp^2-hybridized carbon
L_D	Average inter-defect distance of sp^2-hybridized carbon
λ	Thermal conductivity
m	Shape-related function of dispersed particles
m	Strain-rate sensitivity
n	Stress exponent
η	Viscosity
η_0	Viscosity of the glassy matrix
Q	Activation energy
ρ	Density
R	Universal gas constant

σ	Stress
σ_{true}	True stress
t	Time
T	Absolute temperature
T_g	Glass transition temperature
T_{meas}	Measurement temperature
υ	Poisson's ratio

List of Figures

List of Tables

Curriculum Vitae

Personal data:

Name:	Christina Stabler né Breunig
Date of birth:	22. April 1987
Nationality:	German

Education:

since 05/2014	**Technical University of Darmstadt** PhD candidate in Materials Science
10/2010 – 03/2013	**Friedrich-Alexander University Erlangen-Nürnberg** **Graduation**: M.Sc. Geosciences – Applied Mineralogy
10/2007 – 09/2010	**Friedrich-Alexander University Erlangen-Nürnberg** **Graduation**: B.Sc. Geosciences
04/2007 – 09/2007	**Friedrich-Alexander University Erlangen-Nürnberg** Guest student: Mineralogy (Dipl.-Min.)

Complete List of Publications

C. Stabler, F. Célarié, T. Rouxel, R. Limbach, L. Wondraczek, R. Riedel, E. Ionescu: *Effect of composition and high-temperature annealing on the local deformation behavior of silicon oxycarbides*, **2019**, J. Eur. Ceram. Soc., 39(7), 2287-2296; DOI: 10.1016/j.jeurceramsoc. 2019.02.024

C. Stabler, D. Schliephake, M. Heilmaier, T. Rouxel, H.J. Kleebe, M. Narisawa, R. Riedel, E. Ionescu: *Influence of SiC/silica and carbon/silica interfaces on the high-temperature creep of silicon oxycarbide-based glass ceramics: a case study,* **2018**, Adv. Engin. Mater., 1800596, 1-11; DOI: 10.1002/adem.201800596

C. Stabler, E. Ionescu, M. Graczyk-Zajac, I. Gonzalo-Juan, R. Riedel: Silicon Oxycarbide Glasses and Glass-Ceramics: *"All-Rounder" Materials for Advanced Structural and Functional Applications,* **2018,** J. Am. Ceram. Soc., 101(11), 4817-4856; DOI: 10.1111/jace.15932

C. Stabler, A. Reitz, P. Stein, B. Albert, R. Riedel, E. Ionescu: *Thermal Properties of SiOC Glasses and Glass Ceramics at Elevated Temperatures*, **2018**, Materials, 11(279), 1-18; DOI:10.3390/ma11020279

D. Vrankovic, M. Graczyk-Zajac, C. Kalcher, J. Rohrer, M. Becker, **C. Stabler**, G. Trykowski, K. Albe, R. Riedel: *Highly Porous Silicon Embedded in a Ceramic Matrix: A Stable High-Capacity Electrode for Li-Ion Batteries*, **2017**, ACS nano, 11, 11409-11416; DOI: 10.1021/acsnano.7b06031

K. Kawashima, M. Hojamberdiev, **C. Stabler**, D. Vrankovic, K. Yubuta, R. Riedel, K. Domen, K. Teshima: *Perovskite $Sr_{1-x}Ba_xW_{1-y}Ta_y(O,N)_3$: synthesis by thermal ammonolysis and photocatalytic oxygen evolution under visible light*, **2017**, Mater. Renew. Sustain. Energy, 6, 10; DOI: 10.1007/s40243-017-0094-4

C. Stabler, C. Seemüller, A. Choudhary, M. Heilmaier, S. Lauterbach, H.J. Kleebe, E. Ionescu: *Synthesis and high-temperature creep behavior of a SiLuOC-based glass-ceramic*, **2016**, J. Ceram. Soc. Jpn., 124, 1006-1012; DOI:10.2109/jcersj2.16101

C. Stabler, F. Roth, M. Narisawa, D. Schliephake, M. Heilmaier, S. Lauterbach, H.J. Kleebe, R. Riedel, E. Ionescu: *High-temperature creep behavior of a SiOC glass ceramic free of segregated carbon*, **2016**, J. Eur. Ceram. Soc., 36, 3747–3753; DOI:10.2109/jcersj2.16101

C. Stabler, **C. Breunig**, F. Goetz-Neunhoeffer, J. Neubauer, H. Fryda, R. Kwasny-Echterhagen: *Impact of different calcium sulfate sources on the early hydration of two different grades of calcium aluminate cement*, **2014**, Calcium Aluminates, Proceedings of the International Conference, Avignon, France, May 18-21, 2014, 177-188

C. Stabler, **C. Breunig**, F. Goetz-Neunhoeffer, J. Neubauer, H. Fryda, R. Kwasny-Echterhagen: *Influence of calcium sulfate on the early hydration of a calcium aluminate cement*, 2013, GDCh-Monographie, 46(y), 97-100

1 Motivation and Aim of the Study

Starting in the 1950s, research was conducted on the mechanical improvement of vitreous silica via the incorporation of carbon atoms into the glass network [7]. As a result, polymer-derived silicon oxycarbides (SiOC) were developed, which exhibit improved mechanical properties even at high temperatures, a unique crystallization resistance and excellent stability in harsh environments [8]. Consequently, silicon oxycarbides are potential candidates for high-temperature applications, for example in ceramic heaters, high-temperature reactors, combustion engines or as part of thermal protection systems [8, 9]. For these applications, the precise knowledge of the mechanical properties like hardness, elasticity and creep, but also of the thermal properties like thermal conductivity and thermal expansion is of paramount interest. In order to incorporate SiOCs in more complex structures like thermal barrier coatings, their intrinsic properties must be accurately assessed in the first place.

With almost 50 years of research, silicon oxycarbides are not a new class of materials. Yet, some basic concepts regarding the mechanical and thermal properties still need to be unraveled. This circumstance is related to the variability of the SiOC system itself regarding composition (ranging from low carbon- to high carbon-containing samples) and microstructure (ranging from glass to glass ceramic). The governing parameters for these aspects are architecture, composition and chemical bonding of the starting polymeric precursors as well as synthesis parameters like temperature and atmosphere [8, 10-15]. Furthermore, the high-temperature stability of the final SiOC material is not only depending on its chemical composition, architecture of the polymeric precursor and its residual porosity [16] but as well on the chosen furnace (alumina and graphite furnaces yield different results) [17]. Although there is some information on the mechanical and thermal properties of SiOC materials published in literature, the comparability between the different studies is in some cases not fulfilled. Consequently, a systematic study on a series of samples with identical synthesis procedure and well-characterized compositions and microstructures is lacking, however is mandatory to tap the full potential of the system with respect to tailoring the material properties to desired values.

The aim of the present study is to systematically assess the mechanical and thermal properties of silicon oxycarbides and to obtain a fundamental understanding concerning the relationship between their phase composition, microstructure and properties. Therefore, a SiOC glass and a series of SiOC glass ceramics with varying compositions were synthesized to address the following objectives:

(i) How do different microstructures, i.e. SiOC glass (SiO_xC_y-C) vs. glass ceramic (SiO_2-SiC-C), influence the mechanical and thermal properties of silicon oxycarbides?

(ii) How does a varying amount of the segregated carbon phase impact the mechanical and thermal properties of silicon oxycarbides?

(iii) How do varying phase assemblages in the systems SiO_2-SiC-C and SiO_2-SiC-C-$Lu_2Si_2O_7$ effect the mechanical and thermal properties of silicon oxycarbides?

(iv) How does composition and prolonged exposure to high temperature affect the thermal stability of SiOC glass ceramics?

In the first part of the present study, the samples are characterized in detail with respect to their composition and microstructure, the differences between the individual samples being highlighted. In the second and third part, the (thermo)mechanical and thermal properties of the investigated samples are discussed with special focus on the relation between the intrinsic properties and composition/microstructure, in order to obtain a fundamental understanding of the governing parameters for a precise tuning of the properties of silicon oxycarbides.

2 Critical Assessment of the Present Work

2.1 State of the art

The content of this chapter is partially published in:

[1] **C. Stabler**, E. Ionescu, M. Graczyk-Zajac, I. Gonzalo-Juan, R. Riedel, Silicon oxycarbide glasses and glass-ceramics: "All-Rounder" materials for advanced structural and functional applications, *Journal of the American Ceramic Society*, 101(11) (2018) 4817-4856.

2.1.1 The SiOC system – synthesis, microstructure and high-temperature behavior

In the late 1980s, the fabrication of SiOCs synthesized from the sol-gel route started [18]. Typically, these sol-gel routes include the condensation and co-hydrolysis of silicon alkoxides. Upon choosing different organic groups, molar ratios between different silicon alkoxides and reaction conditions like pH value, the resulting precursor architecture and chemistry can be tuned precisely [8, 10, 19-21]. Additionally, several commercially available, inexpensive polyorganosiloxanes can be used as polymeric precursors. Furthermore, modification of the polymeric precursors is possible upon reaction of their functional groups (e.g. hydroxyl or alkoxy) with (transition) metal alkoxides, acetates and acetylacetonates in a classical wet chemical approach to obtain quaternary SiMOC materials [20, 22-24]. In this way, metal oxides [22, 24], silicates [25], silicides [26] and carbides [27] are incorporated in the final product, introducing/enhancing functional properties like luminescence [28, 29], magnetic behavior [26] or energy storage capacity [30].

The conversion from the precursor state to the final ceramic state (the so-called polymer-to-ceramic transformation) is usually performed upon thermal treatment. This process includes crosslinking of the thermoplastic precursors forming infusible networks (100-400 °C) [31], subsequent various redistribution reactions between Si-O, Si-C and Si-H bonds (300-600 °C) [32, 33], the conversion into inorganic glasses (600-1000 °C) involving the evaporation of hydrocarbons and hydrogen [8, 31] and further polymerization of the glass network (800-1000 °C) [10]. The polymer-to-ceramic transformation is finished at approximately 1000 °C as evidenced by almost constant weight in the thermogravimetric analysis (TGA) [12, 13]. In addition to the establishment of the inorganic glassy network, ^{13}C magic angle spinning nuclear magnetic resonance spectroscopy (MAS NMR) reveals the segregation of a carbon phase starting at 600 °C [34] that is proposed to consist of polycyclic aromatic hydrocarbons (PAHs) [35]. A further increase in temperature leads to linkages of several PAHs accompanied by the evolution of hydrogen to form so-called basic structure units (BSUs) [35] and eventually to

amorphous carbon [36]. However, the lateral size of this so-called segregated carbon phase is still very low at 800 °C, as neither Raman spectroscopy nor high-resolution transmission electron microscopy (HRTEM) are able to detect it [10, 37, 38]. Figure 2-1 displays a model structure for SiOC materials pyrolyzed between 800 and 1000 °C.

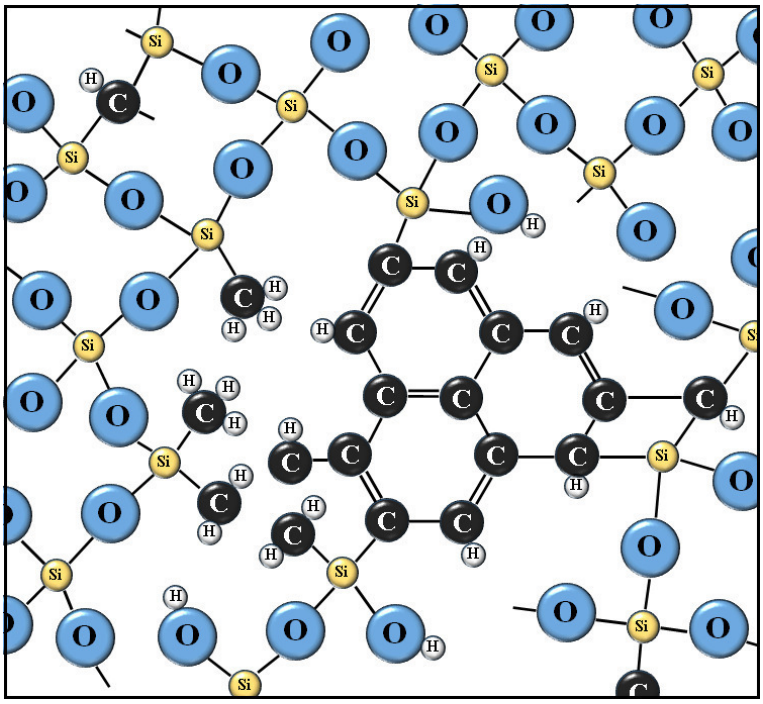

Figure 2-1: Proposed structural model for SiOC materials pyrolyzed between 800 and 1000 °C (modified from [10]).

As evidenced by X-ray diffraction (XRD) and ^{29}Si MAS NMR, SiOC glasses prepared between 1000 to 1250 °C are fully X-ray amorphous [39, 40] and built from corner-shared mixed-bonds $SiO_{4-x}C_x$ tetrahedra (SiO_4, SiO_3C, SiO_2C_2, $SiOC_3$, SiC_4), with oxygen being connected to two and carbon to four silicon tetrahedra [41]. These sp^3-hybridized carbon atoms are generally referred to as network carbon. In addition to the network carbon, usually the sp^2-hybridized segregated carbon phase is homogeneously dispersed [40, 42]. The amount of both, network and segregated carbon, is influenced by the polymeric precursors. For example, upon choosing the proper combination of alkoxysilanes in the sol-gel process, it is possible to tailor specific phase assemblages in the resulting SiOC glasses. Soraru *et al.* [21] demonstrated that molar ratios of triethoxysilane and methyldiethoxysilane of 1, 2 and 10 lead to SiOC glasses with (i) excess of carbon forming a segregated carbon phase, (ii) a “stoichiometric” composition without excess of carbon leading to the absence of the segregated carbon phase and (iii) an undersaturation of carbon leading to the presence of Si-Si bonds where consequently elemental silicon substitutes the segregated carbon phase. SiOC glasses do not contain any C-O bonds as evidenced by ^{13}C MAS NMR [41], infrared (IR) spectroscopy [43] and X-ray photoelectron spectroscopy (XPS) [43]. This fact offers the opportunity of estimating the phase composition of SiOC glasses from

elemental analysis data: all oxygen atoms are allocated to silicon tetrahedra and subsequently the remaining silicon atoms to carbon. Any remaining carbon atoms have to be organized in the segregated carbon phase. A detailed discussion on the calculation can be found in [44]. Typically, SiOC glasses prepared at around 1000 °C possess a significant amount of hydrogen [13, 45, 46]. However, the majority of the hydrogen is removed upon increasing the temperature to approximately 1400 °C, as evidenced by thermogravimetric analysis with evolved gas analysis (TGA-EGA) [12] and elemental analysis [10, 13].

The exact spatial distribution of the mixed-bonds silicon tetrahedra is still open to debate. There are several models proposed in literature, among them the models elaborated by Saha & Raj [47] and Widgeon *et al.* [41]. Both concepts are depicted in Figure 2-2. The main difference relies on the spatial distribution of the mixed-bonds silicon tetrahedra. The model of Saha & Raj (Figure 2-2a) is based on small angle X-ray scattering (SAXS) data and proposes the existence of SiO_4 nanodomains (1 – 3 nm in size) encapsulated by the segregated carbon phase with the remaining mixed-bonds tetrahedra located at the border between silica nanodomain and segregated carbon. In contrast, the model proposed by Widgeon *et al.* (Figure 2-2b) based on NMR studies envisages a more continuous, gradient-like distribution of the mixed-bonds tetrahedra, with the carbon-rich tetrahedra in the vicinity of the segregated carbon phase and predominantly oxygen-rich mixed-bonds tetrahedra located at increasing distance to segregated carbon. In both cases, the glass network consists of a continuous SiOC phase, which exhibits heterogeneity at the nano scale. Whereas Saha & Raj address the segregated carbon phase to be “graphene-like” [47], more recent studies suggest that the segregated carbon phase in SiOC has the nature of amorphous carbon at temperatures between 1000 and 1400 °C [36].

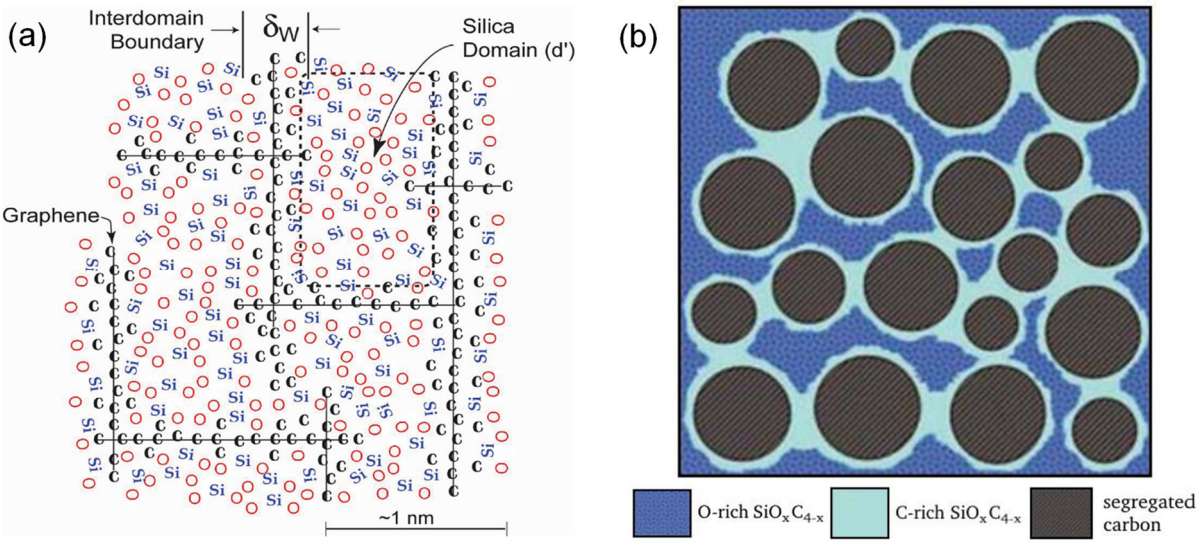

Figure 2-2: Proposed nanostructure of SiOC glasses fired at approximately 1000 to 1250 °C: a) the existence of silica nanodomains with the mixed-bonds tetrahedra located at the interface to the segregated carbon phase [47]; b) a gradient-like, more homogeneous distribution of carbon-rich and oxygen-rich mixed-bonds tetrahedra [41].

When the temperature is increased to approximately 1250 °C, a phase separation of the homogeneous SiOC glassy matrix starts [13]. This can be monitored by ^{29}Si MAS NMR, where an increase of SiO_4 and SiC_4 tetrahedra at the expense of the mixed-bonds tetrahedra SiO_3C, SiO_2C_2 and $SiOC_3$ is detected [13]. At the same time, broad reflections related to β-SiC nanoparticles (2 to 5 nm in size as evidenced by transmission electron microscopy (TEM) imaging [16]) evolve in the X-ray diffractogramms [21]. The phase separation is a continuous process and the majority of the changes are taking place until 1400 °C [13]. It is caused by redistribution reactions of Si-O and Si-C bonds as proven by negligible mass losses during this temperature interval [10, 32, 40, 48]. Consequently, SiOC samples prepared at T > 1400 °C can be regarded as glass ceramics consisting of a vitreous silica matrix in which β-SiC nanoparticles and typically the segregated carbon phase are homogeneously dispersed, as schematically depicted in Figure 2-3. The segregated carbon phase itself gets progressively ordered with increasing temperature and can be described as nano-crystalline carbon at T > 1400 °C [36] and as turbostratic carbon at T > 1600 °C [21, 36].

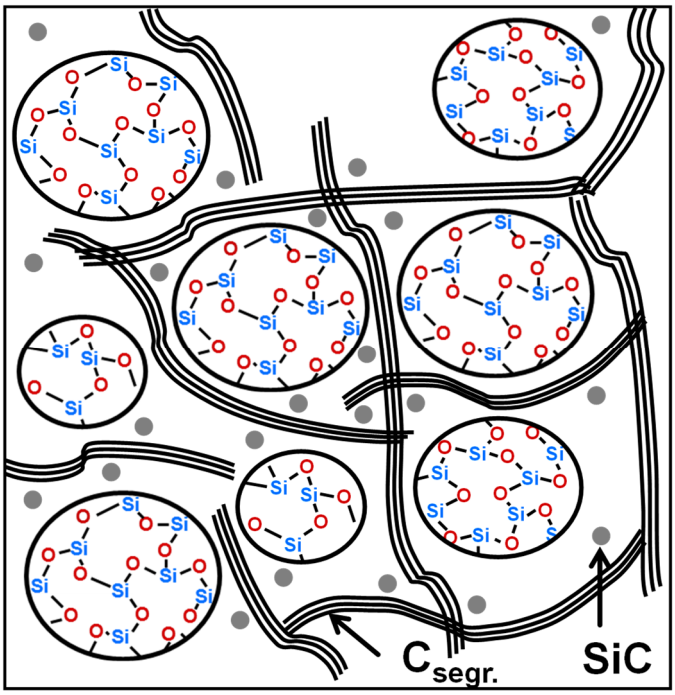

Figure 2-3: Proposed structural model (2D) of SiOC glass ceramics at T > 1400 °C [1]. The silicon atoms are tetrahedrally coordinated, with the 4th bond facing out of plane.

Most interestingly, the glassy silica matrix remains amorphous at temperatures up to 1500 °C [13, 43], whereas in pure vitreous silica cristobalite typically starts to crystallize at T > 1200 °C [40]. Two reasons for the increased crystallization resistance are usually discussed: (i) the segregated carbon phase acts as a diffusion barrier and hinders cristobalite to nucleate and/or grow [13, 48]; (ii) residual Si-C bonds within the silica matrix originating from an incomplete phase separation hinder the nucleation [13].

SiOC materials are compositionally stable up to 1500 °C under inert atmosphere [21, 32, 48]. At higher temperatures, samples display weight loss due to the so-called carbothermal reduction (equations 2-1 to 2-2), where silica reacts with carbon in a two-step reaction under the evaporation of CO [10, 49]:

$$SiO_2(s) + C(s) \rightarrow SiO(l) + CO(g) \qquad \Delta G^0[cal] = 93080 - 52.70\,T \text{ [50]} \qquad (2\text{-}1)$$

$$SiO(l) + 2C(s) \rightarrow SiC(s) + CO(g) \qquad \Delta G^0[cal] = 51520 - 28.57\,T \text{ [50]} \qquad (2\text{-}2)$$

Hence, SiOC samples without segregated carbon phase show a higher thermodynamic stability than SiOC samples which possess a segregated carbon phase [51]. After complete consumption of the segregated carbon phase, SiO_2 can directly react with SiC resulting in a complete decomposition of the material (equation 2-3) [49, 52]:

$$2SiO_2(s) + SiC(s) \rightarrow 3SiO(g) + CO(g) \qquad \Delta G^0[cal] = 354474 - 175.20\,T \text{ [53, 54]} \qquad (2\text{-}3)$$

Considering the weight loss during polymer-to-ceramic transformation and the carbothermal reduction, it is challenging to prepare crack-free and fully dense SiOC monolithic pieces that are mandatory for the assessment of the intrinsic mechanical and thermal properties. Techniques solving this problem include the addition of reactive and passive fillers leading to a decrease of the weight loss while increasing volume stability [55, 56] or polymer infiltration pyrolysis (PIP) cycles [57, 58], that repeatedly fill the originating pores. However, either additional phases (in the case of fillers) or additional grain boundaries (in the case of PIP) are introduced to the SiOC monoliths, which are expected to have an influence on the mechanical and thermal properties. The use of pressure-assisted processing techniques like uniaxial hot-pressing offers a good opportunity of fabricating neat, dense and crack-free monolithic pieces. As the densification during hot-pressing is based on viscous flow, temperatures higher than 1400 °C are necessary to properly densify SiOC glass powders. As a consequence, the resulting dense monolith is always a SiOC glass ceramic. Additionally, it was shown, both by thermodynamic calculations and experimental data, that at elevated pressures applied during hot-pressing the decomposition reactions expressed in equations 2-1 to 2-3 can be suppressed [59, 60].

2.1.2 Elastic and plastic properties of SiOC-based glasses, glass ceramics and nanocomposites

The topology of the network in glasses governs numerous properties, as will be highlighted in the following section. The substitution of bivalent oxygen atoms by tetravalent carbon atoms in SiOC glasses leads to an increase in the glass network connectivity [61]. Consequently, all properties related to the glass network like Young's modulus, glass transition temperature T_g,

viscosity and hardness are expected to be increased in SiOC glasses in comparison to pure vitreous silica [61, 62]. Although some of these properties were already investigated for selected SiOC materials, not much attention was paid to the underlying concepts.

Young's modulus and Poisson's ratio

Elastic properties in glasses are related to the glass network topology. Poisson's ratio describes the negative ratio of transverse strain in relation to its longitudinal strain and can be calculated from Young's modulus E and shear modulus G according to equation 2-4. It is intimately and directly linked to the atomic packing density, i.e. the higher the atomic packing density, the higher is Poisson's ratio [63]. Interestingly, highly condensed glass networks do not possess a high atomic packing density, since 3-dimensional building blocks are more difficult to be closely packed in comparison to 2-dimensional structures like sheets or even 1-dimensional structures like chains [63]. Consequently, highly crosslinked glasses like SiOC glasses show one of the lowest Poisson's ratios of 0.11 [64] known amongst glasses [63]. In comparison, pure vitreous silica possesses a Poisson's ratio of 0.15 – 0.18 [65-70] in accordance to a lower crosslinking degree due to the absence of tetravalent carbon atoms and consequently higher atomic packing density. There is no value available in literature for SiOC glass ceramics.

$$\upsilon = \frac{E}{2G} - 1 \tag{2-4}$$

The elastic or Young's modulus is depending in the first place (i) on the atomic packing density and (ii) on the atomic bond energy. In the second place, it depends as well on coordination, crosslinking degree and molecular organization (rings, chains, layers) [62]. Thus, Young's modulus reflects a mean volume density of energy [62, 71]. Bulk SiOC glasses exhibit higher Young's moduli (usually between 96.1 and 110 GPa [46, 61, 64, 72]) in comparison to vitreous silica (70 GPa) [73], although the atomic packing density is lower in SiOC glasses and the bond energy of Si-C (447 kJ/mol) is lower than the bond energy of Si-O (800 kJ/mol) [62]. The key point governing the increase in Young's modulus in SiOC glasses is the increased crosslinking degree, resulting in a higher mean volume density of energy [62]. Among SiOC glasses, the chemical composition influences Young's modulus (*cf.* Table 2-1). However, no conclusive dependencies were established, yet. In comparison to SiOC glasses, only few values were determined for SiOC glass ceramics in literature, being similar to that of the SiOC glasses (*cf.* Table 2-1) [43, 74]. The lack of data and the variability in measurement techniques does not allow an estimation of the impact of phase separation on Young's modulus. For SiOC glass ceramics in general, Young's modulus is expected to be an additive function of the constituting phases and their respective volume fractions and properties [75, 76].

Table 2-1: Young's moduli for SiOC glasses and glass ceramics reported in literature. Values for vitreous silica, β-SiC and graphite/carbon are included for comparison.

Composition	$T_{synthesis}$ [° C]	E [GPa]	Measurement technique
SiOC glasses			
$SiO_{1.25}C_{0.37}$ + 0.125 C [61]	1000	110±6	3-point-bending
$SiO_{1.33}C_{0.33}$ [61]	1000	104±4	3-point-bending
$SiO_{1.49}C_{0.25}$ + 0.02 C [72]	1200	101±4	3-point-bending
$SiO_{1.60}C_{0.20}$ + 0.60 C [64]	1100	101±15	Indentation
		96.1±0.5	Ultrasonic Echography
$SiO_{1.33}C_{0.33}$ + 6.14 C [46]	1100	66	Nanoindentation
SiOC glass ceramics			
$SiO_{1.59}C_{0.21}$ + 0.45 C [74] 79.7 SiO_2, 9.4 SiC 10.9 C [vol.%]	1600	85	RFDA
$SiO_{1.53}C_{0.24}$ + 0.36 C [43] 79.7 SiO_2, 11.2 SiC, 9.1 C [vol.%]	1650	97.9	Sonic Resonance
Vitreous silica [73, 77]	–	70	Ultrasonic Echography
	–	71.6	Nanoindentation
β-SiC [78]	–	392-448	Load deflection
Amorphous carbons [79]	–	<100-500	Ultrasonic Echography

Hardness of Glasses and Glass Ceramics

For Vicker's microhardness, SiOC glasses exhibit higher values between 6.4 and 9.3 GPa [40, 61, 64] in comparison to vitreous silica (6 GPa [80]). The concepts behind are not further discussed in literature. For glass ceramics in general, hardness is controlled by the properties, volume fractions and particle spacing of the individual crystalline and glassy constituting phases [76]. For a SiOC glass ceramic, a value of 8.7 GPa was determined [40]. Residual porosity in the SiOC glasses and scarce information on SiOC glass ceramics hinder a distinct conclusion on the dominating factors governing hardness in SiOC materials.

High-temperature creep and viscosity

In ceramics and metals, a time-dependent plastic deformation taking place at elevated temperatures at constant stress is traditionally called creep [81]. The time-dependent plastic deformation or strain of glasses at high temperatures is usually proceeding via Newtonian viscous flow [66] and consequently the term viscous flow is often equally used when addressing

the plastic deformation of glasses. Typically, an experimental creep curve (i.e. strain ε vs. time t) of a viscoelastic material reveals three different stages as displayed in Figure 2-4a: (i) the primary creep stage, which is characterized by a continuous decrease in the strain rate; (ii) the steady-state creep regime, where the strain rate stays constant and (iii) the ternary creep regime, which is determined by increasing strain rates due to fracture of the sample [82]. The primary stage is the result of the superposition of instantaneous elastic (reversible) deformation (elasticity), plastic (irreversible) deformation (viscosity) and anelastic deformation (delayed elasticity) [82] as depicted in Figure 2-4b. Delayed elasticity in glasses is based on the idea that glasses are heterogeneously structured at the nano-scale and hence exhibit a deformation rate spectrum, where slow-deforming regions are neighbored to fast-deforming regions stressing each other [83]. The steady-state regime is solely governed by plastic deformation and consequently in this stage conclusions can be drawn regarding creep mechanism and creep viscosity.

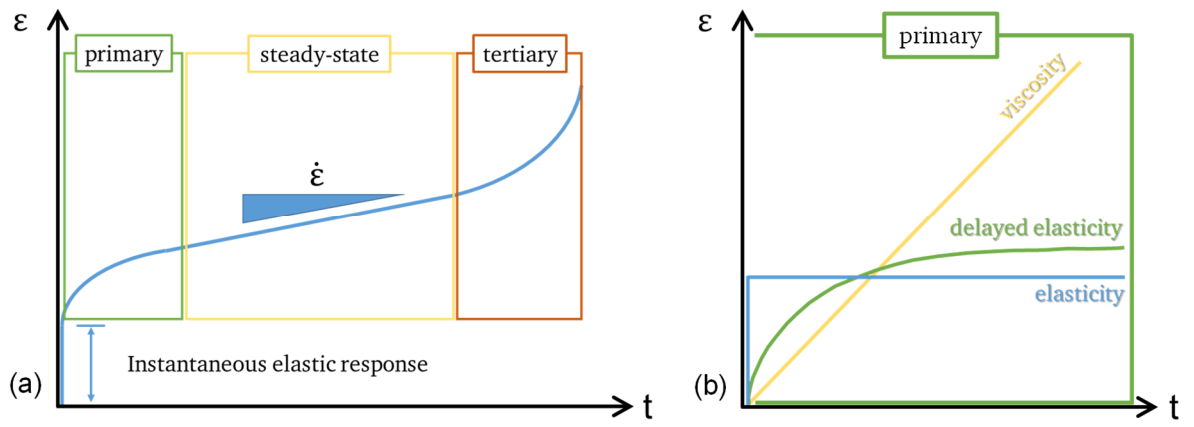

Figure 2-4: (a) Schematic creep curve (strain ε vs. time t) of a viscoelastic material and (b) the contribution of different deformation types to the primary stage (adapted from [82]).

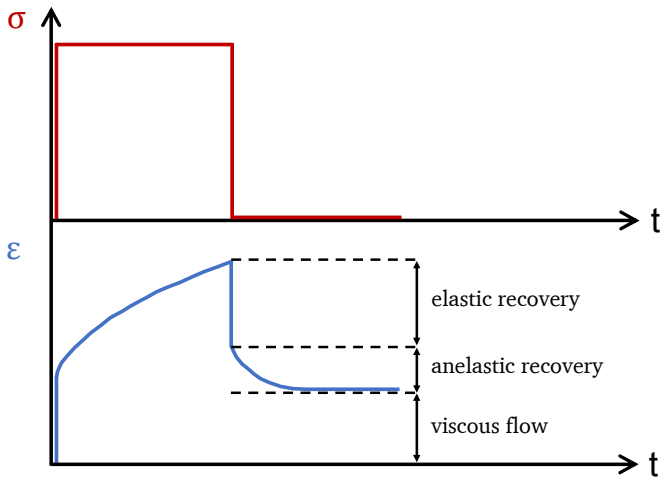

Figure 2-5: Schematic creep recovery curve of a viscoelastic material (adapted from [84]).

The extent of the elastic and anelastic deformation can be assessed from a creep recovery experiment, where the deformation after removal of the applied load is recorded [82]. Figure 2-5 schematically shows the determination.

Mathematically, steady-state creep can be described using the Arrhenius-type Norton power law displayed in equation 2-5 [85, 86], where $\dot{\varepsilon}$ is the steady-state strain rate, B is a material dependent constant, σ is the applied stress, n is the stress exponent and Q is the activation energy for creep. To account for the deformation, the stress normalized to the actual cross section of the specimen, true stress σ_{true} [87], is used. The stress exponent is indicative of the creep mechanism. The equation is described to hold for diffusion-controlled creep and dislocation climb-controlled creep [88]. With respect to glasses, Newtonian viscous flow exhibits n = 1 [88], whereas n = 2 was observed in materials exhibiting grain boundary sliding [89-91]. Polycrystalline ceramic materials show dislocation climb-based creep corresponding to n = 3 – 5 [88, 92]. The activation energy describes the species carrying the deformation or, to put it in another way, the activation volume.

$$\dot{\varepsilon} = B\sigma^n e^{\left(-\frac{Q}{RT}\right)} \tag{2-5}$$

The viscosity η of glasses can be calculated according to equation 2-6 from the steady-state strain rate $\dot{\varepsilon}$ for a certain applied stress σ and if Poisson's ratio υ of the material is known [44]. Additionally, the apparent viscosity η of a glass-crystal composite material can be calculated using equation 2-7 [93], where η_0 is the viscosity of the glassy matrix, f is the volume fraction of the rigid dispersed phase and m is a function related to the shape of the dispersed particles. This function is displayed in equation 2-8 [93], with F being the shape factor, varying from 0 to 0.5 and taking values of 0.01532 for oblate, 1/3 for spherical and 0.48986 for needle-like inclusions with an aspect ratio of 10. Equation 2-7 was demonstrated to hold for isolated inclusions without contact to other inclusions [93]. The percolation threshold is reported to be dependent on the particle size of the inclusions, where the percolation threshold decreases with decreasing particle size [94].

$$\eta = \frac{\sigma}{2(1+\upsilon)\dot{\varepsilon}} \tag{2-6}$$

$$\eta = \eta_0(1-f)^m \tag{2-7}$$

$$m = \frac{3F-2}{3F(1-2F)} \tag{2-8}$$

In glass science, the glass transition temperature T_g is an important parameter. Below T_g, glasses behave like a solid, above more like a liquid. As a consequence, a change in various properties

like heat capacity [95] and thermal expansion [96] occurs. It is well-known, that T_g can be related to a viscosity of 10^{12} – $10^{12.6}$ Pa·s [62].

SiOC glass ceramics were shown to have increased viscosities in comparison to vitreous silica [43, 60]. Furthermore, it was demonstrated that long holding times during creep experiments (e.g. 18 hours) even at temperatures as high as 1400 °C were necessary in order to obtain steady-state conditions [60]. Additionally, true creep experiments were performed on two SiOC glasses with the main difference being their amount of segregated carbon [44, 73]. The true creep behavior of SiOC glass ceramics was assessed for different amounts of segregated carbon and upon incorporation of additional metal oxides [74, 97].

Five distinct features related to the high-temperature creep behavior of SiOC materials have been elucidated: (i) SiOC glasses and glass ceramics seem to exhibit steady-state creep; (ii) SiOC glasses and glass ceramics possess even lower creep rates at ca. 1100 °C than vitreous silica (compare ca. $2.0 \cdot 10^{-06}$ s^{-1} for a SiOC glass [44] and ca. $1.0 \cdot 10^{-05}$ s^{-1} for vitreous silica [98]); (iii) the incorporation of network carbon into the silicate network leads to a decrease of the steady-state creep rates in SiOC glasses as compared to those recorded for pure vitreous silica – this is manifested as an increase in their viscosity of about 2 orders of magnitude; analogous to Young's modulus, this improved creep resistance was attributed to the increased connectivity of the SiOC glass network [44, 73]; for SiOC glass ceramics, the presence of β-SiC nanoparticles leads to an increase in viscosity in comparison to vitreous silica [97]; (iv) the incorporation of segregated carbon leads to a further decrease of the steady-state-creep rates in both SiOC glasses and glass ceramics [44, 73, 74, 97]; (*v*) the incorporation of MO_x in SiOC glass ceramics leads to a decrease in the amount of segregated carbon and consequently to an increase in steady-state creep rates [74]. A quantitative assessment of the different influences is missing so far.

The apparent activation energy of the creep process in SiOC glasses was determined to be 296 kJ/mol [73] for the compositions with relatively low carbon content, being considerably lower than for vitreous silica containing metal impurities (712 kJ/mol) [98]. This is valid for temperatures up to 1200 °C. At higher temperatures, the SiOC glasses start to partition upon precipitation of small β-SiC nanoparticles, leading to a strain hardening during phase separation. The reported values for the activation energy of deformation for SiOC glass ceramics determined from viscosity measurements and for the activation energy of creep scatter (*cf.* Table 2-2) although some samples exhibit similar compositions (259 – 463 kJ/mol [43, 60, 74, 97]; 386 and 476 kJ/mol for SiMOC [74]). However, all of the determined values are considerably lower in comparison to vitreous silica with metal impurities (712 kJ/mol) [98].

Interestingly, the creep strain in SiOC glasses and glass ceramics was shown to be partially recoverable [97, 99]. This viscoelastic behavior was attributed to the presence of the segregated carbon phase, which deforms elastically. The presence of viscoelasticity in SiOC materials suggests that the segregated carbon phase is present as an interconnected network [99].

Table 2-2: Activation energy for creep and stress exponent of SiOC glasses and glass ceramics reported in literature. Values for vitreous silica are displayed as reference.

Composition	$T_{synthesis}$ [° C]	Q [kJ/mol]	Stress exponent n
SiOC glasses			
$SiO_{1.39}C_{0.30}$ + 0.02 C [73]	1000	296	–
SiOC glass ceramics			
$SiO_{1.53}C_{0.24}$ + 0.36 C [43] 79.7 SiO_2, 11.2 SiC, 9.1 C [vol.%]	1650	400[a)]	–
SiO_xC_y (14 wt.% C) [60]	1650	259[a)]	–
$SiO_{1.60}C_{0.21}$ + 0.45 C [74] 77.5 SiO_2, 9.1 SiC, 13.4 C [vol.%]	1600	283	0.69-1.02
$SiO_{1.39}C_{0.31}$ + 0.01 C [97] 82.7 SiO_2, 16.9 SiC, 0.4 C [vol.%]	1600	463	–
$SiO_{1.37}C_{0.32}$ + 0.17 C [97] 77.5 SiO_2, 16.6 SiC, 5.9 C [vol.%]	1600	290	–
Vitreous silica [98]		510-712	–

[a)] Activation energy of deformation as determined from viscosity measurements

2.1.3 Thermal properties – Thermal expansion, specific heat capacity and thermal transport

Most polycrystalline and isotropic materials exhibit a volume expansion with increasing temperature as expressed by a positive coefficient of (linear) thermal expansion (CTE). Both, pure SiOC glasses and glass ceramics are reported to exhibit low CTEs of few ppm·K^{-1}, being though approximately one order of magnitude higher than that of pure vitreous silica (*cf*. Table 2-3) [43, 73, 100]. However, a systematic study on the impact of the chemical composition and phase assemblage on the CTE in the SiOC system is lacking. The chemical composition is expected to influence the CTE, since thermal expansion is regarded as an additive property in glasses (within glasses with similar network architecture) [101] and both pyrolytic carbon [102] and polycrystalline β-SiC [103] reveal higher CTEs in comparison to vitreous silica. The CTE of glasses changes at T_g and hence a dilatometric T_g can be determined via the tangent method [104]. T_g values determined from dilatometry are however expected to yield lower

values in comparison to other measurement techniques, because the pressure used to fix the sample in the device leads to a decrease of dilatometric T_g, this decrease getting more pronounced with higher pressures [96].

No data is available about the specific heat capacity c_p at room temperature or about the Debye temperature of SiOC materials. However, there is some information on the specific heat capacities of vitreous silica, glassy carbon and β-SiC at room temperature and with increasing temperature [53, 105, 106] (*cf.* Table 2-3). Vitreous silica and β-SiC possess a very similar temperature dependent specific heat capacity, whereas glassy carbon shows a slightly steeper increase.

Table 2-3: Thermal properties of dense SiOC glasses and glass ceramics reported in literature. Values for vitreous silica, carbon materials and β-SiC are included as references.

	$T_{synthesis}$ [° C]	CTE[a)] [10^{-6} K^{-1}]	c_p [J/(g·K)]	α [mm^2/s]	λ [W/(m·K)]
SiOC glasses					
$SiO_{1.39}C_{0.30}$ + 0.02 C [73]	1000	3.12	–	–	–
SiOC glass ceramics					
$SiO_{1.53}C_{0.24}$ + 0.36 C [43] 79.7 SiO_2, 11.2 SiC, 9.1 C [vol.%]	1650	3.14	–	–	–
SiO_xC_y [100]	1500	2.1	–	–	–
$SiO_{1.52}C_{0.25}$ + 0.86 C [107] 70.4 SiO_2, 10.2 SiC, 19.4 C [vol.%]	1650	–	–	–	1.8 (RT)
$SiO_{1.61}C_{0.19}$ + 0.21 C [108] 85.2 SiO_2, 9.5 SiC, 5.3 C [vol.%]	1500	–	–	–	1.37 (RT)
$SiO_{1.60}C_{0.21}$ + 0.45 C [109] 77.5 SiO_2, 9.1 SiC, 13.4 C [vol.%]	1600	–	–	–	1.3 (RT) 1.7 (800 °C)
Vitreous silica [73, 105, 110, 111]	–	0.57	0.74 (RT) 1.18 (750 °C)	0.73 (RT)	1.28 (RT) 1.78 (487 °C)
Polycrystalline β-SiC [53, 103, 112]	–	4.3 – 4.9	0.67 (RT) 1.21 (750 °C)	80.9 (RT)	178 (RT)
Pyrolytic carbon [102]	–	4 – 6	–	–	–
Glassy carbon [106]	–	–	0.73 (RT) 1.67 (750 °C)	5 (RT) 4.4 (700°C)	–
Amorphous carbon [113]	–	–	–	–	1.59 (RT) 2.62 (800 °C)

[a)] in the linear range

The thermal transport in solid material is proceeding via lattice vibrations (movement of phonons) [114, 115]. Consequently, the thermal transport is reduced if phonon scattering centers are present. These include in general defects and foreign ions in crystal lattices [115]. Thermal diffusivity α and thermal conductivity λ are connected via heat capacity and density ρ as displayed in Equation 2-9.

$$\lambda(T) = \alpha(T) \cdot c_p(T) \cdot \rho(T) \tag{2-9}$$

Typically, glasses show low thermal transport due to their disordered structure [114]. For instance, vitreous silica possesses very low thermal diffusivity and conductivity, as summarized in Table 2-3. Few data are available on the thermal conductivity of SiOC glass ceramics at room temperature [107, 108, 116], however similar values to vitreous silica were determined (*cf.* Table 2-3). Gurlo *et al.* investigated the temperature-dependent thermal conductivity of glass ceramics and revealed an almost identical behavior to vitreous silica [109]. Hence, it was suggested that the continuous vitreous silica matrix is governing the thermal conductivity of SiOC glass ceramics containing a moderate amount of carbon. However, for thermal conductivity in composite materials (including 3D interconnected networks and particulate systems) there is a variety of theoretical formulae which try to rationalize the impact of the constituting phases [117-120], proving that thermal conductivity is a complex interplay between their distribution, shape and volume fractions.

2.2 Compositional and structural aspects of the investigated SiOC samples

The content of this chapter is published in:

[3] **C. Stabler**, F. Roth, M. Narisawa, D. Schliephake, M. Heilmaier, S. Lauterbach, H.J. Kleebe, R. Riedel, E. Ionescu, High-temperature creep behavior of a SiOC glass ceramic free of segregated carbon, *Journal of the European Ceramic Society*, 36(15) (2016) 3747-3753.

[4] **C. Stabler**, D. Schliephake, M. Heilmaier, T. Rouxel, H.J. Kleebe, M. Narisawa, R. Riedel, E. Ionescu, Influence of SiC/Silica and Carbon/Silica Interfaces on the High-Temperature Creep of Silicon Oxycarbide-Based Glass Ceramics: A Case Study, *Advanced Engineering Materials*, 1800596 (2018) 1-11.

[5] **C. Stabler**, C. Seemüller, A. Choudhary, M. Heilmaier, S. Lauterbach, H.J. Kleebe, E. Ionescu, Synthesis and high-temperature creep behavior of a SiLuOC-based glass-ceramic, *Journal of the Ceramic Society of Japan*, 124(10) (2016) 1006-1012.

[6] **C. Stabler**, A. Reitz, B. Albert, P. Stein, R. Riedel, E. Ionescu, Thermal Properties of SiOC Glasses and Glass Ceramics at Elevated Temperatures, *Materials*, 11(279) (2018) 1-18.

As already pointed out, the SiOC system does not have a fixed chemical composition and the microstructure is depending on the synthesis temperature. In order to understand their varying elastic, plastic and thermal properties as summarized in the previous chapter, it is essential to correlate these properties to the corresponding composition and microstructure. The investigated series of SiOC samples in this study allows for the differentiation of three different aspects of the SiOC system influencing their intrinsic properties:

(1) Varying amount of segregated carbon
(2) Varying microstructure (i.e. SiOC glass vs. glass ceramic)
(3) Varying phase assemblage in the systems SiO_2-SiC-C and SiO_2-SiC-C-$Lu_2Si_2O_7$

These aspects will be addressed in the following and highlighted for each sample series. All samples investigated in this study were carefully characterized, which will be elaborated in the present chapter. Table 2-4 and Table 2-5 summarize the compositions of all investigated samples and Figure 2-6 additionally displays the ternary SiOC samples.

A varying amount of segregated carbon could be realized as denoted by corresponding numbers (C1 refers to 1 vol.%, C12 to 12 vol.%, C16 to 16 vol.% and C17 to 17 vol.% of segregated carbon), while keeping the amount of β-SiC nanoparticles in a comparable range among the samples C1-SiOC to C16-SiOC as indicated by the dashed line in Figure 2-6. However, C17-SiOC reveals a significantly higher amount of β-SiC nanoparticles.

Table 2-4: Elemental composition of the investigated SiOC samples [3-6].

	Chemical Formula	Si [wt.%][a)]	O [wt.%]	C [wt.%]	Lu [wt.%]
C1-SiOC-1100	$SiO_{1.38}C_{0.32}$	52.00±1.04	40.81±0.66	7.19±0.43	–
C1-SiOC-1600	$SiO_{1.41}C_{0.30}$	51.78±1.04	41.59±0.33	6.63±0.40	–
C12-SiOC-1600	$SiO_{1.50}C_{0.71}$	46.36±0.93	39.52±0.23	14.12±0.29	–
C16-SiOC-1600	$SiO_{1.27}C_{0.97}$	46.79±0.94	33.82±0.96	19.39±0.12	–
C17-SiOC-1600	$SiO_{0.94}C_{1.13}$	49.56±0.99	26.57±0.46	23.87±0.22	–
SiC/SiO_2-1600	$SiO_{1.47}C_{0.24}$	51.59±1.03	43.03±0.22	5.38±0.32	–
C/SiO_2-1600	$SiO_{1.94}C_{0.53}$	42.92±0.86	47.36±0.54	9.72±0.29	–
SiLuOC-1600	$SiLu_{0.03}O_{1.51}C_{0.68}$	42.93±0.86	36.74±0.23	12.36±0.34	7.97±0.3

[a)] assumed relative standard deviation = 2%

Table 2-5: Phase composition of the investigated SiOC samples [3-6]. Volume fractions were calculated using the following densities: ρ(SiO_2) = 2.20 g/cm³ [43], ρ(β-SiC) = 3.22 g/cm³ [121], ρ(C_{segr}) = 1.82 g/cm³ (Graphitized Mesoporous Carbons GMC, Sigma-Aldrich, CAS-# 1333-86-4). ρ($Lu_2Si_2O_7$) = 6.21 g/cm³ [122].

	SiO_2 [mol.%]	SiC [mol.%]	C_{segr} [mol.%]	SiO_2 [vol.%]	SiC [vol.%]	C_{segr} [vol.%]	$Lu_2Si_2O_7$ [vol.%]
C1-SiOC-1100	68.1[a)] ±1.1	30.7[a)] ±2.3	1.2[a)] ±2.9	–	–	–	–
C1-SiOC-1600	70.2 ±0.5	29.3 ±2.1	0.5 ±2.7	83.1 ±0.4	16.8 ±1.2	0.1 ±0.7	–
C12-SiOC-1600	51.3 ±0.3	17.2 ±1.4	31.5 ±1.7	75.7 ±0.4	12.3 ±1.0	11.9 ±0.7	–
C16-SiOC-1600	39.6 ±1.1	22.8 ±1.7	37.6 ±1.7	65.7 ±1.9	18.3 ±1.3	16.0 ±0.7	–
C17-SiOC-1600	29.5 ±0.5	33.1 ±1.4	37.4 ±1.5	53.5 ±0.9	29.1 ±1.2	17.4 ±0.7	–
SiC/SiO_2-1600	73.2 ±0.4	26.8 ±2.0	0	85.7 ±0.4	14.3 ±1.1	0	–
C/SiO_2-1600	64.6 ±0.7	2.1 ±1.5	33.3 ±1.9	87.2 ±1.0	1.3 ±1.0	11.5 ±0.6	–
SiLuOC-1600	50.4 ±0.4	19.5 ±1.5	29.0 ±2.0	71.2 ±0.5	13.4 ±1.0	10.5 ±0.7	4.9 ±0.2

[a)] molar fractions of SiC and SiO_2 can be regarded as the amount of Si-C and Si-O bonds, respectively.

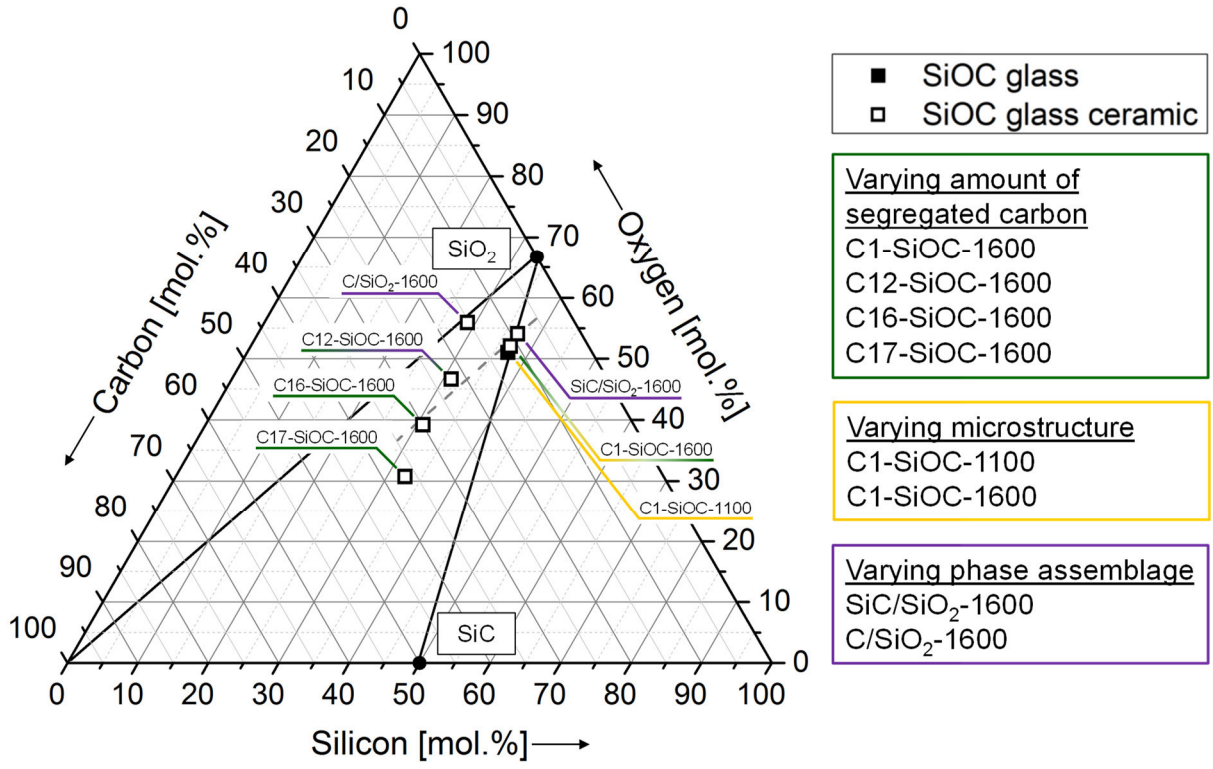

Figure 2-6: Elemental composition of the ternary SiOC samples, revealing the different compositional and microstructural aspects of the investigated samples.

The degree of graphitization of the segregated carbon phase as expressed by the average crystallite size L_a and the average defect distance L_D (calculated from the ratio of areas A_D/A_G beneath the D and G band, respectively [123, 124]) does not change significantly within this series of samples, which was proven by Raman spectroscopy (7.5-9.5 nm; *cf.* Table 2-6). This observation enables an unbiased assessment of the impact of the amount of segregated carbon in SiOC glass ceramics on the intrinsic properties. Additionally, L_a and L_D for sample C/SiO_2-1600 fall in the same range. The segregated carbon in the investigated glass ceramics can be regarded as turbostratic carbon as already investigated in detail by [36].

Table 2-6: Indicators for the degree of graphitization of the segregated carbon phase L_a and L_D as determined from Raman spectroscopy for the investigated SiOC glass ceramics [4, 6].

Sample	A_D/A_G	L_a [nm]	L_D [nm]
C1-SiOC-1600	4.868±1.074	7.9±1.7	7.7±0.8
C12-SiOC-1600	4.215±0.251	9.2±0.6	8.3±0.3
C16-SiOC-1600	4.121±0.521	9.5±1.3	8.4±0.6
C17-SiOC-1600	4.998±0.340	7.5±0.5	7.5±0.2
C/SiO_2-1600	5.164±0.108	7.5±0.2	7.7±0.2

In addition to several SiOC glass ceramics (denoted by their synthesis temperature of 1600 °C), one SiOC glass (denoted by its synthesis temperature of 1100 °C) was synthesized. The elemental composition of C1-SiOC-1100 and C1-SiOC-1600 is not significantly affected during phase separation. However, XRD and ^{29}Si MAS NMR evidence, that the microstructure is changing. C1-SiOC-1100 is X-ray amorphous as shown in Figure 2-7 and possesses the full range of $SiO_{4-x}C_x$ mixed-bonds tetrahedra [13]. On the other hand, C1-SiOC-1600 reveals broad reflections related to β-SiC nanoparticles [121] and a broad halo caused by vitreous silica. In C1-SiOC-1600, only SiO_4 and SiC_4 tetrahedra are detected in ^{29}Si MAS NMR [97]. Consequently, upon comparison of C1-SiOC-1100 and C1-SiOC-1600, the impact of the phase separation on the mechanical and thermal properties of SiOC can be assessed exclusively. Additionally, XRD results shown in Figure 2-7 and ^{29}Si MAS NMR spectra already published in literature [97] prove that phase separation has occurred in samples C12-SiOC-1600, C16-SiOC-1600 and C17-SiOC-1600 and that they can be regarded as SiOC glass ceramics.

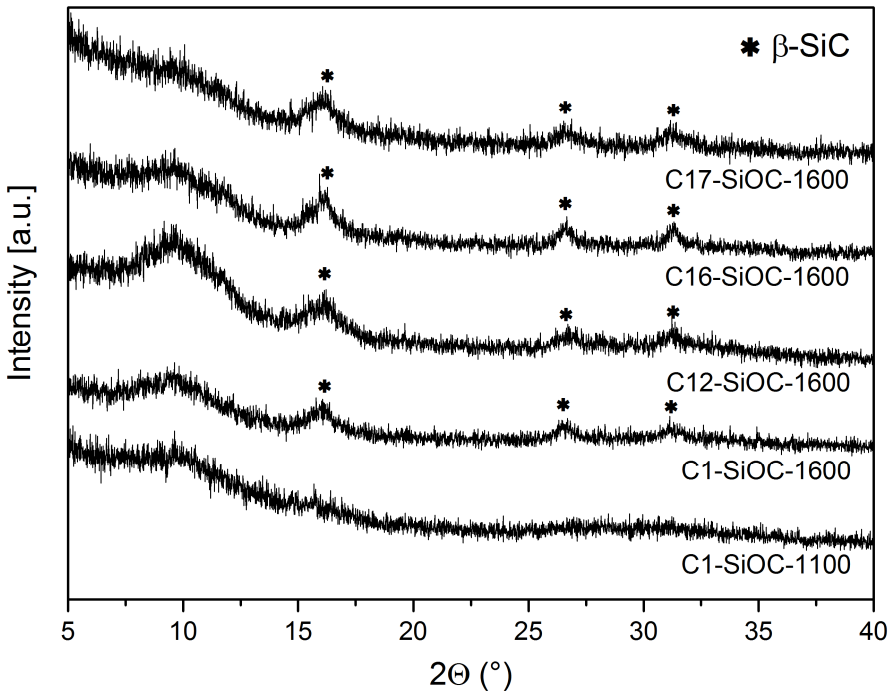

Figure 2-7: XRD spectra of selected SiOC samples revealing the presence of β-SiC nanoparticles [121] for all samples synthesized at 1600 °C, whereas sample C1-SiOC-1100 is fully X-ray amorphous [6].

In order to address the impact of different phase assemblages on the properties of SiOC glass ceramics, two binary compositions (lying on the tie lines SiC-SiO_2 and C-SiO_2, respectively) and one quaternary composition (SiLuOC-1600) were synthesized. Sample SiC/SiO_2-1600 possesses β-SiC nanoparticles but lacks the segregated carbon phase, whereas sample C/SiO_2-1600 comprises only a segregated carbon phase but no β-SiC nanoparticles. This difference is supported by TEM imaging shown in Figure 2-8, XRD and Raman spectra depicted in Figure

2-9 and ^{29}Si MAS NMR spectra shown in Figure 2-10. TEM, XRD and ^{29}Si MAS NMR testify the absence of β-SiC nanoparticles in sample C/SiO_2-1600 (Figure 2-8a, Figure 2-9a and Figure 2-10), whereas the segregated carbon phase is not visible for sample SiC/SiO_2-1600 in TEM (Figure 2-8b) and Raman spectroscopy (Figure 2-9b). Both samples do not exhibit mixed-bonds silicon tetrahedra as revealed by ^{29}Si MAS NMR (*cf.* Figure 2-10) and possess a silica-based amorphous matrix as evidenced by TEM imaging (*cf.* Figure 2-8) and XRD (*cf.* Figure 2-9a). To conclude, SiC/SiO_2-1600 and C/SiO_2-1600 can be considered as binary SiOC glass ceramics in the systems SiO_2-SiC and SiO_2-C, respectively.

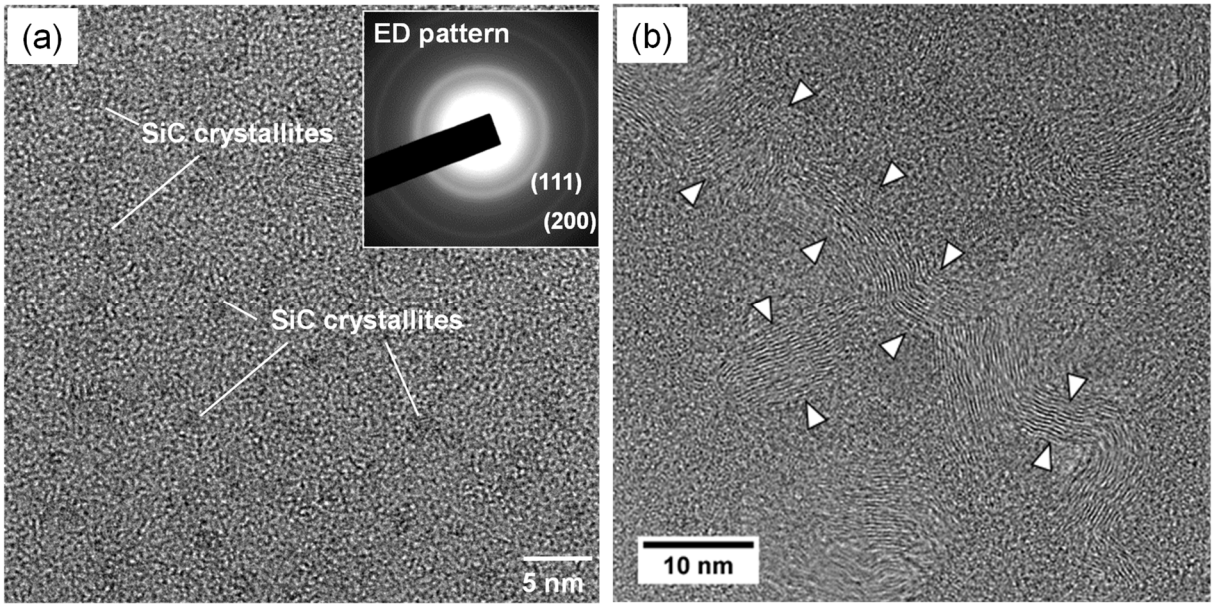

Figure 2-8: TEM images of (a) SiC/SiO_2 revealing the presence of β-SiC nanoparticles indicated by the electron diffraction (ED) pattern and the absence of segregated carbon and (b) C/SiO_2 proving the absence of β-SiC nanoparticles, while the white arrows mark the segregated carbon phase. Both samples possess a silica-based amorphous matrix [3, 4].

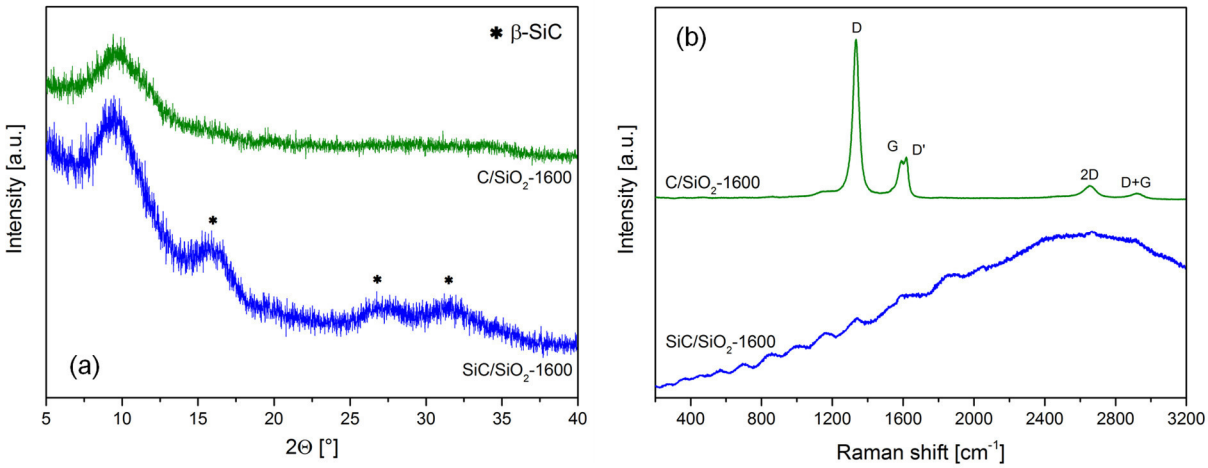

Figure 2-9: XRD and Raman Spectra of SiC/SiO_2-1600 and C/SiO_2-1600 revealing the difference in the presence/absence of β-SiC nanoparticles [121] and the segregated carbon phase; (a) XRD; wavelength Mo K_α [4]; (b) Raman spectroscopy; 633 nm; all bands assigned are related to disordered sp^2-hybridized carbons [125].

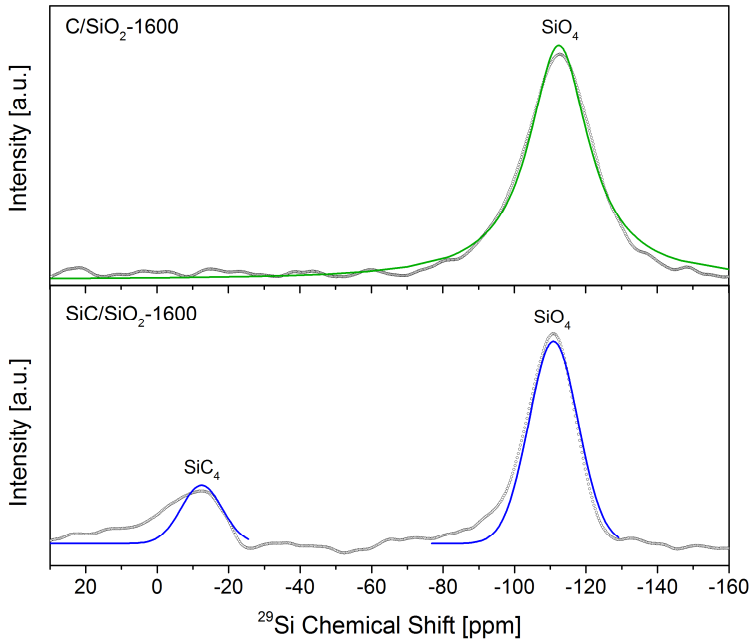

Figure 2-10: 29Si MAS NMR spectra of SiC/SiO2-1600 and C/SiO2-1600 [3, 4] revealing the difference in the presence/absence of β-SiC nanoparticles; the green lines represent the deconvoluted shifts caused by SiO_4 and SiC_4 tetrahedra [41].

In contrast, sample SiLuOC-1600 introduces monoclinic $Lu_2Si_2O_7$ in addition to β-SiC nanoparticles and the segregated carbon phase as dispersed phase which is evidenced by XRD (*cf.* Figure 2-11). TEM imaging reveals almost spherical $Lu_2Si_2O_7$ particles of approximately 50 nm in size as shown in Figure 2-11b. The elemental composition was assessed with a combined approach of elemental analysis and Rietveld refinement using an internal standard approach. 10 wt.% NIST SRM 676 alumina standard was used as internal standard. The appropriate amount of 10 wt.% was estimated from [126]. Mixing was performed in isopropanol with a milk frother and subsequent filtration and drying at 120 °C for 10 minutes. The mixing approach was tested and approved by several mixtures of corundum and periclase of known crystallinity (100 % after thermal annealing according to the experimental parameters described in [127]). The amount of crystalline monoclinic $Lu_2Si_2O_7$ was determined from this XRD approach and the elemental amount of lutetium in SiLuOC-1600 was subsequently calculated provided that all lutetium atoms are incorporated in the crystalline phase. The amount of oxygen and carbon was taken directly from elemental analysis. The amount of silicon was assumed to be the difference to 100 wt.% under the assumption that no other elements are present in SiLuOC-1600. As SiLuOC-1600 was synthesized from the same polymeric precursor as sample C12-SiOC-1600 replacing 15 wt.% by Lu(III)acetate hydrate, the basic phase composition is close to C12-SiOC-1600 (*cf.* Table 2-4 and Table 2-5). The incorporation of $Lu_2Si_2O_7$ is mainly proceeding at the expense of the vitreous silica matrix. Consequently, upon comparison of C12-SiOC-1600 and SiLuOC-1600, the impact of the addition of a metal silicate

on the properties of SiOC glass ceramics can be assessed. $Lu_2Si_2O_7$ is known to have a beneficial impact on the oxidation resistance in Si_3N_4 ceramics [128].

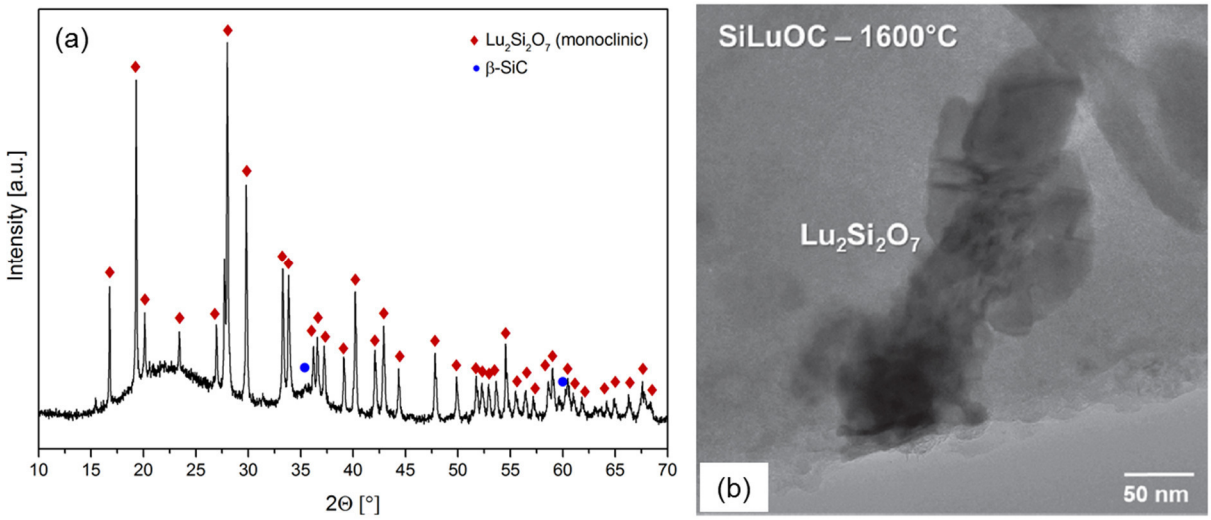

Figure 2-11: (a) XRD spectra of SiLuOC-1600 [5] revealing the presence of monoclinic $Lu_2Si_2O_7$ [122] in addition to β-SiC nanoparticles [121] (wavelength Cu K_α). (b) TEM imaging revealing almost spherical $Lu_2Si_2O_7$ particles (ca. 50 nm in size) [5].

All synthesized samples, except C17-SiOC-1600, which exhibits a small amount of porosity, are fully dense and crack-free as evidenced by the determination of open porosity upon immersion in water (*cf.* Table 2-7) and SEM imaging (not shown). Consequently, the samples allow the precise determination of the intrinsic elastic, plastic and thermal properties of SiOC.

Table 2-7: Skeletal density and porosity of the investigated SiOC glass and glass ceramics [3, 4, 6].

Sample	Skeletal density [g/cm^3]	Open porosity [vol.%]	Closed porosity [vol.%]
C1-SiOC-1100	2.28	0.3	0
C1-SiOC-1600	2.38	0	0
C12-SiOC-1600	2.31	0	0
C16-SiOC-1600	2.34	0	0
C17-SiOC-1600	2.33	1.6	7.0
SiC/SiO_2-1600	2.36	0	0
C/SiO_2-1600	2.20	0	0
SiLuOC-1600	2.46	0	0

To conclude, several series of dense SiOC samples were synthesized and characterized with respect to composition and microstructure. Samples prepared at 1100 °C can be regarded as SiOC glasses, whereas samples prepared at 1600 °C can be addressed as SiOC glass ceramics,

consisting of a vitreous silica matrix and different dispersed phases (β-SiC nanoparticles, segregated carbon and $Lu_2Si_2O_7$), their presence and abundance being alternated in the individual samples. Different phase assemblages are realized, yielding binary (SiC/SiO_2-1600 and C/SiO_2-1600; comprising either β-SiC nanoparticles or segregated carbon, respectively), ternary (C1-SiOC to C17-SiOC; both, β-SiC nanoparticles and the segregated carbon phase being present) and quaternary (SiLuOC-1600; containing β-SiC nanoparticles, segregated carbon and $Lu_2Si_2O_7$) SiOC glass ceramics. Additionally, among the ternary SiOC glass ceramics, the volume fraction of segregated carbon is varying between 0 and 17 vol.%, while most samples show a constant volume fraction of β-SiC nanoparticles.

2.3 Local deformation behavior of SiOC glasses and glass ceramics

2.3.1 Elastic behavior, indentation hardness and strain-rate sensitivity of SiOC glasses and glass ceramics

The content of this chapter is published in:

[2] **C. Stabler**, F. Célarié, T. Rouxel, R. Limbach, L. Wondraczek, R. Riedel, E. Ionescu, Effect of composition and high-temperature annealing on the local deformation behavior of silicon oxycarbides, *Journal of the European Ceramic Society,* 39(7) (2019) 2287-2296.

The present chapter will be dealing with the impact of varying amounts of segregated carbon and varying microstructure on elastic properties, i.e. Young's modulus and Poisson's ratio and on several plastic properties of SiOC, i.e. indentation hardness and strain-rate sensitivity.

As already discussed in chapter 2.1.2, SiOC glasses and glass ceramics exhibit Young's moduli in a wide range but generally reveal higher values in comparison to vitreous silica. In order to rationalize the impact of measurement technique, composition and microstructure, Young's modulus measured at room temperature is shown in Figure 2-12a and b as function of the volume fractions of the segregated carbon phase and β-SiC (in case of SiOC glasses, fraction of Si-C bonds), respectively. Values determined in this study (colored symbols; summarized in Table 2-8) are compared to values available in literature (black symbols). Depending on the measurement technique used, Young's modulus of SiOC samples with identical compositions varies within ca. ± 5 GPa (i.e., ca. ±5%). Consequently, in order to establish general rules for tuning Young's modulus, values obtained from the same measurement technique must be considered. Upon comparison of SiOC glasses and glass ceramics, it can be seen that the phase separation does not drastically affect Young's modulus. The major factor governing Young's modulus in SiOC is the chemical composition. The incorporation of segregated carbon lowers Young's modulus especially when taking [46] into account, following a linear trend. However, a clear linear dependence with even less scatter is seen between Young's modulus and the volume fraction of β-SiC (or in the case of glasses Si-C bonds). This is considered to correlate to the relatively large Young's modulus of the β-SiC nanoparticles that is estimated to lie in the range of 300 GPa [129]. Values in literature show a high scatter due to residual porosity and intrinsic difficulties for some measurement techniques (different loads in indentation measurements and calibration of the bending experiments). Concentrating on the samples of this study and on values obtained from resonant frequency damping analysis (RFDA) (which is considered as a very reliable technique for the determination of Young's modulus), it seems that the contribution of the β-SiC nanoparticles is significantly higher than that of the segregated

carbon phase: sample C16-SiOC-1600, possessing the highest amount of β-SiC nanoparticles, reveals the highest value for Young's modulus among the investigated SiOC glass ceramics (*cf.* values obtained from RFDA) despite showing the highest amount of segregated carbon. This dependency was already suggested by Soraru et al. for a significantly smaller compositional range of SiOC glasses and for thin films [61, 130] and is extended now in this study to bulk SiOC glasses with higher amounts of segregated carbon and monolithic SiOC glass ceramics.

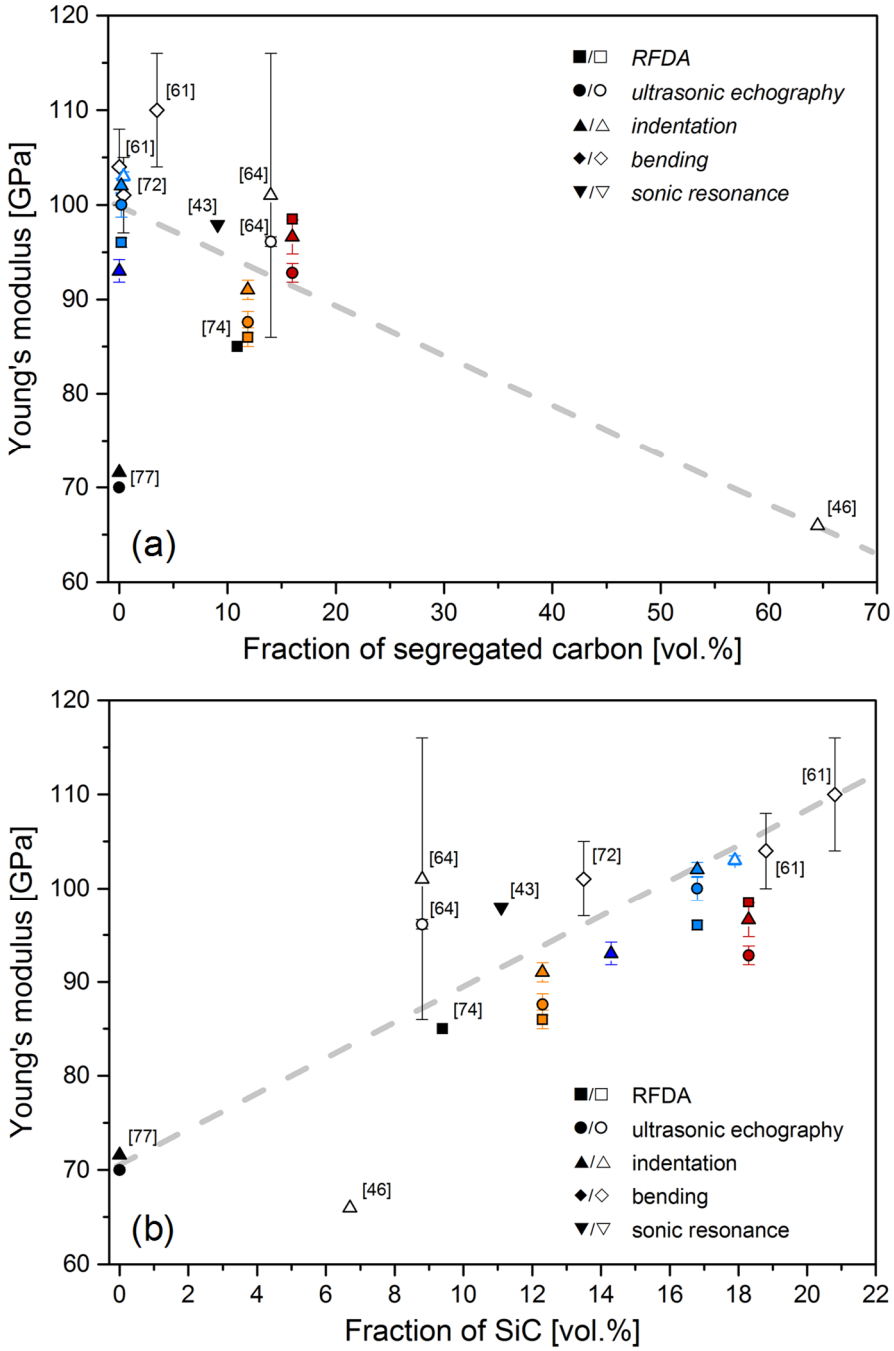

Figure 2-12: Room temperature Young's modulus of ternary SiOC glasses (open symbols) and glass ceramics (filled symbols) as a function of (a) volume fraction of segregated carbon and (b) the volume fraction of Si-C bonds (as for SiOC glass) or β-SiC (as for SiOC glass ceramics). Values from literature (black symbols) are compared to values measured for a SiOC glass and glass ceramics in this study (colored symbols). The gray dashed lines serve to guide the eye [2].

Figure 2-13 reveals stiffening of the investigated SiOC glass ceramics with increasing temperature as measured by RFDA. This rare behavior is already described in literature for one SiOC glass, one SiOC glass ceramic and vitreous silica [73, 74, 131]. In vitreous silica, stiffening is attributed to continuous atomic displacements during an amorphous-amorphous transformation – similar to those associated with the α- to β-cristobalite phase transformation [62, 132]. Since stiffening is independent of the phase composition of the SiOC glass ceramics investigated in this study, it is now clarified that this behavior is governed by the glassy silica matrix which is undergoing the same mechanism like in pure vitreous silica. The amorphous-amorphous transformation is reversible, as the samples did not show hysteresis in the cooling cycles.

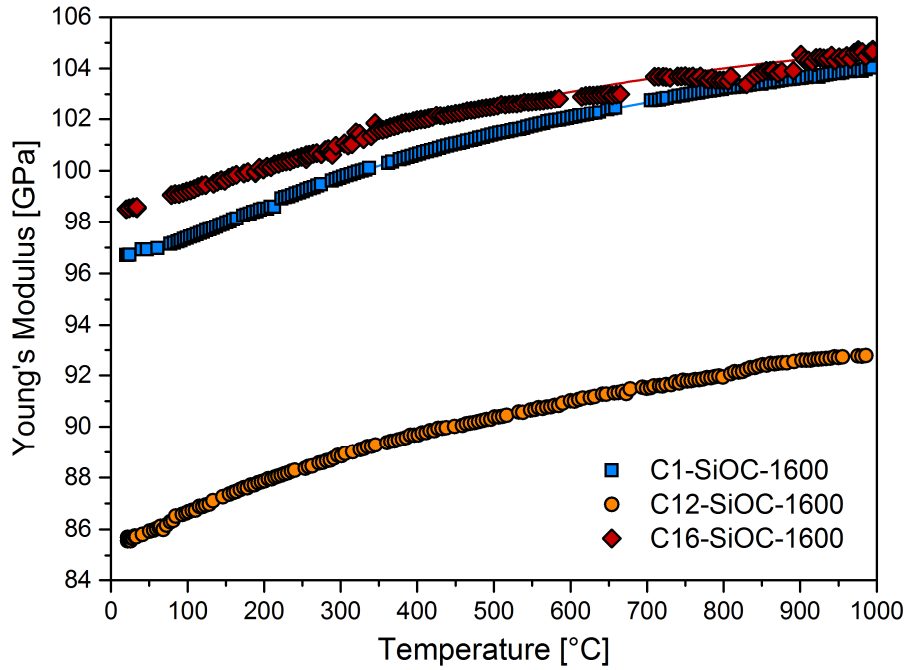

Figure 2-13: Temperature-dependent Young's modulus of selected ternary SiOC glass ceramics. All samples show stiffening with increasing temperature [2].

Similar to Young's modulus, hardness (H) is governed by the average bond strength of the material [133]. The values for SiOC materials determined by nanoindentation are in the range between 10.5 to 11.4 GPa and consequently higher in comparison to vitreous silica (*cf.* Table 2-8). The enhanced network connectivity and the accompanied presence of additional network constraints as described already for silicon oxynitride (SiON) glasses [134] are expected to be responsible for this increase in hardness. The results obtained in this study by nanoindentation are higher than the results stated in literature, typically assessed as Vicker's microhardness (*cf.* chapter 2.1.2), which is caused by the difference in the measurement technique. Phase separation significantly affects indentation hardness, which is evidenced by comparison of C1-SiOC-1100 (H = 11.4 GPa) and C1-SiOC-1600 (H = 11.0 GPa). As previously stated for Young's

modulus, the chemical composition is the governing factor for hardness in SiOC, which is clearly evidenced by the SiOC glass ceramics investigated in this study. Sample C1-SiOC-1600 reveals the highest hardness and at the same time the highest volume fraction of β-SiC. Consequently, higher amounts of β-SiC lead to an increased hardness. This observation is in accordance with the comparably higher hardness of polycrystalline β-SiC (H_V = 27.1 to 34.1 GPa [135]). In contrast, a comparison of SiC/SiO_2-1600 (H = 10.6 GPa) and C12-SiOC-1600 (H = 10.5 GPa) shows that the amount of segregated carbon does not affect hardness, with both samples having a comparable amount of β-SiC, however 0 and 12 vol.% segregated carbon, respectively.

In addition to Young's modulus and hardness, Poisson's ratio is as well intimately linked to the glassy network topology. Thus, further information about the glassy networks can be extracted from the calculation of Poisson's ratio according to equation 2-4. SiOC glasses show low Poisson's ratio of 0.11 [64] (*cf.* chapter 2.1.2). The SiOC glass ceramics investigated in this study reveal values between 0.17 and 0.18 (*cf.* Table 2-8), being close to those known for vitreous silica between 0.15 and 0.18 [65-70]. Consequently, Poisson's ratio indicates, that the plastic deformation of SiOC glass ceramics is governed by the vitreous silica matrix as it is the negative ratio of transverse to axial strain. Moreover, phase separation leads to a higher atomic packing density due to the decrease of the network connectivity. The further increase of Poisson's ratio in sample C1-SiOC-1600 to 0.20 at T_{meas} = 1000 °C indicates, that the mechanisms leading to the stiffening during temperature increase (*cf.* Young's modulus) are at least partially resulting from an increase in the atomic packing density (as expressed by changes in Poisson's ratio). This is in line with the suggested structural amorphous-amorphous rearrangements in vitreous silica [62, 132].

For a potential application of SiOC glasses and glass-ceramics at elevated temperatures, a high creep resistance, i.e., low strain-rate sensitivity, is of paramount importance. Using a nanoindentation strain-rate jump test, very low strain-rate sensitivities of 0.0059 to 0.0107 were determined for the SiOC glass and glass-ceramics. These values are close to those reported for vitreous silica (m = 0.0068 – 0.0150), which displays no significant creep deformation at room temperature. Consequently, the creep response of SiOC materials is expected to be determined by the creep resistance of the vitreous silica glass matrix as already indicated by Poisson's ratio. A slight increase of the strain-rate sensitivity of SiOC glass ceramics from 0.0060 (SiO_2/SiC-1600) to 0.0107 (C12-SiOC-1600) is recorded with increasing amounts of segregated carbon. This indicates, that fertile sites for a shear-mediated plastic flow are created inside the material with the incorporation of the segregated carbon phase.

Table 2-8: Room temperature elastic properties and plasticity of a ternary SiOC glass and glass-ceramics [2]: Young's modulus E, shear modulus G, bulk modulus K, Poisson's ratio υ, hardness H and strain-rate sensitivity m. Literature data for Suprasil vitreous silica [77] are added for comparison.

Sample	RFDA			Ultrasonic Echography				Nanoindentation		
	E [GPa]	G [GPa]	ν	E [GPa]	G [GPa]	K [GPa]	ν	E [GPa]	H [GPa]	m
C1-SiOC-1100	–	–	–	–	–	–	–	101.7±0.5	11.4±0.1	0.0059
C1-SiOC-1600	96 ± 1.0	41	0.18	100.2±1.3	42.7±0.2	51.4±0.6	0.175±0.003	101.1±0.8	11.0±0.1	0.0074
C12-SiOC-1600	86 ± 1.0	37	0.17	87.6±1.1	37.6±0.2	43.7±0.6	0.166±0.003	90.4±1.0	10.5±0.1	0.0107
C16-SiOC-1600	99	–	–	92.8±1.0	39.7±0.2	46.5±0.5	0.167±0.002	96.6±1.8	10.6±0.2	–
SiO_2/SiC-1600	–	–	–	–	–	–	–	92.8±1.2	10.6±0.2	0.0060
SiO_2 (Suprasil) [77]	–	–	–	70.0	39.9	35.4	0.170	71.6±0.3	9.3±0.1	0.0068

To summarize, the amount of Si-C bonds/β-SiC is the dominating factor influencing Young's modulus and hardness of SiOC glasses and glass ceramics. The amount of segregated carbon has only minor influence on these properties, but it is important for the mechanism of plastic deformation in SiOC. However, the plastic deformation on a macroscopic scale of SiOC glass ceramics is expected to be governed by their vitreous silica matrix.

2.3.2 High-temperature creep of SiOC glass ceramics – influence of the interfaces

The content of this chapter is partially published in:

[2] **C. Stabler**, F. Célarié, T. Rouxel, R. Limbach, L. Wondraczek, R. Riedel, E. Ionescu, Effect of composition and high-temperature annealing on the local deformation behavior of silicon oxycarbides, *Journal of the European Ceramic Society,* 39(7) (2019) 2287-2296.

[3] **C. Stabler**, F. Roth, M. Narisawa, D. Schliephake, M. Heilmaier, S. Lauterbach, H.J. Kleebe, R. Riedel, E. Ionescu, High-temperature creep behavior of a SiOC glass ceramic free of segregated carbon, *Journal of the European Ceramic Society*, 36(15) (2016) 3747-3753.

[4] **C. Stabler**, D. Schliephake, M. Heilmaier, T. Rouxel, H.J. Kleebe, M. Narisawa, R. Riedel, E. Ionescu, Influence of SiC/Silica and Carbon/Silica Interfaces on the High-Temperature Creep of Silicon Oxycarbide-Based Glass Ceramics: A Case Study, *Advanced Engineering Materials*, 1800596 (2018) 1-11. Doi: 10.1002/adem.201800596.

[5] **C. Stabler**, C. Seemüller, A. Choudhary, M. Heilmaier, S. Lauterbach, H.J. Kleebe, E. Ionescu, Synthesis and high-temperature creep behavior of a SiLuOC-based glass-ceramic, *Journal of the Ceramic Society of Japan*, 124(10) (2016) 1006-1012.

The present chapter will describe how the high-temperature creep behavior of SiOC glass ceramics changes with varying amounts of segregated carbon and varying phase assemblages, comparing binary, ternary and quaternary SiOC glass ceramics. Additionally, the stability of SiOC glass ceramics upon prolonged exposure to high temperatures will be addressed.

Plastic deformation can occur in different ways, being dependent on the temperature and pressure applied as summarized in deformation mechanism maps for each material [136]. Creep is a thermally activated process and usually occurs at high temperature [81]. A fundamental concept of creep is the preservation of volume under deformation, i.e. no densification during the compression creep experiments is occurring. Precise measurements of the density using the flotation method in a density gradient column [137, 138] of C12-SiOC-1600 specimens before and after creep experiments confirm that no densification during creep

experiments is occurring. Consequently, the chosen measurement parameters (T_{meas} = 1100 – 1300 °C; σ_{true} = 50 – 200 MPa) are suitable to study the creep behavior of SiOC glass ceramics.

In order to assess the creep mechanism in SiOC glass ceramics, it must be confirmed that the samples are not changing during the measurement. As revealed in this study, long holding times of up to 14 days are necessary to achieve steady-state conditions for some samples at low true stresses and temperatures. Hence, the high-temperature stability of SiOC glass ceramics needs to be verified. This was achieved by the assessment of Young's modulus on annealed samples, as Young's modulus is intimately connected with the glass network architecture. Annealing conditions were chosen according to temperatures and holding times of respective creep experiments (for C1-SiOC-1600 6 days at 1100 °C and 2 hours at 1300 °C; for C12-SiOC-1600 and C16-SiOC-1600 6 days at 1200 °C and 12 hours at 1300 °C). A maximum increase in Young's modulus of 1.4 % for C1-SiOC-1600, 7.3 % for C12-SiOC-1600 and 8.8 % for C16-SiOC-1600 is registered after thermal annealing. This increase is however not related to a change of the glassy silica matrix as skeletal density, chemical composition, temperature sensitivity of Young's modulus and Poisson's ratio stay constant. A slightly increased ordering of the dispersed phases β-SiC nanoparticles and segregated carbon proven by XRD and Raman spectroscopy are responsible for the increase in Young's modulus after thermal annealing. However, the differences among annealed samples is smaller in comparison to the difference to the as-prepared samples. It can be concluded, that the long time exposure at high temperatures does not impair the assessment of the creep behavior because the dispersed phases can be regarded as rigid inclusions at the chosen measurements parameters for creep experiments [139, 140] and deformation is expected to occur within the glassy matrix (*cf.* Poisson's ratio and strain-rate sensitivity).

After the stability of SiOC glass ceramics during creep experiments was verified, a case study on sample C12-SiOC-1600 was additionally performed in order to assess the impact of the applied true stress on the activation energy for creep and on viscosity. The activation energy for creep does not reveal significant differences between 50 (740 kJ/mol) and 75 MPa (730 kJ/mol) applied true stress as expressed in Figure 2-14a by the slope in the Arrhenius plot of the steady-state creep rates. Consequently, the activation volume carrying the deformation is not affected in this range. The viscosity calculated using equation 2-6 (υ = 0.17, *cf.* Table 2-8) reveals slight shear thinning between 50 and 100 MPa and significantly lower values for an applied true stress of 200 MPa (*cf.* Figure 2-14b). This possibly indicates a change in creep behavior between 100 and 200 MPa. In order to compare the creep behavior of SiOC glass ceramics with different compositions, measurements were performed between 50 and 100 MPa applied true stress.

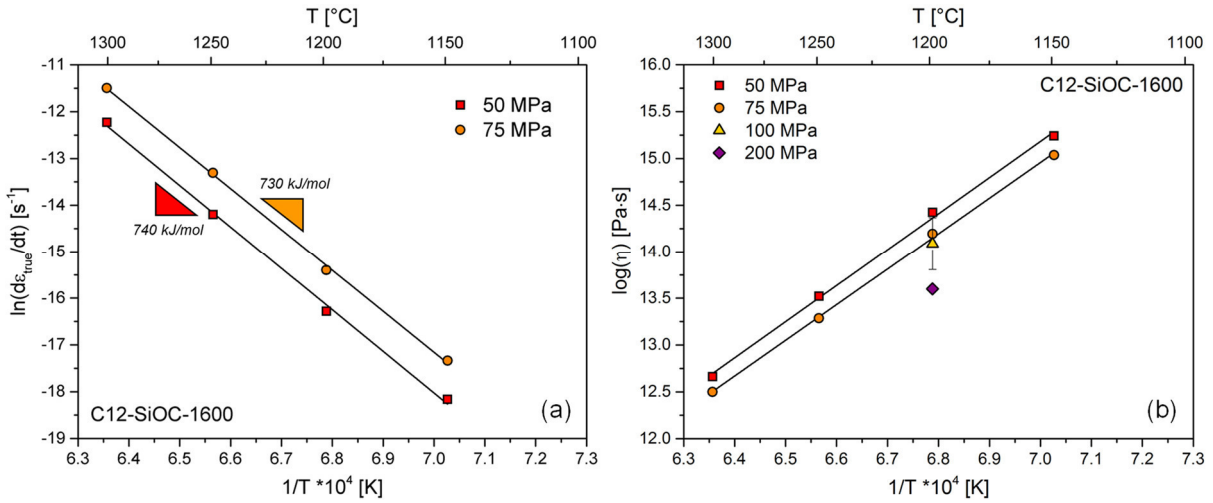

Figure 2-14: Impact of the applied true stress on (a) activation energy for creep and (b) viscosity of C12-SiOC-1600 [4].

Figure 2-15 compares the Arrhenius (a) and Norton (b) plots of C12-SiOC-1600 and the binary SiOC glass ceramics SiC/SiO_2-1600 and C/SiO_2-1600 (which lack the segregated carbon phase or β-SiC nanoparticles, respectively). The activation energy for creep is not affected by the different phase assemblages with values between 696 and 731 kJ/mol (*cf.* Table 2-9), being close to the activation energy of viscous flow in vitreous silica containing few metal impurities (712 kJ/mol) [98]. Consequently, the activation volume carrying the deformation should be similar in SiOC glass ceramics and vitreous silica containing metal impurities. Note, that SiOC glass powders were shown to possess metal impurities in the ppm range [141]. Thus, the deformation is governed, as expected from Poisson's ratio and strain-rate sensitivity (*cf.* chapter 2.3.1), by the vitreous silica matrix and the dispersed phases behave like rigid inclusions.

The values for the activation energy of creep determined in this study are significantly higher in comparison to the values published in literature for other SiOC glass ceramics [43, 60, 74, 97]. It is demonstrated in this study, that e.g. sample C12-SiOC-1600 reached the steady-state regime only after 14 days at the lower measurement temperatures and true stresses. In comparison, the measurement times were rather short (often < 0.5 days at T_{meas} < 1200 °C) in the creep studies published in literature. Hence, the creep rates of SiOC glass ceramics especially at T_{meas} < 1200 °C are expected to be overestimated in literature, which leads to a decrease of the slopes in the Arrhenius plots and consequently to underestimated activation energies for creep. In this study, special focus was placed on long holding times to ensure steady-state conditions and consequently the present values are regarded as being more accurate.

The stress exponent for all three SiOC glass ceramics is close to 2 (values range from 1.70 to 2.05, *cf.* Figure 2-15b), indicating that their creep mechanism involves sliding [89-91]

regardless of the phase assemblage. This result is in line with the slight shear thinning behavior observed between 50 and 100 MPa applied true stress (*cf.* Figure 2-14).

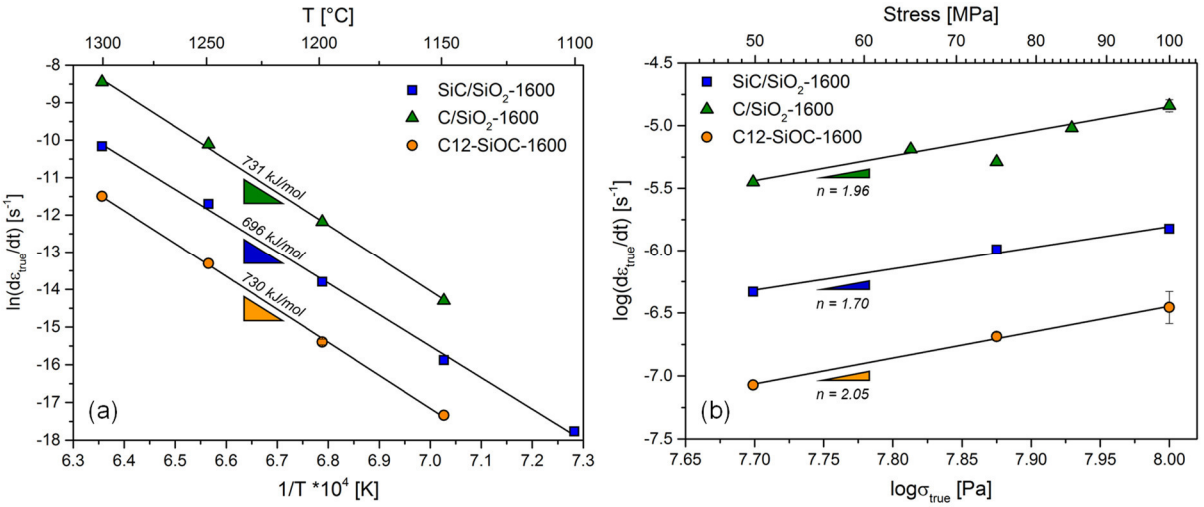

Figure 2-15: Impact of the phase assemblage of SiOC glass ceramics in the ternary system SiO_2-SiC-C on (a) activation energy ($\sigma_{true} = 75$ MPa) and (b) stress exponent (T_{meas} = 1200 °C) [4].

It can be concluded, that neither the volume fraction nor the nature of the dispersed phase among the ternary SiOC glass ceramics investigated in this study affect the activation volume and the creep mechanism (*cf.* Table 2-9), but they have a significant effect on the absolute steady-state creep rates. C12-SiOC-1600 exhibits the lowest steady-state creep rates as expected due to the highest volume fraction of dispersed phases among the investigated samples and consequently the highest degree of particle hardening [94]. Surprisingly, SiC/SiO_2-1600 reveals lower creep rates in comparison to C/SiO_2-1600, despite containing a similar amount of dispersed phase. The opposite would be expected, as the high aspect ratio segregated carbon phase should lead to a higher degree of particle hardening in comparison to spherical β-SiC nanoparticles [142, 143].

Table 2-9: Activation energy for creep and stress exponent of the investigated SiOC glass ceramics [3-5].

Sample	Activation energy for creep [kJ/mol]	Stress exponent	T_g(creep) $\eta = 10^{12.6}$ [° C]
SiC/SiO_2-1600	696 ± 17	1.70 ± 0.20	1255
C/SiO_2-1600	731 ± 15	1.96 ± 0.10	1212
C12-SiOC-1600	730 ± 14	2.05 ± 0.10	1295
SiLuOC-1600	520 ± 22 to 771[a)]	2.10 ± 0.10	1291-1295

[a)] extrapolated

This discrepancy can be further rationalized by the calculation of the viscosity, displayed in Figure 2-16a. The viscosity of SiC/SiO_2-1600 is almost 2 orders of magnitude higher in

comparison to vitreous silica, whereas sample C/SiO_2-1600 exhibits merely an increase of about 1 order of magnitude. The calculation of the effective viscosity of nanocomposites having the same phase composition as SiC/SiO_2-1600 and C/SiO_2-1600 (using equations 2-7 and 2-8 with aspect ratios of 1 for β-SiC and 10 for segregated carbon, respectively; η_0 = vitreous silica) reveals, that the spherical β-SiC nanoparticles should only lead to a slight increase of about a factor of 3 in viscosity (*cf.* Figure 2-16b). On the other hand, the calculated effective viscosity of a nanocomposite containing segregated carbon matches perfectly the measured viscosity of C/SiO_2-1600. This implies, that the increase in viscosity for C/SiO_2-1600 is caused by simple particle hardening, whereas the extraordinary increase in viscosity of sample SiC/SiO_2 should be additionally influenced by other factors. The possible impact of the nano-size of the β-SiC particles (and consequently lower particle percolation threshold [94]) has been assumed to be less important due to the relatively low volume fraction of β-SiC, as also reported in several studies related to the effect of nanofillers on the viscosity of nanofluid-based composites.[144-146].

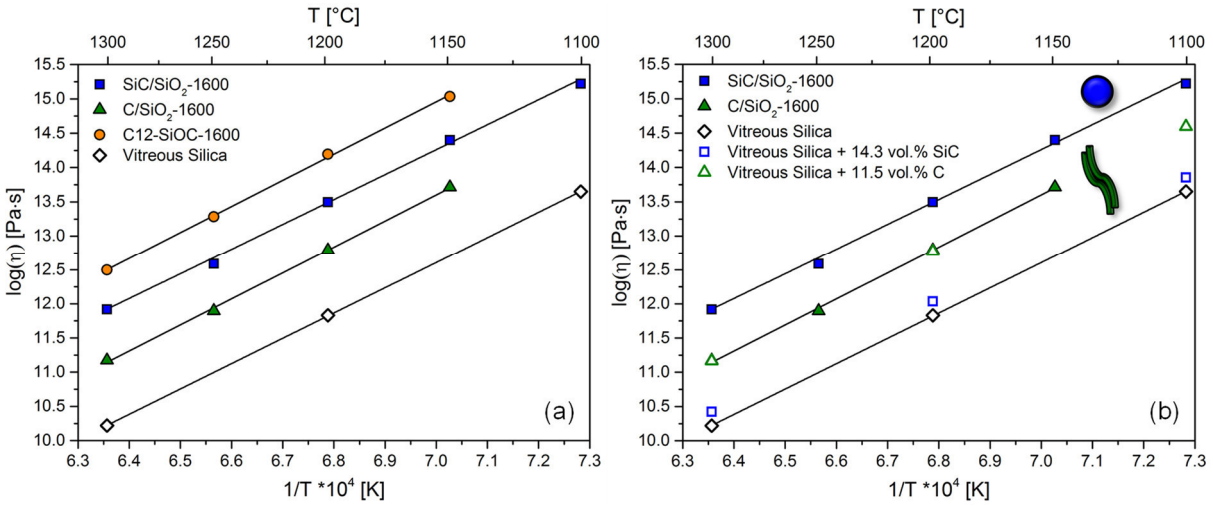

Figure 2-16: (a) Viscosity of SiOC glass ceramics in the ternary system SiO_2-SiC-C (σ_{true} = 75 MPa); (b) Calculated effective viscosities of nanocomposites (open symbols) having the same compositions as SiC/SiO_2-1600 and C/SiO_2-1600 in comparison to the measured viscosities of SiC/SiO_2-1600 and C/SiO_2-1600 (filled symbols). Values for vitreous silica [98] are displayed as reference (black symbols). Blue sphere and green elongated phase schematically represent the aspect ratio's of β-SiC and segregated carbon [4].

It is proposed in literature that the interface of SiC nanoparticles in the vitreous silica matrix still contains a thin layer of mixed-bonds $SiO_{4-x}C_x$ tetrahedra due to their in-situ partitioning during phase separation [40]. This would imply a strong covalent bonding between particle and matrix. On the other hand, computational modelling using density functional theory and molecular dynamics reveal, that the segregated carbon phase is only weakly bound to the vitreous silica matrix [147]. Consequently, the high viscosity in sample SiC/SiO_2-1600 is proposed to be mainly caused by the strong interface between SiC nanoparticles and vitreous

silica matrix, whereas the viscosity in C/SiO_2-1600 can be well explained by particle hardening without significant contribution of the weak interface between segregated carbon and vitreous silica matrix. This demonstrates that not necessarily only the shape but as well the nature of the interfaces of dispersed particles have an important influence on the viscosity of a composite material.

This is further demonstrated when additionally incorporating $Lu_2Si_2O_7$ nanoparticles. Due to very low creep rates at 1100 °C and 75 MPa applied true stress, the measurement did not reach the steady-state regime within a measurement time of 19 hours as can be seen by the logarithmic plot of creep rate vs. true strain (*cf.* Figure 2-17a).

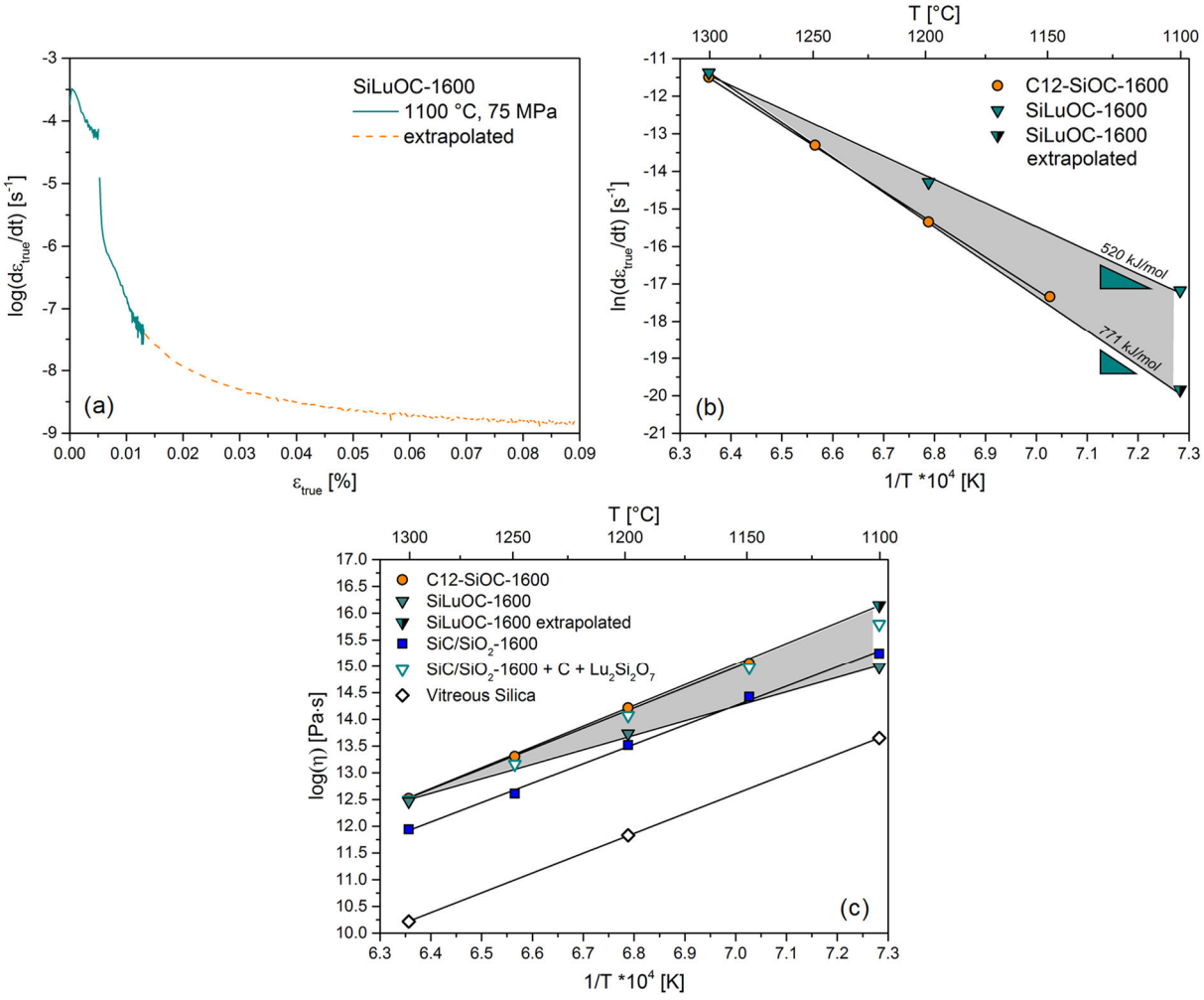

Figure 2-17: Impact of phase assemblage in the quaternary system SiO_2-SiC-C-$Lu_2Si_2O_7$; (a) Logarithmic creep curve of SiLuOC-1600 did not reach the steady-state regime (T_{meas} = 1100 °C; σ_{true} = 75 MPa). The experimental data was extrapolated according to the measurement of C12-SiOC-1600 at 1150 °C and 75 MPa applied true stress assuming identical shape of the creep curves (dashed line); (b) Activation energy for creep: values of SiLuOC-1600 are expected to range between 520 and 771 kJ/mol as indicated by the gray area (σ_{true} = 75 MPa); (c) Viscosity (filled symbols): values of SiLuOC-1600 are expected to range within the indicated gray area, matching the calculated effective viscosity of a corresponding nanocomposite (open symbols). Values for vitreous silica are included as reference (black empty symbols) [98].

Upon the assumption of identical shape of the creep curves obtained from samples C12-SiOC-1600 and SiLuOC-1600, the experimental data of SiLuOC-1600 measured at 1100 °C and 75 MPa applied true stress were extrapolated. As a consequence, the activation energy for creep as well as the viscosity is expected to range between measured and extrapolated value as indicated by the gray areas in Figure 2-17b and c. Within this interval, the addition of 4.9 vol.% $Lu_2Si_2O_7$ nanoparticles does not lead to a significant change of the creep behavior in comparison to C12-SiOC-1600 (with both samples possessing a similar amount of β-SiC nanoparticles and segregated carbon phase, *cf.* Table 2-5) as expressed by an activation energy for creep between 520 – 771 kJ/mol (*cf.* Figure 2-17b). Furthermore, viscosity is not significantly affected in comparison to C12-SiOC-1600 within this interval. For the calculation of the effective viscosity of a nanocomposite with the same composition as SiLuOC-1600 as calculated by equations 2-7 and 2-8, viscosity data of SiC/SiO_2-1600 were used for the viscosity of the matrix. A spherical shape for $Lu_2Si_2O_7$ and an aspect ratio of 10 for the segregated carbon phase was assumed. The extrapolated value matches very well the calculated effective viscosity of a nanocomposite with the same composition as SiLuOC-1600 (*cf.* Figure 2-17c).

Consequently, we demonstrated that different spherical dispersed phases deviate significantly in their potential to enhance viscosity, as the presence of $Lu_2Si_2O_7$ does not lead to a significant increase in viscosity in comparison to β-SiC. In SiOC glass ceramics, the nature of the interface between dispersed particle and vitreous silica matrix is more important than their aspect ratio. This is summarized in Table 2-9 upon comparison of viscosity as expressed by T_g. Furthermore, we demonstrated the potential of SiOC modified with lutetium as creep resistant material, although the creep data of SiLuOC-1600 needed to be extrapolated. In contrast to zirconium and hafnium [74], the incorporation of lutetium does not lead to a significant increase in creep rates, but additionally opens up the prospect of improved oxidation resistance due to the presence of $Lu_2Si_2O_7$ as described for Si_3N_4 ceramics [128].

Although β-SiC nanoparticles have a high impact on the viscosity of SiOC glass ceramics, they have no influence on the anelastic recovery at T_{meas} = 1200 °C. The anelastic recovery of C/SiO_2-1600 and C12-SiOC-1600 is found to be 19.22 % and 20.82 %, respectively, despite the significant difference in β-SiC content. As they possess rather similar amounts of segregated carbon of 11.5 and 11.9 vol.%, it is concluded that the anelastic response is directly correlated to the amount of segregated carbon. The vitreous silica matrix contributes 8.8 % to the anelastic recovery as testified by sample SiC/SiO_2-1600.

To summarize, SiOC glass ceramics are stable during high-temperature creep experiments between 1100 and 1300 °C. The steady-state creep rates are governed by the amount of

dispersed phases but as well by the type of dispersed phase. It is revealed in this study that unexpectedly the spherical β-SiC nanoparticles significantly increase the creep resistance, while the high-aspect-phase segregated carbon only leads to a moderate increase in creep resistance. This is attributed to the different nature of in-situ generated interfaces between both dispersed phases and vitreous silica matrix. The anelastic recovery of the SiOC glass ceramics is dominated by the segregated carbon phase.

2.4 Thermal properties of SiOC glasses and glass ceramics

The content of this chapter is published in:

[6] **C. Stabler**, A. Reitz, B. Albert, P. Stein, R. Riedel, E. Ionescu, Thermal Properties of SiOC Glasses and Glass Ceramics at Elevated Temperatures, *Materials*, 11(279) (2018) 1-18.

The present chapter will address the impact of varying chemical composition and varying microstructure on the thermal properties of ternary SiOCs, i.e. linear thermal expansion, specific heat capacity, thermal diffusivity and thermal conductivity.

Thermal conductivity is one of the most important parameters when addressing thermal insulation problems. It is determined by individual measurements of thermal diffusivity, specific heat capacity and density as expressed by equation 2-9. All of these physical properties are temperature-dependent and this has to be considered when high in-service temperatures are prevailing.

The temperature-dependent specific heat capacity was determined using differential scanning calorimetry (DSC) from room temperature to 1000 °C. Samples C12-SiOC-1600, C16-SiOC-1600 and C17-SiOC-1600 show comparable values due to similar densities (*cf.* Table 2-10) and molar masses and additionally resemble that of vitreous silica [105] and β-SiC [53]. Sample C1-SiOC-1600 displays the lowest values of 0.83 to 1.19 J/(g·K) (100-1000 °C) among the investigated SiOC materials. The phase separation leads to a decrease in the specific heat capacity as evidenced by comparison of C1-SiOC-1100 and C1-SiOC-1600. This is related to the increase in density during phase separation (2.28 to 2.38 g/cm^3, *cf.* Table 2-7).

Table 2-10: Thermal properties of the investigated ternary SiOC glass and SiOC glass ceramics at 100 °C and 800 °C, respectively [6].

Sample	Specific heat capacity [J/(g·K)]	Thermal diffusivity [mm^2/s]	Thermal conductivity [W/(m·K)]
C1-SiOC-1100	0.83 (100 °C) 1.18 (800 °C)	0.62 (100 °C) 0.59 (800 °C)	1.18 (100 °C) 1.58 (800 °C)
C1-SiOC-1600	0.84 (100 °C) 1.08 (800 °C)	0.72 (100 °C) 0.67 (800 °C)	1.43 (100 °C) 1.75 (800 °C)
C12-SiOC-1600	0.85 (100 °C) 1.23 (800 °C)	0.77 (100 °C) 0.68 (800 °C)	1.50 (100 °C) 1.92 (800 °C)
C16-SiOC-1600	0.82 (100 °C) 1.22 (800 °C)	0.81 (100 °C) 0.72 (800 °C)	1.53 (100 °C) 2.06 (800 °C)
C17-SiOC-1600	0.83 (100 °C) 1.22 (800 °C)	1.00 (100 °C) 0.85 (800 °C)	2.15 (100 °C) 2.70 (800 °C)

The evolution of density itself with temperature can be calculated from the coefficient of thermal expansion (CTE) as determined by dilatometric measurements upon the assumption of isotropic behavior, which can be expected for glasses. The SiOC materials investigated possess low thermal expansion (CTE = 1.84 – 3.23 ppm·K^{-1}, *cf.* Table 2-11), however being about one magnitude higher than that of vitreous silica (CTE = 0.57 ppm·K^{-1} [73]). This is in accordance to values published already in literature for SiOC materials [43, 73, 100]. The SiOC glass C1-SiOC-1100 exhibits the highest thermal expansion among the investigated SiOC materials. Phase separation leads to a decrease in the CTE, following the lower values of vitreous silica. Increasing the amount of segregated carbon yields again higher CTE values with sample C17-SiOC-1600 reaching that of C1-SiOC-1100. This observation is in line with the higher values of 4-6 ppm·K^{-1} determined for other disordered carbons like pyrolytic carbon [102]. Consequently, the flexibility in composition as well as microstructure of the SiOC system enables the possibility to tune the thermal expansion in a certain range to a desired value. Furthermore, the dilatometric curves shown in Figure 2-18a reveal values for T_g in SiOC glass ceramics 140-170 °C lower than determined from the compression creep experiments due to the impact of contact pressure in the dilatometer [96]. However, it is clear that at temperatures higher than T_g the CTE significantly increases, as summarized in Table 2-11. This has to be taken into account when using these materials at high in-service temperatures. At T > 1070 °C, sample C1-SiOC-1100 showed failure, because the tested specimen was thin and Euler's critical load is dependent on the second moment of area [148]. The dilatometric curve of C17-SiOC-1600 is regarded as being biased at T > 1300 °C due to the closure of residual porosity.

Table 2-11: Thermal expansion behavior of a ternary SiOC glass and SiOC glass ceramics [6]. The CTE_{HT} corresponds to the coefficient of thermal expansion above glass transition temperature T_g. Values for T_g are expected to be underestimated due to the contact pressure in the dilatometer [96].

Sample	CTE [10^{-6} K^{-1}]	CTE_{HT} [10^{-6} K^{-1}]	T_g (dilatometric) [° C]
C1-SiOC-1100	3.23	–	–
C1-SiOC-1600	1.84	4.41	1060
C12-SiOC-1600	2.02	4.87	1157
C16-SiOC-1600	3.09	5.29	1171
C17-SiOC-1600	3.23	–	–

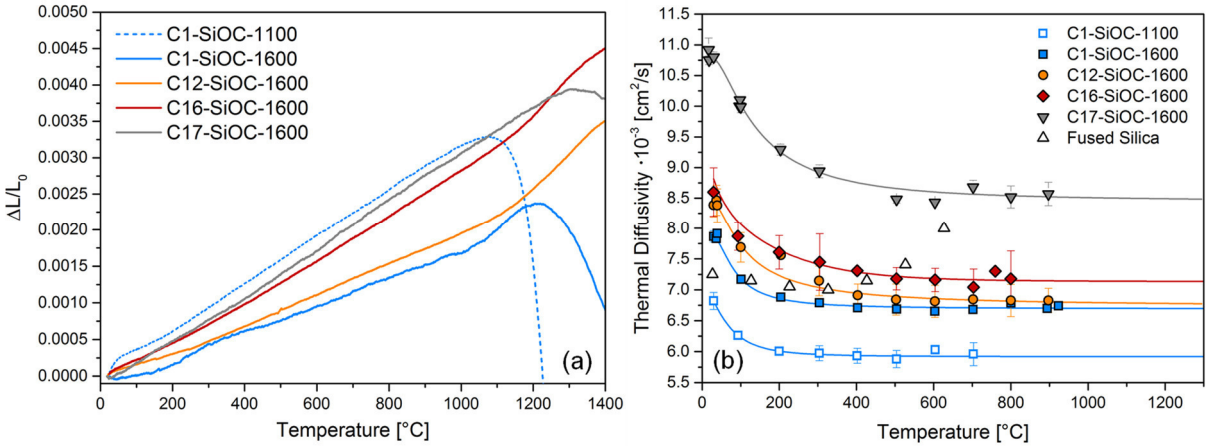

Figure 2-18: Evolution of thermal properties of a ternary SiOC glass and SiOC glass ceramics with increasing temperature [6]. (a) Thermal expansion; (b) Thermal diffusivity; the trend lines are to guide the eye and were used for extrapolation to 1300 °C; the values for fused silica are added as reference [110].

Figure 2-18b and Table 2-10 show the temperature-dependent thermal diffusivities of the investigated ternary SiOC samples as determined from laser flash experiments, including values for fused silica [110]. Sample C1-SiOC-1100 reveals even lower thermal diffusivity than fused silica. We ascribe this decrease to the presence of residual hydrogen and dangling bonds, as known to exist in SiOC glasses [13], acting as phonon scattering centers. Additionally, the network in SiOC glasses exhibits a low mass fractal dimension of 2.5 [41]. It has been demonstrated in literature, that fractal networks show anomalous behavior with respect to thermal transport [149-151]. Similarly it was suggested, that the substitution of two-fold coordinated oxygen by four-fold coordinated carbon atoms lead to the formation of defects and/or oxygen vacancies due to steric hindrance [43]. The phase separation leads to an increase in the thermal diffusivity, most probably due to the elimination of residual hydrogen and dangling bonds. The investigated SiOC glass ceramics exhibit thermal diffusivities similar to fused silica, except C17-SiOC-1600 which shows significantly higher values. Two aspects can be distinguished: (i) an increase in segregated carbon leads to a moderate increase of the thermal diffusivity as evidenced by comparison of C1-SiOC-1600, C12-SiOC-1600 and C16-SiOC-1600; (ii) increasing amounts of β-SiC yield a significant increase in the thermal diffusivity as can be seen by comparison of C16-SiOC-1600 and C17-SiOC-1600.

The same tendencies can be observed for the temperature-dependent thermal conductivity of the investigated SiOC samples as depicted in Figure 2-19. Values for C17-SiOC-1600 were corrected with respect to their volume fraction of open and closed porosity by the equations proposed by Loeb [152] and Maxwell-Eucken [153], respectively. C1-SiOC-1100 shows the lowest thermal conductivity due to the previously discussed amount of phonon scattering centers (residual hydrogen and dangling bonds) and the fractal nature of the glass network. Phase separation leads to an increase in thermal conductivity and sample C1-SiOC-1600 reveals

values almost identical to fused silica [111]. An increase in the segregated carbon content leads to an increase in the thermal conductivity, following the higher values published for amorphous carbon [113]. However, this increase does not scale linearly as C17-SiOC-1600 exhibits significantly higher values in comparison to C16-SiOC-1600 despite having similar amounts of segregated carbon. A variation in the degree of graphitization of the segregated carbon phase can be excluded due to the results from Raman spectroscopy (*cf.* Table 2-6).

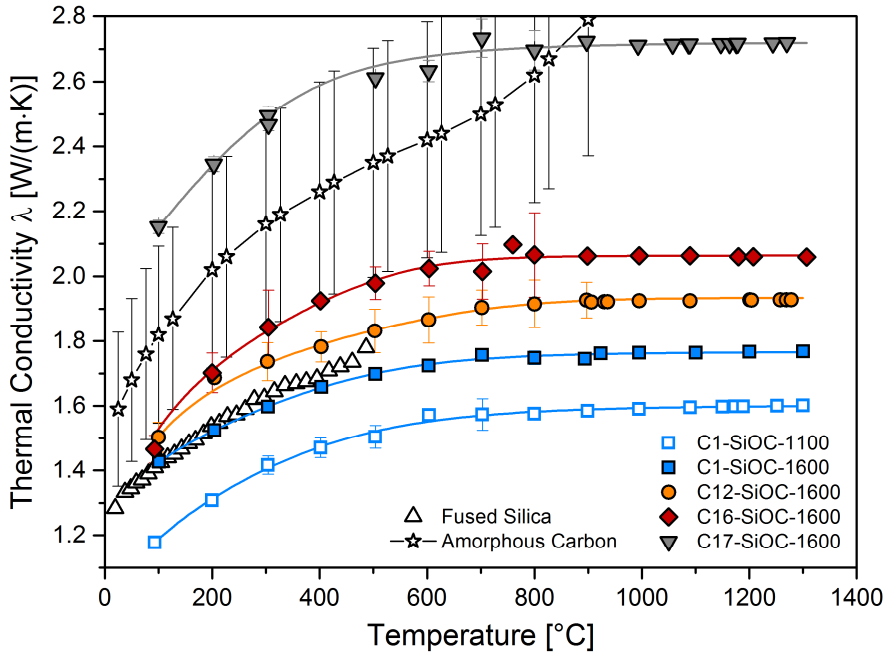

Figure 2-19: Temperature-dependent thermal conductivity of a ternary SiOC glass and SiOC glass ceramics [6]. Values for C17-SiOC-1600 are corrected with respect to the amount of porosity present. Trend lines are to guide the eyes. The values for fused silica [111] and amorphous carbon [113] are included as reference.

To explain the different characteristics of C16-SiOC-1600 and C17-SiOC-1600, a comparison of the thermal conductivities of SiOC glass ceramics at 800 °C is shown in Figure 2-20. Samples C1-SiOC-1600, C12-SiOC-1600 and C16-SiOC-1600 reveal a comparable amount of β-SiC and the increase of their thermal conductivities can be described with a linear function within the standard deviations with increasing amount of segregated carbon (as depicted in Figure 2-20 by the connecting line between fused silica and amorphous carbon). Sample C17-SiOC-1600 does not follow this linear dependence. A linear dependence on the volume fraction between two constituting phases is expected from interpenetrating 3D-networks [118]. The measurement of the electrical conductivity reveals that the segregated carbon phase in C12-SiOC-1600 is close to the percolation threshold [36, 154]. At higher volume fractions, a fully percolating path is present. Furthermore, the vitreous silica matrix is expected to be a continuous 3D phase. Consequently, the model of interpenetrating 3D-networks can be adapted to SiOC glass ceramics. However, the interpenetrating phases are expected to change with increasing β-SiC content. Depending on the particle spacing, thermally interacting percolating

paths can be formed [114]. In the present case, a thermal coupling of the segregated carbon phase and the β-SiC nanoparticles due to increasing volume fraction of dispersed particles or, vice versa, due to decreasing particle spacing is proposed.

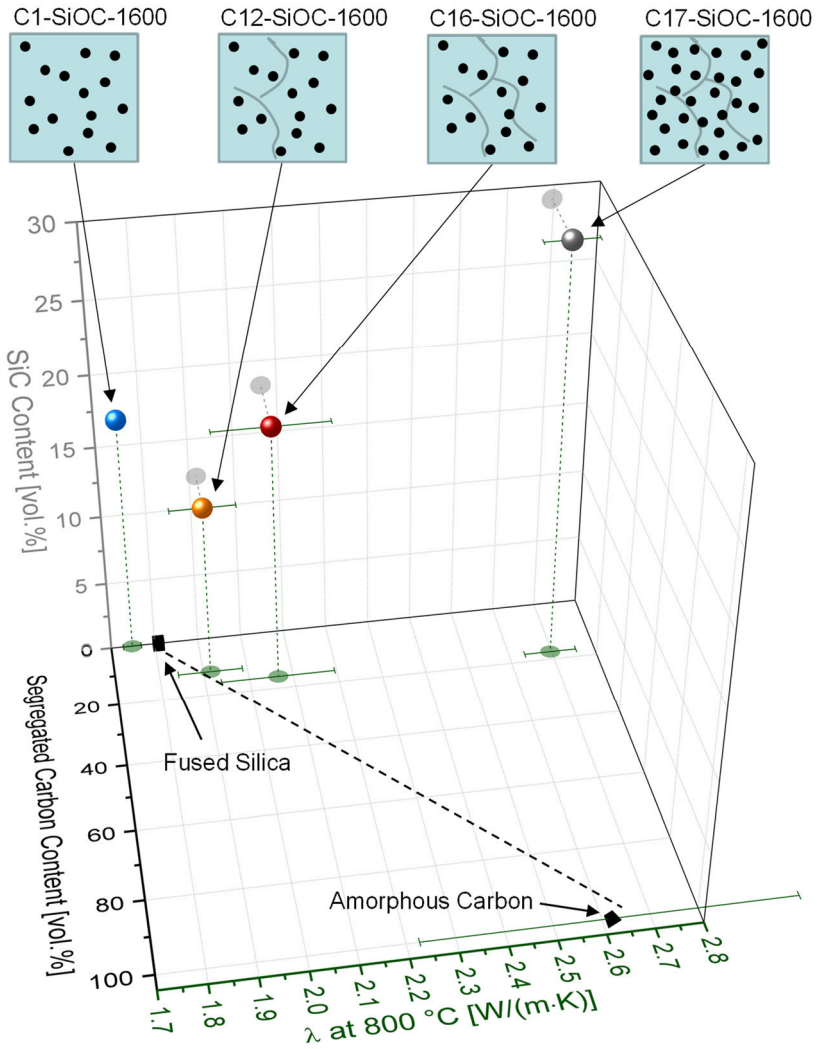

Figure 2-20: Impact of the amount of segregated carbon and β-SiC nanoparticles on the thermal conductivity of ternary SiOC glass ceramics at 800 °C [6]. The particle spacing in the individual samples is schematically shown in the sketches at the top. Values for fused silica [111] and amorphous carbon [113] are included as reference. The linear dependence on the volume fractions of two constituting phases is expected from an interpenetrating 3D-network as depicted on the right side (modified after [118]).

For sample C1-SiOC-1600, the only continuous phase is the vitreous silica matrix. In samples C12-SiOC-1600 and C16-SiOC-1600, two interconnected 3D phases are present, namely the vitreous silica matrix and the segregated carbon phase. Sample C16-SiOC-1600 lies at the upper border of the linear trend of thermal conductivity vs. volume fraction of segregated carbon and a slight contribution of β-SiC nanoparticles cannot be excluded. The strong increase in the thermal conductivity of C17-SiOC-1600 is finally caused by the contribution of 30 vol.% β-SiC nanoparticles, as the thermal conductivity of polycrystalline β-SiC is comparably high (178.2 W/(m·K) [112]). Consequently, the two percolating phases expected in C17-SiOC-1600

are the low thermal conductivity (low-λ) vitreous silica matrix and the high-λ phase, which is consisting of the thermally interacting segregated carbon and β-SiC nanoparticles.

The determined thermal conductivities (summarized in Table 2-10) are in good agreement to values published in literature ranging between 1.3-1.8 W/(m·K) for SiOC glass ceramics at room temperature [107-109]. The thermal conductivity of the glass sample C1-SiOC-1100 (1.18 W/(m·K)) is significantly higher in comparison to the SiOC glass sample in Ref. [109] (0.5 W/(m·K)), which however comprises open porosity and an unknown amount of closed porosity, leading to the decrease of the thermal transport.

In summary, the thermal properties of SiOC are influenced by both chemical composition and microstructure. The thermal expansion is mainly governed by the amount of segregated carbon and even more by the phase separation. The thermal transport is significantly increased during phase separation. Especially, high amounts of β-SiC lead to a dramatic increase in thermal transport. Nonetheless, the intrinsic thermal conductivities of the bulk SiOC glass and bulk SiOC glass ceramics investigated in this study as summarized in Table 2-10 are even lower than that for commercially used yttria-stabilized zirconia (YSZ; ~ 2.0 W/(m·K) at 800 °C [155, 156]), making SiOC materials suitable candidates for thermal insulation applications.

3 Summary and Outlook

This PhD work has been focused on the assessment of the intrinsic (thermo)mechanical and thermal properties of SiOC glasses and glass ceramics. As the SiOC system does not have a fixed chemical composition and the microstructure is depending on the synthesis temperature, particular attention was paid to the interplay between composition/microstructure of SiOC and its intrinsic properties. This was achieved by a systematic study of different series of well characterized SiOC materials synthesized at constant conditions. The comparison with its "origin structure" vitreous silica additionally gives valuable insights. Upon the proper choice of composition and microstructure, tailored mechanical and thermal properties can be realized as unraveled in this study.

The amount of Si-C bonds in SiOC glasses or β-SiC nanoparticles in SiOC glass ceramics has a significant influence on Young's modulus, indentation hardness, creep resistance and viscosity. In all cases, the values for the respective property are increased with increasing amount of Si-C bonds/β-SiC nanoparticles in comparison to vitreous silica. In SiOC glasses, this is related to the increased network connectivity due to the substitution of two-fold coordinated oxygen by four-fold coordinated carbon atoms. For SiOC glass ceramics, Young's modulus, indentation hardness, creep resistance and viscosity can be treated as additive functions of the volume fractions, shape and distribution of the constituting phases. Despite SiOC glass ceramics comprise a vitreous silica matrix with lower performance in comparison to SiOC glasses, they are greatly benefitting from the good mechanical properties of the well dispersed β-SiC nanoparticles and are able to reach values comparable to SiOC glasses. In the case of creep resistance and viscosity, this is enabled by the presence of a strong interface between β-SiC nanoparticles and the vitreous silica matrix. The strong interface between particles and matrix was shown to be vital, as $Lu_2Si_2O_7$ nanoparticles did not induce a significant increase in creep resistance. A special case is the impact of Si-C bonds/β-SiC on the thermal transport. For SiOC glasses, the thermal transport is reduced upon the incorporation of carbon atoms in comparison to vitreous silica as lower mass fractal networks and defects/oxygen vacancies are formed. In contrast, in SiOC glass ceramics thermal transport is increased, when the volume fraction of β-SiC is high enough to participate in a thermally conducting percolating path.

The segregated carbon phase is present in both SiOC glasses and glass ceramics, as it is already formed at $T > 600$ °C. The degree of graphitization of the segregated carbon phase in SiOC glasses and glass ceramics is expected to be the only difference between glasses and glass ceramics with respect to the segregated carbon phase. We further assume, that the segregated carbon phase can be treated as additive phase in a nanocomposite in both, SiOC glasses and

glass ceramics, and that the observations made for varying amounts of segregated carbon in SiOC glass ceramics can be adapted to SiOC glasses. As the segregated carbon phase has a higher aspect ratio (ca. 10) than that of the spherical β-SiC nanoparticles, already smaller amounts in comparison to spherical β-SiC nanoparticles lead to a significant increase in thermal transport as well as in thermal expansion of SiOC glass ceramics. The segregated carbon phase is responsible for the enhanced anelastic recovery of SiOC glass ceramics. In comparison to Si-C bonds/β-SiC, the segregated carbon phase has only a moderate influence on Young's modulus, creep resistance and viscosity. Young's modulus is decreased upon incorporation of segregated carbon, whereas creep resistance and viscosity are increased. Hardness remains unbiased by the segregated carbon phase.

Ultimately, in SiOC glass ceramics the vitreous silica matrix itself is governing mechanical and thermal properties on the macroscopic scale. The basic aspects of deformation are related to the vitreous silica matrix as expressed by Poisson's ratio, strain-rate sensitivity and the activation energy for creep. Thermal properties exhibit low values due to the disordered nature of the vitreous silica matrix. Furthermore, the elastic behavior upon temperature increase, i.e. stiffening, is caused by the vitreous silica matrix.

The concept of phase separation is important in SiOC materials. It has a large impact on thermal expansion, thermal transport and the activation volume carrying deformation at high temperatures (as expressed by the activation energy for creep). However, SiOC glass ceramics cannot simply be interpreted as profane mixtures between $SiC/C/SiO_2$ giving linear dependencies between volume fraction and properties of the respective phases. Although many properties can be regarded as additive function of the constituting phases like in regular nanocomposites, creep resistance proves that the continuous partitioning of β-SiC nanoparticles during phase separation leads to a unique interface between β-SiC and vitreous silica matrix, giving rise to the extraordinary creep resistance that could not be achieved by a simple mechanically mixed nanocomposite.

Now, with the systematic knowledge of the intrinsic (thermo)mechanical and thermal properties of SiOC glasses and glass ceramics, future work can be focused on the fabrication of protective coatings based on silicon oxycarbides. The low thermal transport in SiOC materials is the basic requirement for efficiently creating a temperature gradient in these kind of coatings that reduce the temperature transfer to underlying layers. Such protective coatings consist of several layers taking over different functions and an evolving oxidic layer. Therefore, the thermal expansion plays a key role when working at high temperatures, where mismatches in CTE in the different layers lead to thermal stresses in the materials. The elastic properties of the

individual materials determine the amount of stress the material can withstand without cracking. Finally, hardness and a high creep resistance are key factors for long-lasting protective coatings that can withstand external forces and stresses.

4 References

1. C. Stabler, E. Ionescu, M. Graczyk-Zajac, I. Gonzalo-Juan and R. Riedel, *Silicon oxycarbide glasses and glass-ceramics: "All-Rounder" materials for advanced structural and functional applications*, J. Am. Ceram. Soc., **2018**, 101(11), 4817-4856.
2. C. Stabler, F. Célarié, T. Rouxel, R. Limbach, L. Wondraczek, R. Riedel and E. Ionescu, *Effect of composition and high-temperature annealing on the local deformation behavior of silicon oxycarbides*, J. Eur. Ceram. Soc., **2019**, 39(7), 2287-2296.
3. C. Stabler, F. Roth, M. Narisawa, D. Schliephake, M. Heilmaier, S. Lauterbach, H.-J. Kleebe, R. Riedel and E. Ionescu, *High-temperature creep behavior of a SiOC glass ceramic free of segregated carbon*, J. Eur. Ceram. Soc., **2016**, 36(15), 3747-3753.
4. C. Stabler, D. Schliephake, M. Heilmaier, T. Rouxel, H.-J. Kleebe, M. Narisawa, R. Riedel and E. Ionescu, *Influence of SiC/Silica and Carbon/Silica Interfaces on the High-Temperature Creep of Silicon Oxycarbide-Based Glass Ceramics: A Case Study*, Adv. Eng. Mater., **2018**, 1800596, 1-11.
5. C. Stabler, C. Seemueller, A. Choudhary, M. Heilmaier, S. Lauterbach, H.-J. Kleebe and E. Ionescu, *Synthesis and high-temperature creep behavior of a SiLuOC-based glass-ceramic*, J. Ceram. Soc. Jpn., **2016**, 124(10), 1006-1012.
6. C. Stabler, A. Reitz, B. Albert, P. Stein, R. Riedel and E. Ionescu, *Thermal Properties of SiOC Glasses and Glass Ceramics at Elevated Temperatures*, Materials, **2018**, 11(279), 1-18.
7. R.B. Ellis, *Electrically conducting glass*, 1951, U.S. Pat.No. 2556616.
8. P. Colombo, G. Mera, R. Riedel and G.D. Soraru, *Polymer-derived ceramics: 40 years of research and innovation in advanced ceramics*, J. Am. Ceram. Soc., **2010**, 93(7), 1805-1837.
9. M. Gan and V. Tomar, *Role of length scale and temperature in indentation induced creep behavior of polymer derived Si-C-O ceramics*, Mater. Sci. Eng., A, **2010**, 527, 7615-7623.
10. C.G. Pantano, A.K. Singh and H. Zhang, *Silicon oxycarbide glasses*, J. Sol-Gel Sci. Technol., **1999**, 14(1), 7-25.
11. G.D. Soraru, *Silicon oxycarbide glasses from gels*, J. Sol-Gel Sci. Technol., **1994**, 2, 843-848.
12. L. Bois, J. Maquet, F. Babonneau, H. Mutin and D. Bahloul, *Structural Characterization of Sol-Gel Derived Oxycarbide Glasses. 1. Study of the Pyrolysis Process*, Chem. Mater., **1994**, 6(6), 796-802.
13. H. Brequel, J. Parmentier, S. Walter, R. Badheka, G. Trimmel, S. Masse, J. Latournerie, P. Dempsey, C. Turquat, A. Desmartin-Chomel, L.L. Neindre-Prum, U.A. Jayasooriya, D. Hourlier, H.J. Kleebe, G.D. Soraru, S. Enzo and F. Babonneau, *Systematic Structural Characterization of the High-Temperature Behavior of Nearly Stoichiometric Silicon Oxycarbide Glasses*, Chem. Mater., **2004**, 16(13), 2585-2598.
14. M. Narisawa, F. Funabiki, A. Iwase, F. Wakai and H. Hosono, *Effects of Atmospheric Composition on the Molecular Structure of Synthesized Silicon Oxycarbides*, J. Am. Ceram. Soc., **2015**, 98(10), 3373-3380.
15. G.D. Soraru, L. Pederiva, J. Latournerie and R. Raj, *Pyrolysis kinetics for the conversion of a polymer into an amorphous silicon oxycarbide ceramic*, J. Am. Ceram. Soc., **2002**, 85(9), 2181-2187.
16. G. Gregori, H.-J. Kleebe, Y.D. Blum and F. Babonneau, *Evolution of C-rich SiOC ceramics: part II. Characterization by high lateral resolution techniques: electron energy-loss spectroscopy, high-resolution TEM and energy-filtered TEM*, Int. J. Mater. Res., **2006**, 97(6), 710-720.
17. G.D. Soraru and D. Suttor, *High temperature stability of sol-gel-derived SiOC glasses*, J. Sol-Gel Sci. Technol., **1999**, 14(1), 69-74.

18. F. Babonneau, K. Thorne and J.D. Mackenzie, *Dimethyldiethoxysilane/tetraethoxysilane copolymers: precursors for the silicon-carbon-oxygen system*, Chem. Mater., **1989**, 1(5), 554-558.
19. U. Schubert and N. Husing, *Synthesis of Inorganic Materials*, 3rd ed., **2012**, Wiley-VCH: Weinheim, 392 pp.
20. S. Dire, F. Babonneau, C. Sanchez and J. Livage, *Sol-gel synthesis of siloxane-oxide hybrid coatings [Si(CH3)2O.MOx: M = silicon, titanium, zirconium, aluminum] with luminescent properties*, J. Mater. Chem., **1992**, 2(2), 239-244.
21. G.D. Soraru, G. D'Andrea, R. Campostrini, F. Babonneau and G. Mariotto, *Structural characterization and high-temperature behavior of silicon oxycarbide glasses prepared from sol-gel precursors containing Si-H bonds*, J. Am. Ceram. Soc., **1995**, 78(2), 379-387.
22. E. Ionescu, B. Papendorf, H.J. Kleebe, F. Poli, K. Muller and R. Riedel, *Polymer-Derived Silicon Oxycarbide/Hafnia Ceramic Nanocomposites. Part I: Phase and Microstructure Evolution During the Ceramization Process*, J. Am. Ceram. Soc., **2010**, 93(6), 1774-1782.
23. M. Fukushima, E. Yasuda, Y. Nakamura and Y. Tanabe, *Pyrolysis behavior of organic-inorganic hybrids with Si-O-Nb/Si-O-Ta oxygen bridged heterometallic bonds*, J. Ceram. Soc. Jpn., **2003**, 111(Nov.), 857-859.
24. E. Ionescu, C. Linck, C. Fasel, M. Mueller, H.-J. Kleebe and R. Riedel, *Polymer-derived SiOC/ZrO2 ceramic nanocomposites with excellent high-temperature stability*, J. Am. Ceram. Soc., **2010**, 93(1), 241-250.
25. E. Ionescu, S. Sen, G. Mera and A. Navrotsky, *Structure, energetics and bioactivity of silicon oxycarbide-based amorphous ceramics with highly connected networks*, J. Eur. Ceram. Soc., **2018**, 38(4), 1311-1319.
26. M. Hojamberdiev, R.M. Prasad, C. Fasel, R. Riedel and E. Ionescu, *Single-source-precursor synthesis of soft magnetic Fe3Si- and Fe5Si3-containing SiOC ceramic nanocomposites*, J. Eur. Ceram. Soc., **2013**, 33(13-14), 2465-2472.
27. S. Kaur, G. Cherkashinin, C. Fasel, H.J. Kleebe, E. Ionescu and R. Riedel, *Single-source-precursor synthesis of novel V8C7/SiC(O)-based ceramic nanocomposites*, J. Eur. Ceram. Soc., **2016**, 36(15), 3553-3563.
28. S. Boninelli, G. Bellocchi, G. Franzo, M. Miritello and F. Iacona, *New strategies to improve the luminescence efficiency of Eu ions embedded in Si-based matrices*, J. Appl. Phys. (Melville, NY, U. S.), **2013**, 113(14), 143503/143501-143503/143508.
29. S. Gallis, M. Huang, H. Efstathiadis, E. Eisenbraun, A.E. Kaloyeros, E.E. Nyein and U. Hommerich, *Photoluminescence in erbium doped amorphous silicon oxycarbide thin films*, Appl. Phys. Lett., **2005**, 87(9), 091901/1-091901/3.
30. J. Kaspar, C. Terzioglu, E. Ionescu, M. Graczyk-Zajac, S. Hapis, H.J. Kleebe and R. Riedel, *Stable SiOC/Sn Nanocomposite Anodes for Lithium-Ion Batteries with Outstanding Cycling Stability*, Adv Funct Mater, **2014**, 24(26), 4097-4104.
31. R. Riedel, G. Mera, R. Hauser and A. Klonczynski, *Silicon-based polymer-derived ceramics: synthesis properties and applications - a review. Dedicated to Prof. Dr. Fritz Aldinger on the occasion of his 65th birthday*, J. Ceram. Soc. Jpn., **2006**, 114(June), 425-444.
32. G.T. Burns, R.B. Taylor, Y. Xu, A. Zangvil and G.A. Zank, *High-temperature chemistry of the conversion of siloxanes to silicon carbide*, Chem. Mater., **1992**, 4(6), 1313-1323.
33. V. Belot, R.J.P. Corriu, D. Leclercq, P.H. Mutin and A. Vioux, *Thermal redistribution reactions in crosslinked polysiloxanes*, J. Polym. Sci., Part A: Polym. Chem., **1992**, 30(4), 613-623.
34. H.-J. Kleebe, G. Gregori, F. Babonneau, Y.D. Blum, D.B. MacQueen and S. Masse, *Evolution of C-rich SiOC ceramics: part I. Characterization by integral spectroscopic techniques: solid-state NMR and Raman spectroscopy*, Int. J. Mater. Res., **2006**, 97(6), 699-709.
35. M. Monthioux and O. Delverdier, *Thermal behavior of (organosilicon) polymer-derived ceramics. V: Main facts and trends*, J. Eur. Ceram. Soc., **1996**, 16(7), 721-737.

36. F. Rosenburg, *The state of carbon and the piezoresistive effect in silicon oxycarbide ceramics*, **2018**, PhD work, Technical University of Darmstadt, 117 pp.
37. P. Lespade, A. Marchand, M. Couzi and F. Cruege, *Raman microspectrometric characterization of carbonaceous materials*, Carbon, **1984**, 22(4-5), 375-385.
38. D.S. Knight and W.B. White, *Characterization of diamond films by Raman spectroscopy*, J. Mater. Res., **1989**, 4(2), 385-393.
39. G.D. Soraru, S. Modena, E. Guadagnino, P. Colombo, J. Egan and C. Pantano, *Chemical durability of silicon oxycarbide glasses*, J. Am. Ceram. Soc., **2002**, 85(6), 1529-1536.
40. H.-J. Kleebe, C. Turquat and G.D. Soraru, *Phase separation in an SiCO glass studied by transmission electron microscopy and electron energy-loss spectroscopy*, J. Am. Ceram. Soc., **2001**, 84(5), 1073-1080.
41. S.J. Widgeon, S. Sen, G. Mera, E. Ionescu, R. Riedel and A. Navrotsky, *29Si and 13C Solid-State NMR Spectroscopic Study of Nanometer-Scale Structure and Mass Fractal Characteristics of Amorphous Polymer Derived Silicon Oxycarbide Ceramics*, Chem. Mater., **2010**, 22(23), 6221-6228.
42. F. Rosenburg, E. Ionescu, N. Nicoloso and R. Riedel, *High-Temperature Raman Spectroscopy of Nano-Crystalline Carbon in Silicon Oxycarbide*, Materials, **2018**, 11(93), 1-9.
43. G.M. Renlund, S. Prochazka and R.H. Doremus, *Silicon oxycarbide glasses. Part II. Structure and properties*, J. Mater. Res., **1991**, 6(12), 2723-2734.
44. T. Rouxel, G.-D. Soraru and J. Vicens, *Creep viscosity and stress relaxation of gel-derived silicon oxycarbide glasses*, J. Am. Ceram. Soc., **2001**, 84(5), 1052-1058.
45. E. Radovanovic, M.F. Gozzi, M.C. Goncalves and I.V.P. Yoshida, *Silicon oxycarbide glasses from silicone networks*, J. Non-Cryst. Solids, **1999**, 248(1), 37-48.
46. S. Martinez-Crespiera, E. Ionescu, H.-J. Kleebe and R. Riedel, *Pressureless synthesis of fully dense and crack-free SiOC bulk ceramics via photo-crosslinking and pyrolysis of a polysiloxane*, J. Eur. Ceram. Soc., **2011**, 31(5), 913-919.
47. A. Saha, R. Raj and D.L. Williamson, *A model for the nanodomains in polymer-derived SiCO*, J. Am. Ceram. Soc., **2006**, 89(7), 2188-2195.
48. F.I. Hurwitz, P. Heimann, S.C. Farmer and D.M. Hembree, Jr., *Characterization of the pyrolytic conversion of polysilsesquioxanes to silicon oxycarbides*, J. Mater. Sci., **1993**, 28(24), 6622-6630.
49. J.J. Biernacki and G.P. Wotzak, *Stoichiometry of the carbon + silica reaction*, J. Am. Ceram. Soc., **1989**, 72(1), 122-129.
50. M. Nagamori, I. Malinsky and A. Claveau, *Thermodynamics of the silicon-carbon-oxygen system for the production of silicon carbide and metallic silicon*, Metall. Trans. B, **1986**, 17(3), 503-514.
51. A.H. Tavakoli, M.M. Armentrout, M. Narisawa, S. Sen and A. Navrotsky, *White Si-O-C Ceramic: Structure and Thermodynamic Stability*, J. Am. Ceram. Soc., **2015**, 98(1), 242-246.
52. A. Saha and R. Raj, *Crystallization maps for SiCO amorphous ceramics*, J. Am. Ceram. Soc., **2007**, 90(2), 578-583.
53. M.W.J. Chase, *NIST-JANAF Thermochemical Tables*, 4th ed., J. Phys. Chem. Ref. Data Monograph, **1998**, 1-1951 pp.
54. V.I. Koshchenko, Y.K. Grinberg and R.V. Koshchenko, *Thermodynamic functions of boron arsenide (B6As) (5-600 K), β-silicon carbide (5-2500 K), and silicon nitride (Si3N4) (5-4000 K)*, Izv. Akad. Nauk SSSR, Neorg. Mater., **1985**, 21(2), 244-248.
55. P. Greil, *Near net shape manufacturing of polymer derived ceramics*, J. Eur. Ceram. Soc., **1998**, 18(13), 1905-1914.
56. P. Greil, *Advancements in polymer-filler derived ceramics*, J. Korean Ceram. Soc., **2012**, 49(4), 279-286.

57. S. Kaur, R. Riedel and E. Ionescu, *Pressureless fabrication of dense monolithic SiC ceramics from a polycarbosilane*, J. Eur. Ceram. Soc., **2014**, 34(15), 3571-3578.
58. D.L. Poerschke, A. Braithwaite, D. Park and F. Lauten, *Crystallization behavior of polymer-derived Si-O-C for ceramic matrix composite processing*, Acta Materialia, **2018**, 147, 329-341.
59. M. Narisawa, K. Terauds, G. Ma, H. Hokazono, R. Raj and A. Iwase, *Evaluation of high temperature resistance of white Si-O-C(-H) ceramics in an inert atmosphere*, J. Non-Cryst. Solids, **2015**, 410, 106-111.
60. M. Hammond, E. Breval and C.G. Pantano, *Microstructure and viscosity of hot pressed silicon oxycarbide glasses*, Ceram. Eng. Sci. Proc., **1993**, 14(9-10), 947-954.
61. G.D. Soraru, E. Dallapiccola and G. D'Andrea, *Mechanical characterization of sol-gel-derived silicon oxycarbide glasses*, J. Am. Ceram. Soc., **1996**, 79(8), 2074-2080.
62. T. Rouxel, *Elastic properties and short-to medium-range order in glasses*, J. Am. Ceram. Soc., **2007**, 90(10), 3019-3039.
63. G.N. Greaves, A.L. Greer, R.S. Lakes and T. Rouxel, *Poisson's ratio and modern materials*, Nat. Mater., **2011**, 10(11), 823-837.
64. C. Moysan, R. Riedel, R. Harshe, T. Rouxel and F. Augereau, *Mechanical characterization of a polysiloxane-derived SiOC glass*, J. Eur. Ceram. Soc., **2006**, 27(1), 397-403.
65. R. Limbach, B.P. Rodrigues and L. Wondraczek, *Strain-rate sensitivity of glasses*, J. Non-Cryst. Solids, **2014**, 404, 124-134.
66. R. Bruckner, Y. Yue and J. Deubener, *Progress in the rheology of glass melts. A survey*, Glass Sci. Technol., **1997**, 70(9), 261-271.
67. A. Pedone, G. Malavasi, A.N. Cormack, U. Segre and M.C. Menziani, *Insight into Elastic Properties of Binary Alkali Silicate Glasses; Prediction and Interpretation through Atomistic Simulation Techniques*, Chem. Mater., **2007**, 19(13), 3144-3154.
68. Q. Zhao, M. Guerette and L. Huang, *Nanoindentation and Brillouin light scattering studies of elastic moduli of sodium silicate glasses*, J. Non-Cryst. Solids, **2012**, 358(3), 652-657.
69. P. Sellappan, T. Rouxel, F. Celarie, E. Becker, P. Houizot and R. Conradt, *Composition dependence of indentation deformation and indentation cracking in glass*, Acta Mater., **2013**, 61(16), 5949-5965.
70. S. Sawamura, R. Limbach, H. Behrens and L. Wondraczek, *Lateral deformation and defect resistance of compacted silica glass: Quantification of the scratching hardness of brittle glasses*, J. Non-Cryst. Solids, **2018**, 481, 503-511.
71. L. Wondraczek, J.C. Mauro, J. Eckert, U. Kuehn, J. Horbach, J. Deubener and T. Rouxel, *Towards ultrastrong glasses*, Adv. Mater. (Weinheim, Ger.), **2011**, 23(39), 4578-4586.
72. S. Walter, G.D. Soraru, H. Brequel and S. Enzo, *Microstructural and mechanical characterization of sol gel-derived Si-O-C glasses*, J. Eur. Ceram. Soc., **2002**, 22(13), 2389-2400.
73. T. Rouxel, G. Massouras and G.-D. Soraru, *High temperature behavior of a gel-derived SiOC glass: elasticity and viscosity*, J. Sol-Gel Sci. Technol., **1999**, 14(1), 87-94.
74. B. Papendorf, E. Ionescu, H.-J. Kleebe, C. Linck, O. Guillon, K. Nonnenmacher and R. Riedel, *High-temperature creep behavior of dense SiOC-based ceramic nanocomposites: microstructural and phase composition effects*, J. Am. Ceram. Soc., **2013**, 96(1), 272-280.
75. A.J. Stryjak and P.W. McMillan, *Microstructure and properties of transparent glass-ceramics. Part 2. The physical properties of spinel transparent glass-ceramics*, J. Mater. Sci., **1978**, 13(8), 1794-1804.
76. N. Miyata and H. Jinno, *Discussion of the indentation hardness of a glass-ceramic with participate microstructure*, Journal of Materials Science, **1982**, 17(9), 2693-2699.
77. R. Limbach, A. Winterstein-Beckmann, J. Dellith, D. Moencke and L. Wondraczek, *Plasticity, crack initiation and defect resistance in alkali-borosilicate glasses: From normal to anomalous behavior*, J. Non-Cryst. Solids, **2015**, 417-418, 15-27.

78. G.L. Harris, *Properties of Silicon Carbide*. EMIS datareviews series, Vol. 13., **1995**, INSPEC, Institution of Electrical Engineers: London, UK, 282 pp.
79. B. Schultrich, H.J. Scheibe, G. Grandremy, D. Drescher and D. Schneider, *Elastic modulus as a measure of diamond likeness and hardness of amorphous carbon films*, Diamond Relat. Mater., **1996**, 5(9), 914-918.
80. H. Li and R.C. Bradt, *The indentation load/size effect and the measurement of the hardness of vitreous silica*, J. Non-Cryst. Solids, **1992**, 146(2-3), 197-212.
81. M.E. Kassner, *Fundamentals of Creep in Metals and Alloys*, 2nd ed., **2009**, Elsevier: Oxford, UK, 320 pp.
82. R. Lakes, *Viscoelastic Materials*, 1st paperback ed., **2014**, Cambridge University Press: New York, U.S., 480 pp.
83. A.S. Argon, *Delayed elasticity in inorganic glasses*, J. Appl. Phys., **1968**, 39(9), 4080-4086.
84. R. Morrell and K.H.G. Ashbee, *High temperature creep of lithium zinc silicate glass-ceramics. 2. Compression creep and recovery*, J. Mater. Sci., **1973**, 8(9), 1271-1277.
85. A.K. Mukherjee, J.E. Bird and J.E. Dorn, *Experimental correlations for high-temperature creep*, ASM (Amer. Soc. Metals) Trans. Quart., **1969**, 62(1), 155-179.
86. A.M. Brown and M.F. Ashby, *On the power-law creep equation*, Scr. Metall., **1980**, 14(12), 1297-1302.
87. J.R. Davis, *Tensile Testing*, 2 ed., **2004**, ASM International: Materials Park, Ohio, US, 283 pp.
88. T.E. Mitchell, J.P. Hirth and A. Misra, *Apparent activation energy and stress exponent in materials with a high Peierls stress*, Acta Mater., **2002**, 50(5), 1087-1093.
89. T.G. Nieh, T. Mukai, C.T. Liu and J. Wadsworth, *Superplastic behavior of a Zr-10Al-5Ti-17.9Cu-14.6Ni metallic glass in the supercooled liquid region*, Scr. Mater., **1999**, 40(9), 1021-1027.
90. J.H. Li and D.R. Uhlmann, *Flow of glass at high stress levels. I. Non-Newtonian behavior of homogeneous 0.08 Rb20.0.92 SiO2 glasses*, J. Non-Cryst. Solids, **1969**, 3(1), 127-147.
91. J.H. Simmons, R. Ochoa, K.D. Simmons and J.J. Mills, *Non-Newtonian viscous flow in soda-lime-silica glass at forming and annealing temperatures*, J. Non-Cryst. Solids, **1988**, 105(3), 313-322.
92. E.M. Heuse and G. Partridge, *Creep testing of glass ceramics*, J. Mater. Sci., **1974**, 9(8), 1255-1261.
93. A.R. Boccaccini, *On the viscosity of glass composites containing rigid inclusions*, Mater. Lett., **1998**, 34(3-6), 285-289.
94. T. Rouxel, B. Baron, P. Verdier and T. Sakuma, *SiC particle reinforced oxynitride glass: stress relaxation, creep and strain-rate imposed experiments*, Acta Mater., **1998**, 46(17), 6115-6130.
95. B.S.S. Daniel, A. Reger-Leonhard, M. Heilmaier, J. Eckert and L. Schultz, *Thermal relaxation and high temperature creep of Zr55Cu30Al10Ni5 bulk metallic glass*, Mech. Time-Depend. Mater., **2002**, 6(2), 193-206.
96. O.V. Mazurin, *Problems of compatibility of the values of glass transition temperatures published in the world literature*, Glass Phys. Chem., **2007**, 33(1), 22-36.
97. E. Ionescu, C. Balan, H.-J. Kleebe, M.M. Mueller, O. Guillon, D. Schliephake, M. Heilmaier and R. Riedel, *High-temperature creep behavior of SiOC glass-ceramics: influence of network carbon versus segregated carbon*, J. Am. Ceram. Soc., **2014**, 97(12), 3935-3942.
98. G. Hetherington, K.H. Jack and J.C. Kennedy, *Viscosity of vitreous SiO2*, Phys. Chem. Glasses, **1964**, 5(5), 130-136.
99. A. Scarmi, G.D. Soraru and R. Raj, *The role of carbon in unexpected visco(an)elastic behavior of amorphous silicon oxycarbide above 1273K*, J. Non-Cryst. Solids, **2005**, 351(27-29), 2238-2243.

100. E. Reitz, K.G. Schell, E.C. Bucharsky, R. Oberacker and M.J. Hoffmann, *Precursor derived SiOC/MoSi2-composites for diesel glow plugs: preparation and high temperature properties*, J. Ceram. Soc. Jpn., **2016**, 124(10), 1017-1022.
101. M.D. Karkhanavala and F.A. Hummel, *Thermal expansion of some simple glasses*, J. Am. Ceram. Soc., **1952**, 35, 215-219.
102. R. Piat and E. Schnack, *Identification of coefficients of thermal expansion of pyrolytic carbon with different texture degrees*, Key Eng. Mater., **2003**, 251-252(Advances in Fracture and Damage Mechanics), 333-338.
103. Z. Li and R.C. Bradt, *Thermal expansion of the cubic (3C) polytype of silicon carbide*, J. Mater. Sci., **1986**, 21(12), 4366-4368.
104. S.Z.D. Cheng and S. Jin, *Crystallization and melting of metastable crystalline polymers*, in *Handbook of Thermal Analysis and Calorimetry*, S.Z.D. Cheng, Editor, **2002**, Elsevier Science B.V.: Amsterdam, Netherlands. 167-195 pp.
105. R.B. Sosman, *The Properties of Silica: an Introduction to the Properties of Substances in the Solid Non-conducting State*, **1927**, The Chemical Catalog Company, Inc.: New York, NY, USA pp.
106. J. Yokoyama, M. Murabayashi, Y. Takahashi and T. Mukaibo, *Measurement of high-temperature thermal properties of glassy carbon by laser flash method*, Tanso, **1971**, 65, 44-47.
107. J.-H. Eom, Y.-W. Kim, K.J. Kim and W.-S. Seo, *Improved electrical and thermal conductivities of polysiloxane-derived silicon oxycarbide ceramics by barium addition*, J. Eur. Ceram. Soc., **2018**, 38(2), 487-493.
108. M.A. Mazo, C. Palencia, A. Nistal, F. Rubio, J. Rubio and J.L. Oteo, *Dense bulk silicon oxycarbide glasses obtained by spark plasma sintering*, J. Eur. Ceram. Soc., **2012**, 32(12), 3369-3378.
109. A. Gurlo, E. Ionescu, R. Riedel and D.R. Clarke, *The Thermal Conductivity of Polymer-Derived Amorphous Si-O-C Compounds and Nano-Composites*, J. Am. Ceram. Soc., **2016**, 99(1), 281-285.
110. H. Kanamori, N. Fujii and H. Mizutani, *Thermal diffusivity measurement of rock-forming minerals from 300 to 110°K*, J. Geophys. Res., **1968**, 73(2), 595-605.
111. D.G. Cahill, *Thermal Conductivity Data*, **2014**, Available online: http://users.mrl.illinois.edu/cahill/tcdata/tcdata.html, (accessed on 14. December 2017).
112. K.J. Kim, K.-Y. Lim and Y.-W. Kim, *Electrical and Thermal Properties of SiC Ceramics Sintered with Yttria and Nitrides*, J. Am. Ceram. Soc., **2014**, 97(9), 2943-2949.
113. C.Y. Ho, R.W. Powell and P.E. Liley, *Thermal conductivity of the elements*, J. Phys. Chem. Ref. Data, **1972**, 1(2), 279-421.
114. H.S. Kim, J.-u. Jang, H. Lee, S.Y. Kim, S.H. Kim, J. Kim, Y.C. Jung and B.J. Yang, *Thermal Management in Polymer Composites: A Review of Physical and Structural Parameters*, Adv. Eng. Mater., **2018**, 1800204/1-1800204/12.
115. D.G. Cahill and R.O. Pohl, *Lattice vibrations and heat transport in crystals and glasses*, Annu. Rev. Phys. Chem., **1988**, 39, 93-121.
116. M.A. Mazo, A. Tamayo, A.C. Caballero and J. Rubio, *Electrical and thermal response of silicon oxycarbide materials obtained by spark plasma sintering*, J. Eur. Ceram. Soc., **2017**, 37(5), 2011-2020.
117. K. Pietrak and T.S. Wisniewski, *A review of models for effective thermal conductivity of composite materials*, J. Power Technol., **2015**, 95(1), 14-24.
118. R.M. German, *A model for the thermal properties of liquid-phase sintered composites*, Metall. Trans. A, **1993**, 24A(8), 1745-1752.
119. Y. Benveniste, *Effective thermal conductivity of composites with a thermal contact resistance between the constituents: nondilute case*, J. Appl. Phys., **1987**, 61(8), 2840-2843.

120. J. Wang, J.K. Carson, M.F. North and D.J. Cleland, *A new structural model of effective thermal conductivity for heterogeneous materials with co-continuous phases*, Int. J. Heat Mass Transfer, **2008**, 51(9-10), 2389-2397.
121. J.M. Bind, *Phase transformation during hot-pressing of cubic silicon carbide*, Mater. Res. Bull., **1978**, 13(2), 91-96.
122. F. Soetebier and W. Urland, *Crystal structure of lutetium disilicate, Lu2Si2O7*, Z. Kristallogr. - New Cryst. Struct., **2002**, 217(1), 22.
123. L.G. Cancado, K. Takai, T. Enoki, M. Endo, Y.A. Kim, H. Mizusaki, A. Jorio, L.N. Coelho, R. Magalhaes-Paniago and M.A. Pimenta, *General equation for the determination of the crystallite size La of nanographite by Raman spectroscopy*, Appl. Phys. Lett., **2006**, 88(16), 163106/1-163106/3.
124. L.G. Cancado, A. Jorio, E.H.M. Ferreira, F. Stavale, C.A. Achete, R.B. Capaz, M.V.O. Moutinho, A. Lombardo, T.S. Kulmala and A.C. Ferrari, *Quantifying Defects in Graphene via Raman Spectroscopy at Different Excitation Energies*, Nano Lett., **2011**, 11(8), 3190-3196.
125. A.C. Ferrari and J. Robertson, *Interpretation of Raman spectra of disordered and amorphous carbon*, Phys. Rev. B: Condens. Matter Mater. Phys., **2000**, 61(20), 14095-14107.
126. T. Westphal, *Quantitative Rietveld-Analyse von amorphen Materialien: am Beispiel von Hochofenschlacken und Flugaschen*, **2007**, PhD work, Martin-Luther-Universität Halle-Wittenberg, 145 pp.
127. A.G. De La Torre, S. Bruque and M.A.G. Aranda, *Rietveld quantitative amorphous content analysis*, J. Appl. Crystallogr., **2001**, 34(2), 196-202.
128. M.K. Cinibulk, G. Thomas and S.M. Johnson, *Fabrication and secondary-phase crystallization of rare-earth disilicate-silicon nitride ceramics*, J. Am. Ceram. Soc., **1992**, 75(8), 2037-2043.
129. G.D. Soraru, V.M. Sglavo, S. Dirè, G. D'Andrea and F. Babonneau. *High-Strength, High-Modulus Silicon-Oxycarbide glasses*, in 3rd EURO-CERAMICS, **1993**: Faenza Editrice Ibérica S.L., 1157-1162.
130. G.D. Sorarù, L. Kundanati, B. Santhosh and N. Pugno, *Influence of free carbon on the Young's modulus and hardness of polymer-derived silicon oxycarbide glasses*, J. Am. Ceram. Soc., **2018**, 0(0), 1-7.
131. S. Spinner and G.W. Cleek, *Temperature dependence of Young's modulus of vitreous germania and silica*, J. Appl. Phys., **1960**, 31, 1407-1410.
132. D.J. Lacks, *First-Order Amorphous-Amorphous Transformation in Silica*, Phys. Rev. Lett., **2000**, 84(20), 4629-4632.
133. M. Yamane and J.D. Mackenzie, *Vicker's hardness of glass*, J. Non-Cryst. Solids, **1974**, 15(2), 153-164.
134. G.L. Paraschiv, S. Gomez, J.C. Mauro, L. Wondraczek, Y. Yue and M.M. Smedskjaer, *Hardness of Oxynitride Glasses: Topological Origin*, J. Phys. Chem. B, **2015**, 119(10), 4109-4115.
135. Y.C. Cha, G. Kim, H.J. Doerr and R.F. Bunshah, *Effects of activated reactive evaporation process parameters on the microhardness of polycrystalline silicon carbide thin films*, Thin Solid Films, **1994**, 253(1-2), 212-217.
136. H.J. Frost and M.F. Ashby, *Deformation mechanism maps: the plasticity and creep of metals and ceramics*, 1st ed., **1982**, Pergamon Press: Oxford [u.a], 166 pp.
137. F.H. Horn, *Densitometric and electrical investigation of boron in silicon*, Phys. Rev., **1955**, 97, 1521-1525.
138. T. Rouxel, H. Ji, V. Keryvin, T. Hammouda and S. Yoshida, *Poisson's ratio and the glass network topology- relevance to high pressure densification and indentation behavior*, Adv. Mater. Res., **2008**, 39-40(Glass), 137-146.
139. G.M. Jenkins and K. Kawamura, *Polymeric Carbons: Carbon Fibre, Glass and Char*, **1976**, Camebridge University Press: Camebridge, UK, 185 pp.

140. C.H. Carter, Jr., R.F. Davis and J. Bentley, *Kinetics and mechanisms of high-temperature creep in silicon carbide: II, chemically vapor deposited*, J. Am. Ceram. Soc., **1984**, 67(11), 732-740.
141. G.M. Renlund, S. Prochazka and R.H. Doremus, *Silicon oxycarbide glasses. Part I. Preparation and chemistry*, J. Mater. Res., **1991**, 6(12), 2716-2722.
142. B.A. Wilcox and A.H. Clauer, *Role of grain size and shape in strengthening of dispersion-hardened nickel alloys*, Acta Met., **1972**, 20(5), 743-757.
143. A. Mortensen, *Concise Encyclopedia of Composite Materials*, 2nd ed., **2006**, Elsevier Science: Amsterdam, Netherlands, 1050 pp.
144. S.K. Verma and A.K. Tiwari, *Progress of nanofluid application in solar collectors: A review*, Energy Convers. Manage., **2015**, 100, 324-346.
145. C.T. Nguyen, F. Desgranges, G. Roy, N. Galanis, T. Mare, S. Boucher and H. Angue Mintsa, *Temperature and particle-size dependent viscosity data for water-based nanofluids - Hysteresis phenomenon*, Int. J. Heat Fluid Flow, **2007**, 28(6), 1492-1506.
146. A.T. Utomo, H. Poth, P.T. Robbins and A.W. Pacek, *Experimental and theoretical studies of thermal conductivity, viscosity and heat transfer coefficient of titania and alumina nanofluids*, Int. J. Heat Mass Transfer, **2012**, 55(25-26), 7772-7781.
147. P. Kroll, *Searching insight into the atomistic structure of SiCO ceramics*, J. Mater. Chem., **2010**, 20(46), 10528-10534.
148. I.A. MacLeod, *Modern structural analysis: modelling process and guidance*, **2005**, Thomas Telford Ltd.: London, 191 pp.
149. D. Posselt, J.K. Kjems, A. Bernasconi, T. Sleator and H.R. Ott, *The thermal conductivity of silica aerogel in the phonon, the fracton, and the particle-mode regime*, Europhys. Lett., **1991**, 16(1), 59-65.
150. T. Nakayama, *Boson peak and terahertz frequency dynamics of vitreous silica*, Rep. Prog. Phys., **2002**, 65(8), 1195-1242.
151. S. Alexander, C. Laermans, R. Orbach and H.M. Rosenberg, *Fracton interpretation of vibrational properties of cross-linked polymers, glasses, and irradiated quartz*, Phys. Rev. B: Condens. Matter, **1983**, 28(8), 4615-4619.
152. A.L. Loeb, *Thermal conductivity. VIII. A theory of thermal conductivity of porous materials*, J. Am. Ceram. Soc., **1954**, 37, 96-99.
153. A. Eucken, *The heat conductivities of ceramic refractory materials. Calculations of heat conductivity from the constituents*, Forsch. Geb. Ingenieurwes., **1932**, 16(353), 353-360.
154. F. Roth, P. Waleska, C. Hess, E. Ionescu and N. Nicoloso, *UV Raman spectroscopy of segregated carbon in silicon oxycarbides*, J. Ceram. Soc. Jpn., **2016**, 124(10), 1042-1045.
155. D.P.H. Hasselman, L.F. Johnson, L.D. Bentsen, R. Syed, H.L. Lee and M.V. Swain, *Thermal diffusivity and conductivity of dense polycrystalline zirconium dioxide ceramics: a survey*, Am. Ceram. Soc. Bull., **1987**, 66(5), 799-806.
156. K.W. Schlichting, N.P. Padture and P.G. Klemens, *Thermal conductivity of dense and porous yttria-stabilized zirconia*, J. Mater. Sci., **2001**, 36(12), 3003-3010.

5 Cumulative Part of the Thesis

5.1 Statement of personal contribution

[1] **C. Stabler**, E. Ionescu, M. Graczyk-Zajac, I. Gonzalo-Juan, R. Riedel, Silicon oxycarbide glasses and glass-ceramics: "All-Rounder" materials for advanced structural and functional applications, *Journal of the American Ceramic Society*, 101(11) (2018) 4817-4856.
Invited Feature Article, Cover Feature.

The majority of this feature article was written by myself. Revision and approval was performed by PD Dr. Emanuel Ionescu and Prof. Ralf Riedel.

[2] **C. Stabler**, F. Célarié, T. Rouxel, R. Limbach, L. Wondraczek, R. Riedel, E. Ionescu, Effect of composition and high-temperature annealing on the local deformation behavior of silicon oxycarbides, *Journal of the European Ceramic Society,* 39(7) (2019) 2287-2296.

All experimental work and data analysis in this study, except nanoindentation and ultrasonic echography, were performed by myself. The measurement plan was developed by myself. The manuscript was written by myself and revised and approved by PD Dr. Emanuel Ionescu, Prof. Ralf Riedel, Dr. René Limbach, Prof. Wondraczek, Prof. Fabrice Célarié and Prof. Tanguy Rouxel.

[3] **C. Stabler**, F. Roth, M. Narisawa, D. Schliephake, M. Heilmaier, S. Lauterbach, H.J. Kleebe, R. Riedel, E. Ionescu, High-temperature creep behavior of a SiOC glass ceramic free of segregated carbon, *Journal of the European Ceramic Society*, 36(15) (2016) 3747-3753.

The synthesis, characterization (except TEM imaging), and processing of the investigated samples were done by myself. The measurement parameters for creep experiments were planned by myself and performed by Dr. Daniel Schliephake. The data evaluation of the creep experiments was performed by myself. The manuscript was written by myself and revised and approved by PD Dr. Emanuel Ionescu, Prof. Ralf Riedel, Prof. Masaki Narisawa, Dr. Daniel Schliephake and Prof. Martin Heilmaier.

[4] **C. Stabler**, D. Schliephake, M. Heilmaier, T. Rouxel, H.J. Kleebe, M. Narisawa, R. Riedel, E. Ionescu, Influence of SiC/Silica and Carbon/Silica Interfaces on the High-Temperature Creep of Silicon Oxycarbide-Based Glass Ceramics: A Case Study, *Advanced Engineering Materials*, 1800596 (2018) 1-11. Doi: 10.1002/adem.201800596.

The synthesis, characterization (including density measurements in a density gradient column) except TEM imaging and processing of the investigated samples was done by myself. The measurement parameters for creep experiments were planned by myself and performed by Dr. Daniel Schliephake and Dipl.-Ing. Hans Chen (AK Prof. Heilmaier). The data evaluation and interpretation of the creep experiments was performed by myself. The manuscript was written by myself and revised and approved by PD Dr. Emanuel Ionescu, Prof. Ralf Riedel, Prof. Tanguy Rouxel, Dr. Daniel Schliephake, Prof. Martin Heilmaier and Prof. Masaki Narisawa.

[5] **C. Stabler**, C. Seemüller, A. Choudhary, M. Heilmaier, S. Lauterbach, H.J. Kleebe, E. Ionescu, Synthesis and high-temperature creep behavior of a SiLuOC-based glass-ceramic, *Journal of the Ceramic Society of Japan*, 124(10) (2016) 1006-1012.

The synthesis and characterization of the investigated samples (except TEM imaging and thermal analysis) was done by myself. The data evaluation and interpretation of the creep experiments was performed by myself. The manuscript was written by myself and revised and approved by PD Dr. Emanuel Ionescu, Prof. Ralf Riedel, Prof. Martin Heilmaier.

[6] **C. Stabler**, A. Reitz, B. Albert, P. Stein, R. Riedel, E. Ionescu, Thermal Properties of SiOC Glasses and Glass Ceramics at Elevated Temperatures, *Materials (Basel)*, 11(2, 279) (2018) 1-18.

The synthesis, characterization and processing of the investigated samples was done by myself. The measurement outline for the determination of the thermal properties was planned by myself. Data interpretation and writing of the manuscript was performed by myself. Revision and approval was performed by PD Dr. Emanuel Ionescu, Prof. Ralf Riedel, M.Sc. Andreas Reitz, Prof. Barbara Albert and Dr. Peter Stein.

5.2 List of selected reprints

Received: 22 March 2018 | Revised: 15 June 2018 | Accepted: 15 June 2018

DOI: 10.1111/jace.15932

Journal of the American Ceramic Society

INVITED FEATURE ARTICLE

Silicon oxycarbide glasses and glass-ceramics: "All-Rounder" materials for advanced structural and functional applications

Christina Stabler | **Emanuel Ionescu** | **Magdalena Graczyk-Zajac** | **Isabel Gonzalo-Juan** | **Ralf Riedel**

Institute for Materials Science, Technische Universität Darmstadt, Darmstadt, Germany

Correspondence: Emanuel Ionescu, Institute for Materials Science, Technische Universität Darmstadt, Otto-Berndt-Str. 3, D-64287 Darmstadt, Germany (ionescu@materials.tu-darmstadt.de).

Funding information
European Cooperation in Science and Technology, Grant/Award Number: CM1302; Deutsche Forschungsgemeinschaft, Grant/Award Number: IO 64/7-1, IO 64/9-1

Abstract

Silicon oxycarbides can be considered as being carbon-containing silicates consisting of glass networks in which oxygen and carbon share bonds with silicon. The carbon-for-oxygen substitution in silicate glass networks has been shown to induce significant changes in the network connectivity and consequently strong improvements in the properties of the silicate glass network. For instance, SiOC glasses exhibit Young's moduli, hardness values, glass transition, and crystallization temperatures which are superior to those of vitreous silica. Moreover, the silicon oxycarbide glass network exhibits unique structural features such as reduced mass fractal dimension and nano-heterogeneity, which significantly affect and/or dictate its properties and behavior. In the present Review, a consideration of the current state of the art concerning the synthesis, processing, and various structural and functional properties of silicon-oxycarbide-based glasses and glass-ceramics is done. Thus, the synthesis of silicon oxycarbides starting from macromolecular precursors such as polysiloxanes or alkoxysilanes-based sol-gel systems as well as current advances related to their processing will be critically reviewed. In addition, various structural and functional properties of silicon oxycarbides are presented. Specific emphasis will be put on the intimate correlation between the molecular architecture of the precursors and the structural features and properties of the resulting silicon oxycarbides.

KEYWORDS

glass, glass-ceramics, polymer precursor, silicon oxycarbide

1 | INTRODUCTION

Silicon oxycarbide-based (SiOC) glasses (also referred to as black glasses) are materials which may be formally described as resulting products from the carbon incorporation into silicate glass networks. Although the first attempts to incorporate carbon into silica date back to the early 1950s,[1] silicon oxycarbide glasses have been synthesized only since less than three decades. Besides some exceptions reported in literature,[2,3] the only suitable synthetic access to silicon oxycarbide glasses and glass-ceramics relies on the use of sol-gel precursors based on the organically modified alkoxysilanes as well as of polyorganosiloxanes.[4,5] Both types of preceramic precursors exhibit Si–C and Si–O bonds within their backbone, which are preserved upon thermal conversion of the precursor into glass. Silicon oxycarbides remain amorphous up to T = 1200°C, present unique creep resistance up to high temperatures and excellent behavior in oxidative and corrosive environments.[5] The incorporation of additional elements into the Si–O–C systems can lead to a further improvement of those properties.[5,6] Especially, the excellent creep behavior of SiOC

glasses at temperatures beyond 1000°C is rather unique and makes this class of materials highly interesting for high and ultrahigh temperature applications.[7–10]

The structure of silicon oxycarbide glass is composed of a network of corner-shared silicon-centered tetrahedra incorporating both Si–C and Si–O but no C–O bonds (SiO_xC_{4-x} tetrahedra). The network is distinct from a mixture of separate, intergrown silicon carbide and silicon oxide nanophases and exhibits the full range of mixed bonded SiO_xC_{4-x} tetrahedra (i.e., SiO_4, SiO_3C, SiO_2C_2, $SiOC_3$, and SiC_4).[11] The presence of carbon within the amorphous network indicates that the Si tetrahedra are corner-shared not only via oxygens (i.e., two tetrahedra corner-sharing an oxygen) but also by carbons (i.e., four tetrahedra corner-shared by one carbon). This leads formally to a significantly higher degree of cross-linking of the silicon oxycarbide network as compared to that of a fully connected SiO_2 glass (consisting of corner-shared Q^4 tetrahedra via bridging oxygens). Thus, the presence of carbon within the network of silicon oxycarbide provides a fully connected network by corner sharing and a different local structure than that of silica or silicate networks. Extensive studies based on magic-angle-spinning nuclear magnetic resonance (MAS NMR) spectroscopy, small-angle x-ray scattering (SAXS), high-temperature creep, and transmission electron microscopy (TEM) data indicate that the SiOC amorphous network has a nano-heterogeneous and fractal nature (mass fractal dimension of 2.4-2.5).[7,8,11–14] This unique network architecture was shown to be responsible for their relatively high Young's moduli (90-120 GPa[15,16]; compared to that for silica glass, 70-75 GPa), hardness values[17,18] as well as for their very high glass transition temperatures (T_g ~ 1350°C[7,8,15,19]; compared to ~1170°C for vitreous silica). The highly connected glass network of silicon oxycarbide was shown to exhibit extremely high resistance to phase separation and crystallization up to temperatures significantly higher than 1000°C.[20,21]

There has also been success in incorporating different metal cations into the silicon oxycarbide glassy network, including alkali metals,[22] alkaline earth metals,[23] and transition metals,[24–27] as well as main group semimetals and metals.[27–29] The incorporation of metals into SiOC was shown to affect the high-temperature evolution of its phase composition as well as the network architecture.[25,26,30] Interestingly, there are different ways of incorporation metal into silicon oxycarbide: (a) upon substituting silicon for (semi)metal in the network (as for boron; B substitution occurs via generation of BO_xC_{3-x} mixed-bond sites in the network[31,32]); (b) introduction of metal into the network via MO_x sites (no mixed bonds at the metallic sites in the network), which show high tendency to partition from the network as metal oxide secondary phase (as typically for transition metals,[24,30,33]); (c) upon generating non-bridging oxygens in the network (i.e., metals as network modifiers, such as alkali and earth-alkaline metals[22,34]).

In the present Review, a critical consideration of the past and current activities related to the preparation, structural characterization as well as various structural and functional properties of silicon oxycarbide-based glasses and glass-ceramics is done. Following aspects will be addressed: (a) The synthesis and structural features of single-source precursors as well as their thermal conversion into SiOC glasses and glass-ceramics will be briefly introduced; (b) A general consideration of the energetics, nano/microstructure as well as high-temperature evolution of SiOC glasses and glass-ceramics will be done; and (c) Various structural and functional properties of SiOC glasses and glass-ceramics will be highlighted; emphasis will be put on the intimate correlation between their properties and the network architecture and nano/microstructure of these unique materials.

2 | SYNTHESIS OF SILICON OXYCARBIDES (SiOC)

2.1 | Synthesis of preceramic polymers

SiOC glasses and glass-ceramics are complex nanostructured materials without a fixed composition or microstructure. The chemical composition, phase composition, and the microstructure of SiOC materials can be tuned by choosing different single-source precursors.[21,35,36] Important parameters are their molecular structure, composition, and chemical bonding. To obtain SiOC materials, the precursors are thermally converted to ceramics in a controlled (typically inert) atmosphere. The parameters upon heat treatment such as temperature of pyrolysis, heating rate, dwelling time, and gas atmosphere further influence the final chemical and phase composition of SiOC glasses and glass-ceramics.

Suitable precursors for the synthesis of SiOC glasses and glass-ceramics should possess a high molecular weight to minimize the weight loss during conversion, appropriate visco-elastic behavior and solubility for various shaping processes, as well as curable functional groups. Thus, several processing techniques known for polymer processing can be applied for the shaping of SiOC glasses and glass-ceramics such as injection molding, extrusion, spin coating, fiber drawing or polymer infiltration pyrolysis (PIP).[4,35,37] Appropriate single-source precursors for SiOC are polyorganosiloxanes and sol-gel derived precursors based on organically modified alkoxysilanes.[4,5]

2.2 | Polysiloxanes and polysilsesquioxanes

Polysiloxanes are widely common precursors for the synthesis of SiOC glasses and glass-ceramics.[35,37] Usually,

they are commercially available, inexpensive polymers that are synthesized upon reaction of organylchlorosilanes with water.[38] Depending on the synthesis conditions, their molecular architecture consists of linear chain polymers, various branching as well as highly cross-linked structures (Figure 1).[39] Their excellent thermomechanical properties (e.g., low-temperature elasticity, low glass transition temperatures, etc.) as well as their high stability at elevated temperatures and oxidative environments allow an efficient processing of polysiloxanes to green bodies. The enhanced high temperature stability with respect to decomposition as compared to carbon-based organic polymers is considered to relay on the inherent strength of the siloxane bond (Si–O bond) itself, as it possesses both partially ionic character as well as double bond character.[39] Consequently, for the Si–O bond a dissociation energy of 108 kJ/mol is determined, which is considerably higher than for C–C (82.6 kJ/mol), C_{arom}–C (97.6 kJ/mol), and C–O (85.2 kJ/mol) bonds.[39] Due to the high dynamic flexibility of their Si–O chains, polysiloxanes possess the lowest reported glass transition temperatures T_g among polymeric materials, making them easy to process.[40]

A category of polysiloxanes with special, relatively high cross-linking degrees and therefore high ceramic yield is represented by the polysilsesquioxanes (Figure 1C), with the general formula $[RSiO_{1.5}]_n$ (with R being, e.g., H, methyl, ethyl, vinyl, aryl). The nature of the R groups and the molecular structure influence the rheological properties and thus the processing of the polysilsesquioxanes, which were also successfully used as SiOC precursors.[35,37,41] In addition, hyperbranched polysiloxanes and polycarbosiloxanes are reported in literature (Figure 1D).[42–46]

2.3 | Sol-gel synthesis–Silicon alkoxides

Since the late 1980s, several sol-gel routes using the co-hydrolysis and condensation of various silicon alkoxides to synthesize precursors for silicon oxycarbide glasses and glass-ceramics have been established and reported.[36,50,51] The resulting gels have the general formula $R_xSi(OR')_{4-x}$ (with R being alkyl, allyl, aryl and R' being methyl, ethyl). The composition of the gels can precisely be tuned with altering the molar ratios of the respective silicon alkoxides as well as the selection of the alkoxides themselves. For example, trifunctional alkoxides $Si(OR)_3R'$ are used to alter the total amount of carbon in the gel. Furthermore, by choosing an appropriate pH value the architecture of the resulting gel can be directly influenced from highly cross-linked network (basic conditions) to elongated chains (acidic conditions).[52]

The flexibility of this approach is demonstrated by the impact of different components on the formation of the gel network. With the use of trifunctional alkoxides (Si$(OR)_3R'$; R, R' = methyl, ethyl, vinyl, etc.), organic groups are introduced within the hybrid gel, governing the final content of carbon in the resulting ceramic. Bifunctional alkoxides ($Si(OR)_2R'_2$) tend to form polymeric chains and large rings during hydrolysis and condensation, providing flexibility of the gel network. Orthosilicates ($Si(OR)_4$) as well as metal alkoxides ($M(OR)_x$, M = main group or transition metal) lead to higher cross-linking degrees of the resulting gel. As already pointed out, a higher cross-linking degree of the preceramic precursor has a direct influence on the ceramic yield of the resulting silicon oxycarbide glass/glass-ceramic.

Especially in the 1990s, systematic studies were performed to unravel the role of the different sol-gel systems on the resulting silicon oxycarbide (e.g., Ref. 21,53). It was demonstrated, that the use of unsaturated hydrocarbon organic groups (e.g., vinyl, allyl, and phenyl groups) leads to an increased carbon content in comparison to saturated hydrocarbon organic groups (e.g., methyl, ethyl, and propyl groups).[21] Furthermore, the retention of Si–C bonds in the polymeric backbone while reducing the excess of carbon can be enhanced by the incorporation of Si–H bonds.[21,53,54]

Another possibility of tuning the composition of SiOC glasses is by changing the molar ratios of the used silicon alkoxides. Gels can be derived for instance from different mixtures of triethoxysilane (TREOS) and methyldiethoxysilane (MDES) and can be converted into SiOC glasses with tightly controllable compositions, such as those exhibiting excess of carbon, some having no segregated carbon and others containing excess of silicon.[54]

2.4 | Chemically modified single-source precursors

For both, the polymer precursors and the sol-gel derived precursors, synthesis routes for the incorporation of additional elements such as boron as well as different main group and transition metals have been developed.[25,53,55,56] For instance, boron can be incorporated within the SiOC glass network upon polymer-to-ceramic conversion of suitable boron-containing preceramic polysiloxanes and sol-gel systems. Thus, boric acid was used to modify alkoxysilane-derived sol-gel systems or polysiloxanes through condensation reactions (Figure 2).[31] The boron modification can be also performed in the monomer state, followed by polymerization, as reported in Ngoumeni-Yappi et al[32] (Figure 2); thus, in the mentioned case study, a dichloro-methyl-vinylsilane was chemically modified in a first step with borane dimethyl sulfide complex via hydroboration and subsequently polymerized via condensation reactions with methanol and water. Typically, the extent of chemical cross-linking of the sol-gel systems or polysiloxanes was

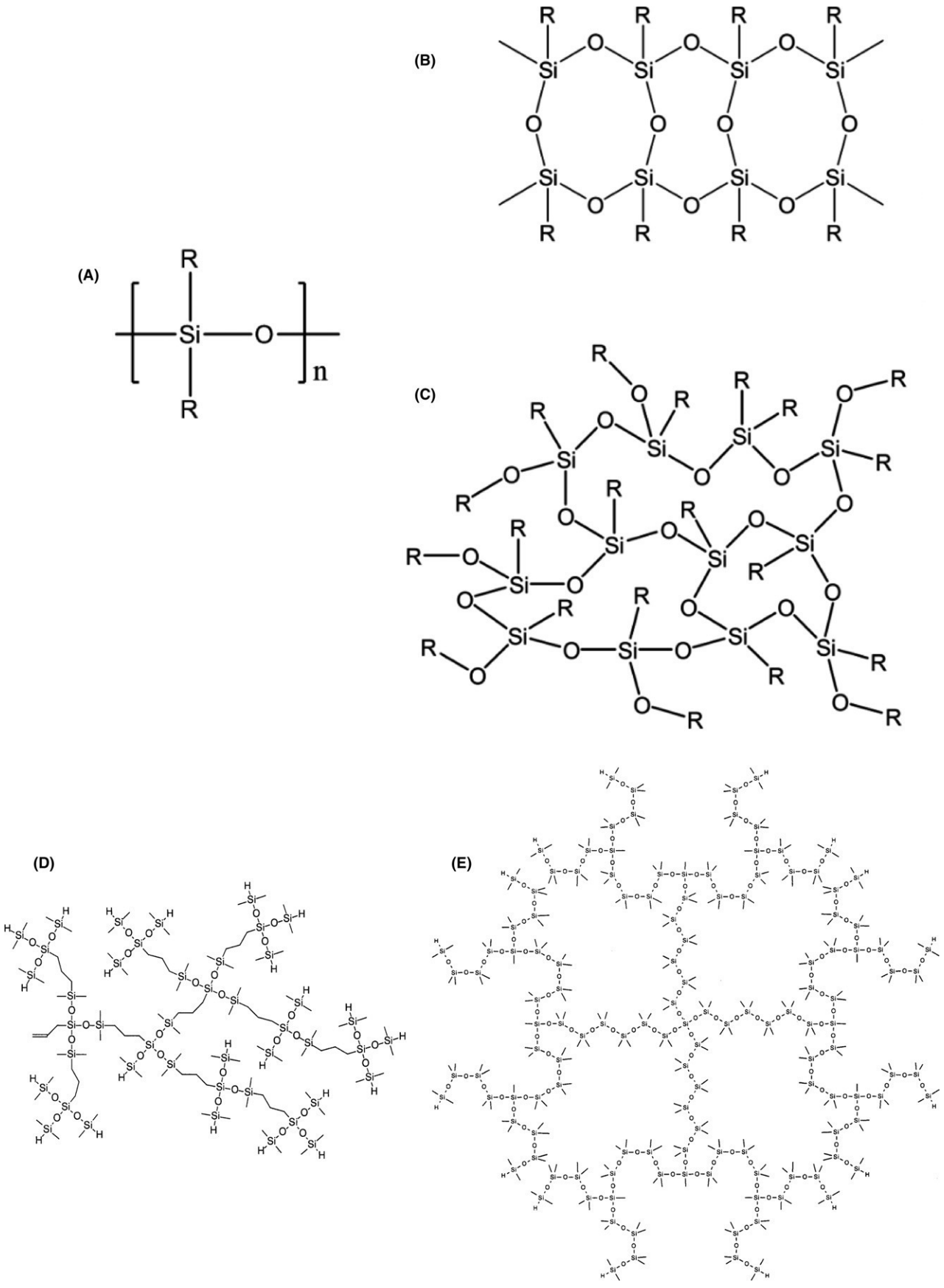

FIGURE 1 Schematic structure of A, polysiloxanes; B, ladder-like polysilsesquioxanes and C, amorphous/disordered polysilsesquioxanes,[41,47] D, hyperbranched polycarbosiloxanes,[48] and E, dendritic polysiloxanes[49]

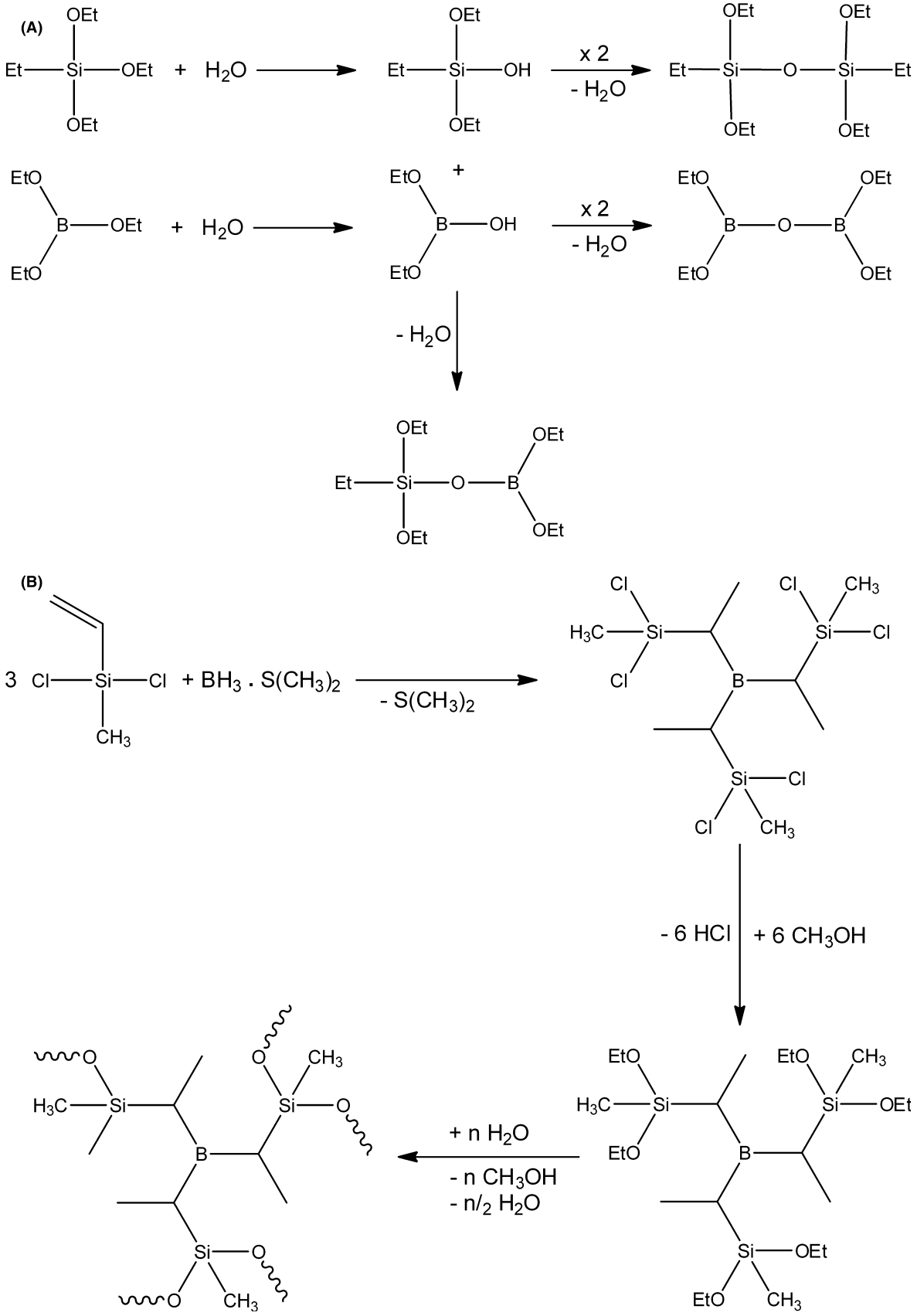

FIGURE 2 A, Synthesis of a single-source precursor for boron-modified SiOC glass based on the sol-gel process involving ethyltriethoxy silane and triethylborate[31]; B, Synthesis of a boron-modified polysiloxane via hydroboration of a vinyl dichloro silane followed by alcoholysis, hydrolysis, and polycondensation[32]

shown to be related to the amount of boric acid or borane complex and to determine the visco-elastic properties of the obtained precursor systems.

Similarly, other elements can be incorporated within the SiOC network, as shown for numerous main group and transition metals. For instance, suitable functional groups (e.g., hydroxyl or alkoxy) can be reacted with (transition) metal alkoxides, metal acetates or acetylacetonates. FTIR spectroscopy studies indicated that the chemical modification of the polysiloxanes occurs indifferent of the metal precursor used (alkoxides, acetates, acetylacetonates etc.) and leads to the formation of single-source precursors for metal-modified silicon oxycarbide glasses. It was demonstrated that the modification of polysil(sesqui)oxanes with metal alkoxides, acetylacetonates or acetates leads to an increase of their cross-linking degree.[25,56,57] Hence, the rheological behavior of the resulting single-source precursors can be adjusted as necessary for the individual processing techniques and moreover the mass loss upon thermal conversion into glass or glass-ceramics can be tuned.[25]

2.5 | Conversion of preceramic polymers into silicon oxycarbides

The transformation of the single-source precursors to the final inorganic product (SiOC glass or glass-ceramic) follows several steps[25,37]: (a) crosslinking of the thermoplastic precursors at low temperatures (100-400°C) to produce infusible organic/inorganic networks; (b) thermal conversion into glass *via* pyrolysis at temperatures ranging from 600 to 1000°C; (c) phase separation (at T > 1200°C) followed by crystallization. Further heat treatment at higher temperatures leads to predominantly polycrystalline materials. The crosslinking step is of significant relevance, as it prevents the loss of low-molecular-weight components of the precursor and increases the ceramic yield during pyrolysis. The conversion from thermosetting to infusible precursor allows moreover the fabrication of green bodies with complex shapes that are preserved during pyrolysis.[56] The overall process is schematically depicted in Figure 3.

Depending on the organic functional groups present in the precursor, several reactions can occur during crosslinking of polysiloxanes and polysilsesquioxanes[56]: (a) Condensation of Si–OH units from hydroxyl and alkoxy groups with the in situ release of water, leading to Si–O–Si bond formation[57]; (b) Hydrosilylation between Si–H and Si–vinyl groups, resulting in Si–C bond formation. Through the addition of catalysts, the temperature as well as the time necessary for reaction can be significantly reduced[58,59]; (c) Vinyl polymerization which is weight conservative. This reaction proceeds at higher temperatures (>300°C), by the addition of free radical initiators and UV light irradiation or by addition of transition metal catalysts.[60] Furthermore, the crosslinking of polysiloxanes containing either methyl or vinyl groups can be performed thermally, using peroxides.[61] In the temperature range from 300 to 600°C, various redistribution reactions between Si–O, Si–C, and Si–H bonds lead to the formation and evaporation of low-molecular-weight oligomers.[62] Belot et al performed a careful examination of the possible redistribution reactions that might occur in crosslinked polysiloxanes.[62] They are summarized in Figure 4 and can be divided in three groups, that is, Si–O/Si–O exchange, Si–C/Si–O exchange and Si–H/Si–O exchange processes.

The conversion of the crosslinked precursors into SiOC glass takes place at elevated temperatures, that is, between 600 and 1000°C, with the cleavage and subsequent volatilization of organic groups in the form of hydrocarbons and hydrogen.[35,37] The precise mechanisms involved during ceramization are rather complex and difficult to be clarified in detail. During the thermal conversion of the single-source precursors, a significant amount of Si–C and Si–O bonds is preserved in the resulting SiOC glasses.[21,25,50,63] Besides conventional oven heating, the polymer-to-ceramic conversion can be achieved using microwaves.[64] Small differences in the resulting SiOC microstructure were observed at high temperatures (~1500°C), where a slightly diminished carbothermal decomposition (*cf.* Equations (3) and (4) in Chapter 5.2) leads to lower amounts of β-SiC nanoparticles.

In some few case studies, the fabrication of SiOC via non-thermal conversion of polysiloxanes was studied and demonstrated. For instance, Pivin et al showed that the conversion can be performed by ion beam irradiation of the preceramic polymers. The ion beam produces radicals which randomly react with functional groups and oligomers in the preceramics to produce, for example, Si–CH_x–Si bonds and hydrogen. The chemical composition, that is, the carbon content, can be tuned upon variation of the ion fluence.[65,66] Besides ion bombardment, X-rays were used as an alternative route for crosslinking of polysiloxanes,[67] which were subsequently converted via pyrolysis into SiOC. For SiCN precursors, it was demonstrated that flash pyrolysis using IR irradiation is possible,[68] opening an interesting concept to be possibly transferred to polysiloxanes in the future.

Whereas the pyrolysis of silicon alkoxide-based sol-gel systems of preceramic polysiloxanes leads to ternary SiOC glassy systems, metal-modified polysiloxanes were shown to be suitable single-source precursors to ceramic nanocomposites. In a recent study, it was shown that the ceramization process of metal-modified polysiloxanes is dictated by thermodynamic stability of the in situ precipitated MO_x phase with respect to the system C–CO.[6] Based on structural studies related to the evolution of the phase

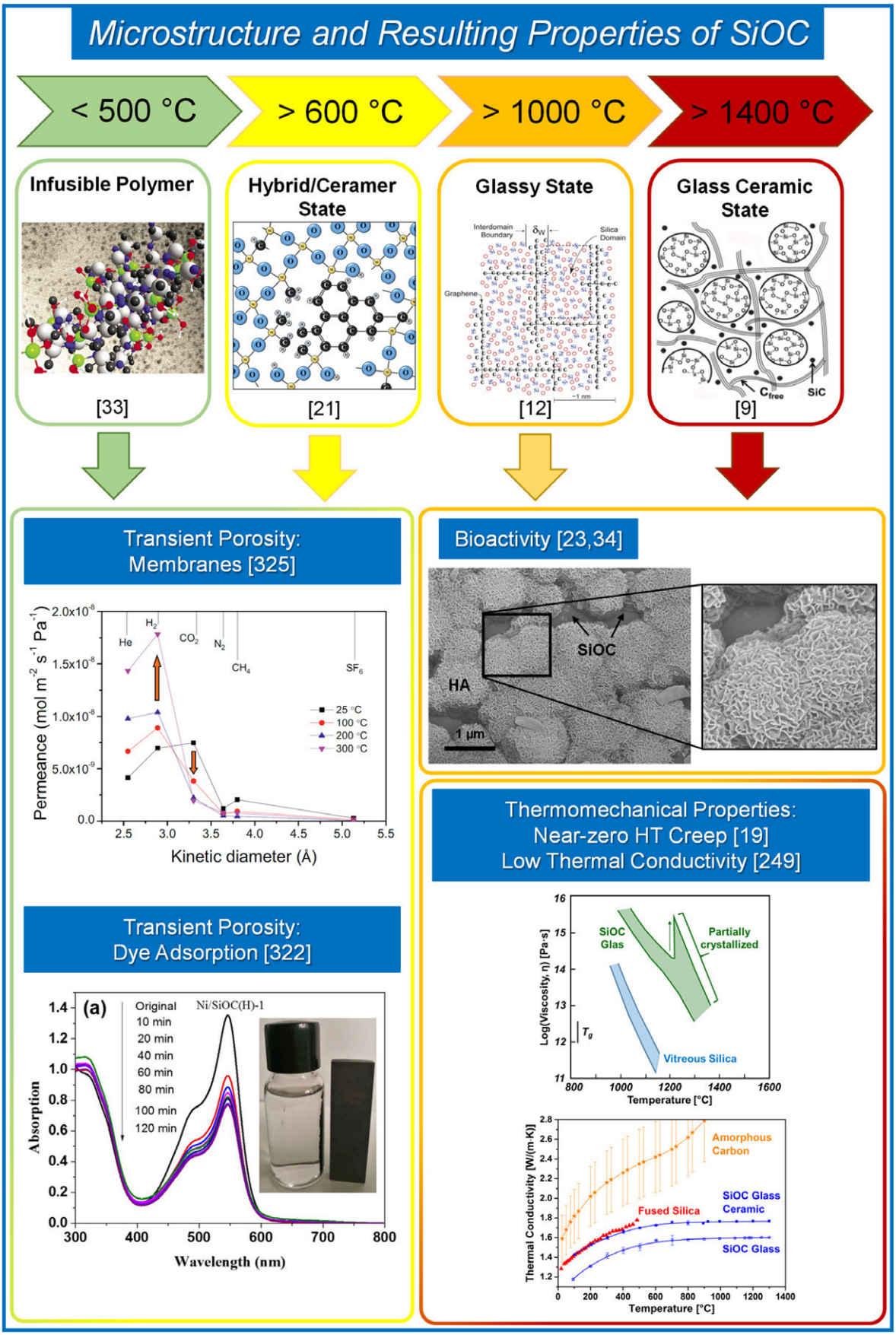

FIGURE 3 Microstructure and selected properties of SiOC materials

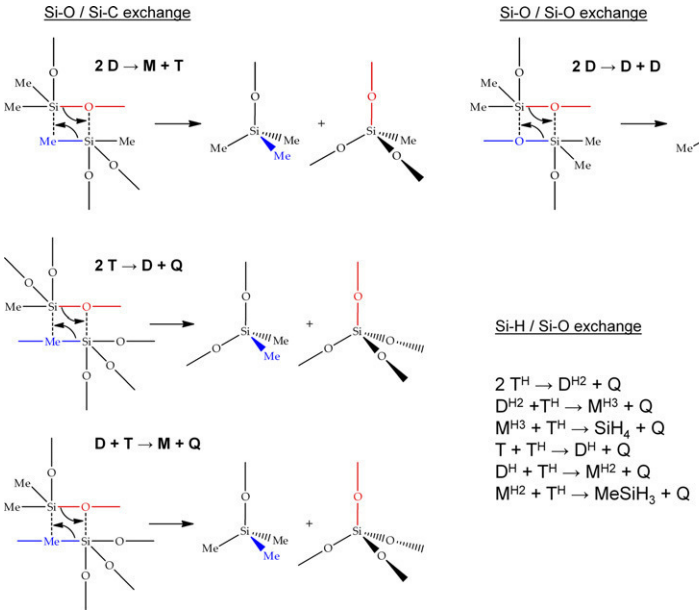

FIGURE 4 Possible redistribution reactions between Si–O, Si–C, and Si–H bonds during conversion of the organic polymer to an inorganic SiOC glass. The different silicon sites are assigned according to the MDTQ-nomenclature, with M being ($SiOR_3$), D (SiO_2R_2), T (SiO_3R), and Q units (SiO_4) if R is, for example, methyl. An index "H^x" indicates the presence of x Si–H groups at one silicon site (drawn after Ref. 62)

composition of SiMOC materials at high temperatures,[22,30] it has been concluded that metal-modified polysiloxanes convert at temperatures below 1000°C into a single-phase amorphous SiMOC material; its exposure to higher temperatures leads in a first step to the in situ generation of a MO_x phase homogeneously dispersed within a Si(M)OC glassy matrix.[25,33,56] Subsequent evolution of the phase composition of the intermediary generated MO_x/SiOC nanocomposites is considered to be thermodynamically driven.[6] Thus, the phase composition of different SiMOC systems (M = Li, Mg, Ca, Sn, Fe, Mn, V, and Lu) was investigated. Depending on the metal, different ceramic phases formed. For M = Li, Mg, Ca, and Lu $MSiO_x$/SiOC nanocomposites were generated[22,34]; for M = Mn, MO_x/SiOC ceramic nanocomposites were formed,[10] whereas other compositions revealed the formation of M/SiOC (M = Sn),[29] MSi_x/SiOC (M = Fe)[27] or MC_x/SiOC (M = V)[69] upon pyrolysis (*cf.* Figure 5). The different phase compositions of the SiMOC materials were rationalized by a simple thermodynamic approach which is able to correctly predict which type of ceramic nanocomposite is expected upon ceramization of the metal-modified precursors. Calculations show that the thermodynamic stability of the MO_x phase with respect to that of the C–CO system is the most important factor to predict phase formation in polymer-derived SiMOC ceramic systems. In addition to the stability of the oxides with respect to reduction, some other aspects have to be taken into account for estimating the phase composition of SiMOC-based nanocomposites, such as thermodynamic stabilization through conversion into silicates (for MO_x being stable with respect to carbothermal conversion into M) or into silicides or carbides (for MO_x not being stable against carbothermal reduction).[6]

3 | PROCESSING OF SILICON OXYCARBIDES

Numerous processing techniques can be used to obtain SiOC ceramics from liquid or soluble preceramic polymers. For instance, polysil(sesqui)oxanes were used to in applications as joining materials, for example, for reaction bonded silicon carbide specimens.[71] Moreover, SiOC-based ceramic matrix composite materials were studied, based on the fact that polysil(sesqui)oxanes can be easily integrated in liquid polymer infiltration (LPI) processes to fabricate CMCs.[72–75]

3.1 | Monolithic silicon oxycarbides

SiOC monolithic specimens can be prepared via the fabrication of a green-body shaped in a uniaxial or isostatic press operating at moderate temperatures (from ambient temperature to 300-400°C) and its subsequent pyrolysis. For an optimum result of a crack-free and dense monolithic ceramic piece, the optimum temperature for the formation of a green-body and the applied pressure during the green-body formation must be determined and adjusted for every polymeric system as demonstrated for polysilazanes as SiCN precursors[76–78] and a polysilsesquioxane.[79] Thermo-mechanical analysis (TMA) is a useful tool to identify the best processing parameters. Two other ways are described to obtain monolithic green-bodies: (a) casting of sol-gel systems followed by careful aging and drying[18,80,81]; (b) cold isostatic pressing (CIP) of pre-cross-linked preceramic polymers.[82] The subsequent transformation from the green-body to the glass is performed upon pressureless pyrolysis in inert gas atmosphere (Ar, He, or N_2).

Typically, the cleavage processes during conversion of the preceramic polymer to the final ceramic lead to mass loss and

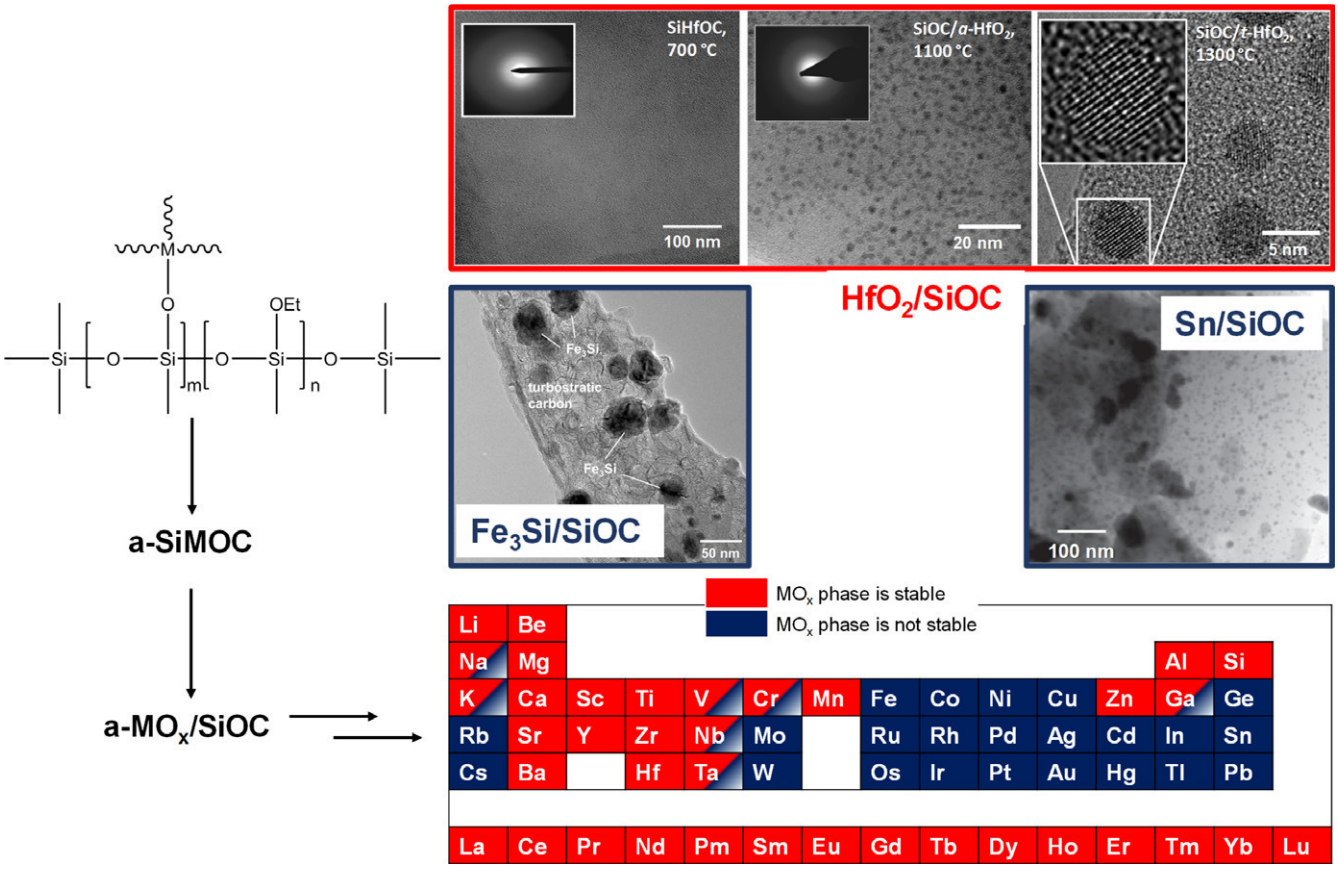

FIGURE 5 Ceramization of metal-modified polysiloxanes. In a first step, single-phase amorphous SiMOC ceramics are obtained (at temperatures of 700-1000°C), which at higher temperatures partition leading to MO_x-containing SiOC amorphous nanocomposites. The subsequent evolution of the phase composition in MO_x/SiOC is thermodynamically controlled and correlates to the stability of MO_x in the presence of the segregated carbon phase[6] (reprinted with permission of Wiley). TEM micrographs show the evolution of the phase composition and microstructure of HfO_2/SiOC[25] (HfO_x phase stable at high temperatures in the presence of carbon) as well as of Sn/SiOC[29] (reprinted with permission of Wiley) and Fe_3Si/SiOC[27,70] (SnO_x and FeO_x not stable in the presence of carbon)[6]

consequently to porosity. Thus, cracking may occur during the ceramization, making it difficult to obtain pore- and crack-free monoliths. Therefore, considerable efforts were made to develop techniques that increase the ceramic yield and prevent or act against shrinkage and pore formation, including the usage of inert and reactive fillers[83,84] or multiple polymer-infiltration-pyrolysis (PIP) cycles.[85,86] With the use of inert fillers, the overall shrinkage can be reduced to negligible values though not being effective in acting against porosity. Inert fillers for SiOC include metal oxides, carbides or nitrides. The volumetric shrinkage of the filler/preceramic polymer mixture w_V(IF) can be calculated by Equation (1),[87] where V_F is the volume fraction of the inert filler, V_F^* is the critical volume fraction of the inert filler (maximum packing density) and w_F(P) is the volumetric shrinkage of the preceramic polymer.

$$w_V(\mathrm{IF}) = \left(1 - \frac{V_F}{V_F^*}\right) w_V(\mathrm{P}) \quad (1)$$

Active fillers react with the gaseous species that are released upon pyrolysis leading to expansion which can compensate the shrinkage of the polymeric precursor.[83,84,88] Thus, elemental metals Ti, Zr, Mo, Al, B, and Si as well as silicides $MoSi_2$, $CrSi_2$, and $TiSi_2$ were used as active fillers.[84] They react with hydrocarbons or with the pyrolysis atmosphere itself, forming carbides, nitrides, and oxides.[84,88] The total maximum volume change of an active filler/preceramic polymer mixture w_V(AF) is expressed through Equation (2),[89] where V_F is the filler volume fraction, V_F^* is the critical filler volume fraction (maximum particle packing density of the reacted filler phase), α and α_F is the mass change of the polymer and filler, respectively, and β and β_F is the density change of polymer and filler, respectively. The homogeneous distribution of the active fillers can be preserved with the addition of inactive filler, minimizing sedimentation effects.[88]

$$w_V(\mathrm{AF}) = \left(1 - \frac{V_F}{V_F^*}\right)(\alpha\beta - 1) + V_F(\alpha_F\beta_F - 1) \quad (2)$$

Figure 6 summarizes the differences in shrinkage and its impact on the porosity obtained when using passive and active fillers, respectively.

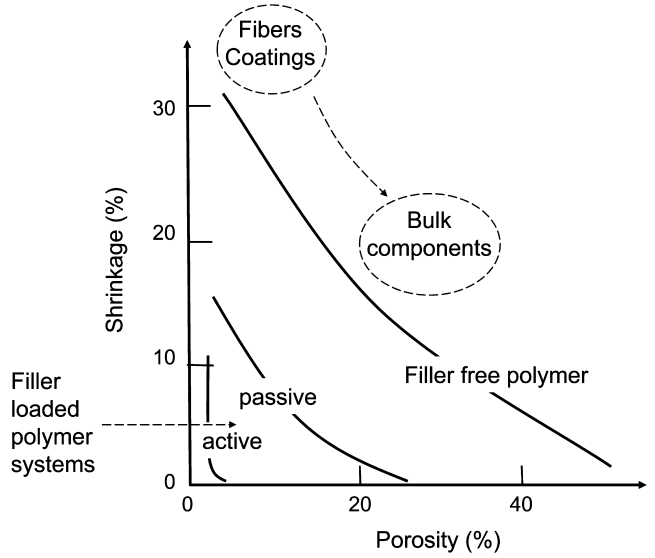

FIGURE 6 Effect of active and passive fillers on the shrinkage and porosity in preceramic polymer systems[83,84,89] (taken from Ref. 83 with permission from the Korean Ceramic Society)

In addition to the aspects related to preventing shrinkage, cracking, and porosity in SiOC-based parts, various functional properties can be enhanced or introduced to the SiOC system upon the incorporation of fillers. For instance, the electrical conductivity of SiOC foams could be increased by the addition of SiC, C, $MoSi_2$ or Cu_2O.[90] The incorporation of iron silicide fillers was shown to introduce magnetic properties into SiOC, as shown for SiOC-based ferromagnetic foams.[91]

Cracking can be further prevented by rate-controlled decomposition procedures, where slower heating rates are employed during temperature intervals with large weight losses,[83] or upon pyrolysis of green-bodies with one dimension below 1 mm.[17,18] Fully dense monolithic pieces can be furthermore obtained using pressure-assisted techniques such as uniaxial hot pressing,[7,92,93] hot isostatic pressing[94] or spark plasma sintering.[95–98]

3.2 | SiOC-based thin films and coatings

As most preceramic polymers are liquid or easily soluble in various organic solvents, a wealth of processing techniques established for polymers can be employed for the fabrication of SiOC coatings: dip coating,[99–103] spin coating,[101,104] spray coating,[105] thermal chemical vapor deposition (TCVD),[106] simple soaking,[107] and melting,[108] tape casting[109] as well as brush film application[110] are described in literature. In addition to these polymer-related processing techniques, non-polymer precursor techniques were also employed, such as the radio frequency magnetron sputtering (RF magnetron sputtering),[111,112] ultra-high vacuum RF magnetron sputtering (UHV RF magnetron sputtering)[113] and reactive laser evaporation[2] methods. A review on SiOC-based coatings was published recently.[114] Depending on the technique used, suitable visco-elastic properties for the deposition of the polymeric films can be obtained upon mixing appropriate amounts of solvents with the preceramic polymers. The concentration of the preceramic polymer in the polymer-solvent solutions is reported to influence the formation of continuous coatings giving an optimum concentration for maximum adhesion to the substrate.[107] In a similar manner, coatings derived from sol-gel synthesis show an optimum amount of water-to-siloxane ratio to obtain continuous preceramic coatings.[110] Various factors influence the successful conversion of the preceramic polymer to the final coating without the formation of pores or cracks or without spallation, such as coating time[102] and withdrawal speed.[110] For instance, it was found that in the case of spray coating the preparation of continuous coating is conditioned by an optimized wettability of the preceramic polymer on the substrate.[105] In addition, smoother substrate surfaces were shown to enhance the quality of the SiOC coatings.[105] Mathematical modeling for the determination of relevant parameters during the fabrication of a SiOC coating, such as gas residence time and precursor pump rate during the CVD process, were reported in Ref. 115.

As coatings possess higher surface areas than those of bulk monolithic pieces, they are more prone to influences of the atmosphere during pyrolysis. As a result, the chemical composition of SiOC coatings is highly dependent on the pyrolysis atmosphere, mainly its oxygen content.[101,111] In a case study, sol-gel-based SiOC thin films were prepared upon pyrolysis in inert gas atmosphere containing different oxygen partial pressures as well as in vacuum. It was shown that even small amounts of oxygen present in the pyrolysis atmosphere may lead to the conversion of the sol-gel coatings into silica instead of SiOC.[101] This strong effect of the atmosphere on the composition of the resulting ceramic thin films was also shown for SiC[101] and SiCN coatings.[116]

SiOC coatings can be applied on various substrates such as Silicon,[105,113,117] graphite fibers,[99,100,106] stainless steel,[101,108] sapphire,[101] SiC fibers,[101] α-Al_2O_3,[102] silica,[104,111] multi-walled carbon nanotubes (MWCNT),[107] carbon,[110] porcelain,[108] Ni-based superalloy,[103] Saphikon fibers,[118] and Nicalon fibers.[118] Figure 7A,B show examples for intact SiOC coatings on a silicon substrate[113] and on MWCNTs,[107] respectively. With the usage of focusing mirror furnaces, softer templates are even realizable, meanwhile ensuring a full conversion of the preceramic coating to the ceramic coating.[105] The shrinkage due to the cleavage of functional groups during the conversion of the preceramic coatings to ceramic coatings, limits the maximum coating thickness to few micrometer, as thicker coatings lead to cracking.[105] In order to increase the maximum possible film thickness, SiOC composite coatings

were developed based on the idea of minimizing the effective shrinkage by the addition of appropriate fillers.[119]

Using microphase-separation processes of block copolymers during spin coating followed by the reactive removal of one phase, tailored nano-porous SiOC thin films can be achieved, as shown in a case study using a polystyrene-*b*-polydimethylsiloxane block copolymer[117] (*cf.* Figure 7C). Moreover, porous SiOC films were also prepared using the Breath Figure technique, which involves the condensation of water droplets on a cooled polymer solution, the subsequent control of the sink-in of these droplets in the polymeric solution and the final removal of the water droplets by evaporation.[120]

3.3 | Porous SiOC

A variety of different approaches is used to synthesize SiOC materials with different degree of porosity, classes of pore sizes (micro-, meso-, or macro porosity), pore size distribution (narrow to hierarchical), pore connectivity (open or closed porosity), and resulting specific surface areas.[121] Comprehensive reviews about porous SiOC materials were published in Refs. 122,123. The generation of pores involves the intrinsic decomposition characteristics of the neat SiOC system, the insertion of templates and fillers and the production of highly porous green bodies like foams and aerogels. The combination of any of the mentioned techniques allows the fabrication of more complex porous structures.[124]

Special care has to be taken to preserve the porous structures upon pyrolysis. Important factors are heating rate and maximum pyrolysis temperature,[125] where slow heating rates prevent cracking and low temperatures preserve smaller pore sizes (microporosity). Furthermore, the chemical composition of the starting preceramic polymer has implications on the stability of the network formed up to 600°C. Especially polymer systems which allow the occurrence of a hydrosilylation reaction through the presence of Si–H and C–C double bonds show enhanced network stabilities.[122]

As will be explained in the following (*cf.* Section 5.2), at temperatures higher than approximately 1250°C, the glassy SiOC-based materials partition and consequently can be regarded as consisting of SiC and C nano-precipitates dispersed within a silica(-rich) matrix. This phase assemblage enables decomposition reactions at higher temperatures (*cf.* Section 5.2, Equations (3), (4), (5)) which lead to the release of gaseous species resulting in the formation of pores[126] with sizes of few nanometers to tens of nanometers.[122] The addition of inert fillers such as ZnO or TiO_2 can shift the pore sizes from usually microporosity (for the neat SiOC systems) to mesoporosity (with filler addition).[127,128]

The aforementioned phase separation enables the possibility to introduce porosity also through a subsequent selective removal of SiO_2, SiC or C. The removal of silica from phase separated SiOC can be achieved for instance *via* etching in HF solution,[129–135] which can be hindered if high carbon content is present.[91] SiC particles can be etched by reaction with gaseous chlorine[136,137]; whereas the selective removal of carbon can be realized upon pyrolysis in reactive atmosphere, for example, NH_3, water vapor[134,138] or H_2.[139] The complete removal of silicon and oxygen can be achieved upon etching with chlorine gas at high temperature to obtain carbide-derived carbons (CDCs).[137] The obtained SiOC-derived CDS were tested for H_2 and CH_4 storage[137] as well as adsorption purposes.[140]

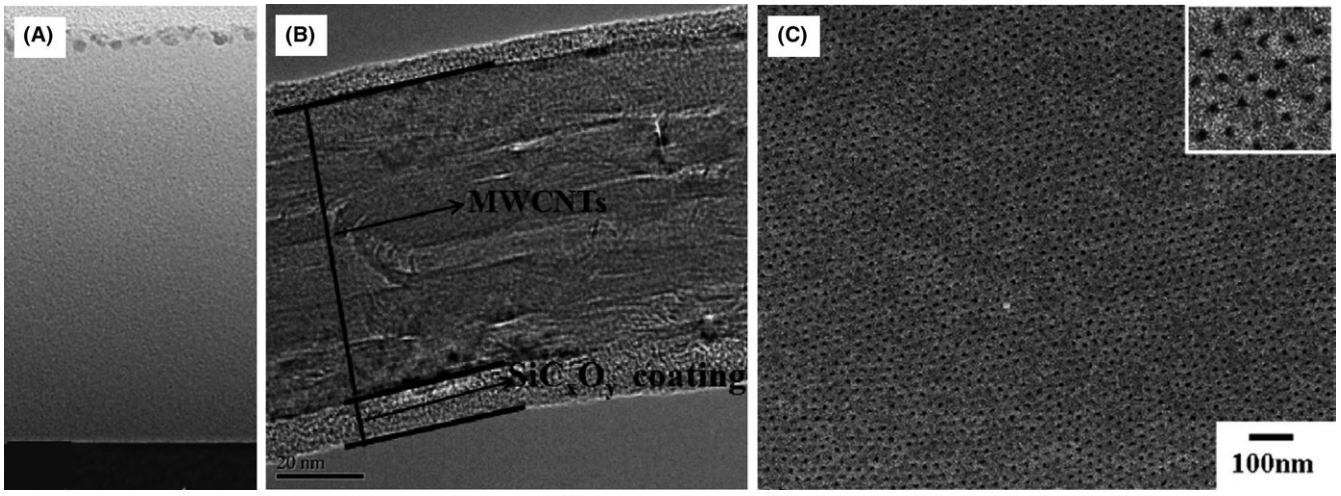

FIGURE 7 SiOC-based coatings on A, silicon substrate[113] (reprinted with permission of IOP Publishing) and B, MWCNTs[107] (reprinted with permission of Elsevier); C, Nano-patterned porous SiOC thin film prepared from a polystyrene-*b*-polydimethylsiloxane block copolymer as preceramic precursor[117] (reprinted with permission of the American Chemical Society)

Templated-assisted preparation of porous SiOC uses synthetic sponges and foams,[141] or biomorphic templates such as wood[142,143] or rice bran[144] as well as inorganic templates like LDH[145] or close-packed spheres. Water/(oil-polysiloxanes) emulsions can also be converted to SiOC under the preservation of the emulsion microstructure (i.e., hollow SiOC-based capsules are accessible in this way, see[146]). Consequently, pore sizes, pore size distribution, porosity, and surface area are highly depending on the templates used. Synthetic templates usually offer a better control of the final porous material and enable the fabrication of specimens with narrow pore size distributions and tailored pore sizes. Fillers can be dispersed directly in liquid polysiloxanes or in prepared polymeric solutions. Sacrificial templates and fillers typically used are PMMA (poly (methyl methacrylate)) microspheres[147,148] or microbeads,[149–153] polyurethane template[154] as well as polystyrene beads.[155] Carbon templates can be removed in reactive gases atmospheres like air and ammonia.[156,157] Frequently used inert materials are silica spheres,[130,158] that can be removed by subsequent etching in HF after pyrolysis. Hierarchical porosity can be obtained for example upon the combination of ceramic supports and SiOC foaming techniques.[159,160]

Highly porous SiOC materials can be furthermore provided via direct foaming procedures. Direct foaming involves the formation of open or closed spherical pores with sizes in the range of hundreds of micrometers up to several millimeters with the use of gas bubbles. The gases can be produced in situ by self-blowing due to condensation of functional groups[161,162] or by the addition of blowing agents that react or decompose[149,150,163–165] (chemical blowing) or volatilize[125,150] (physical blowing) during the cross-linking process of the preceramic polymer. Moreover, it is possible to introduce gas externally during the cross-linking of the preceramic polymer to produce SiOC glasses.[166]

In the last years, increasing activities were done related to the preparation of silicon-oxycarbide-based porous part by means of freeze-casting.[167–171] It has been shown that the aligned porosity resulting from the freeze-casting process can adopt various pore morphologies, depending on the solvent used, preceramic polymer loading as well as the conditions of the freezing process. Thus, SiOC monoliths with variable volume fractions of aligned porosity as well as tunable pore shapes and hierarchical morphologies can be produced by controlling/adjusting the freeze-casting process (Figure 8).

Also, silicon oxycarbide-based aerogels can be obtained *via* supercritical drying of alkoxy silane-based gels[172,173] or polysiloxane-based systems.[174] Also, slow aging of the gels by continuous exchange of the produced solvents with low surface tension solvents[175,176] may lead to silica- and SiOC-based gels; their fractal structure can be preserved, for example, upon subsequent freeze-drying.[169,170]

Porous capsules and spheres were obtained upon electro hydrodynamic spraying[177] and microfluidics techniques using emulsions.[178]

3.4 | SiOC-based fibers and tubes

The formation of SiOC fibers usually comprises the fabrication of preceramic fibers and the subsequent pyrolysis to ceramic SiOC fibers. In order to preserve the fiber geometry made from polymers, cross-linking via like electron beam irradiation or chemical vapor curing[179] is performed. The curing in metal chloride vapors allows as well the formation of SiMOC-based fibers, as shown in a case study for TiO_2/SiOC fibers.[180]

The fabrication of fibers from silicon-based polymers started in 1975 with the invention of the Yajima process yielding SiC-based fibers. Depending on the quality grade, these fibers can possess some amount of oxygen. Although important as they marked the start of processing polymer-derived fibers,[181,182] these fibers are not discussed in the present study, as the focus lies on SiOC materials. The potential of fiber preparation upon spinning of alkoxide sols prepared by the sol-gel method was demonstrated by Sakka and Kamiya.[183] A first attempt to produce SiOC fibers was performed by Hurwitz in the late 1980s upon melt spinning of a polysilsesquioxane.[41] SiOC and SiBOC preceramic fibers were also produced from a combined sol-gel synthesis approach[184–186] as well as from polymer solutions.[187]

In general, ceramic fibers can be obtained by fiber spinning like melt spinning, electrospinning or dry spinning. Spinning solutions need to possess appropriate viscosities and should be easy to solidify. In order to enhance both aspects, several polysiloxane systems were spun with the aid of carrier polymers or spinning agents like polyvinylpyrrolidone (PVP)[188,189] or secondary cellulose acetate[190] (as for electrospinning processes). Recently, electrospinning of a silicon resin without the use of a carrier polymer but with partial pre-crosslinking of the resin was reported.[191] Electrospinning can be performed with sol gel-derived solutions[188] or preceramic polymer solutions[189,191] and enables the formation of thinner SiOC fibers[188] (Figure 9A). Important factors influencing the fiber diameter are the surface tension, the electrical conductivity, and the dielectric constant of the spinning solutions.[189] In sol gel-derived systems, the water to alkoxide ratio is crucial to obtain spinnable solutions.[188] Few examples for SiOC melt spun fibers exist in literature. Hollow and dense SiOC fibers (*cf.* Figure 9C,D) were obtained from a polycarbosilane/polysiloxane mixture via melt spinning.[192] For melt spinning, the diameter of polymethylsilsequioxane-derived SiOC fibers is depending on the spinning temperature and

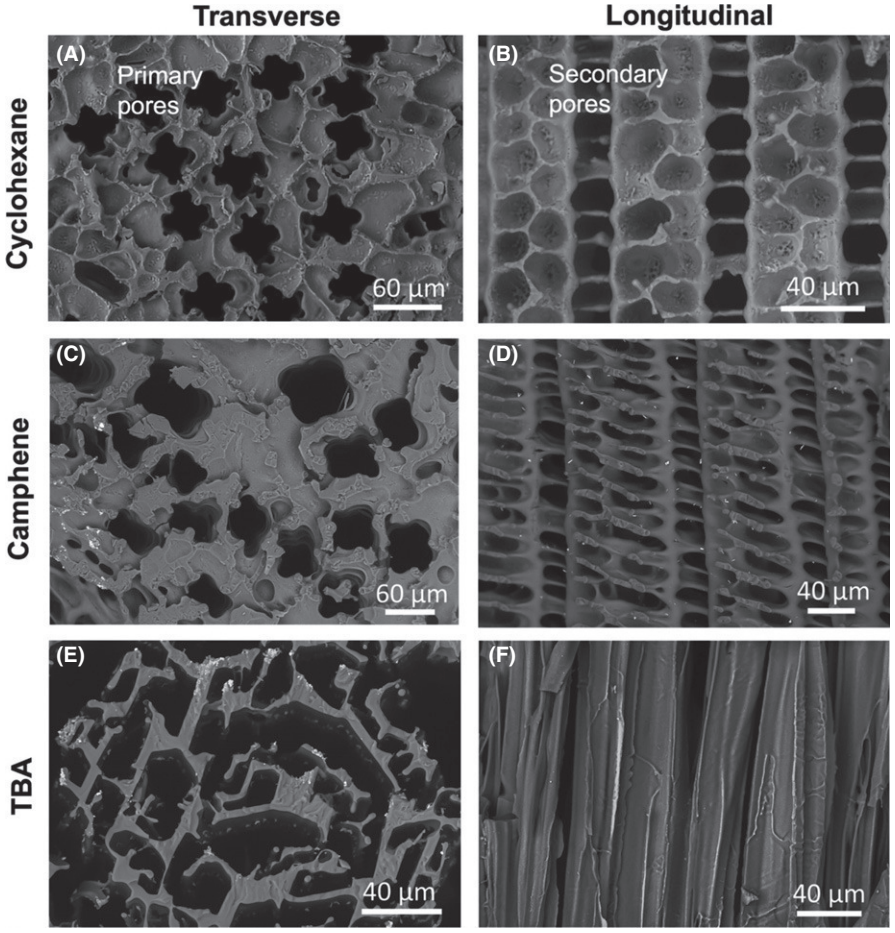

FIGURE 8 Effects of solvent choice on pore structure of free-casted SiOC. The samples from (A-F) were prepared using 20 wt% polymer solutions in cyclohexane (A, B), camphene (C, D), and tert-butyl alcohol (E, F). Samples are shown in transverse (A, C, E) and longitudinal (B, D, F) directions. Primary (A, C) and secondary pores (B, D) are related to the formation of primary and secondary dendrites (reprinted with premission of Elsevier).[169]

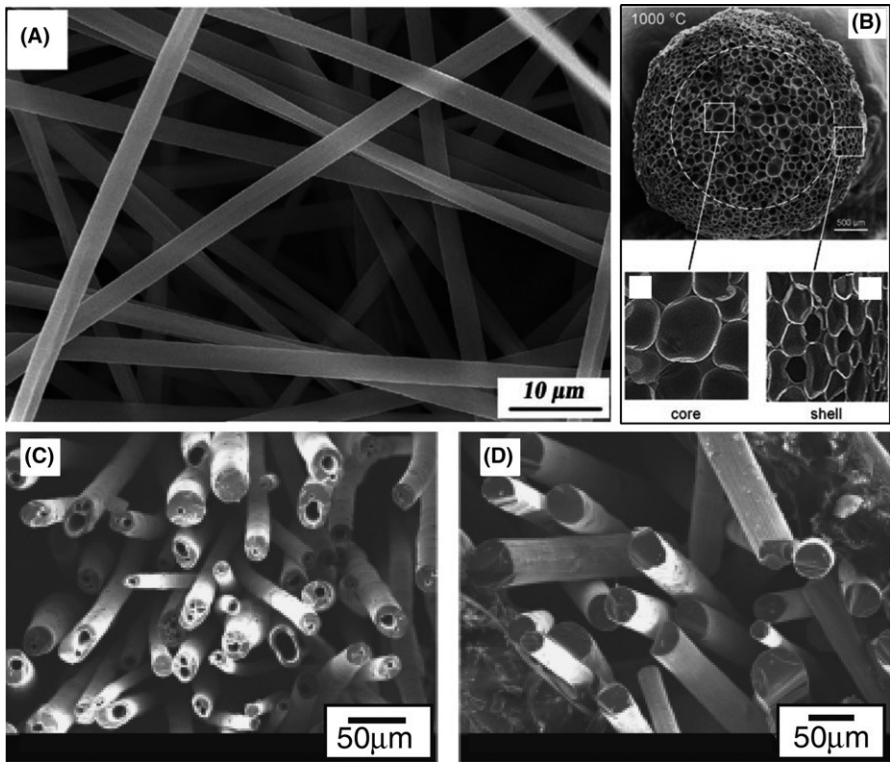

FIGURE 9 SEM images of A, as spun fibers from electrospinning[189] (reprinted with permission of Wiley), and B, pyrolyzed fibers of extrusion foamed filaments[193] (reprinted with permission of Wiley); C, SEM micrographs of hollow and D, dense melt-spun SiOC fibers[192] (reprinted with permission of Wiley) [Color figure can be viewed at wileyonlinelibrary.com]

the holding time, where an increase in each of both is leading to larger diameters.[179] Upon continuous extrusion foaming of a polymethylsilsequioxane, porous filaments could be produced[193] under preservation of the porous structure as evidenced in Figure 9B. SiOC tubes were also obtained by casting of prepared slurries.[194] SiOC microtubes can be obtained upon extrusion using a microextruder.[195] The inner and outer diameter can be tuned by varying the pull rate or the pressure and temperature within the extruder.

3.5 | Complex-shaped and miniaturized parts

The pyrolysis of preceramic miniaturized part which are patterned via different micromachining techniques, has gained the attention of the scientific community as it represents a facile access to, for example, three-dimensional ceramic-based micro electromechanical systems (MEMS) at relatively low costs. Preceramic materials include polymer as well as sol-gel precursors. Some studies combining sol-gel precursor solutions with micromolding technologies (mainly soft-lithography) in order to obtain oxidic ceramic MEMS or more complex ceramic MEMS such as lead zirconate titanate ($PbZr_xTi_{1-x}O_3$, PZT), $Sr_2Nb_2O_7$ or others have been reported.[196,197] The addition of organic components or ceramic nanoparticles reduces the high shrinkage that occurs during drying and pyrolysis.[198]

Various micromachining processes have been reported in the literature for the manufacturing of complex-shaped PDC-based microcomponents. General reviews about additive manufacturing of polymer-derived ceramics and ceramic matrix composites (CMCs) were recently published.[199–201] Some of them are used to obtain the master or the mold that will be used to shape the precursors. The same processes and others are used to directly shape the precursors. In particular, these processes include lithography, LIGA, stereolithography as well as micromolding techniques (e.g., hot-embossing or soft lithography).

Straub et al demonstrated the potential of polysiloxanes for stereolithographic processing.[202] Ceramic SiOC/SiC composite parts from stereolithography were fabricated by mixing a polymethylsilsequioxane, 40%-60% SiC filler and a cross-linking agent followed by selective laser curing.[203] Due to the use of the passive SiC fillers, the polymer-to-ceramic conversion was provided as a near-net-shape process. Also, other recent studies showed the preparative access to complex-shaped and miniaturized SiOC-based parts using UV-photolithography/laser stereolithography followed by pyrolysis.[204–207] Figure 10 demonstrates the high flexibility and accuracy in achieving different shapes and complex shapes for SiOC ceramic parts via laser stereolithography.

Also, other additive manufacturing methods for the preparation of complex SiOC parts were reported, such as powder (bed) 3D printing,[203,208,209] inkjet printing,[210] direct ink printing,[211] laminated object manufacturing[212,213] or fused deposition modeling.[199] The reader is referred to refs.[199,201] which critically compare those methods and discuss on their advantages and limitations.

Besides stereolithography, photolithographic and soft-lithographic procedures were utilized to obtain SiOC complex-shaped parts.[214,215] Within this context, PDMS was used successfully as a common mold for soft lithographic processing of various free-standing micropatterned SiOC materials.[214,215] The production of SiOC microstructures on a substrate was realized using photolithography[214] as well as electron beam lithography.[216] Micro-patterned SiOC parts were also obtained by hot embossing of a polymethylsilsequioxane preceramic polymer using a mold with micro gear cavities.[57] With this procedure, miniaturized structures were obtained as shown in Figure 11.

FIGURE 10 Photographs of preceramic and the corresponding pyrolyzed ceramic parts prepared via stereolithographic processing of polysiloxanes, indicating the high flexibility and accuracy in providing complex-shaped parts[206] (reprinted with permission of Elsevier)

4 | NANO- AND MICRO-STRUCTURE OF SILICON OXYCARBIDES

The phase composition and the nano/microstructure of silicon oxycarbides is highly depending on their synthesis temperature. Thus, samples prepared at temperatures below approximately 1250°C can be regarded as amorphous, glass-like inorganic materials. SiOC materials prepared at temperatures higher than 1250°C possess a microstructure characteristic for glass-ceramics, as will be discussed in the following.

Silicon oxycarbide materials prepared upon pyrolysis of suitable single-source precursors are considered to be glassy,[217,218] though possessing heterogeneity at the nanoscale.[29]Si magic-angle-spinning (MAS) NMR spectroscopy was used to probe the coordination of SiC_xO_{4-x} tetrahedra present in the glass network. The SiO_4, SiO_3C, SiO_2C_2, $SiOC_3$, and SiC_4 structural units typically exhibit different[29]Si isotropic chemical shifts that can be resolved and quantified as shown in Figure 12A. Interestingly, the fractions of the SiO_4 and SiC_4 sites in silicon oxycarbide were found to be significantly higher than those expected from a random distribution of Si–O and Si–C bonds. As there is no significant carbon–oxygen bonding in the silicon oxycarbide glass structure,[11,13,14,219] this NMR finding indicates a partial segregation and clustering of oxygen-rich and carbon-rich SiC_xO_{4-x} units in the SiOC glass network.

In addition, Raman spectroscopy (Figure 12B) reveals the presence of a segregated secondary phase consisting of sp^2-hybridized carbon. This carbon phase can be described as highly disordered, turbostratic carbon.[54,220–222] Consequently, two types of carbon can be defined in SiOC glasses: (a) the carbidic carbon (i.e., the carbon incorporated within the SiOC glassy network, which is sp^3-hybridized) and (b) a secondary, segregated carbon phase (sp^2-hybridized carbon).

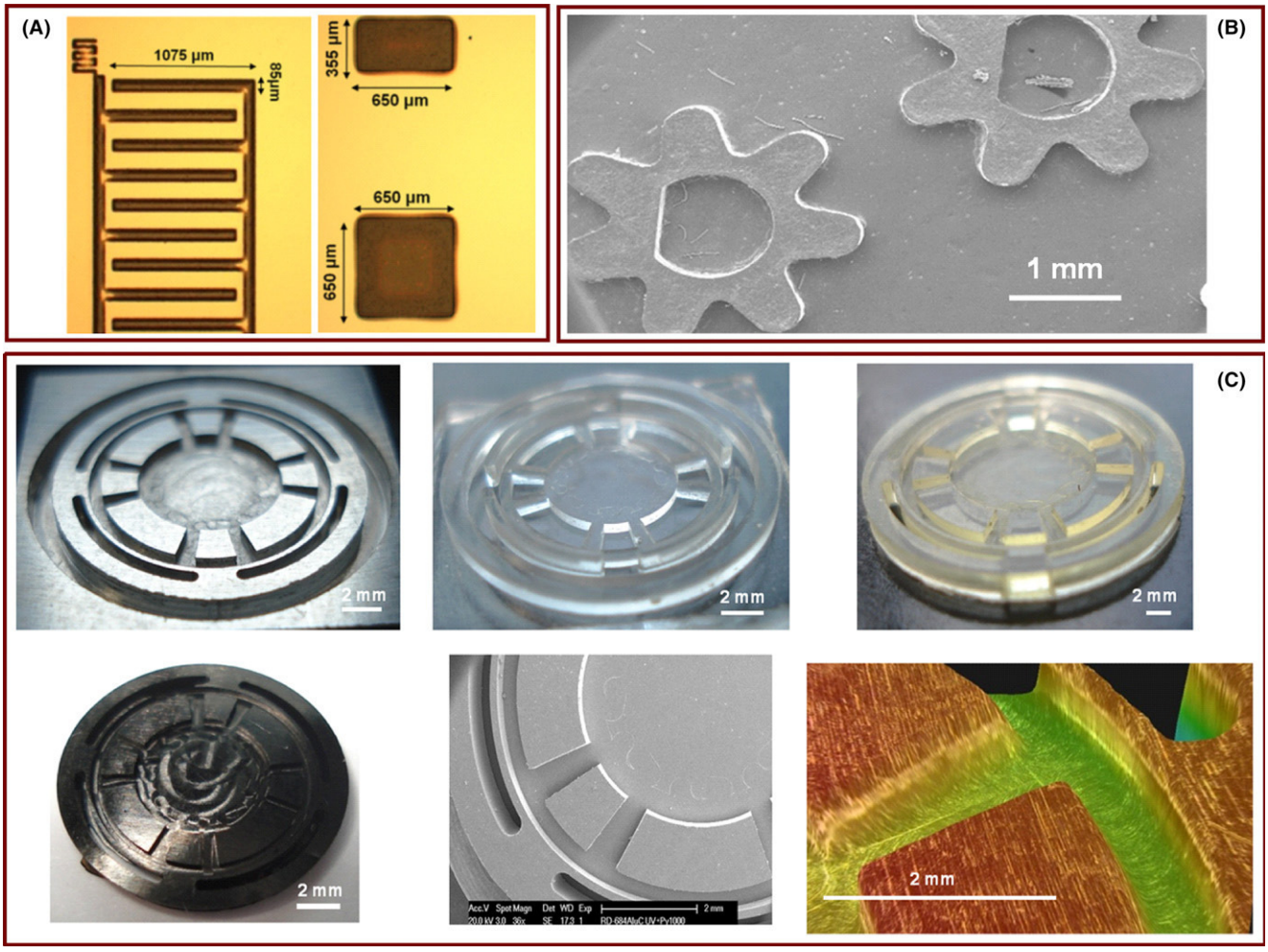

FIGURE 11 Optical photographs of SiOC-based micropatterns (microcombs and squares) (A) and SEM micrograph of SiOC-based microgears (B) obtained via photolithography of a polysiloxane followed by pyrolysis; C, Soft-lithographic processing of a complex-shaped SiOC-based valve seat for a micro-burner[214] (reprinted with permission of Elsevier)

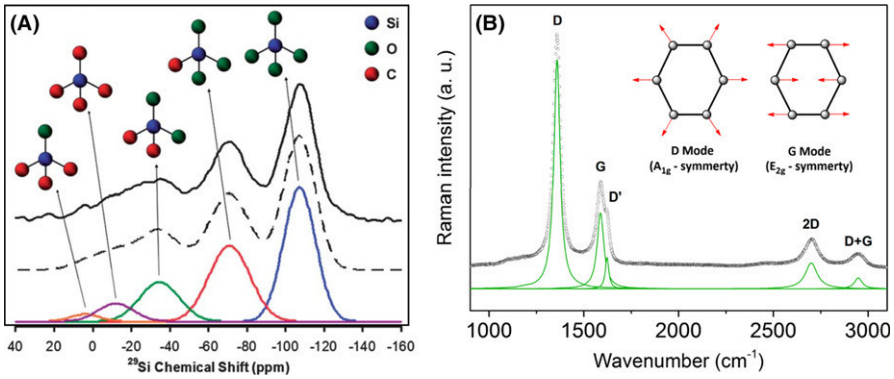

FIGURE 12 A, ^{29}Si MAS NMR spectrum of a $SiO_{1.5}C_{0.68}$ glass as prepared via pyrolysis of a polysiloxane in argon atmosphere (solid curve represents the experimental spectrum; dashed line: simulated spectrum; solid curves at the bottom: individual simulated ocmponents). Peaks from right to left correspond to SiO_4, SiO_3C, SiO_2C_2, SiC_4, and $SiOC_3$ units[11,13] (reprinted with permission of American Chemical Society); B, Typical Raman spectrum of an SiOC glass showing the presence of a disordered sp2 hybridized secondary carbon phase (all indicated phonon modes, i.e., D, G, D', 2D, and D+G, can be attributed to the segregated, disordered sp^2 carbon phase)[220–222] (reprinted from Ref. 222 with permission of MDPI)

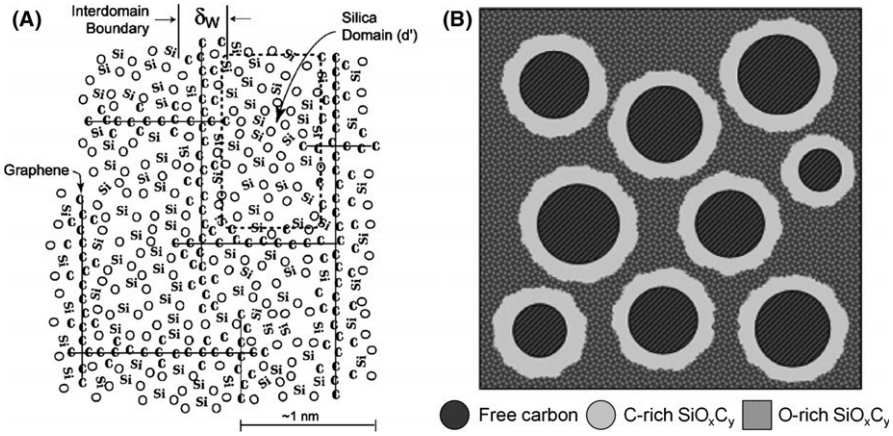

FIGURE 13 2D representations of structural models for SiOC glasses: A, model showing SiO_2 nanodomains embedded within a graphene-like network[12] (reprinted with permission of Wiley); B, model consisting of two continuous silica-rich and carbon phases with a carbon-rich SiO_xC_{4-x} interface[11] (reprinted with permission of American Chemical Society)

Despite of several decades of research related to the structure of SiOC glasses, the detailed nano/microstructure is still not fully elucidated. Only model descriptions of the nano/microstructure of SiOC glasses have been found in the literature. In addition, computational modeling was used to get a more comprehensive idea of the structure of SiOC materials and supported the proposed nano-heterogeneous nature thereof.[223–225] One model suggests the presence of silica-rich nanodomains embedded in a graphene-like nano-network exhibiting mixed-bonded SiO_xC_{4-x} tetrahedra at the interface (Figure 13A),[12] whereas other models propose the presence of two continuous interpenetrating phases (oxygen-rich silicon oxycarbide and carbon) and a carbon-rich SiO_xC_y-based interface (Figure 13B).[11]

The first proposed model relies on small X-ray scattering (SAXS) experimental data obtained from SiOC glasses[12] and can explain satisfactorily the visco-elastic properties of SiOC glass at elevated temperatures (see Section 6.1.2 below). Whereas the second proposed model bases on ^{29}Si NMR spin-lattice relaxation studies performed on silicon oxycarbide to probe the fractal spatial distribution of the SiC_xO_{4-x} structural units.[11] Within few nanometers, the mass of those structural units, M, scales with distance r as $M \sim r^d$ (d being the mass fractal dimension). Experimentally, d was found to exhibit values between 2.3 and 2.5 instead of a value of 3, which is typical for a tri-dimensionally homogeneous space filling/distribution.[11,14,219] Thus, the mass-fractal nature of the oxygen-rich part of the SiOC network was concluded to be a consequence of a frustrated packing of the SiC_xO_{4-x} structural units giving rise to a spatially continuous though fractal glass network with "voids" filled by segregated sp^2 hybridized carbon phase. At large volume fractions of segregated carbon, the proposed network architecture consists of spatially bi-continuous nanodomains of carbon and SiC_xO_{4-x} structural units.

5 | ENERGETICS AND HIGH-TEMPERATURE BEHAVIOR of SiOC

5.1 | Energetics of SiOC glasses

Remarkably, silicon oxycarbides retain their amorphous nature up to temperatures as high as 1500°C,[226] whereas in silica-based systems, the crystallization of cristobalite has been observed at temperatures as low as 1000-1200°C (depending on composition, e.g., content of hydroxyl groups etc.). It is clear that the incorporation of carbon within the silica-based network should be considered as responsible for the increased crystallization resistance of SiOC glass as compared to other silica-based vitreous materials (e.g., high-purity silica with various hydroxyl contents). Interestingly, calorimetry measurements suggest that probably there is an (unexpected) thermodynamic contribution to the enhanced crystallization resistance in silicon oxycarbides. As shown in Table 1, the enthalpies of formation for different SiOC glasses are negative with respect to their corresponding crystalline phases in the Si–O, Si–C, and C systems. Thus, amorphous silicon oxycarbide seems to be energetically stable with respect to iso-compositional crystalline mixtures of cristobalite, silicon carbide and graphite. This is valid especially for silicon oxycarbide materials prepared upon pyrolysis at temperatures between 1000 and 1200°C.[227,228] The mixed bonding between silicon, oxygen, and carbon and the possible presence of hydrogen in the interfacial regions have been considered to play a key role in the thermodynamic stabilization of SiOC.[13,228–230]

TABLE 1 Enthalpy of formation ΔH_f for different SiOC glasses from elements, ΔH_f(elem) or from the binary crystalline phases SiO_2 and SiC and carbon, ΔH_f(comp). SiOC samples were prepared via pyrolysis at 1000°C, if not otherwise specified

Sample	$\Delta H_{f(elem)}$ at 25°C [kJ/mol]	$\Delta H_{f(comp)}$ at 25°C [kJ/mol]
$SiO_{1.10}C_{0.73}$[227,341]	−242 ± 3.6	−53.9 ± 3.6
$SiO_{0.72}C_{2.10}$[227]	−149.9 ± 4.4	−51.9 ± 4.4
$SiO_{1.50}C_{0.63}$[342]	−232.3 ± 2.3	−6.5 ± 2.4
$SiO_{1.49}C_{0.26}$[342]	−256.6 ± 3.3	−13.0 ± 3.4
$SiO_{1.50}C_{0.75}$ (1200°C)[230]	−219.76 ± 2.87	−4.92 ± 2.95
$SiO_{1.50}C_{0.75}$ (1450°C)[230]	−209.17 ± 3.14	+6.13 ± 3.21
$SiO_{1.50}C_{0.75}$ (1600°C)[230]	−214.34 ± 1.10	−10.25 ± 1.34

5.2 | High-temperature evolution of SiOC glasses

The chemical composition of SiOC glasses is stable up to 1500°C, beyond this temperature decomposition reactions forming volatile CO and SiO occur[54,231] (this applies for monolithic SiOC; for high-surface-area materials, such powders, the onset temperature for decomposition is significantly lower, see discussion below). Starting with temperatures of approximately 1250°C, a partitioning process of the SiOC glass network begins.[226] During this process, the mixed-bonds Si-tetrahedra ($SiO_{4-x}C_x$, $x = 1, 2, 3$) vanish (Figure 14A).[232] During this process, a multi-phase glass-ceramic is formed, consisting of an amorphous SiO_2 matrix in which nanosized β-SiC particles (Figure 14B) are dispersed and located next to the segregated carbon phase[20,232,233] (*cf.,* Figure 3).

The segregated carbon phase itself gets progressively ordered with increasing temperature,[220,221] leading to graphite-like structures (*cf.*, Figure 15). At temperatures exceeding 1500°C, a carbothermal reduction of the silica matrix with the segregated carbon phase takes place, leading to the formation of β-SiC and gaseous CO according to the following reactions[234,235]:

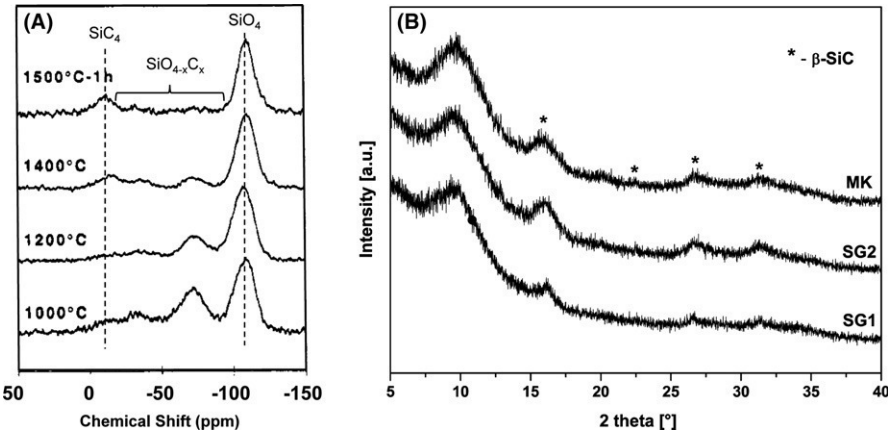

FIGURE 14 Phase separation in a silicon oxycarbide glass: A, ^{29}Si MAS NMR of samples prepared at temperatures between 1000 and 1600°C[226] (reprinted with permission of American Chemical Society); B, XRD patterns of silicon oxycarbide samples prepared at 1600°C; the precipitation of small β-SiC nanocrystallites is clearly visible at this temperature[8] (reprinted with permission of Wiley)

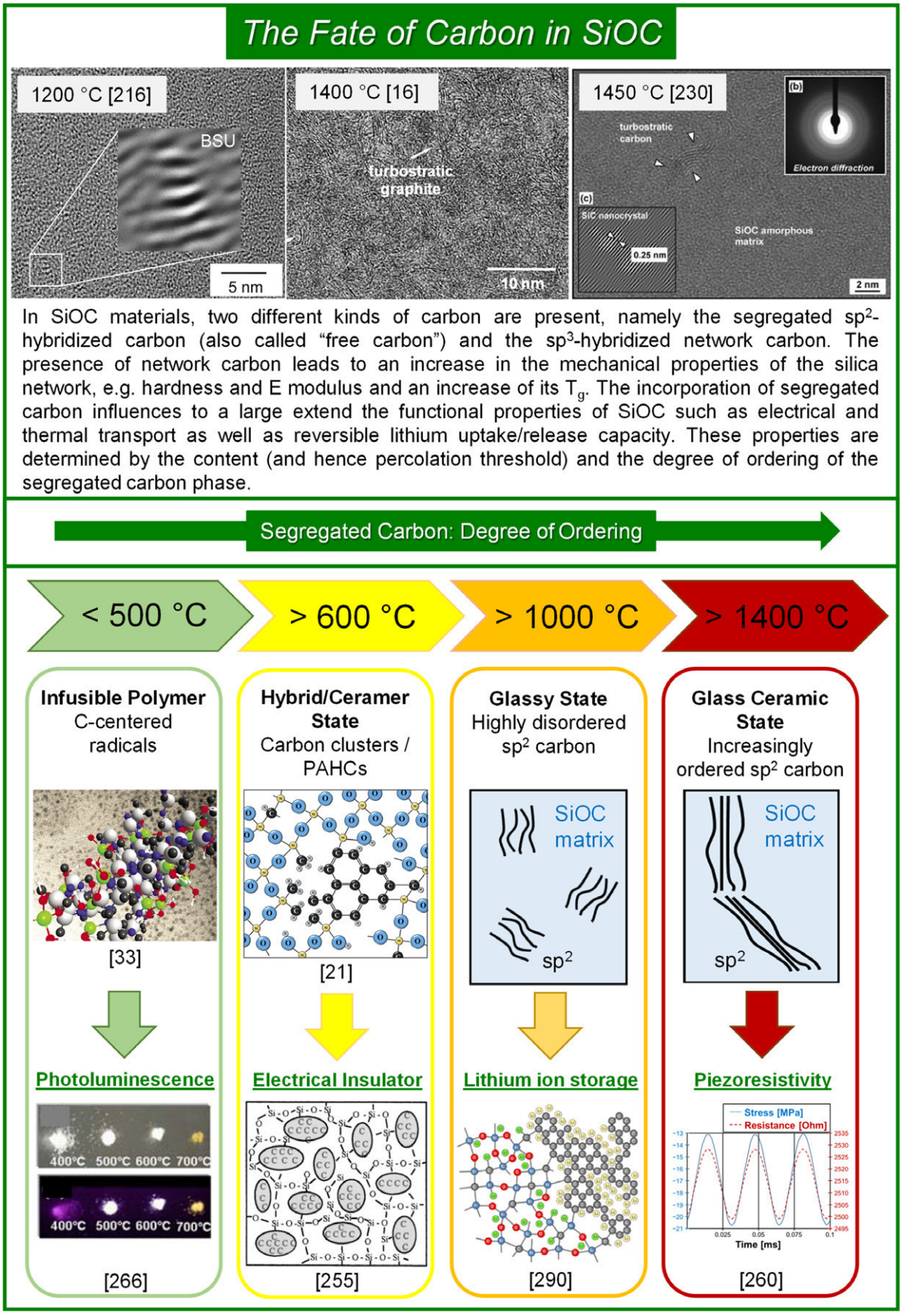

FIGURE 15 The fate of Carbon in SiOC Materials

$$SiO_2 + C \rightarrow SiO \uparrow + CO \uparrow \quad (3)$$

$$SiO + 2C \rightarrow \beta\text{-}SiC + CO \uparrow \quad (4)$$

The segregated carbon phase gets consumed during this reaction; at the same time, the crystallization of SiC is significantly enhanced.[18,20,21,236]

In addition to the above mentioned carbothermal reduction, SiO_2 and SiC can directly react with each other upon complete decomposition according to Equation (5). This occurs after the complete consumption of the segregated carbon phase[235] and at higher temperatures.[20]

$$2SiO_2 + SiC \rightarrow 3SiO \uparrow + CO \uparrow \quad (5)$$

The overall processes occurring in SiOC at high temperature involve on the one hand phase separation of the glassy matrix and on the other hand decomposition reactions with evolution of gaseous species. Both may lead to the crystallization of SiC particles. One should emphasize that phase separation and decomposition in silicon oxycarbides are not isolated processes but can take place in parallel (Figure 16).[20]

The effective stability of SiOC at high temperature is generally depending on its porosity and specific surface area. Dense SiOC monoliths show an increased stability than their porous or powdery counterparts.[237–239] In addition, pressure-assisted processing techniques extend the stability, as the gaseous species developing during the above mentioned decomposition reactions cannot or are hindered to leave the system.[226,239,240]

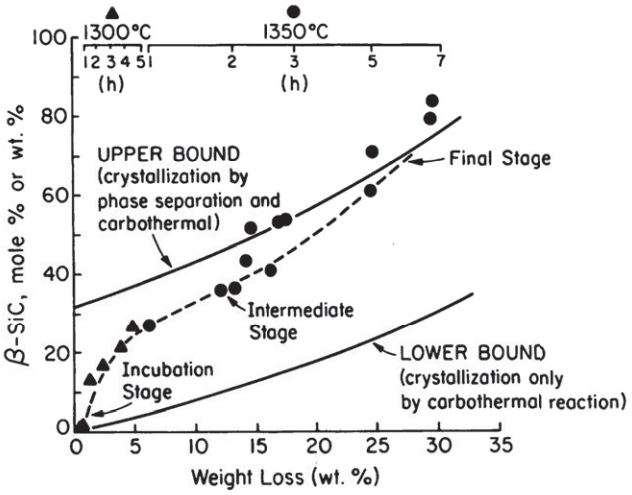

FIGURE 16 Crystallization of SiOC glasses upon high-temperature annealing—the upper and lower bound of the evolution of the β-SiC content as a function of the annealing temperature describes the contribution of the partitioning process and of the carbothermal decomposition to the crystallization of silicon oxycarbides[20] (reprinted with permission of Wiley) [Color figure can be viewed at wileyonlinelibrary.com]

6 | PROPERTIES OF SiOC

6.1 | Structural properties of SiOC

6.1.1 | Elastic properties and hardness of SiOC glasses and glass-ceramics

Renlund et al[92] determined the Young's modulus of SiOC glass-ceramics to be 98.0 GPa and thus significantly higher than that of vitreous silica (72.9 GPa).[241] Soraru et al[17] showed for SiOC glasses similar Young's modulus values. Moreover, it was indicated that the Youngs' modulus depends on the composition of SiOC glasses. Thin glass sheets of SiOC glass/colloidal silica composites showed even higher values of 120-130 GPa.[80] The increase in Young's modulus of SiOC glasses in comparison to vitreous silica was attributed to the higher connectivity of glass network upon incorporation of tetravalent carbon sites. Upon measurements using ultrasonic technique, Moysan et al determined a Poisson's ratio of 0.11 for a SiOC glass. This value is among the lowest for glasses and indicates a more open network structure than that of vitreous silica.[242]

As Young's modulus is sensitive to structural changes, Rouxel et al[15] used in situ measurements to follow possible changes in SiOC glasses during high-temperature creep experiments. At temperatures below the phase separation temperature in SiOC glass, a slight increase in the Young's modulus was observed, which was assigned to a relaxation phenomenon of the glass matrix and to densification, as the studied samples showed some residual porosity at the beginning of the experiment.[15] Upon precipitation of SiC nanoparticles, an irreversible increase of the Young's modulus was identified. In addition, it was demonstrated that SiOC glasses and glass-ceramics show an increase of the Young's modulus with increasing temperature.[7,15] This unusual behavior was observed also in the case of vitreous silica.[15]

Silicon oxycarbides show values of Vicker's hardness between 6.4 and 9.3 GPa[17,218,243] (compared to hardness values for silica, 6-7 GPa[243]). The indentations in silicon oxycarbides glasses containing low segregated carbon amounts reveal circular Hertzian cracks rather than radial-median cracks, analogous to anomalous glasses like vitreous silica[17]; whereas compositions with higher carbon content show radial-median cracks. It was suggested that the incorporation of carbon leads to a less flexible glass network at the molecular scale. Consequently, deformation would transform from densification to shear deformation.[244] For compositions with a moderate amount of segregated carbon, the influence of the composition on the hardness is negligible.[17] However, higher values of segregated carbon seem to lower the Vicker's hardness slightly

to values of ca. 7.2 GPa.[95] Phase separation leads to an increase in Vicker's hardness, most probably due to the simultaneous increase in density.[218]

6.1.2 | High-temperature creep of silicon oxycarbides

Among the outstanding properties of SiOC glasses and glass-ceramics, their remarkable high temperature viscosities and creep resistance are quite unique. This is generally attributed to the increased connectivity of the SiOC glass network, as a consequence of the partial exchange of bivalent oxygen by tetravalent carbon.[15,17] For both SiOC glasses and glass-ceramics, an increase in viscosity in the range of two orders of magnitude in comparison to vitreous silica is reported.[9,19,92]

The first data on the high-temperature creep behavior of SiOC glasses was reported by Rouxel et al in the late 1990s and early 2000s using three-point-bending experiments.[15,19] The apparent viscosity of the glasses was calculated from creep experiments using Equation (6), where σ is the applied stress, υ is the Poisson's ratio and $\dot{\varepsilon}$ is the steady-state creep rate:

$$\eta = \frac{\sigma}{2(1+\upsilon)\dot{\varepsilon}} \tag{6}$$

Four distinct features related to the high-temperature creep behavior of silicon oxycarbide have been considered: (a) SiOC glasses seem to exhibit steady state creep; (b) Silicon oxycarbide possess extremely low creep rates at ca. 1000°C (as low as 1.8×10^{-08}/s[19]); (c) the incorporation of carbidic carbon into the silicate network leads to a remarkable decrease of the steady-state-creep rates as compared to those recorded for pure vitreous silica–this is manifested as an increase in their viscosity of about 2 orders of magnitude (*cf.*, Figure 3); (d) the incorporation of segregated carbon leads to a further decrease of the steady-state-creep rates.[8,15,19]

The apparent activation energy of the creep process in silicon oxycarbides was determined to be 296 kJ/mol for the compositions with relatively low carbon content, being considerably lower than for vitreous silica (500-700 kJ/mol).[245] This is valid for temperatures up to 1200°C. At higher temperatures, the samples started to partition upon precipitation of small β-SiC nanocrystallites, as mentioned above and consequently leads to a strain hardening in the SiOC glass-ceramics. Remarkably, the activation energy for the structural relaxation of the same composition was determined to be 617 kJ/mol up to 1200°C, indicating that the relaxation of SiOC glasses proceeds via viscous flow of the silica-rich domains in the glassy matrix. The viscosity of the SiOC glasses was found to be significantly higher than that of vitreous silica, as shown in Figure 17.[19] Consequently, SiOC glasses exhibit T_g values being markedly higher than that of vitreous silica (Figure 17).

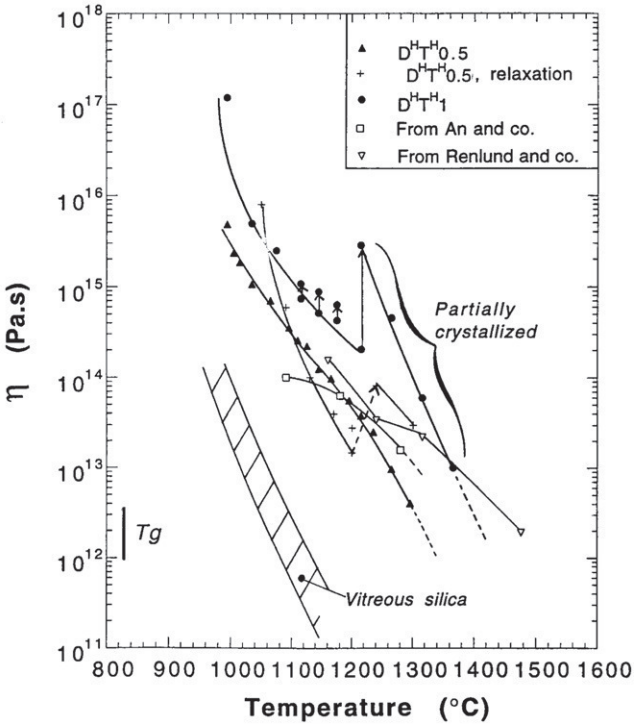

FIGURE 17 Viscosity of SiOC glasses with different compositions; the values were calculated from creep and relaxation experiments[19] (reprinted with permission of Wiley) [Color figure can be viewed at wileyonlinelibrary.com]

Interestingly, the creep strain in SiOC glasses was shown to be partially recoverable.[246] This viscoelastic behavior was attributed to the presence of the segregated carbon phase, which deforms elastically and is slowed down during recovery through the slower viscous flow of the embedding silicon oxycarbide glass. The presence of viscoelasticity in silicon oxycarbides suggests that the segregated carbon phase is present as an interconnected network, as discussed above.

First investigations considering the plastic deformation of SiOC glass-ceramics were performed in 1991 by Renlund et al[92] who measured the viscosity of a phase-separated SiOC from load-deflection curves. The determined activation energy for the plastic deformation of the mentioned glass-ceramic was 400 kJ/mol. The viscosity of the SiOC glass-ceramic was found to be 2 orders of magnitude higher as compared to that of vitreous silica[92,245] and may relate to the presence of the secondary carbon phase within the silica matrix.[8] Similar values for viscosity where obtained shortly later by Hammond et al[247] using constant strain rate measurements via four-point-bending for a SiOC glass-ceramic with a comparable content of segregated carbon. However, a lower value for the apparent activation energy was determined (i.e., 259 kJ/mol).

In true creep experiments under constant loading conditions, SiOC glass-ceramics were shown to exhibit a viscoelastic behavior at 1300°C. It was reported that the elastic recovery of the SiOC glass-ceramics increases as the amount of segregated carbon present in the samples increases.[8] This supports the idea that the elastic contribution most probably relates to the segregated carbon phase. On the other hand, creep experiments at constant temperature but varying pressures revealed a stress exponent of approximately 1[7] as expected for Newtonian viscous flow, implying that the plastic deformation of SiOC glass-ceramics is governed by the viscous flow of the silica matrix.[8]

In addition, it was shown that the incorporation of both —carbidic and segregated carbon—leads to lower creep rates and consequently higher viscosities,[7–9] as also demonstrated for the SiOC glasses.[19] A recent case study correlated the content of carbidic and segregated carbon in SiOC glass and glass-ceramic with their creep behavior and consequently revealed following features: (a) SiOC glasses exhibit relatively large T_g values (1350-1400°C) and rather low activation energies for creep (ca. 280-300 kJ/mol) - they may be materials of choice for near-zero-creep applications at HT; (b) SiOC glass-ceramics have significantly lower T_g values (i.e., 1250°C for phase-separated SG1, Figure 18) and larger activation energy for creep (463 kJ/mol) than those of their glassy counterparts.[8] Their creep behavior can be significantly improved by incorporation of segregated carbon. Interestingly, small contents of segregated carbon (e.g., 5.8 vol% as for SG2, Figure 18) are sufficient to provide the SiOC glass-ceramic samples with similar T_g and E_a values as compared to silicon oxycarbide glasses. Thus, SiOC possessing excess carbon are suitable materials when high-temperature applications are anticipated.[8]

The viscosity of a SiOC glass-ceramic which contains only carbidic carbon (i.e., β-SiC nanoparticles) but no segregated carbon, showed an increase in viscosity of about two orders of magnitude in comparison to vitreous silica,[9] indicating that phase-separated SiOC glass-ceramics are not just plain mixtures consisting of SiO_2 matrix and dispersed SiC nanoparticles. It seems that the interface between matrix and precipitates plays an important role concerning their creep behavior. It was suggested that after the phase separation of SiOC glasses is complete, there might still be a considerable fraction of mixed-bonds Si-tetrahedra located at the interfaces, which may be responsible for the unique creep resistance of SiOC glass-ceramics. The existence and the nature of this interface in SiOC glass-ceramics has been though still a matter of debate.[9,218]

The modification of silicon oxycarbide with zirconium and hafnium leads to slightly lower shear viscosities as compared to that of the corresponding ternary SiOC glass-ceramic.[7] At the same time, the activation energy for creep of the SiOC glass-ceramic (283 kJ/mol) was in the range of the values reported before (i.e., 293 kJ/mol); whereas the activation energies for the metal-modified SiOC glasses slightly increased to 386 and 476 kJ/mol (as for SiZrOC and SiHfOC, respectively). Both effects were attributed to the decreased content of the segregated carbon phase in the metal-modified SiOC glass-ceramic samples, which was considered to induce an increase in the matrix silica domain size.[7] In comparison, modification of SiOC glass-ceramic with lutetium does not significantly influence the amount of segregated carbon and the creep rates in SiOC.[7,8,10]

6.2 | Functional properties of SiOC

6.2.1 | Thermal transport

Usually, glasses exhibit poor thermal transport due to their low degree of ordering. The value for the thermal

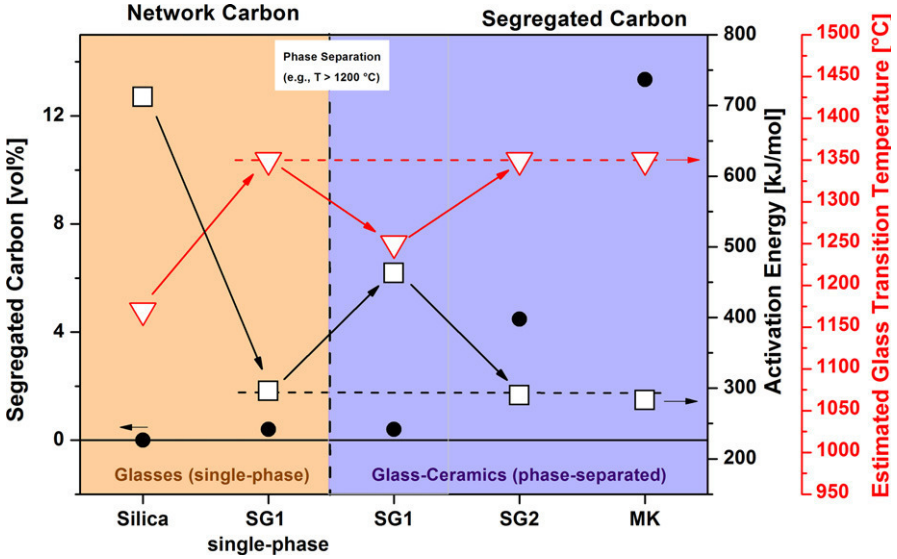

FIGURE 18 Dependence of the activation energy (red triangles) and of the T_g values (black squares) on the volume fraction of segregated carbon (filled circles) in various silicon oxycarbides. SG1 contains ca. 1 vol% segregated carbon; in SG2 and MK the content of segregated carbon was ca. 6 and 13 vol%, respectively. Vitreous silica has been used besides SG1 as additional bench mark material for comparison, i.e., 0 vol% segregated carbon[8] (reprinted with permission of Wiley)

conductivity of fused silica is reported to be 1.3 W/(m K) at room temperature.[248] Information on the thermal conductivity of SiOC glasses is scarce. However, it was recently shown, that SiOC glasses with a very low amount of segregated carbon exhibit an even lower thermal conductivity than fused silica of approximately 1.2 W/(m K).[249] This was attributed to the lower mass fractal dimension of the SiOC glass network, residual hydrogen, and the existence of dangling bonds (*cf.*, Figure 3).

Upon partitioning, SiOC glasses with a very low amount of segregated carbon convert into silica-matrix glass-ceramics and reveal a thermal conductivity similar to that of vitreous silica.[249] Upon increasing the segregated carbon or the SiC content, the thermal conductivity can be raised to values up to ca. 2.2 W/(m K) at room temperature (Figure 19).[249–253] The thermal conductivity can be further tuned by the incorporation of additional phases such as ZrO_2 or HfO_2.[251] At higher temperatures (up to 1300°C), the thermal conductivity of SiOC glass-ceramics increases to values between ca. 1.6 W/(m K) for low carbon-containing samples and ca. 2.7 W/(m K) for high carbon-containing samples.[249,251]

Upon incorporation of porosity into SiOC materials, the thermal conductivity can be significantly suppressed to values as low as 0.041 to 0.078 W/(m K) (as for samples with up to 80 vol% porosity).[254]

6.2.2 | Electrical properties and piezoresistive behavior

The presence of the segregated carbon phase in SiOC materials opens the possibility of electronic transport. It was demonstrated *via* electrical conductivity measurements, that the behavior of SiOC materials ranges from insulating[255,256] to semiconducting,[255] with values for the electrical conductivity at room temperature covering a

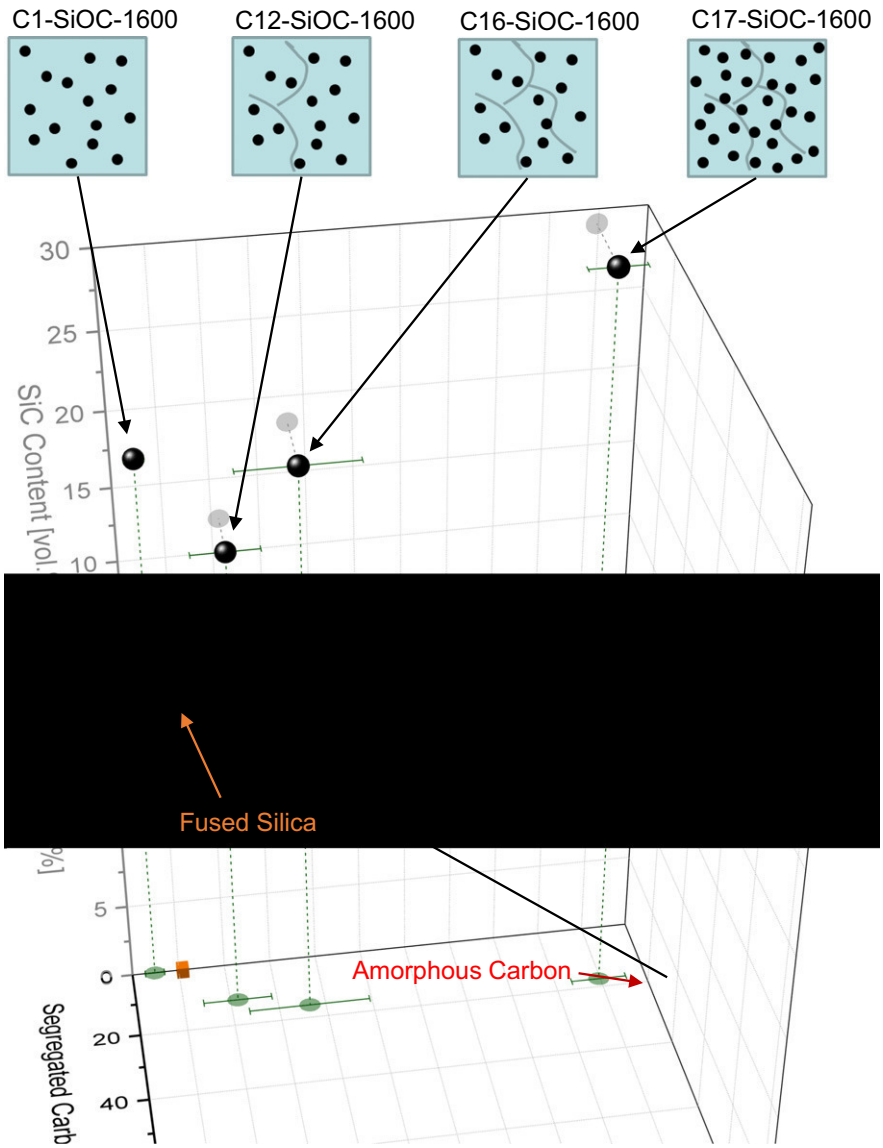

FIGURE 19 Thermal conductivity values of SiOC glass ceramics, fused silica and amorphous carbon at 800°C. Samples with moderate amount of SiC nanoparticles reveal a linear dependence of the thermal conductivity on the amount of segregated carbon. Samples with higher amount of SiC reveal a steep increase in the values for thermal conductivity[249] (reprinted with permission of MDPI)

large range between 4.3×10^{13} $(\Omega \bullet cm)^{-1}$ and 7.1 $(\Omega \bullet cm)^{-1}$.[92,257] This continuous transition from insulator to semiconductor is mostly attributed to the content and the degree of ordering of the segregated carbon phase.[255] Below the percolation threshold, the conduction is suggested to take place *via* tunneling of localized electrons.[255] Above the percolation threshold, electron conduction[255] was proposed as active mechanism. However, a recent study discussing Hall measurements of SiOC materials suggest the conduction *via* p-type carriers in the segregated carbon phase.[258] The percolation threshold (vol.%) of the segregated carbon phase is depending on two aspects: (a) the amount of segregated carbon; (b) the synthesis temperature, as the segregated carbon phase is proposed to evolve from basic structural units (BSU) to a high aspect phase with increasing temperature[255] (*cf.*, Figure 15), thus for the lower fractions of segregated carbon in SiOC, higher synthesis temperature is needed in order to provide an electrical conductivity comparable to SiOC materials with large contents of carbon. Thus, the electrical conductivity in silicon oxycarbides seems also to scale with the synthesis temperature.[16,92,257,259,260] This is attributed to an increase in the graphitization degree of the segregated carbon phase (*cf.*, Figure 15) as monitored by Raman spectroscopy,[222] whereas the partitioning of the SiOC glass network, which typically occurs at temperatures beyond 1100-1200°C, is thought to have less impact on the electrical conductivity.[255] The amount of segregated carbon has also an impact on the absolute values of the electrical conductivity, as discussed above.[255,257–259] Finally, the electrical conductivity is increasing with increasing the measurement temperature,[257,259] indicating the semiconducting behavior of the sp^2-carbon-containing silicon oxycarbides. The incorporation of other elements that have an impact on the segregated carbon phase can lead to an increase in the electrical conductivity. In case of boron, the formation of BC_3 units within the segregated carbon phase produces additional hole-type charge carriers.[261] In case of a barium-modified SiOC, an increase of the volume fraction of the sp^2-hybridzed carbon was observed.[253]

In 2010, a silicon oxycarbide glass-ceramic which was prepared from a polysilsesquioxane via pyrolysis at 1100°C and subsequent annealing at 1400°C was reported to exhibit piezoresistive behavior. Thus, the SiOC material was shown to change its resistivity upon mechanical load as shown in Figure 20A.[260] The gauge factor (*GF*, defined *cf.* $GF = \frac{E}{\Delta\sigma}\frac{\Delta R}{R_0}$ with E being the Youngs' modulus, R_0 the zero-load resistivity of the sample, ΔR the change in resistivity upon applying a mechanical load $\Delta\sigma$) determined from room temperature measurements was ca. 145, indicating a high sensitivity of SiOC.[260,262] The observed piezoresistive behavior in SiOC was assumed to rely on a percolative network of the segregated carbon present in the SiOC matrix.[262] Apart from coherent tunneling over short distances (1-2 nm), incoherent hopping transport over longer distances as well as processes occurring at intermediate scale regime (involving both mechanisms) in the SiOC matrix were proposed to be responsible for conductivity and the piezoresistive response of silicon oxycarbides.[260,262,263] Moreover, polaron transport and bond changes ($sp^2 \rightarrow sp^3$) within the carbon phase might also contribute to the piezoresistive effect.[263] Recently, extremely large *GF* values between 7000 and 16000 were

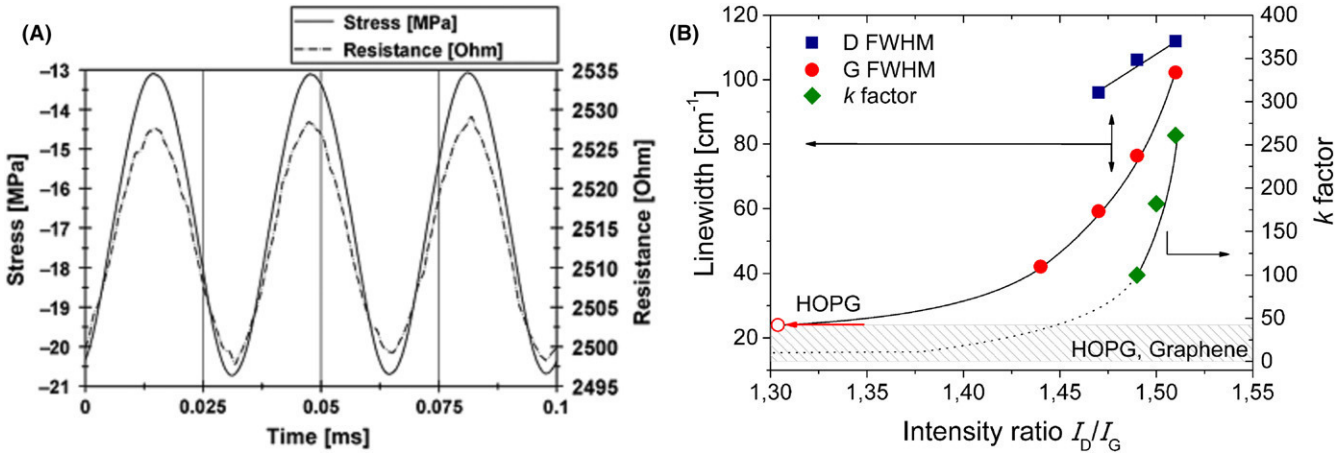

FIGURE 20 A, Piezoresistive response of SiOC upon dynamic loading conditions; the resistivity of the sample follows precisely the stress level[260] (reprinted with permission of Wiley); B, Temperature dependence of the GF and of the D and G line widths (FWHM, full width at half maximum) of sp^2 carbon for an SiOC glass-ceramic (the two horizontal lines indicate values for FWHM (red line) and *GF* (green line) of highly ordered sp^2 carbon, for example, highly ordered pyrolytic graphite or graphene)[220] (reprinted with permission of Copernicus Publications)

reported for a SiAlOC glass.[264] However, the reason for the origin of these giant values is still not clear.

Interestingly, recent studies indicate that silicon oxycarbide-based materials exhibit a pronounced piezoresistive behavior also at temperatures beyond 1000°C. Thus, gauge factor values in the range of 50-100 were reported at 1100-1300°C[220] (Figure 20B); whereas a case study on a SiOCN sample mentioned even higher values, that is, in the order of 10^3.[256] As only a very limited number piezoresistive materials is currently available for applications at elevated temperatures (i.e., $T \gg 400$°C), silicon oxycarbides and related materials may be interesting candidates for piezoresistive sensing purposes at high temperatures, event beyond 1000°C.

6.2.3 | Optical properties

Usually, monolithic SiOC glasses and glass-ceramics are not transparent or translucent under visible light due to the presence of segregated carbon and/or porosity. It was however demonstrated, that colorless, fully transparent monolithic pieces can be fabricated upon pyrolysis of aerogels at 800°C under hydrogen atmosphere.[265]

SiOC materials show intrinsic photoluminescence in the visible range when excited under UV light already upon pyrolysis at low temperatures.[266] SiOC can also be excited by blue light (457 nm), showing white luminescence.[267]

As the luminescence of SiOC is strongly affected by the presence of segregated carbon,[104,266] mainly SiOC glasses and glass-ceramics with a minimum amount of segregated carbon were investigated for the assessment of their photoluminescent properties. Such SiOC glasses show maximum luminescence in the UV to blue-white range,[104,267] while a continuous red-shift to green-yellow luminescence is observed with increasing the pyrolysis temperature[104,113] (*cf.* Figure 21A). For a SiOC glass with no segregated carbon, a blue-white to yellow-white luminescence was reported (Figure 21B).[139]

In addition, it was observed that an increasing amount of carbidic carbon in the SiOC network leads to a red-shift of the emission spectra under UV light excitation,[268] to a decrease of the optical gap and to an increase of the refractive index.[216]

The origin of the luminescence in pure SiOC is still in debate. The blue-white luminescence is proposed to originate from defects in the SiOC matrix such as dangling bonds,[104,266,268] C-related oxygen vacancies,[268] C-related oxygen deficiency centers,[139,267] oxygen deficiency centers,[139] carbon-centered radicals,[268] carbon clusters formation[269] or by the radiative recombination of photo-excited electron-hole pairs of Si–C and C–Si–O bonds.[268] It was as well proposed that the white luminescence is due to a strained silica network. Thus, the incorporation of carbon should lead to strain in the network which induces an energy gap change with respect to unstrained silica. Strain would lead to the red-shift yielding white luminescence in comparison to the UV-blue luminescence of unstrained silica.[270]

The red-shift of the luminescence upon high-temperature annealing of SiOC glass is discussed to be due to the formation of SiC nano-particles, as they emit in the yellow range.[104,139] This is further supported by the luminescence behavior of boron-containing silicon oxycarbides. Boron incorporation is known to enhance the phase separation and consequently SiC formation at relatively low annealing temperatures. Thus, the shift of the luminescence from blue to green-yellow is observed in SiBOC samples pyrolyzed at temperatures as low as 900°C.[271] However, Narisawa et al point out, that the presence of SiC cannot be the only optical active species, as the luminescence intensity is decreasing with ongoing SiC formation.[139] In addition, the yellow range of the photoluminescence (560-580 nm) prevails short time after the excitation is turned-off, even for the samples pyrolyzed at higher temperature.[272]

Moreover, SiOC glasses were shown to be suitable host materials for optically active rare-earth (RE) ions. It was demonstrated that Eu has a higher solubility in SiOC than in SiO_2.[113,273] Furthermore, Eu^{3+} ions get reduced to Eu^{2+} ions during the polymer to ceramic transformation,[113,273]

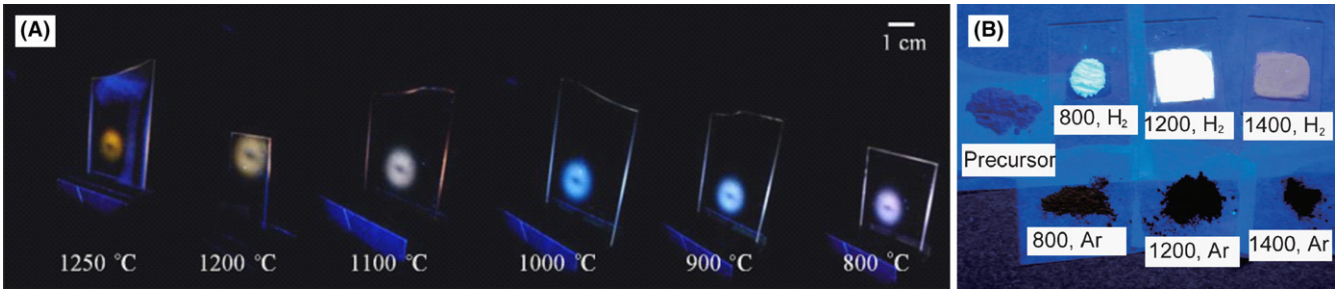

FIGURE 21 A, Photoluminescence of SiOC glasses and glass-ceramics with low amount of segregated carbon[104] (reprinted with permission of Wiley). B, The pyrolysis atmosphere determines the amount of segregated carbon and hence the luminescence properties[139] (reprinted with permission of the Chemical Society of Japan)

resulting in the emission in the blue range (440 nm) under UV excitation[113,273,274] The luminescence at room temperature of Eu:SiOC was reported to be 200-400 times more intense than for Eu:SiO_2 films[273]; whereas the luminescence of an Er:SiOC layer was 20 times more intense than that of analogous Er:SiO_2.[275]

6.2.4 | (Photo)Catalytic properties

Only few studies are available on the (photo)catalytic properties of SiOC materials. Usually, additional phases such as ZnO and TiO_2 are added to improve the catalytic activity, as pure SiOC glasses pyrolyzed at temperatures as low as 700°C show only low photocatalytic behavior.[127,128,155,276] However, it was demonstrated that even pure SiOC glasses are able to degrade methylene blue under UV light irradiation.

Apart from the photocatalytic activity, SiOC-based glasses and ceramers (i.e., hybrid materials resulting from the pyrolysis of the precursors at temperatures well below 1000°C[277]) were tested as catalytic support materials for Ni, Co[278] or Pt particles.[155,276] For instance Pt/SiOC was shown to be active for the conversion of CO to CO_2; its efficiency was increased upon improving the distribution of the Pt particles.[155] Hence, the incorporation of Pt within a single-source precursor, as enabled by the PDC route, is a highly promising synthesis route for catalytic applications. Furthermore, the fabrication of porous SiOC with thin struts is possible, preventing difficulties with the mass transport and enabling an efficient accessibility of the Pt particles.[155]

6.2.5 | Energy storage in silicon oxycarbides

The electrochemical properties of silicon oxycarbide ceramics with respect to a reversible storage of lithium ions have been studied for the first time in the middle of the 1990s.[279–284] The group of Dahn demonstrated the ability of silicon oxycarbides to reversibly intercalate Li-ions with a capacity of ~ 600 mAh/g. In following studies, it was shown that silicon oxycarbides processed at 1000°C reveal higher reversible capacity in line with a lower irreversible loss. Raj and co-workers[285–289] concluded that the electrochemical performance of SiOC storing hosts originates from their unique microstructure. Accordingly, silicon oxycarbides having Si-mixed bonds with O and C atoms display the highest lithium insertion capacities. The influence of mixed bond configurations on the electrochemical properties of porous SiOC ceramics has been addressed recently by Graczyk-Zajac et al[290] It has been stated that the presence of mixed bonds in the glass induces (a) the formation of a more disordered/defective carbon phase with a higher reversible storage capacity and/or (b) directly provides reversible storing sites at the interface between the SiOC network and the free carbon. Highly porous SiOC ceramics have also demonstrated much better rate capability, that is, high stability with respect to fast charge/discharge rates. Specifically, capacities up to 400 mAh/g have been recovered at 2C rate (charge/discharge in 30 minutes).[291–294]

In the last 10 years, numerous studies from the research teams of Riedel, Kanamura and Soraru revealed that among the various chemical compositions of SiOC, stoichiometries with an exceptionally high content of carbon are most promising ion-storage materials in terms of high gravimetric capacity (600-700 mAh/g), good rate capability and reliable cycling stability over hundreds of cycles.[294–310] In consistence with the above feature, three electrochemically active sites for Li-ion storage were identified in carbon-rich silicon oxycarbides by ^{7}Li–MAS–NMR measurements[290,295,296,298,311] (*cf.* Figure 22). Major Li-ion host sites are interstitial spaces and edges of graphene and carbon layers within the segregated carbon phase. Minor storage contribution is assigned to less ionic Li-species that are stored in micropores. Finally, some diamagnetic Li-species are directly or indirectly stored in the amorphous Si–O–C network. The comparison of the voltage profiles of carbon-rich SiOC and amorphous carbon confirms the Li-ion insertion and extraction within the free carbon phase in the ceramic microstructure.[295,303,306,312]

The segregated carbon phase plays a crucial role in lithium storage within SiOC (*cf.*, Figure 15), but no linearity between the capacity and the segregated carbon content has been found.[306] It has been however evidenced that the lithium storage within the silicon oxycarbide can be directly correlated with the electron transfer through the SiOC.[309] As the storage of ions must be accompanied by a fast electron countercharge transport, materials with low carbon content show initially high capacities though fading rapidly upon cycling; whereas silicon oxycarbides with high volume fractions of segregated carbon exhibit stable and reversible Li-ion storage performance. For these materials, the increase of the content of the segregated carbon affects the electrical conductivity and the capacity less significantly, as discussed above in Section 6.2.2.

The experimental findings have been examined and confirmed by a modeling approach. Kroll[313] applied a density functional theory (DFT) approach to model the lithium insertion into SiOC materials. Storage of Li-ions in amorphous silica (a–SiO_2) and SiOC containing no segregated carbon was found energetically unfavorable due to a large gap between their valence and conduction band. In contrast, in the presence of a free carbon phase providing low-laying unoccupied states significantly decreases the band gap. Consequently, on the one hand the free carbon phase facilitates lithium bonded to oxygen sites, leading to

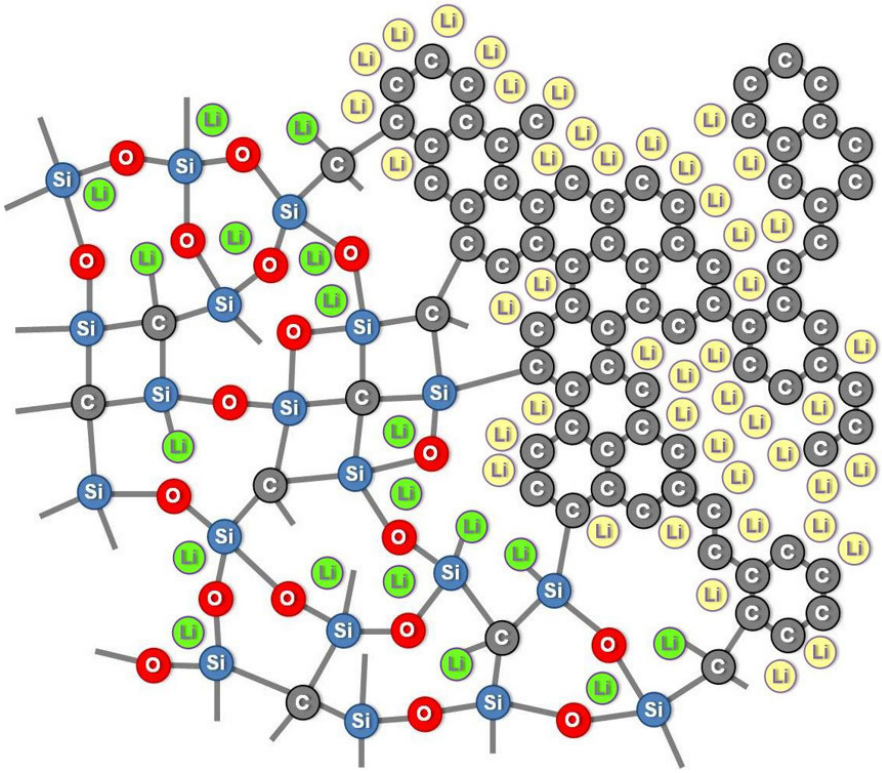

FIGURE 22 Schematic representation of the reversible and irreversible Li-ions storage in SiOC ceramics. The green lithium ions represent lithium irreversibly captured while lithium stored reversibly is marked yellow

irreversible lithium uptake; on the other hand, the segregated carbon provides a major part of the reversible lithium storage capacity. First-principles calculations[314–316] are in agreement with DFT findings. The theoretical specific capacity and reversible capacities of different SiOC compositions have been calculated. It is stated that the stoichiometric SiOC glass presents very low reversible capacity. According to the calculations, the reversible capacity of SiOC should increase with higher carbon concentration; however, it after reaching a maximum value the capacity would begin to decrease with further increase in the carbon content.

6.2.6 | Silicon oxycarbides as (ad)sorbent materials

Silicon oxycarbide glasses were investigated as potential sorbent materials for the purification of waste water. In comparison to activated carbons, SiOC materials allow for an easy desorption of hydrocarbons[317] or methylene blue[318] and exhibit promising ability of regeneration. In addition, HF-etched SiOC glass-ceramics are reported to efficiently remove model-dye systems like Methylene Blue, Rhodamin B, and Crystal Violet, but have a limited capacity of removing metal ions like Cr(III), Pb(II), and Cd(II).[319] It has been shown that mesoporosity is necessary for an efficient removal of model dye systems such as methylene blue or Rhodamine B. In a case study, it was demonstrated that the incorporation of ZnO nanoparticles induces a change from microporosity in the pure SiOC system to mesoporosity in the ZnO/SiOC nanocomposite and thus enhances the adsorption capacity.[127] The adsorption capacity of an SiOC aerogel was shown to be higher than of a mesoporous silica, which possessed a three times larger surface area than that of SiOC.[320] It was stated that this is due to the possibility of van der Waals interactions of methylene blue and Rhodamine B and the segregated carbon phase in addition to adsorbate-adsorbent ionic interactions with the amorphous SiOC network, whereas silica shows only adsorbate-adsorbent ionic interactions. The adsorption capacity of methylene blue is pH dependent, being maximized at pH 6.6 for porous high-carbon SiOC derived from a wood powder template process.[318]

Besides SiOC glasses, polysiloxane-derived micro- and mesoporous ceramers were shown to also be suitable for adsorption of *n*-heptane[321] and acid fuchsin.[322] Due to the hydrophobic nature of the SiOC ceramers, water adsorbs only to a negligible degree on their surface.[321] SiOC ceramers were used furthermore also as heptane or water vapor gas sorbent materials. By tailoring the functional groups of the preceramic polymers, their hydrophobicity can be adjusted.[323]

6.2.7 | Hot-gas separation and gas sensing with silicon oxycarbides

Whereas polymer-derived SiC, SiCN and SiBCN ceramics were prepared and studied with respect to their gas

separation capability, especially concerning H_2 separation from other molecules such as CO, CO_2, CH_4, H_2O etc., only few studies were reported on the use of silicon oxycarbides as materials for micro-/mesoporous membranes for gas separation purposes. For instance, polysiloxane-derived SiOC ceramic membranes were prepared on mesoporous substrates such as γ–Al_2O_3 and ZrO_2.[324] SiOC membrane showed nearly ten times higher permeances for hydrogen than for carbon dioxide, indicating excellent molecular sieving properties in separation of H_2/CO_2. The SiOC membranes prepared on ZrO_2 substrates were shown to possess improved hydrothermal stability.

A recent case study investigated mechanistic aspects related to the gas permeance behavior of SiOC-based microporous membranes deposited on a meso-/macroporous γ–Al_2O_3/α-Al_2O_3 bi-layer substrate. Single gas permeance investigations at elevated temperature indicate promising H_2/CO_2 and H_2/SF_6 ideal permselectivities (ca. 10 and 320, respectively). The experimental gas permeance data were rationalized using solid-state diffusion (as for He and H_2) and gas translational diffusion (for CO_2 and SF_6) mechanisms.[325] It was found that microporous SiOC membranes possess higher permeance for hydrogen than that reported for silica membranes. At the same time, the activation energies for permeation of CO_2 and SF_6 through the SiOC membrane are higher than those reported for silica-based membranes. The different behavior of SiOC membranes as compared to that of silica-based membranes was attributed to differences in their pore structure/morphology.

SiOC were also shown recently to be suitable materials for gas sensing purposes.[326,327] Thus, mesoporous SiOC aerogel-derived glasses with a specific surface area of ca. 150 m^2/g showed good sensing ability to NO_2 in a temperature range from 300 to 400°C; at higher temperatures, the NO_2 response was shown to disappear and the investigated SiOC samples were demonstrated to sense hydrogen, with an optimum sensitivity at 500°C. Moreover, the SiOC-based chemiresistive sensors are highly selective, being able to sense NO_2 and H_2 in the presence of rather high concentrations of other gases such as acetone or CO.[326] For an HF-etched SiOC glass-ceramic it was demonstrated, that even small amounts of 5 ppm NO_2 can be detected at room temperature.[328]

6.2.8 | Chemical durability

Silicate glasses can be etched in highly alkaline or in hydrofluoric acid (HF) solutions. Both, SiOC glasses and glass-ceramics show a higher resistance to strong basic or HF solutions as compared to fused silica or soda-lime glasses.[217]

Etching experiments of carbon-rich SiOC glasses revealed a mass loss of 40% after 8 hour treatment with HF.[129] Longer exposition times did not change the overall weight loss, although still significant amounts of oxygen were present. This was attributed to the presence of a passivating Si–C layer. The molar ratios between silicon and oxygen remained almost constant. Interestingly, some carbon seems to be additionally removed during the treatment with HF.[129]

Typically, the chemical durability of SiOC materials was shown to be dependent on the degree of phase separation and the amount of carbon.[217] The higher the degree of phase separation, the lower the chemical durability in highly alkaline or HF solutions, as SiO_4 tetrahedra (that are increasingly formed during phase separation) are preferentially attacked. Second, Si–C bonds and the segregated carbon phase are not significantly attacked by highly alkaline and HF solutions and therefore act as a chemical and/or physical barrier. Consequently, SiOC glasses with high amount of carbon exhibit improved chemical durability.[217]

After etching, the surface of SiOC glass-ceramics consists of segregated carbon and Si–C bonds. Consequently, the surface properties turn from acidic in the as-prepared state into basic.[329]

6.2.9 | Biocompatibility and bioactivity of SiOC-based glasses

There are only few studies available in literature concerning the biocompatibility and bioactivity of silicon oxycarbide glasses and glass-ceramics. The biocompatibility and antimicrobial effects of a silicon oxycarbide coating (30-50 nm thickness) containing silver nanoparticles (5-50 nm) were reported firstly in 2010.[330] The Ag/SiOC coatings were prepared by a two-step process involving the deposition of Ag nanoparticles by PVD on a substrate followed by the formation of the SiOC glass matrix via a CVD step using hexamethyldisiloxane. The Ag/SiOC coatings exhibit excellent in vitro and ex vivo antimicrobial activity against several gram-positive bacteria (*Staphilococus aureus*, *Staphilococus epidermidis, Methicillin-resistant Staphilococus aureus*). Biocompatibility testing, conducted according to ISO 10993-5, did not indicate any cytotoxic effects of the Ag/SiOC coatings. Those results were confirmed in several recent studies, clearly indicating high intrinsic tissue compatibility of the silicon oxycarbides.[23,331,332]

A polysiloxane-derived SiOC glass was studied moreover concerning its hemocompatibility.[333] The hemocompatibility of SiOC glasses was shown to be tunable via controlling the carbon/oxygen ratio. Especially, the surface-near composition was shown to dictate the blood compatibility of SiOC glasses, with a rather narrow compositional range for oxygen (50-60 at.%) being required to provide high blood compatibility, that is, to inhibit procoagulant

activity which typically leads to thrombus formation at the contact with blood. It was additionally shown that the incorporation of carbon contents of ca. 20 at.% greatly improves the hemocompatibility of SiOC. In fact, the activation properties of SiOC glasses with a broad range of carbon/oxygen ratios for the plasma phase of blood coagulation were found to be comparable to those of pyrolytic carbon (which is the material of choice for blood-contacting biomedical devices[334,335]); whereas SiOC glasses with compositions exceeding 60 at.% carbon were even more blood compatible. The reported results suggest SiOC glasses as a suitable alternative to be use in medical applications requiring good tribological properties and high blood compatibility.[333]

The bioactivity of silicon-oxycarbide-based glasses was reported for the first time in 2016.[23] Thus, a Ca- and Mg-containing SiOC glass was prepared from a single-source precursor synthesized via chemical modification of a polysilsesquioxane with Ca and Mg acetylacetonate. The as-prepared glass showed the mineralization of hydroxyapatite upon exposure to simulated body fluid (SBF) for 3 days, indicating promising bioactivity. Interestingly, the SiOC-based bioactive glass exhibited an outstanding resistance against devitrification, maintaining its amorphous nature even after thermal annealing at 1300°C.[23]

Recently, the concept of partly substituting oxygen in silicate glasses with elements showing higher valence than that of oxygen, in order to improve the network robustness of bioactive glasses, was reported for silicon oxycarbide-[34] as well as silicon oxynitride-based glasses.[336] For instance, a Ca- and Mg-containing glass composition was shown to be bioactive despite of a network connectivity value of 5.26,[34] which is higher than that of vitreous silica (itself being not bioactive; network connectivity value of 4) and much higher than that of Bioglass® (network connectivity of 2.1). This behavior of the silicon oxycarbide glass is quite unique and should be studied further in detail. Because the silicon oxycarbide glasses have complex interpenetrating network structures with carbon rich and silica rich regions connected by complex interfaces, reactivity at such interfaces may be a contributing factor to bioactivity. Thus, it seems that strong carbon-for-oxygen substitution in silicon oxycarbide glasses significantly improves their thermal and mechanical properties due to very high network connectivity; whereas at the same time, the bioactivity can be provided via minor depolymerization of the network with, for example, alkaline earth metals in combination with the intrinsic open network architecture of silicon oxycarbides. Such a rational design of these materials may allow for significantly improving their performance and expand the scope of their applications. Silicon oxycarbide glasses may also serve as model compounds for developing advanced design concepts for highly connected bioactive glasses.[34]

6.2.10 | Drug delivery with silicon oxycarbides

Due to the ease of fabricating porous samples and because it is highly biocompatible, the SiOC system was investigated as possible drug delivery system. Thus, micro- and mesoporous SiOC glasses prepared at 1100°C were shown to be able to adsorb acyclovir molecules with subsequent release in acidified H_2O solution.[337] It was demonstrated that the specific surface area has an influence on the adsorption capacity, but the presence and nature of functional groups at the surface is dominating the adsorption capacity. Modification of the surface of silicon oxycarbide with amino groups enhances the maximum adsorption and the degree of release of acyclovir molecules.[338] The oxidation of the segregated carbon phase in SiOC glasses enables the introduction of carboxylic and phenolic functional groups to the surface of the glass particles,[337] opening the possibility to tune the interaction with other substances. Recently, the suitability of bi-modal porous silicon oxycarbides as part of a delivery system for tenofovir was demonstrated.[339] More than one drug molecule can be delivered at the same time by the usage of hierarchical porous SiOC. This was demonstrated for vancomycin (small molecule) and bovine serum albumin (BSA, larger molecule). Thus, vancomycin can be loaded into the micropores of SiOC; whereas BSA can be loaded into mesopores.[340] For both molecules, the hierarchically micro-/mesoporous SiOC exhibits a higher loading capacity as that of commercially available mesoporous silica.

7 | CONCLUSIONS AND PERSPECTIVES

Silicon oxycarbides represent a class of materials with exciting structural and functional properties which has received increased attention in the glass and ceramic community within the last two decades. Their glassy as well as glass-ceramic state are characterized by unique network architectures and nano/microstructures, respectively, which primarily dictate their structural behavior and functional property profiles. Within the last 20 years, significant efforts were done in order to endeavor new materials compositions and properties related to silicon oxycarbides. Thus, remarkable preparative progress was achieved with respect to accessing interesting phase compositions based on silicon oxycarbide as complex fractal glass networks with outstanding high-temperature creep and environmental resistance or bioactivity as well as thermodynamically controlled glass-ceramics with attractive functional properties, for example, piezoresistive sensing behavior, reversible Li (and Na) uptake/release, optical properties, gas sensing as well as bioactivity,

(photo)catalytic properties or drug release behavior. It is considered that silicon oxycarbide may provide a highly versatile and easy-to-access platform of novel phase compositions and morphologies to address various structural and functional applications. Moreover, significant advancements recorded within the last years concerning the processing of preceramic polymers into complex-shaped and miniaturized/MST-compatible glass/glass-ceramic parts (e.g., lithographic processing, additive manufacturing, etc.) are expected to open new avenues of accessing new applications for silicon oxycarbides as well as innovative approaches to device integration of functional SiOC materials.

ACKNOWLEDGMENTS

Financial support from the Deutsche Forschungsgemeinschaft (IO 64/7-1 and IO 64/9-1) is gratefully acknowledged. EI acknowledges furthermore support from the EU COST Action CM1302 (European network "Smart Inorganic Polymers", SIPs).

ORCID

Emanuel Ionescu http://orcid.org/0000-0002-3266-3031

Isabel Gonzalo-Juan http://orcid.org/0000-0003-4257-1189

REFERENCES

1. Ellis RB. Method of making electrically conducting glass and articles made therefrom. U.S. Patent 2,556,616. 1951.
2. Tavakoli AH, Armentrout MM, Sen S, Navrotsky A. Hydrogenated Si-O-C nanoparticles: synthesis, structure, and thermodynamic stability. J Mater Res. 2015;30:295–303.
3. Tahir MS, Weinberger M, Balasubramanian P, Diemant T, Behm RJ, Linden M, et al. Silicon carboxylate derived silicon oxycarbides as anodes for lithium ion batteries. J Mater Chem A. 2017;5:10190–9.
4. Mera G, Ionescu E. Silicon-containing preceramic polymers. In: *Encyclopedia of polymer science and technology*, 4th edn. Matyjaszewski K (ed). Hoboken, NJ: John Wiley & Sons. Inc.; 2014: pp. 432–64.
5. Mera G, Gallei M, Bernard S, Ionescu E. Ceramic nanocomposites from tailor-made preceramic polymers. Nanomaterials. 2015;5:468–540.
6. Ionescu E, Terzioglu C, Linck C, Kaspar J, Navrotsky A, Riedel R. Thermodynamic control of phase composition and crystallization of metal-modified silicon oxycarbides. J Am Ceram Soc. 2013;96:1899–903.
7. Papendorf B, Ionescu E, Kleebe H-J, Linck C, Guillon O, Nonnenmacher K, et al. High-temperature creep behavior of dense SiOC-based ceramic nanocomposites: microstructural and phase composition effects. J Am Ceram Soc. 2013;96:272–80.
8. Ionescu E, Balan C, Kleebe H-J, Linck C, Guillon O, Nonnenmacher K, et al. High-temperature creep behavior of SiOC glass-ceramics: influence of network carbon versus segregated carbon. J Am Ceram Soc. 2014;97:3935–42.
9. Stabler C, Roth F, Narisawa M, Schliephake D, Heilmaier M, Lauterbach S, et al. High-temperature creep behavior of a SiOC glass ceramic free of segregated carbon. J Eur Ceram Soc. 2016;36:3747–53.
10. Stabler C, Seemueller C, Choudhary A, Heilmaier M, Lauterbach S, Kleebe HJ, et al. Synthesis and high-temperature creep behavior of a SiLuOC-based glass-ceramic. J Ceram Soc Jpn. 2016;124:1006–12.
11. Widgeon SJ, Sen S, Mera G, Ionescu E, Riedel R, Navrotsky A. 29Si and 13C solid-state NMR spectroscopic study of nanometer-scale structure and mass fractal characteristics of amorphous polymer derived silicon oxycarbide ceramics. Chem Mater. 2010;22:6221–8.
12. Saha A, Raj R, Williamson DL. A model for the nanodomains in polymer-derived SiCO. J Am Ceram Soc. 2006;89:2188–95.
13. Mera G, Navrotsky A, Sen S, Kleebe HJ, Riedel R. Polymer-derived SiCN and SiOC ceramics - structure and energetics at the nanoscale. J Mater Chem A. 2013;1:3826–36.
14. Sen S, Widgeon S. On the mass fractal character of Si-based structural networks in amorphous polymer derived ceramics. Nanomaterials. 2015;5:366–75.
15. Rouxel T, Massouras G, Soraru G-D. High temperature behavior of a gel-derived SiOC glass: elasticity and viscosity. J Sol-Gel Sci Technol. 1999;14:87–94.
16. Martinez-Crespiera S, Ionescu E, Kleebe HJ, Riedel R. Pressureless synthesis of fully dense and crack-free SiOC bulk ceramics via photo-crosslinking and pyrolysis of a polysiloxane. J Eur Ceram Soc. 2011;31:913–9.
17. Soraru GD, Dallapiccola E, D'Andrea G. Mechanical characterization of sol-gel-derived silicon oxycarbide glasses. J Am Ceram Soc. 1996;79:2074–80.
18. Walter S, Soraru GD, Brequel H, Enzo S. Microstructural and mechanical characterization of sol gel-derived Si-O-C glasses. J Eur Ceram Soc. 2002;22:2389–400.
19. Rouxel T, Soraru G-D, Vicens J. Creep viscosity and stress relaxation of gel-derived silicon oxycarbide glasses. J Am Ceram Soc. 2001;84:1052–8.
20. Saha A, Raj R. Crystallization maps for SiCO amorphous ceramics. J Am Ceram Soc. 2007;90:578–83.
21. Pantano CG, Singh AK, Zhang H. Silicon oxycarbide glasses. J Sol-Gel Sci Technol. 1999;14:7–25.
22. Sen S, Widgeon SJ, Navrotsky A, Mera G, Tavakoli A, Ionescu E, et al. Carbon substitution for oxygen in silicates in planetary interiors. Proc Natl Acad Sci USA. 2013;110:15904–7.
23. Gonzalo-Juan I, Detsch R, Mathur S, Ionescu E, Boccaccini AR, Riedel R. Synthesis and in vitro activity assessment of novel silicon oxycarbide-based bioactive glasses. Materials. 2016;9:959.
24. Dire S, Ceccato R, Gialanella S, Babonneau F. Thermal evolution and crystallisation of polydimethylsiloxane-zirconia nanocomposites prepared by the sol-gel method. J Eur Ceram Soc. 1999;19:2849–58.
25. Ionescu E, Papendorf B, Kleebe HJ, Poli F, Müller K, Riedel R. Polymer-derived silicon oxycarbide/hafnia ceramic nanocomposites.

Part I: phase and microstructure evolution during the ceramization process. J Am Ceram Soc. 2010;93:1774–82.
26. Ionescu E, Papendorf B, Kleebe HJ, Riedel R. Polymer-derived silicon oxycarbide/hafnia ceramic nanocomposites. Part II: stability toward decomposition and microstructure evolution at T1000 degrees C. J Am Ceram Soc. 2010;93:1783–9.
27. Hojamberdiev M, Prasad RM, Fasel C, Riedel R, Ionescu E. Single-source-precursor synthesis of soft magnetic Fe3Si- and Fe5Si3-containing SiOC ceramic nanocomposites. J Eur Ceram Soc. 2013;33:2465–72.
28. Babonneau F, Soraru GD, Thorne KJ, Mackenzie JD. Chemical characterization of Si-Al-C-O precursor and its pyrolysis. J Am Ceram Soc. 1991;74:1725–8.
29. Kaspar J, Terzioglu C, Ionescu E, Graczyk-Zajac M, Hapis S, Kleebe HJ, et al. Stable SiOC/Sn nanocomposite anodes for lithium-ion batteries with outstanding cycling stability. Adv Funct Mater. 2014;24:4097–104.
30. Umicevic AB, Cekic BD, Belosevic-Cavor JN, Koteski VJ, Papendorf B, Riedel R, et al. Evolution of the local structure at Hf sites in SiHfOC upon ceramization of a hafnium-alkoxide-modified polysilsesquioxane: a perturbed angular correlation study. J Eur Ceram Soc. 2015;35:29–35.
31. Gervais C, Babonneau F, Dallabonna N, Sorarù G. Sol-gel-derived silicon-boron oxycarbide glasses containing mixed silicon oxycarbide (SiCxO4-x) and boron oxycarbide (BCYO3-y) units. J Am Ceram Soc. 2001;84:2160–4.
32. Ngoumeni-Yappi R, Fasel C, Riedel R, Ischenko V, Pippel E, Woltersdorf J, et al. Tuning of the rheological properties and thermal behavior of boron-containing polysiloxanes. Chem Mater. 2008;20:3601–8.
33. Ionescu E, Kleebe H-J, Riedel R. Silicon-containing polymer-derived ceramic nanocomposites (PDC-NCs): preparative approaches and properties. Chem Soc Rev. 2012;41:5032–52.
34. Ionescu E, Sen S, Mera G, Navrotsky A. Structure, energetics and bioactivity of silicon oxycarbide-based amorphous ceramics with highly connected networks. J Eur Ceram Soc. 2018;38:1311–9.
35. Colombo P, Mera G, Riedel R, Soraru GD. Polymer-derived ceramics: 40 years of research and innovation in advanced ceramics. J Am Ceram Soc. 2010;93:1805–37.
36. Soraru GD. Silicon oxycarbide glasses from gels. J Sol-Gel Sci Technol. 1994;2:843–8.
37. Riedel R, Mera G, Hauser R, Klonczynski A. Silicon-based polymer-derived ceramics: synthesis properties and applications - a review. Dedicated to Prof. Dr. Fritz Aldinger on the occasion of his 65th birthday. J Ceram Soc Jpn. 2006;114:425–44.
38. Narisawa M. Silicone resin applications for ceramic precursors and composites. Materials. 2010;3:3518–36.
39. Jones RG, Ando W, Chojnowski J (eds). *Silicon-containing polymers: the science and technology of their synthesis and applications*, 1st edn. Dordrecht, The Netherlands: Kluwer Academic Publishers; 2000.
40. Mark JE. Overview of siloxane polymers. ACS Symp Ser. 2000;729:1–10.
41. Hurwitz FI, Hyatt L, Gorecki J, DAmore L. Silsesquioxanes as precursors to ceramic composites. Ceram Eng Sci Proc. 1987;8:732–43.
42. Wang S-J, Fan X-D, Kong J, Wang X, Liu YY, Zhang GB. A new controllable approach to synthesize hyperbranched poly (siloxysilanes). J Polym Sci A. 2008;46:2708–20.
43. Kong J, Fan X, Si Q, Zhang G, Wang S, Wang X. Hyperbranched polycarbosiloxane with dendritic boron cores: synthesis, characterization, and structure regulation. J Polym Sci A. 2006;44:3930–41.
44. Wang S-J, Fan X-D, Kong J, Lu JR. Synthesis, characterization and UV curing kinetics of hyperbranched polysiloxysilanes from A2 and CB2 type monomers. Polymer. 2009;50:3587–94.
45. Chojnowski J, Cypryk M, Fortuniak W, Ścibiorek M, Rozga-Wijas K. Synthesis of branched polysiloxanes with controlled branching and functionalization by anionic ring-opening polymerization. Macromolecules. 2003;36:3890–7.
46. Miyasaka M, Fujiwara Y, Kudo H, Nishikubo T. Synthesis and characterization of hyperbranched polymer consisting of silsesquioxane derivatives. Polym J. 2010;42:799.
47. Chavez R, Ionescu E, Fasel C, Riedel R. Imide-containing ladder polyphenylsilsesquioxanes with high thermal stability and thermoplastic properties. J Appl Polym Sci. 2014;131:40081–8.
48. Mathias LJ, Carothers TW. Hyperbranched poly(siloxysilanes). J Am Chem Soc. 1991;113:4043–4.
49. Uchida H, Kabe Y, Yoshino K, Kawamata A, Tsumuraya T, Masamune S. General strategy for the systematic synthesis of oligosiloxanes. Silicone dendrimers. J Am Chem Soc. 1990;112:7077–9.
50. Babonneau F, Thorne K, Mackenzie JD. Dimethyldiethoxysilane/tetraethoxysilane copolymers: precursors for the silicon-carbon-oxygen system. Chem Mater. 1989;1:554–8.
51. Brinker C, Scherer G. *Sol-gel science: the physics and chemistry of sol-gel processing*, 1st edn. San Diego, CA: Academic Press; 1990.
52. Schubert U, Husing N. *Synthesis of inorganic materials*, 3rd edn. Weinheim, Germany: Wiley-VCH; 2012.
53. Dire S, Babonneau F, Sanchez C, Livage J. Sol-gel synthesis of siloxane-oxide hybrid coatings [Si(CH3)2O.MOx: M = silicon, titanium, zirconium, aluminum] with luminescent properties. J Mater Chem. 1992;2:239–44.
54. Soraru GD, D'Andrea G, Campostrini R, Babonneau F, Mariotto G. Structural characterization and high-temperature behavior of silicon oxycarbide glasses prepared from sol-gel precursors containing Si-H bonds. J Am Ceram Soc. 1995;78:379–87.
55. Fukushima M, Yasuda E, Nakamura Y, Tanabe Y. Pyrolysis behavior of organic-inorganic hybrids with Si-O-Nb/Si-O-Ta oxygen bridged heterometallic bonds. J Ceram Soc Jpn. 2003;111:857–9.
56. Ionescu E, Linck C, Fasel C, Müller M, Kleebe HJ, Riedel R. Polymer-derived SiOC/ZrO2 ceramic nanocomposites with excellent high-temperature stability. J Am Ceram Soc. 2010;93:241–50.
57. Harshe R, Balan C, Riedel R. Amorphous Si(Al)OC ceramic from polysiloxanes: bulk ceramic processing, crystallization behavior and applications. J Eur Ceram Soc. 2004;24:3471–82.
58. Valles EM, Macosko CW. Properties of networks formed by end linking of poly(dimethylsiloxane). Macromolecules. 1979;12:673–9.
59. Heidingsfeldova M, Capka M. Rhodium complexes as catalysts for hydrosilylation crosslinking of silicone rubber. J Appl Polym Sci. 1985;30:1837–46.
60. Kroke E, Li Y-L, Konetschny C, Lecomte E, Fasel C, Riedel R. Silazane-derived ceramics and related materials. Mater Sci Eng, R. 2000;R26:97–199.
61. Dunham ML, Bailey DL, Mixer RY. New curing system for silicone rubber. Ind Eng Chem. 1957;49:1373–6.

62. Belot V, Corriu RJP, Leclercq D, Mutin PH, Vioux A. Thermal redistribution reactions in crosslinked polysiloxanes. J Polym Sci A. 1992;30:613–23.
63. Corriu RJP, Leclercq D, Mutin PH, Vioux A. Preparation and structure of silicon oxycarbide glasses derived from polysiloxane precursors. J Sol-Gel Sci Technol. 1997;8:327–30.
64. Danko GA, Silberglitt R, Colombo P, Woltersdorf J. Comparison of microwave hybrid and conventional heating of preceramic polymers to form silicon carbide and silicon oxycarbide ceramics. J Am Ceram Soc. 2000;83:1617–25.
65. Pivin JC, Colombo P. Ceramic coatings by ion irradiation of polycarbosilanes and polysiloxanes. Part I. Conversion mechanism. J Mater Sci. 1997;32:6163–73.
66. Pivin JC, Colombo P, Soraru GD. Comparison of ion irradiation effects in silicon-based preceramic thin films. J Am Ceram Soc. 2000;83:713–20.
67. Schulz M, Boerner M, Hausselt J, Heldele R. Polymer derived ceramic microparts from x-ray lithography: cross-linking behavior and process optimization. J Eur Ceram Soc. 2005;25:199–204.
68. Zoli L, Sciti D, Liew L-A, Terauds K, Azarnoush S, Raj R. Additive manufacturing of ceramics enabled by flash pyrolysis of polymer precursors with nanoscale layers. J Am Ceram Soc. 2016;99:57–63.
69. Kaur S, Cherkashinin G, Fasel C, Kleebe HJ, Ionescu E, Riedel R. Single-source-precursor synthesis of novel V8C7/SiC(O)-based ceramic nanocomposites. J Eur Ceram Soc. 2016;36:3553–63.
70. Zhou C, Fasel C, Ishikawa R, Gallei M, Ikuhara Y, Lauterbach S, et al. One-pot synthesis of a C/SiFeN(O)-based ceramic paper with in-situ generated hierarchical micro/nano-morphology. J Eur Ceram Soc. 2017;37:5193–203.
71. Colombo P, Sglavo V, Pippel E, Woltersdorf J. Joining of reaction-bonded silicon carbide using a preceramic polymer. J Mater Sci. 1998;33:2405–12.
72. Nejhad MNG, Chandramouli MV, Yousefpour A. Processing and performance of continuous fiber ceramic composites by preceramic polymer pyrolysis: I - Filament winding. J Compos Mater. 2001;35:2207–37.
73. De Omena Pina SR, Pardini LC, Yoshida IVP. Carbon fiber/ceramic matrix composites: processing, oxidation and mechanical properties. J Mater Sci. 2007;42:4245–53.
74. Weichand P, Gadow R. Basalt fibre reinforced SiOC-matrix composites: manufacturing technologies and characterisation. J Eur Ceram Soc. 2015;35:4025–30.
75. Hurwitz FI, Heimann PJ, Gyekenyesi JZ, Masnovi J, Bu XY. Polymeric routes to silicon carbide and silicon oxycarbide CMC. In: Wachtman JB Jr, editors. Chapter 28 in *Ceramic engineering and science proceedings*. Weinheim, Germany: Wiley-VCH, 1991; p. 1292–303.
76. Seitz J, Bill J. Production of compact polysilazane-derived Si/C/N-ceramics by plastic forming. J Mater Sci Lett. 1996;15:391–3.
77. Haug R, Weinmann M, Bill J, Aldinger F. Plastic forming of preceramic polymers. J Eur Ceram Soc. 1998;19:1–6.
78. Konetschny C, Galusek D, Reschke S, Fasel C, Riedel R. Dense silicon carbonitride ceramics by pyrolysis of cross-linked and warm pressed polysilazane powders. J Eur Ceram Soc. 1999;19:2789–96.
79. Harshe R. Synthesis and Processing of Amorphous Si(Al)OC Bulk Ceramics. Materials and Earth Sciences. Technical university of Darmstadt. PhD. 2004. 236 pp.
80. Suyal N, Krajewski T, Mennig M. Sol-gel synthesis and microstructural characterization of silicon oxycarbide glass sheets with high fracture strength and high modulus. J Sol-Gel Sci Technol. 1998;13:995–9.
81. Suyal N, Hoebbel D, Mennig M, Schmidt H. A solid state 29Si and 13C NMR study on the synthesis of thin silicon oxycarbide glass sheets by a sol-gel route. J Mater Chem. 1999;9:3061–7.
82. Eom J-H, Kim Y-W. Effect of starting particle size and barium addition on flexural strength of polysiloxane-derived SiOC ceramics. J Ceram Soc Jpn. 2015;123:142–6.
83. Greil P. Advancements in polymer-filler derived ceramics. J Korean Ceram Soc. 2012;49:279–86.
84. Greil P. Near net shape manufacturing of polymer derived ceramics. J Eur Ceram Soc. 1998;18:1905–14.
85. Kaur S, Riedel R, Ionescu E. Pressureless fabrication of dense monolithic SiC ceramics from a polycarbosilane. J Eur Ceram Soc. 2014;34:3571–8.
86. Poerschke DL, Braithwaite A, Park D, Lauten F. Crystallization behavior of polymer-derived Si-O-C for ceramic matrix composite processing. Acta Mater. 2018;147:329–41.
87. Ionescu E, Riedel R. Polymer processing of ceramics. In: Narottam PB, Boccaccini AR, editors. Chapter 7 in *Ceramics and composites processing methods*. Hoboken, NJ: John Wiley & Sons, Inc., 2012; p. 235.
88. Greil P. Active-filler-controlled pyrolysis of preceramic polymers. J Am Ceram Soc. 1995;78:835–48.
89. Greil P, Seibold M. Modeling of dimensional changes during polymer-ceramic conversion of bulk component fabrication. J Mater Sci. 1992;27:1053–60.
90. Colombo P, Gambaryan-Roisman T, Scheffler M, Buhler P, Greil P. Conductive ceramic foams from preceramic polymers. J Am Ceram Soc. 2001;84:2265–8.
91. Biasetto L, Francis A, Palade P, Principi G, Colombo P. Polymer-derived microcellular SiOC foams with magnetic functionality. J Mater Sci. 2008;43:4119–26.
92. Renlund GM, Prochazka S, Doremus RH. Silicon oxycarbide glasses. Part II. Structure and properties. J Mater Res. 1991;6:2723–34.
93. Linck C, Ionescu E, Papendorf B, Galuskova D, Galusek D, Ŝajgalík P, et al. Corrosion behavior of silicon oxycarbide-based ceramic nanocomposites under hydrothermal conditions. Int J Mater Res. 2012;103:31–9.
94. Ishihara S, Gu H, Bill J, Aldinger F, Wakai F. Densification of precursor-derived Si-C-N ceramics by high-pressure hot isostatic pressing. J Am Ceram Soc. 2002;85:1706–12.
95. Esfehanian M, Oberacker R, Fett T, Hoffmann MJ. Development of dense filler-free polymer-derived SiOC ceramics by field-assisted sintering. J Am Ceram Soc. 2008;91:3803–5.
96. Wen QB, Xu YP, Xu BB, et al. Single-source-precursor synthesis of dense SiC/HfCxN1-x-based ultrahigh-temperature ceramic nanocomposites. Nanoscale. 2014;6:13678–89.
97. Yuan J, Li D, Johanns KE, Fasel C, Durst K, Kleebe HJ, et al. Preparation of dense SiHf(B)CN-based ceramic nanocomposites via rapid spark plasma sintering. J Eur Ceram Soc. 2017;37:5157–65.
98. Bechelany MC, Salameh C, Viard A, Guichaoua L, Rossignol F, Chartier T, et al. Preparation of polymer-derived Si–B–C–N monoliths by spark plasma sintering technique. J Eur Ceram Soc. 2015;35:1361–74.

99. Chaudhry TM, Ho H, Drzal LT, Harris M, Laine RM. Silicon oxycarbide coatings on graphite fibers II. Adhesion, processing, and interfacial properties. Mater Sci Eng, A. 1995;A195:237–49.
100. Harris M, Chaudhary T, Drzal L, Laine RM. Silicon oxycarbide coatings on graphite fibers: chemistry, processing, and oxidation resistance. Mater Sci Eng, A. 1995;A195:223–36.
101. Colombo P, Paulson TE, Pantano CG. Atmosphere effects in the processing of silicon carbide and silicon oxycarbide thin films and coatings. J Sol-Gel Sci Technol. 1994;2:601–4.
102. Godini HR, Trivedi H, de Villasante AG, Görke O, Jašo S, Simon U, et al. Design and demonstration of an experimental membrane reactor set-up for oxidative coupling of methane. Chem Eng Res Des. 2013;91:2671–81.
103. Wang K, Guenthner M, Motz G, Bordia RK. High performance environmental barrier coatings, Part II: active filler loaded SiOC system for superalloys. J Eur Ceram Soc. 2011;31:3011–20.
104. Karakuscu A, Guider R, Pavesi L, Soraru GD. White luminescence from sol-gel-derived SiOC thin films. J Am Ceram Soc. 2009;92:2969–74.
105. Goerke O, Feike E, Heine T, Trampert A, Schubert H. Ceramic coatings processed by spraying of siloxane precursors (polymer-spraying). J Eur Ceram Soc. 2004;24:2141–7.
106. Gallis S, Nikas V, Huang M, Eisenbraun E, Kaloyeros AE. Comparative study of the effects of thermal treatment on the optical properties of hydrogenated amorphous silicon-oxycarbide. J Appl Phys. 2007;102:024301–9.
107. Luo M, Li Y, Jin S, Sang S, Zhao L. Oxidation resistance of multi-walled carbon nanotubes coated with polycarbosilane-derived SiCxOy ceramic. Ceram Int. 2011;37:3055–62.
108. Reznik B, Denev J, Bockhorn H. Adaptive silicon oxycarbide coatings with controlled hydrophilic or hydrophobic properties. Adv Eng Mater. 2016;18:703–10.
109. Cromme P, Scheffler M, Greil P. Ceramic tapes from preceramic polymers. Adv Eng Mater. 2002;4:873–7.
110. Manocha LM, Manocha SM. Studies on solution-derived ceramic coatings for oxidation protection of carbon-carbon composites. Carbon. 1995;33:435–40.
111. Ryan JV, Pantano CG. Synthesis and characterization of inorganic silicon oxycarbide glass thin films by reactive rf-magnetron sputtering. J Vac Sci Technol, A. 2007;25:153–9.
112. Ryan JV, Colombo P, Howell JA, Pantano CG. Tribology-structure relationships in silicon oxycarbide thin films. Int J Appl Ceram Technol. 2010;7:675–86.
113. Bellocchi G, Franzo G, Boninelli S, Miritello M, Cesca T, Iacona F, et al. Structural and luminescence properties of undoped and Eu-doped SiOC thin films. IOP Conf Ser Mater Sci Eng. 2014;56:12001–6.
114. Lu K, Erb D. Polymer derived silicon oxycarbide-based coatings. Int Mater Rev. 2018;63:139–61.
115. Clark TJ, Banash MA, Cruse RW, Mininni RM, Rohman SJ. Model for chemical vapor deposition of nanostructured ceramics inside tubes under high temperature laminar flow conditions. Nanostruct Mater. 1994;4:723–35.
116. Klausmann A, Morita K, Johanns KE, Fasel C, Durst K, Mera G, et al. Synthesis and high-temperature evolution of polysilylcarbodiimide-derived SiCN ceramic coatings. J Eur Ceram Soc. 2015;35:3771–80.
117. Chao CC, Wang TC, Ho RM, Georgopanos P, Avgeropoulos A, Thomas EL. Robust block copolymer mask for nanopatterning polymer films. ACS Nano. 2010;4:2088–94.
118. Hellmann JR, Petervary MP, Priest JM, Pantano CG. Effect of Si-O-C coatings on the strength of Saphikon and Nicalon fibers. Ceram Trans. 1999;94:361–70.
119. Torrey JD, Bordia RK. Processing of polymer-derived ceramic composite coatings on steel. J Am Ceram Soc. 2008;91:41–5.
120. Carlomagno C, Speranza G, Aswath P, Sorarù GD, Migliaresi C, Maniglio D. Breath figures decorated silica-based ceramic surfaces with tunable geometry from UV cross-linkable polysiloxane precursor. J Eur Ceram Soc. 2017;38:1320–6.
121. Colombo P. Engineering porosity in polymer-derived ceramics. J Eur Ceram Soc. 2008;28:1389–95.
122. Lu K. Porous and high surface area silicon oxycarbide-based materials—A review. Mater Sci Eng, R. 2015;97:23–49.
123. Manoj Kumar BV, Kim Y-W. Processing of polysiloxane-derived porous ceramics: a review. Sci Technol Adv Mater. 2010;11:1–16.
124. Assefa D, Zera E, Campostrini R, Soraru GD, Vakifahmetoglu C. Polymer-derived SiOC aerogel with hierarchical porosity through HF etching. Ceram Int. 2016;42:11805–9.
125. Schmidt H, Koch D, Grathwohl G, Colombo P. Micro-/macroporous ceramics from preceramic precursors. J Am Ceram Soc. 2001;84:2252–5.
126. Duan L, Ma Q. Effect of pyrolysis temperature on the pore structure evolution of polysiloxane-derived ceramics. Ceram Int. 2012;38:2667–71.
127. Hojamberdiev M, Prasad RM, Morita K, Schiavon MA, Riedel R. Polymer-derived mesoporous SiOC/ZnO nanocomposite for the purification of water contaminated with organic dyes. Microporous Mesoporous Mater. 2012;151:330–8.
128. Hojamberdiev M, Prasad RM, Morita K, Zhu Y, Schiavon MA, Gurlo A, et al. Template-free synthesis of polymer-derived mesoporous SiOC/TiO2 and SiOC/N-doped TiO2 ceramic composites for application in the removal of organic dyes from contaminated water. Appl Catal B. 2012;115–116:303–13.
129. Wilson AM, Zank G, Eguchi K, Xing W, Yates B, Dahn JR. Pore creation in silicon oxycarbides by rinsing in dilute hydrofluoric acid. Chem Mater. 1997;9:2139–44.
130. Li J, Lu K, Lin T, Shen F. Preparation of micro-/mesoporous SiOC bulk ceramics. J Am Ceram Soc. 2015;98:1753–61.
131. Dire S, Tagliazucca V, Salvadori L, Soraru GD. Preparation of dense and porous silicon oxycarbide submicrometer-sized spheres using a modified Stober process. J Am Ceram Soc. 2011;94:3819–24.
132. Biasetto L, Pena-Alonso R, Soraru GD, Colombo P. Etching of SiOC ceramic foams. Adv Appl Ceram. 2008;107:106–10.
133. Duan L-Q, Ma Q-S, Chen Z-H. The production of high surface area porous carbonaceous materials from polysiloxane. New Carbon Mater. 2013;28:235–40.
134. Erb D, Lu K. Additive and pyrolysis atmosphere effects on polysiloxane-derived porous SiOC ceramics. J Eur Ceram Soc. 2017;37:4547–57.
135. Soraru GD, Pena-Alonso R, Kleebe HJ. The effect of annealing at 1400 degrees C on the structural evolution of porous C-rich silicon (boron)oxycarbide glass. J Eur Ceram Soc. 2012;32:1751–7.
136. Meier A, Weinberger M, Pinkert K, Oschatz M, Paasch S, Giebeler L, et al. Silicon oxycarbide-derived carbons from a polyphenylsilsequioxane precursor for supercapacitor applications. Microporous Mesoporous Mater. 2014;188:140–8.

137. Vakifahmetoglu C, Presser V, Yeon S-H, Colombo P. Enhanced hydrogen and methane gas storage of silicon oxycarbide derived carbon. Microporous Mesoporous Mater. 2011;144:105–12.
138. Li J, Lu K. Highly porous SiOC bulk ceramics with water vapor assisted pyrolysis. J Am Ceram Soc. 2015;98:2357–65.
139. Narisawa M, Watase S, Matsukawa K, Dohmaru T, Okamura K. White Si-O-C(-H) particles with photoluminescence synthesized by decarbonization reaction on polymer precursor in a hydrogen atmosphere. Bull Chem Soc Jpn. 2012;85:724–6.
140. Volker P, Sun-Hwa Y, Cekdar V, Howell CA, Sandeman SR, Colombo P, et al. Hierarchical porous carbide-derived carbons for the removal of cytokines from blood plasma. Adv Healthcare Mater. 2012;1:796–800.
141. Soraru GD, Campostrini R, Ejigu AA, Zera E, Jana P. Processing and characterization of polymer derived SiOC foam with hierarchical porosity by HF etching. J Ceram Soc Jpn. 2016;124:1023–9.
142. Pan J, Pan J, Cheng X, Yan X, Lu Q, Zhang C. Synthesis of hierarchical porous silicon oxycarbide ceramics from preceramic polymer and wood biomass composites. J Eur Ceram Soc. 2014;34:249–56.
143. Choudhary A, Pratihar SK, Behera SK. Hierarchically porous biomorphic polymer derived C-SiOC ceramics. RSC Adv. 2016;6:95897–902.
144. Hassan MM, Takahashi T, Koyama K. Preparation and characterisation of SiOC ceramics made from a preceramic polymer and rice bran. J Eur Ceram Soc. 2013;33:1207–17.
145. Yan X, Sahimi M, Tsotsis TT. Fabrication of high-surface area nanoporous SiOC ceramics using pre-ceramic polymer precursors and a sacrificial template: precursor effects. Microporous Mesoporous Mater. 2017;241:338–45.
146. Vakifahmetoglu C, Balliana M, Colombo P. Ceramic foams and micro-beads from emulsions of a preceramic polymer. J Eur Ceram Soc. 2011;31:1481–90.
147. Lee EJ, Kim JJ, Cho SO. Fabrication of porous hierarchical polymer/ceramic composites by electron irradiation of organic/inorganic polymers: route to a highly durable. Large-area superhydrophobic coating. Langmuir. 2010;26:3024–30.
148. Kim Y-W, Eom J-H, Park CB, Zhai W, Guo Y, Balasubramanian M. Processing of silicon oxycarbide foams by steam chest molding and pyrolysis. J Am Ceram Soc. 2010;93:3099–101.
149. Biasetto L, Colombo P, Innocentini MDM, Mullens S. Gas permeability of microcellular ceramic foams. Ind Eng Chem Res. 2007;46:3366–72.
150. Colombo P, Bernardo E. Macro- and micro-cellular porous ceramics from preceramic polymers. Compos Sci Technol. 2003;63:2353–9.
151. Kim Y-W, Wang C, Park CB. Processing of porous silicon oxycarbide ceramics from extruded blends of polysiloxane and polymer microbead. J Ceram Soc Jpn. 2007;115:419–24.
152. Shibuya M, Takahashi T, Koyama K. Microcellular ceramics by using silicone preceramic polymer and PMMA polymer sacrificial microbeads. Compos Sci Technol. 2006;67:119–24.
153. Reschke V, Laskowsky A, Kappa M, Wang K, Bordia RK, Scheffler M. Polymer derived ceramic foams with additional strut porosity. Épìtöanyag. 2011;63:57–61.
154. Schelm K, Schwidder M, Samuel J, Scheffler F, Scheffler M. Tailored surface properties of ceramic foams for liquid multiphase reactions. Adv Eng Mater. 2017;19:1700418.
155. Adam M, Kocanis S, Fey T, Wilhelm M, Grathwohl G. Hierarchically ordered foams derived from polysiloxanes with catalytically active coatings. J Eur Ceram Soc. 2014;34:1715–25.
156. Shi Y, Wan Y, Zhai Y, Liu R, Meng Y, Tu B, et al. Ordered mesoporous SiOC and SiCN ceramics from atmosphere-assisted in situ transformation. Chem Mater. 2007;19:1761–71.
157. Yuan X, Jin H, Yan X, Cheng L, Hu L, Xue Q. Synthesis of ordered mesoporous silicon oxycarbide monoliths via preceramic polymer nanocasting. Microporous Mesoporous Mater. 2011;147:252–8.
158. Hoffmann C, Biemelt T, Seifert A, Pinkert K, Gemming T, Spange S, et al. Polymer-derived nanoporous silicon carbide with monodisperse spherical pores. J Mater Chem. 2012;22:24841–7.
159. Costacurta S, Biasetto L, Pippel E, Woltersdorf J, Colombo P. Hierarchical porosity components by infiltration of a ceramic foam. J Am Ceram Soc. 2007;90:2172–7.
160. Zampieri A, Colombo P, Mabande GTP, Selvam T, Schwieger W, Scheffler F. Zeolite coatings on microcellular ceramic foams: a novel route to microreactor and microseparator devices. Adv Mater. 2004;16:819–23.
161. Nedunchezhian S, Sujith R, Kumar R. Processing and characterization of polymer precursor derived silicon oxycarbide ceramic foams and compacts. J Adv Ceram. 2013;2:318–24.
162. da Rocha RM, Moura EAB, Bressiani JC, Bressiani AH. Effect of electron beam radiation dose on the foam formation in preceramic polymer. Radiat Phys Chem. 2010;79:301–5.
163. Colombo P, Hellmann JR, Shelleman DL. Thermal shock behavior of silicon oxycarbide foams. J Am Ceram Soc. 2002;85:2306–12.
164. Kim Y-W, Lee K-H, Lee S-H, Park CB. Fabrication of porous silicon oxycarbide ceramics by foaming polymer liquid and compression molding. J Ceram Soc Jpn. 2003;111:863–4.
165. Colombo P, Modesti M. Silicon oxycarbide ceramic foams from a preceramic polymer. J Am Ceram Soc. 1999;82:573–8.
166. Tian H, Ma Q-S. Effects of exterior gas pressure on the structure and properties of highly porous SiOC ceramics derived from silicone resin. Mater Lett. 2012;66:13–5.
167. Soltani N, Simon U, Bahrami A, Wang X, Selve S, Epping JD, et al. Macroporous polymer-derived SiO2/SiOC monoliths freeze-cast from polysiloxane and amorphous silica derived from rice husk. J Eur Ceram Soc. 2017;37:4809–20.
168. Zhang H, D'Angelo Nunes P, Wilhelm M, Rezwan K. Hierarchically ordered micro/meso/macroporous polymer-derived ceramic monoliths fabricated by freeze-casting. J Eur Ceram Soc. 2016;36:51–8.
169. Naviroj M, Miller SM, Colombo P, Faber KT. Directionally aligned macroporous SiOC via freeze casting of preceramic polymers. J Eur Ceram Soc. 2015;35:2225–32.
170. Naviroj M, Wang MM, Johnson MT, Faber KT. Nucleation-controlled freeze casting of preceramic polymers for uniaxial pores in Si-based ceramics. Scr Mater. 2017;130:32–6.
171. Grebenyuk Y, Zhang HX, Wilhelm M, Rezwan K, Dreyer ME. Wicking into porous polymer-derived ceramic monoliths fabricated by freeze-casting. J Eur Ceram Soc. 2017;37:1993–2000.
172. Liu C, Chen HZ, Komarneni S, Pantano CG. High surface area SiC/silicon oxycarbide glasses prepared from phenyltrimethoxysilane-tetramethoxysilane gels. J Porous Mater. 1996;2:245–52.

173. Feng J, Xiao Y, Jiang Y, Feng J. Synthesis, structure, and properties of silicon oxycarbide aerogels derived from tetraethylortosilicate/polydimethylsiloxane. Ceram Int. 2015;41:5281–6.
174. Pradeep VS, Zera E, Graczyk-Zajac M, Riedel R, Soraru GD. Structural design of polymer-derived SiOC ceramic aerogels for high-rate Li ion storage applications. J Am Ceram Soc. 2016;99:2977–83.
175. Aravind PR, Soraru GD. Porous silicon oxycarbide glasses from hybrid ambigels. Microporous Mesoporous Mater. 2011;142:511–7.
176. Ma J, Ye F, Lin S, Zhang B, Yang H, Ding J, et al. Large size and low density SiOC aerogel monolith prepared from triethoxyvinylsilane/tetraethoxysilane. Ceram Int. 2017;43:5774–80.
177. Nangrejo M, Bernardo E, Colombo P, Farook U, Ahmad Z, Stride E, et al. Electrohydrodynamic forming of porous ceramic capsules from a preceramic polymer. Mater Lett. 2009;63:483–5.
178. Ye C, Chen A, Colombo P, Martinez C. Ceramic microparticles and capsules via microfluidic processing of a preceramic polymer. J R Soc Interface. 2010;7:S461–73.
179. Narisawa M, Sumimoto R-I, Kita K-I, Mabuchi H, Kim YW, Sugimoto M, et al. Investigation of curing process on melt spun polymethylsilsesquioxane fiber as precursor for silicon oxycarbide fibers. Adv Mater Res. 2009;66:1–4.
180. Narisawa M, Satoh Y, Sumimoto R, Kamegawa T, Yamashita H. Synthesis of SiOC base fibers from silicone resin with low carbon content and control of surface functionality by metal chloride treatment in vapor. Mater Sci Forum. 2010;658:400–3.
181. Ichikawa H. Polymer-derived ceramic fibers. Annu Rev Mater Res. 2016;46:335–56.
182. Okamura K, Shimoo T, Suzuya K, Suzuki K. SiC-based ceramic fibers prepared via organic-to-inorganic conversion process - A review. J Ceram Soc Jpn. 2006;114:445–54.
183. Sakka S, Kamiya K. The sol-gel transition in the hydrolysis of metal alkoxides in relation to the formation of glass fibers and films. J Non-Cryst Solids. 1982;48:31–46.
184. Kamiya K, Katayama A, Suzuki H, Nishida K, Hashimoto T, Matsuoka J, et al. Preparation of silicon oxycarbide glass fibers by sol-gel method - effect of starting sol composition on tensile strength of fibers. J Sol-Gel Sci Technol. 1999;14:95–102.
185. Ruan D-S, Li Y-L, Wang L, Su D, Hou F. Fabrication of silicon oxycarbide fibers from alkoxide solutions along the sol-gel process. J Sol-Gel Sci Technol. 2010;56:184–90.
186. Nguyen VL, Proust V, Quievryn C, Bernard S, Miele P, Soraru GD. Processing, mechanical characterization, and alkali resistance of siliconboronoxycarbide (SiBOC) glass fibers. J Am Ceram Soc. 2014;97:3143–9.
187. Hu Y. Preparation of silicon oxycarbide glass fibers from organically modified silicates. J Mater Sci. 2000;35:3155–9.
188. Wang X, Gong C, Fan G. Preparation and mechanical properties of silicon oxycarbide fibers from electrospinning/sol-gel process. Mater Res Bull. 2011;46:2398–402.
189. Guo A, Roso M, Modesti M, Liu J, Colombo P. Preceramic polymer-derived SiOC fibers by electrospinning. J Appl Polym Sci. 2014;131:39810–31.
190. Chen LF, Cai ZH, Zhou W, Lan L, Chen XJ, Zeng J. Preparation and properties of silicon oxycarbide fibers. J Mater Sci. 2005;40:3497–501.
191. Tolosa A, Kruener B, Jaeckel N, Aslan M, Vakifahmetoglu C, Presser V. Electrospinning and electrospraying of silicon oxycarbide-derived nanoporous carbon for supercapacitor electrodes. J Power Sources. 2016;313:178–88.
192. Kita K, Narisawa M, Mabuchi H, Itoh M, Sugimoto M, Yoshikawa M. Formation of continuous pore structures in Si-C-O fibers by adjusting the melt spinning condition of a polycarbosilane-polysiloxane polymer blend. J Am Ceram Soc. 2009;92:1192–7.
193. Ceron-Nicolat B, Wolff F, Dakkouri-Baldauf A, Fey T, Münstedt H, Greil P. Graded cellular ceramics from continuous foam extrusion. Adv Eng Mater. 2012;14:1097–103.
194. Melcher R, Cromme P, Scheffler M, Greil P. Centrifugal casting of thin-walled ceramic tubes from preceramic polymers. J Am Ceram Soc. 2003;86:1211–3.
195. Colombo P, Perini K, Bernardo E, Capelletti T, Maccagnan G. Ceramic microtubes from preceramic polymers. J Am Ceram Soc. 2003;86:1025–7.
196. Marzolin C, Smith SP, Prentiss M, Whitesides GM. Fabrication of glass microstructures by micro-molding of sol-gel precursors. Adv Mater. 1998;10:571–4.
197. Seraji S, Wu Y, Jewell-Larson NE, Forbess MJ, Limmer SJ, Chou TP, et al. Patterned microstructure of sol-gel derived complex oxides using soft lithography. Adv Mater. 2000;12:1421–4.
198. Chan CM, Cao GZ, Stoebe TG. Net shape ceramic microcomponents by modified sol–gel casting. Microsyst Technol. 2000;6:200–4.
199. Colombo P, Schmidt J, Franchin G, Zocca A, Günster J. Additive manufacturing techniques for fabricating complex ceramic components from preceramic polymers. Am Ceram Soc Bull. 2017;96:16–23.
200. Thomas DJ. 3-D printing of polymer-derived CMCs for next-generation turbine blade manufacture. Am Ceram Soc Bull. 2017;96:28–30.
201. Zocca A, Colombo P, Gomes CM, Günster J. Additive manufacturing of ceramics: issues, potentialities, and opportunities. J Am Ceram Soc. 2015;98:1983–2001.
202. Straub M, Nguyen LH, Fazlic A, Gu M. Complex-shaped three-dimensional microstructures and photonic crystals generated in a polysiloxane polymer by two-photon microstereolithography. Opt Mater. 2005;27:359–64.
203. Friedel T, Travitzky N, Niebling F, Scheffler M, Greil P. Fabrication of polymer derived ceramic parts by selective laser curing. J Eur Ceram Soc. 2005;25:193–7.
204. Eckel ZC, Zhou C, Martin JH, Jacobsen AJ, Carter WB, Schaedler TA. Additive manufacturing of polymer-derived ceramics. Science. 2016;351:58–62.
205. Zanchetta E, Cattaldo M, Franchin G, Schwentenwein M, Homa J, Brusatin G, et al. Stereolithography of SiOC ceramic microcomponents. Adv Mater. 2016;28:370–6.
206. de Hazan Y, Penner D. SiC and SiOC ceramic articles produced by stereolithography of acrylate modified polycarbosilane systems. J Eur Ceram Soc. 2017;37:5205–12.
207. Schmidt J, Colombo P. Digital light processing of ceramic components from polysiloxanes. J Eur Ceram Soc. 2018;38:57–66.
208. Zocca A, Gomes CM, Staude A, Bernardo E, Günster J, Colombo P. SiOC ceramics with ordered porosity by 3D-printing of a preceramic polymer. J Mater Res. 2013;28:2243–52.

209. Zocca A, Elsayed H, Bernardo E, Gomes CM, Lopez-Heredia MA, Knabe C, et al. 3D-printed silicate porous bioceramics using a non-sacrificial preceramic polymer binder. Biofabrication. 2015;7:025008.
210. Scheffler M, Bordia R, Travitzky N, Greil P. Development of a rapid crosslinking preceramic polymer system. J Eur Ceram Soc. 2005;25:175–80.
211. Pierin G, Grotta C, Colombo P, Mattevi C. Direct Ink Writing of micrometric SiOC ceramic structures using a preceramic polymer. J Eur Ceram Soc. 2016;36:1589–94.
212. Windsheimer H, Travitzky N, Hofenauer A, Greil P. Laminated object manufacturing of preceramic-paper-derived Si-SiC composites. Adv Mater. 2007;19:4515–9.
213. Sieber H, Friedrich H, Zeschky J, Greil P. Light weight ceramic composites from laminated paper structures. In: Jessen T, Ustundag E, editors. *24th annual conference on composites, advanced ceramics, materials, and structures: B: ceramic engineering and science proceedings*. Hoboken, NJ: John Wiley & Sons, Inc., 2008;p. 129–34.
214. Martinez-Crespiera S, Ionescu E, Schlosser M, Flittner K, Mistura G, Riedel R, et al. Fabrication of silicon oxycarbide-based microcomponents via photolithographic and soft lithography approaches. Sens Actuators, A. 2011;169:242–9.
215. Grossenbacher J, Gullo MR, Grandjean R, Kiefer T, Brugger J. Sub micrometer ceramic structures fabricated by molding a polymer-derived ceramic. Microelectron Eng. 2012;97:272–5.
216. Nikas V, Tabassum N, Ford B, Smith L, Kaloyeros AE, Gallis S. Strong visible light emission from silicon-oxycarbide nanowire arrays prepared by electron beam lithography and reactive ion etching. J Mater Res. 2015;30:3692–9.
217. Soraru GD, Modena S, Guadagnino E, Colombo P, Egan J, Pantano C. Chemical durability of silicon oxycarbide glasses. J Am Ceram Soc. 2002;85:1529–36.
218. Kleebe H-J, Turquat C, Soraru GD. Phase separation in an SiCO glass studied by transmission electron microscopy and electron energy-loss spectroscopy. J Am Ceram Soc. 2001;84:1073–80.
219. Bai W, Widgeon S, Sen S. Structure and topological characteristics of amorphous silicon oxycarbide networks: results from reverse monte carlo simulations. J Non-Cryst Solids. 2014;386:29–33.
220. Roth F, Schmerbauch C, Ionescu E, Nicoloso N, Guillon O, Riedel R. High-temperature piezoresistive C/SiOC sensors. J Sens Sens Syst. 2015;4:133–6.
221. Roth F, Waleska P, Hess C, Ionescu E, Nicoloso N. UV Raman spectroscopy of segregated carbon in silicon oxycarbides. J Ceram Soc Jpn. 2016;124:1042–5.
222. Rosenburg F, Ionescu E, Nicoloso N, Riedel R. High-temperature raman spectroscopy of nano-crystalline carbon in silicon oxycarbide. Materials. 2018;11:1–9.
223. Kroll P. Modeling the 'free carbon' phase in amorphous silicon oxycarbide. J Non-Cryst Solids. 2005;351:1121–6.
224. Kroll P. Searching insight into the atomistic structure of SiCO ceramics. J Mater Chem. 2010;20:10528–34.
225. Nimmo JP, Kroll P. First-principles calculations and analysis of 29Si nuclear magnetic resonance chemical shifts in silicon oxycarbide ceramics. J Phys Chem C. 2014;118:29952–61.
226. Brequel H, Parmentier J, Walter S, Badheka R, Trimmel G, Masse S, et al. Systematic structural characterization of the high-temperature behavior of nearly stoichiometric silicon oxycarbide glasses. Chem Mater. 2004;16:2585–98.
227. Morcos RM, Navrotsky A, Varga T, Blum Y, Ahn D, Poli F, et al. Energetics of SixOyCz polymer-derived ceramics prepared under varying conditions. J Am Ceram Soc. 2008;91:2969–74.
228. Varga T, Navrotsky A, Moats JL, Morcos RM, Poli F, Müller K, et al. Thermodynamically stable SixOyCz polymer-like amorphous ceramics. J Am Ceram Soc. 2007;90:3213–9.
229. Chen JW, King SW, Muthuswamy E, Koryttseva A, Wu D, Navrotsky A. Thermodynamic stability of low-k amorphous SiOCH dielectric films. J Am Ceram Soc. 2016;99:2752–9.
230. Niu M, Wang HJ, Chen JW, Su L, Wu D, Navrotsky A. Structure and energetics of SiOC and SiOC-modified carbon-bonded carbon fiber composites. J Am Ceram Soc. 2017;100:3693–702.
231. Burns GT, Taylor RB, Xu Y, Zangvil A, Zank GA. High-temperature chemistry of the conversion of siloxanes to silicon carbide. Chem Mater. 1992;4:1313–23.
232. Bois L, Maquet J, Babonneau F, Bahloul D. Structural characterization of sol-gel derived oxycarbide glasses. 2. Study of the thermal stability of the silicon oxycarbide phase. Chem Mater. 1995;7:975–81.
233. Gregori G, Kleebe H-J, Blum YD, Babonneau F. Evolution of C-rich SiOC ceramics: Part II. Characterization by high lateral resolution techniques: electron energy-loss spectroscopy, high-resolution TEM and energy-filtered TEM. Int. J Mater Res. 2006;97:710–20.
234. Belot V, Corriu RJP, Leclercq D, Mutin PH, Vioux A. Organosilicon gels containing silicon-silicon bonds, precursors to novel silicon oxycarbide compositions. J Non-Cryst Solids. 1992;144:287–97.
235. Biernacki JJ, Wotzak GP. Stoichiometry of the carbon + silica reaction. J Am Ceram Soc. 1989;72:122–9.
236. Turquat C, Kleebe H-J, Gregori G, Walter S, Sorarù GD. Transmission electron microscopy and electron energy-loss spectroscopy study of nonstoichiometric silicon-carbon-oxygen glasses. J Am Ceram Soc. 2001;84:2189–96.
237. Soraru GD, Liu Q, Interrante LV, Apple T. Role of precursor molecular structure on the microstructure and high temperature stability of silicon oxycarbide glasses derived from methylene-bridged polycarbosilanes. Chem Mater. 1998;10:4047–54.
238. Sorarù GD, Suttor D. High temperature stability of sol-gel-derived SiOC glasses. J Sol-Gel Sci Technol. 1999;14:69–74.
239. Parmentier J, Soraru GD, Babonneau F. Influence of the microstructure on the high temperature behaviour of gel-derived SiOC glasses. J Eur Ceram Soc. 2001;21:817–24.
240. Breval E, Hammond M, Pantano CG. Nanostructural characterization of silicon oxycarbide glasses and glass-ceramics. J Am Ceram Soc. 1994;77:3012–8.
241. Bansal NP, Doremus RH. *Handbook of glass properties*, 1st edn. Orlando, FL: Academic Press INC.; 1986.
242. Greaves GN, Greer AL, Lakes RS, Rouxel T. Poisson's ratio and modern materials. Nat Mater. 2011;10:823–37.
243. Moysan C, Riedel R, Harshe R, Rouxel T. Mechanical characterization of a polysiloxane-derived SiOC glass. J Eur Ceram Soc. 2006;27:397–403.
244. Rouxel T, Sangleboeuf J-C, Guin J-P, Keryvin V, Soraru GD. Surface damage resistance of gel-derived oxycarbide glasses:

hardness, toughness, and scratchability. J Am Ceram Soc. 2001;84:2220–4.
245. Hetherington G, Jack KH, Kennedy JC. Viscosity of vitreous SiO2. Phys Chem Glasses. 1964;5:130–6.
246. Scarmi A, Soraru GD, Raj R. The role of carbon in unexpected visco(an)elastic behavior of amorphous silicon oxycarbide above 1273K. J Non-Cryst Solids. 2005;351:2238–43.
247. Hammond M, Breval E, Pantano CG. Microstructure and viscosity of hot pressed silicon oxycarbide glasses. Ceram Eng Sci Proc. 1993;14:947–54.
248. Cahill DG. Thermal Conductivity Data. 2014. Availabe online: http://users.mrl.illinois.edu/cahill/ tcdata/tcdata.html (accessed on 14 December 2017).
249. Stabler C, Reitz A, Stein P, Albert B, Riedel R, Ionescu E. Thermal properties of SiOC glasses and glass ceramics at elevated temperatures. Materials. 2018;11:1–18.
250. Mazo MA, Palencia C, Nistal A, Rubio F, Rubio J, Oteo JL. Dense bulk silicon oxycarbide glasses obtained by spark plasma sintering. J Eur Ceram Soc. 2012;32:3369–78.
251. Gurlo A, Ionescu E, Riedel R, Clarke DR. The thermal conductivity of polymer-derived amorphous Si-O-C compounds and nano-composites. J Am Ceram Soc. 2016;99:281–5.
252. Mazo MA, Tamayo A, Caballero AC, Rubio J. Electrical and thermal response of silicon oxycarbide materials obtained by spark plasma sintering. J Eur Ceram Soc. 2017;37:2011–20.
253. Eom J-H, Kim Y-W, Kim KJ, Seo WS. Improved electrical and thermal conductivities of polysiloxane-derived silicon oxycarbide ceramics by barium addition. J Eur Ceram Soc. 2018;38:487–93.
254. Qiu L, Li YM, Zheng XH, Zhu J, Tang DW, Wu JQ, et al. Thermal-conductivity studies of macro-porous polymer-derived SiOC ceramics. Int J Thermophys. 2014;35:76–89.
255. Cordelair J, Greil P. Electrical conductivity measurements as a microprobe for structure transitions in polysiloxane derived Si-O-C ceramics. J Eur Ceram Soc. 2000;20:1947–57.
256. Terauds K, Sanchez-Jimenez PE, Raj R, Vakifahmetoglu C, Colombo P. Giant piezoresistivity of polymer-derived ceramics at high temperatures. J Eur Ceram Soc. 2010;30:2203–7.
257. Kim KJ, Eom J-H, Kim Y-W, Seo WS. Electrical conductivity of dense, bulk silicon-oxycarbide ceramics. J Eur Ceram Soc. 2015;35:1355–60.
258. Kim KJ, Eom J-H, Koh TY, Kim Y-W, Seo WS. Effects of carbon addition on the electrical properties of bulk silicon-oxycarbide ceramics. J Eur Ceram Soc. 2016;36:2705–11.
259. Lu K, Erb D, Liu M. Thermal stability and electrical conductivity of carbon-enriched silicon oxycarbide. J Mater Chem C. 2016;4:1829–37.
260. Riedel R, Toma L, Janssen E, Nuffer J, Melz T, Hanselka H. Piezoresistive effect in SiOC ceramics for integrated pressure sensors. J Am Ceram Soc. 2010;93:920–4.
261. Soraru GD, Kacha G, Campostrini R, Ponzoni A, Donarelli M, Kumar A, et al. The effect of B-doping on the electrical conductivity of polymer-derived Si(B)OC ceramics. J Am Ceram Soc. 2017;100:4611–21.
262. Toma L, Kleebe H-J, Mueller MM, Janssen E, Riedel R, Melz T, et al. Correlation between intrinsic microstructure and piezoresistivity in a SiOC polymer-derived ceramic. J Am Ceram Soc. 2012;95:1056–61.
263. Wang YS, Zhang LG, Fan Y, Jiang D, An L. Stress-dependent piezoresistivity of tunneling-percolation systems. J Mater Sci. 2009;44:2814–9.
264. Cao Y, Yang X, Zhao R, Chen Y, Li N, An L. Giant piezoresistivity in polymer-derived amorphous SiAlCO ceramics. J Mater Sci. 2016;51:5646–50.
265. Dire S, Borovin E, Narisawa M, Soraru GD. Synthesis and characterization of the first transparent silicon oxycarbide aerogel obtained through H2 decarbonization. J Mater Chem A. 2015;3:24405–13.
266. Menapace I, Mera G, Riedel R, Erdem E, Eichel RA, Pauletti A, et al. Luminescence of heat-treated silicon-based polymers: promising materials for LED applications. J Mater Sci. 2008;43:5790–6.
267. Gallis S, Nikas V, Suhag H, Huang M, Kaloyeros AE. White light emission from amorphous silicon oxycarbide (a-SiCxOy) thin films: role of composition and postdeposition annealing. Appl Phys Lett. 2010;97:081901–3.
268. Nikas V, Gallis S, Huang M, Kaloyeros AE, Nguyen AP, Stesmans A, et al. The origin of white luminescence from silicon oxycarbide thin films. Appl Phys Lett. 2014;104:061901–4.
269. Pivin JC, Sendova-Vassileva M, Colombo P, Martucci A. Photoluminescence of composite ceramics derived from polysiloxanes and polycarbosilanes by ion irradiation. Mater Sci Eng, B. 2000;B69–70:574–7.
270. Ishikawa Y, Sato K, Kawasaki S, et al. White light emission from amorphous silicon-oxycarbide materials. Phys Status Solidi A. 2012;209:1022–5.
271. Karakuscu A, Guider R, Pavesi L, Ishii Y, Matsumura A, Muto S. Broad-band tunable visible emission of sol-gel derived SiBOC ceramic thin films. Thin Solid Films. 2011;519:3822–6.
272. Narisawa M, Kawai T, Watase S, Matsukawa K, Dohmaru T, Okamura K, et al. Long-lived photoluminescence in amorphous Si-O-C(-H) ceramics derived from polysiloxanes. J Am Ceram Soc. 2012;95:3935–40.
273. Boninelli S, Bellocchi G, Franzo G, Miritello M, Iacona F. New strategies to improve the luminescence efficiency of Eu ions embedded in Si-based matrices. J Appl Phys. 2013;113:143501–8.
274. Zhang Y, Quaranta A, Domenico Soraru G. Synthesis and luminescent properties of novel Eu2 + -doped silicon oxycarbide glasses. Opt Mater. 2004;24:601–5.
275. Gallis S, Huang M, Efstathiadis H, Eisenbraun E, Kaloyeros AE, Nyein EE, et al. Photoluminescence in erbium doped amorphous silicon oxycarbide thin films. Appl Phys Lett. 2005;87:091901–3.
276. Adam M, Vakifahmetoglu C, Colombo P, Wilhelm M, Grathwohl G. Polysiloxane-derived ceramics containing nanowires with catalytically active tips. J Am Ceram Soc. 2014;97:959–66.
277. Huang HH, Orler B, Wilkes GL. Ceramers: hybrid materials incorporating polymeric/oligomeric species with inorganic glasses by a sol-gel process. 2. Effect of acid content on the final properties. Polym Bull. 1985;14:557–64.
278. Schubert M, Wilhelm M, Bragulla S, Sun C, Neumann S, Gesing TM, et al. The influence of the pyrolysis temperature on the material properties of cobalt and nickel containing precursor derived ceramics and their catalytic use for CO2 Methanation and Fischer-Tropsch synthesis. Catal Lett. 2017;147:472–82.

279. Wilson AM, Reimers JN, Fuller EW, Dahn JR. Lithium insertion in pyrolyzed siloxane polymers. Solid State Ionics. 1994;74:249–54.
280. Wilson AM, Xing W, Zank G, Yates B, Dahn JR. Pyrolysed pitch-polysilane blends for use as anode materials in lithium ion batteries II: the effect of oxygen. Solid State Ionics. 1997;100:259–66.
281. Wilson AM, Zank G, Eguchi K, Xing W, Dahn JR. Pyrolysed silicon-containing polymers as high capacity anodes for lithium-ion batteries. J Power Sources. 1997;68:195–200.
282. Wilson AM, Zank G, Eguchi K, Xing W, Yates B, Dahn JR. Polysiloxane pyrolysis. Chem Mater. 1997;9:1601–6.
283. Xing W, Wilson AM, Eguchi K, Zank G, Dahn JR. Pyrolyzed polysiloxanes for use as anode materials in lithium-ion batteries. J Electrochem Soc. 1997;144:2410–6.
284. Xing W, Wilson AM, Zank G, Dahn JR. Pyrolysed pitch-polysilane blends for use as anode materials in lithium ion batteries. Solid State Ionics. 1997;93:239–44.
285. Ahn D, Raj R. Cyclic stability and C-rate performance of amorphous silicon and carbon based anodes for electrochemical storage of lithium. J Power Sources. 2011;196:2179–86.
286. Ahn D, Raj R. Thermodynamic measurements pertaining to the hysteretic intercalation of lithium in polymer-derived silicon oxycarbide. J Power Sources. 2010;195:3900–6.
287. Sanchez-Jimenez PE, Raj R. Lithium insertion in polymer-derived silicon oxycarbide ceramics. J Am Ceram Soc. 2010;93:1127–35.
288. Shen J, Ahn D, Raj R. C-rate performance of silicon oxycarbide anodes for Li+ batteries enhanced by carbon nanotubes. J Power Sources. 2011;196:2875–8.
289. Shen J, Raj R. Silicon-oxycarbide based thin film anodes for lithium ion batteries. J Power Sources. 2011;196:5945–50.
290. Graczyk-Zajac M, Vrankovic D, Waleska P, Hess C, Sasikumar PV, Lauterbach S, et al. The Li-storage capacity of SiOC glasses with and without mixed silicon oxycarbide bonds. J Mater Chem A. 2018;6:93–103.
291. Shi H, Yuan A, Xu J. Tailored synthesis of monodispersed nano/submicron porous silicon oxycarbide (SiOC) spheres with improved Li-storage performance as an anode material for Li-ion batteries. J Power Sources. 2017;364:288–98.
292. Xia K, Wu Z, Xuan C, Xiao W, Wang J, Wang D. Effect of KOH etching on the structure and electrochemical performance of SiOC anodes for lithium-ion batteries. Electrochim Acta. 2017;245:287–95.
293. Ma M, Wang H, Niu M, Su L, Fan X, Deng J, et al. High rate capabilities of HF-etched SiOC anode materials derived from polymer for lithium-ion batteries. RSC Adv. 2016;6:43316–21.
294. Pradeep VS, Ayana DG, Graczyk-Zajac M, Soraru GD, Riedel R. High rate capability of SiOC ceramic aerogels with tailored porosity as anode materials for Li-ion batteries. Electrochim Acta. 2015;157:41–5.
295. Fukui H, Hisashi O, Hino T, Kanamura K. A Si-O-C composite anode: high capability and proposed mechanism of lithium storage associated with microstructural characteristics. Appl Mater Interfaces. 2010;4:998–1008.
296. Fukui H, Ohsuka H, Hino T, Kanamura K. Influence of polystyrene/phenyl substituents in precursors on microstructures of Si-O-C composite anodes for lithium-ion batteries. J Power Sources. 2011;196:371–8.
297. Fukui H, Ohsuka H, Hino T, Kanamura K. Polysilane/Acenaphthylene blends toward Si–O–C composite anodes for rechargeable lithium-ion batteries. J Electrochem Soc. 2011;158:A550–5.
298. Fukui H, Eguchi K, Ohsuka H, Hino T, Kanamura K. Structures and lithium storage performance of SiOC composite materials depending on pyrolysis temperatures. J Power Sources. 2013;243:152–8.
299. Dibandjo P, Graczyk-Zajac M, Riedel R, Pradeep VS, Soraru GD. Lithium insertion into dense and porous carbon-rich polymer-derived SiOC ceramics. J Eur Ceram Soc. 2012;32:2495–503.
300. Pradeep VS, Graczyk-Zajac M, Wilamowska M, Riedel R, Soraru GD. Influence of pyrolysis atmosphere on the lithium storage properties of carbon-rich polymer derived SiOC ceramic anodes. Solid State Ionics. 2014;262:22–4.
301. Pradeep VS, Graczyk-Zajac M, Riedel R, Soraru GD. New insights in to the lithium storage mechanism in polymer derived SiOC anode materials. Electrochim Acta. 2014;119:78–85.
302. Graczyk-Zajac M, Toma L, Fasel C, Riedel R. Carbon-rich SiOC anodes for lithium-ion batteries: Part I. Influence of material UV-pre-treatment on high power properties. Solid State Ionics. 2012;225:522–6.
303. Kaspar J, Graczyk-Zajac M, Riedel R. Carbon-rich SiOC anodes for lithium-ion batteries: Part II. Role of thermal cross-linking. Solid State Ionics. 2012;225:527–31.
304. Kaspar J, Graczyk-Zajac M, Riedel R. Lithium insertion into carbon-rich SiOC ceramics: influence of pyrolysis temperature on electrochemical properties. J Power Sources. 2013;244:450–5.
305. Wilamowska M, Pradeep VS, Graczyk-Zajac M, Riedel R, Sorarù GD. Tailoring of SiOC composition as a way to better performing anodes for Li-ion batteries. Solid State Ionics. 2014;260:94–100.
306. Graczyk-Zajac M, Reinold LM, Kaspar J, Sasikumar PV, Soraru GD, Riedel R. New insights into understanding irreversible and reversible lithium storage within SiOC and SiCN ceramics. Nanomaterials. 2015;5:233–45.
307. Fukui H, Harimoto Y, Akasaka M, Eguchi K. Lithium species in electrochemically lithiated and delithiated silicon oxycarbides. ACS Appl Mater Interfaces. 2014;6:12827–36.
308. Fukui H, Ohsuka H, Hino T, Kanamura K. Silicon oxycarbides in hard-carbon microstructures and their electrochemical lithium storage. J Electrochem Soc. 2013;160:A1276–81.
309. Kaspar J, Graczyk-Zajac M, Choudhury S, Riedel R. Impact of the electrical conductivity on the lithium capacity of polymer-derived silicon oxycarbide (SiOC) ceramics. Electrochim Acta. 2016;216:196–202.
310. Wilamowska-Zawlocka M, Puczkarski P, Grabowska Z, Kaspar J, Graczyk-Zajac M, Riedel R, et al. Silicon oxycarbide ceramics as anodes for lithium ion batteries: influence of carbon content on lithium storage capacity. RSC Adv. 2016;6:104597–607.
311. Haaks M, Kaspar J, Franz A, Graczyk-Zajac M, Riedel R, Vogel M. 7Li NMR studies of lithium ion dynamics in polymer-derived silicon oxycarbide ceramics. Solid State Ionics. 2016;287:28–35.
312. Kaspar J, Graczyk-Zajac M, Riedel R. Determination of the chemical diffusion coefficient of Li-ions in carbon-rich silicon oxycarbide anodes by electro-analytical methods. Electrochim Acta. 2014;115:665–70.

313. Kroll P. Tracing reversible and irreversible li insertion in SiCO Ceramics with modeling and Ab-Initio simulations. MRS Online Proc Libr. 2011;1313:1–6.
314. Liao N, Zheng B, Zhang M, Xue W. Atomic investigation on reversible lithium storage in amorphous silicon oxycarbide as a high power anode material. J Mater Chem A. 2016;4:12328–33.
315. Liao N, Zheng B, Zhou H, Xue W. Lithiation behavior of high capacity SiCO anode material for lithium-ion battery: a first principle study. Electrochim Acta. 2015;156:115–20.
316. Liao N, Zheng B, Zhou H, Xue W. Effect of carbon segregation on performance of inhomogeneous SiCyO6/5 as anode materials for lithium-ion battery: a first-principles study. J Power Sources. 2016;334:39–43.
317. Wilhelm M, Soltmann C, Koch D, Grathwohl G. Ceramers-functional materials for adsorption techniques. J Eur Ceram Soc. 2004;25:271–6.
318. Pan J, Ren J, Xie Y, Wei X, Guan Y, Yan X, et al. Porous SiOC composites fabricated from preceramic polymers and wood powders for efficient dye adsorption and removal. Res Chem Intermed. 2017;43:3813–32.
319. Zeydanli D, Akman S, Vakifahmetoglu C. Polymer-derived ceramic adsorbent for pollutant removal from water. J Am Ceram Soc. 2018;101:2258–65.
320. Bruzzoniti MC, Appendini M, Rivoira L, Onida B, Del Bubba M, Jana P, et al. Polymer-derived ceramic aerogels as sorbent materials for the removal of organic dyes from aqueous solutions. J Am Ceram Soc. 2018;101:821–30.
321. Wilhelm M, Adam M, Baeumer M, Grathwohl G. Synthesis and properties of porous hybrid materials containing metallic nanoparticles. Adv Eng Mater. 2008;10:241–5.
322. Yu Z, Li S, Zhang P, Feng Y, Liu X. Polymer-derived mesoporous Ni/SiOC(H) ceramic nanocomposites for efficient removal of acid fuchsin. Ceram Int. 2017;43:4520–6.
323. Prenzel T, Wilhelm M, Rezwan K. Pyrolyzed polysiloxane membranes with tailorable hydrophobicity, porosity and high specific surface area. Microporous Mesoporous Mater. 2013;169:160–7.
324. Juttke Y, Richter H, Voigt I, Prasadb RM, Bazarjanib MS, Gurlob A, et al. Polymer derived ceramic membranes for gas separation. Chem Eng Trans. 2013;32:1891–6.
325. Prasad RM, Juettke Y, Richter H, Voigt I, Riedel R, Gurlo A. Mechanism of gas separation through amorphous silicon oxycarbide membranes. Adv Eng Mater. 2016;18:721–7.
326. Karakuscu A, Ponzoni A, Aravind PR, Sberveglieri G, Soraru GD. Gas sensing behavior of mesoporous SiOC glasses. J Am Ceram Soc. 2013;96:2366–9.
327. Karakuscu A, Ponzoni A, Ayana D, Soraru GD, Sberveglieri G. High carbon-high porous SiOC glasses for room temperature NO2 sensing. Procedia Eng. 2014;87:160–3.
328. Vakifahmetoglu C, Buldu M, Karakuscu A, Ponzoni A, Assefa D, Soraru GD. High surface area carbonous components from emulsion derived SiOC and their gas sensing behavior. J Eur Ceram Soc. 2015;35:4447–52.
329. Tamayo A, Pena-Alonso R, Rubio J, Raj R, Sorarù GD, Oteo JL. Surface energy of sol gel-derived silicon oxycarbide glasses. J Am Ceram Soc. 2011;94:4523–33.
330. Khalilpour P, Lampe K, Wagener M, Stigler B, Heiss C, Ullrich MS, et al. Ag/SiOxCy plasma polymer coating for antimicrobial protection of fracture fixation devices. J Biomed Mater Res, Part B. 2010;94B:196–202.
331. Lagonegro P, Rossi F, Galli C, Smerieri A, Alinovi R, Pinelli S, et al. A cytotoxicity study of silicon oxycarbide nanowires as cell scaffold for biomedical applications. Mater Sci Eng, C. 2017;73:465–71.
332. Gaweda M, Jelen P, Dlugon E, Wajda A, Leśniak M, Simka W, et al. Bioactive layers based on black glasses on titanium substrates. J Am Ceram Soc. 2018;101:590–601.
333. Zhuo R, Colombo P, Pantano C, Vogler EA. Silicon oxycarbide glasses for blood-contact applications. Acta Biomater. 2005;1:583–9.
334. Bokros JC. Carbon biomedical devices. Carbon. 1977;15:353–71.
335. Bokros JC. Carbon in medical devices. Ceram Int. 1983;9:3–7.
336. Bachar A, Mercier C, Tricoteaux A, Leriche A, Follet C, Hampshire S. Bioactive oxynitride glasses: synthesis, structure and properties. J Eur Ceram Soc. 2016;36:2869–81.
337. Tamayo A, Ruiz-Caro R, Mazo A, Veiga-Ochoa MD, Rubio J. Chemical oxidation of silicon oxycarbide ceramics for advanced drug delivery systems. J Mater Sci. 2016;51:1382–91.
338. Tamayo A, Mazo MA, Ruiz-Caro R, Martín-Illana A, Bedoya LM, Veiga-Ochoa MD, et al. Mesoporous silicon oxycarbide materials for controlled drug delivery systems. Chem Eng J (Amsterdam, Neth). 2015;280:165–74.
339. Tamayo A, Mazo MA, Veiga MD, Ruiz-Caro R, Notario-Pérez F, Rubio J. Drug kinetics release from Eudragit - Tenofovir@SiOC tablets. Mater Sci Eng, C. 2017;75:1097–105.
340. Vakifahmetoglu C, Zeydanli D, Ozalp VC, Borsa BA, Soraru GD. Hierarchically porous polymer derived ceramics: a promising platform for multidrug delivery systems. Mater Des. 2018;140:37–44.
341. Tavakoli AH, Campostrini R, Gervais C, Babonneau F, Bill J, Soraru GD, et al. Energetics and structure of polymer-derived Si-(B-)O-C glasses: effect of the boron content and pyrolysis temperature. J Am Ceram Soc. 2014;97:303–9.
342. Tavakoli AH, Armentrout MM, Narisawa M, Sen S, Navrotsky A. White Si-O-C ceramic: structure and thermodynamic stability. J Am Ceram Soc. 2015;98:242–6.

AUTHOR BIOGRAPHIES

Christina Stabler Christina Stabler has been a PhD candidate at the Institute of Materials Science at the Technical University of Darmstadt since 2014. She received her Master of Science in Geoscience with specialization in Applied Minerology in 2013 at the Institute of Mineralogy at the Friedrich-Alexander University of Erlangen-Nuremberg, where she spent 1 year as research fellow after her graduation. Her current research interests are focused on the assessment of the (thermo)mechanical and thermal properties of silicon oxycarbides at high temperatures.

Emanuel Ionescu Emanuel Ionescu has been Senior Researcher and Docent at the Institute for Materials Science of Darmstadt University of Technology since 2006. He studied Chemistry and Physics at the University Bucharest and at Braunschweig University of Technology and received his PhD degree in Inorganic Chemistry in 2005 from the University of Bonn. In 2015, he finished his Habilitation at Darmstadt University of Technology in the field of Ceramic Nanocomposites and received his *venia legendi*. His scientific background and interests relate in general to (inorganic) materials synthesis and processing and in particular to the development of advanced ceramics with tailor-made chemical/phase compositions, morphologies, microstructures and property profiles for structural applications (construction materials, high-temperature resistant materials, materials for extreme, harsh environmental conditions) as well as for energy-related, environmental or biomedical applications. Dr. Ionescu authored and co-authored more than 115 publications, among them more than 95 papers in peer-reviewed journals, more than 10 books and book chapters and three patents as well as gave more than 60 invited talks at domestic and international conferences and workshops. He served as Guest Editor for numerous Special Issues related to advanced materials synthesis and ceramics in various journals such as *J. Eur. Ceram. Soc.*, *J. Ceram. Soc. Jpn.*, *Nanomaterials*, *Soft Materials* etc. and has been currently Topic Editor for "*Nanophase Materials and Nanoceramics*" of the journal *Nanomaterials and Nanotechnology*. He is member of the American Ceramic Society, German Materials Society (DGM) and German Chemical Society (GdCh).

Magdalena Graczyk-Zajac Magdalena Graczyk-Zajac graduated in Chemistry from Gdansk University of Technology, Poland. In 2006 she received a PhD degree in Physical Chemistry. This work on functional conducting polymers for the application in catalysis and solar energy conversion was realized at Burgundy University, Dijon, France. From 2007 to 2008 she worked on the development of new materials for Li-ion batteries in Laboratory of Components for Energy, CEA, Grenoble, France. Since June 2008 she has been a postdoctoral research associate in the Institute of Materials Science, Technische Universität Darmstadt, Germany. Polymer-derived ceramics with tailored properties for the application in Li-ion, Na-ion and Li-S batteries are in the focus of her scientific interest. The correlation between the microstructure of ceramics and their charge storage properties is one of the main topics of her research.

Isabel Gonzalo-Juan Isabel Gonzalo-Juan received her B.A. in chemistry from University of Valladolid, Spain. She earned her M.S. and Ph. D. degrees from the Autonoma University of Madrid (Spain) in the Ceramic & Glass Institute of the Spanish National Research Council (ICV-CSIC) in 2008 and 2010, respectively. From 2010 to 2012, Dr. Gonzalo-Juan held a postdoctoral research fellowship at Vanderbilt University (USA), where she worked with Prof. James Dickerson. Thereafter, she joined the Department of Materials Science at the Technical University of Darmstadt (Germany) under Prof. Ralf Riedel. She is now working on her habilitation in the fields of development of 1) a wide variety of visible-light-active photocatalytic materials for energy conversion and environmental remediation and 2) bioactive materials for regenerative medicine and therapeutic applications. Her current research involves materials synthesis, development of new processing techniques and advanced materials characterization.

Ralf Riedel Prof. Riedel got a PhD degree in Inorganic Chemistry in 1986 at the University of Stuttgart. After a Postdoc period at the Max-Planck Institute for Metals Research in Stuttgart, he became Full Professor at the Institute of Materials Science at the Technical University of Darmstadt in 1993. He is an elected member of the World Academy of Ceramics, Fellow of the American Ceramic Society, the European Ceramic Society as well as Fellow of the School of Engineering at The University of Tokyo in Japan. Prof. Riedel was awarded with the Gold Medal for Merits in Natural Sciences and with a honorary doctorate of the Slovak Academy of Science as well as with the Gustav

Tammann Prize of the German Society of Materials Science (DGM). In 2009, he received an honorary Professorship at the Tianjin University in Tianjin, China. He is Guest Professor at the Jiangsu University in Zhenjiang and at the Xiamen University in China. Presently, Prof. Riedel holds an Adjunct Professorship at the Northwestern Polytechnical University in Xi´an and is Professor at the Frontier Research Institute for Materials Science, Nagoya Institute of Technology (NIT), Nagoya, Japan. is Editor in Chief of the *Journal of The American Ceramic Society* and of *Ceramics International*. His current research interest is focused on two main research areas, namely i) synthesis and structural and functional properties of advanced ceramics as well as ii) ultrahigh pressure materials synthesis.

How to cite this article: Stabler C, Ionescu E, Graczyk-Zajac M, Gonzalo-Juan I, Riedel R. Silicon oxycarbide glasses and glass-ceramics: "All-Rounder" materials for advanced structural and functional applications. *J Am Ceram Soc*. 2018;101:4817–4856. https://doi.org/10.1111/jace.15932

Journal of the European Ceramic Society 39 (2019) 2287–2296

Contents lists available at ScienceDirect

Journal of the European Ceramic Society

journal homepage: www.elsevier.com/locate/jeurceramsoc

Original Article

Effect of composition and high-temperature annealing on the local deformation behavior of silicon oxycarbides

Christina Stabler[a], Fabrice Celarie[b], Tanguy Rouxel[b], René Limbach[c], Lothar Wondraczek[c], Ralf Riedel[a], Emanuel Ionescu[a,*]

[a] Technische Universität Darmstadt, Institute of Materials Science, Otto-Berndt-Str. 3, D-64287, Darmstadt, Germany
[b] University of Rennes 1, Campus Beaulieu, Physics Institute, IPR UMR UR1-CNRS 6251, Glass and Mechanics Department, 35042, Rennes cedex, France
[c] University of Jena, Otto Schott Institute of Materials Research, Fraunhoferstr. 6, D-07743, Jena, Germany

ARTICLE INFO

Keywords:
Silicon oxycarbide
Elastic properties
Poisson's ratio
Plastic deformation
Thermal annealing

ABSTRACT

Silicon oxycarbides with varying compositions were investigated concerning their elastic and plastic properties. Additionally, the impact of thermal annealing on their elastic properties was assessed. Phase separation of SiOC seems to have no significant impact on Young's modulus (high values of β-SiC compensate the low values of the vitreous silica matrix) and hardness. However, it leads to an increase in Poisson's ratio, indicating an increase in the atomic packing density. The phase composition of SiOC significantly influences Young's modulus, hardness, brittleness and strain-rate sensitivity: the amount of both β-SiC and segregated carbon governs Young's modulus and hardness, whereas the fraction of free carbon determines brittleness and strain-rate sensitivity. Thermal annealing of SiOC glass-ceramics leads to an increase in Young's modulus. However, the temperature sensitivity of Young's modulus and Poisson's ratio is not affected, indicating the glassy matrix being stable during thermal annealing. A slightly improved ordering of the segregated carbon and the β-SiC nanoparticles upon thermal annealing was observed. It is suggested that this is responsible for the increase in Young's modulus.

1. Introduction

Amorphous silicon oxycarbides (SiOC) can basically be regarded as SiO_2 glasses which are mechanically strengthened by the presence of tetrahedrally coordinated carbon atoms. Their synthesis relies on the thermal conversion of polyorganosiloxanes or precursors derived from sol-gel synthesis of organically modified alkoxysilanes [1,2]. Via this procedure, SiOC glasses with varying chemical compositions are obtainable. Depending on the carbon content, a distinction is usually made between two groups of amorphous SiOC materials, i.e., glasses with low amounts of segregated carbon and carbon-rich compositions (i.e. > 20 wt.% segregated carbon [1,3,4]). The chemical composition of SiOC glasses determines their structural and functional properties. Due to the remarkable high temperature stability, with a notable resistance against crystallization up to about 1500 °C [1], SiOC glasses have attracted a growing attention for applications in combustion engines or as coatings on turbine blades. In these, knowledge on the elastic properties and plasticity of SiOC glasses, like their Young's modulus, brittleness, hardness or creep behavior, is inevitable. In particular, this includes information on the mechanical performance under extreme conditions of high temperatures and extended exposure times.

SiOC glasses are X-ray amorphous and built-up of corner-sharing $SiO_{4-x}C_x$ tetrahedral units (SiO_4, SiO_3C, SiO_2C_2, $SiOC_3$ and SiC_4) [5,6]. The abundance of each tetrahedral unit depends on the chemical composition and thus, the polymeric precursor used for the glass preparation. In addition to the covalently bonded C linked to Si (network carbon), typical SiOC glasses also contain a sp^2-hybridized segregated carbon phase, which is homogeneously dispersed in the SiOC glass matrix [7,8]. At temperatures above 1250 °C, phase separation of the amorphous SiOC glass starts, as evident from the vanishing signals for SiO_3C, SiO_2C_2 and $SiOC_3$ tetrahedral units in the ^{29}Si MAS NMR spectra [7,9]. This phase separation results in the formation of SiOC glass-ceramics within the system SiO_2-SiC-C, where the residual glass matrix is composed of SiO_2 with homogeneously dispersed β-SiC nanoparticles and segregated carbon. Controlling the polymeric precursor along with the synthesis conditions enables the preparation of SiOC materials with a tailored microstructure.

The partial substitution of two-fold coordinated O atoms by four-fold coordinated C atoms in SiOC glasses is known to improve the glass network connectivity and, by extension, to enhance the thermal and mechanical stability. In comparison to vitreous silica, SiOC glasses typically exhibit higher Young's modulus, hardness and glass transition

* Corresponding author.
E-mail address: ionescu@materials.tu-darmstadt.de (E. Ionescu).

https://doi.org/10.1016/j.jeurceramsoc.2019.02.024
Received 30 September 2018; Received in revised form 7 January 2019; Accepted 11 February 2019
Available online 12 February 2019
0955-2219/

temperature [10–14]. Similar trends have previously been reported also for SiOC glass-ceramics [15–18]. Although the creep rates and viscosity of SiOC glass-ceramics have been found as being determined by both the chemical composition and phase composition [17,19], information on the influence of the chemical composition and phase composition on the elastic properties of SiOC glass-ceramics remains limited. Moreover, only little is known about the impact of annealing on the elastic properties of SiOC glasses and glass-ceramics. Rouxel et al. [11] studied the Young's modulus of a SiOC glass during a thermal treatment at temperatures up to 1400 °C. Upon the phase separation above 1250 °C, an irreversible increase of Young's modulus was observed, which has been attributed to the precipitation of β-SiC nanoparticles. Beside the technological significance of these findings, there is a fundamental interest on the underlying structural changes inside the glass network. Since the Young's modulus is intimately related to the atomic structure of glasses, i.e., strength and density of the interatomic bonds [20], it can serve as an indicator for structural modifications inside the glass network during annealing or even high-temperature creep experiments [11].

Here, we report on the elastic properties and plasticity of a SiOC glass as well as a series of SiOC glass-ceramics with varying chemical and phase compositions. For selected SiOC glass-ceramics, the elastic properties were also monitored up to temperatures of around 1000 °C. This has also been done for SiOC glass-ceramics, which have been subjected to a prior thermal treatment comparable to previous high temperature creep experiments performed on these SiOC glass-ceramics [18,19].

2. Experimental procedure

2.1. Materials synthesis and processing

The synthesis procedure of the investigated SiOC glass and glass-ceramics is described in detail in Refs. [18] and [21]. Different polymeric precursors were used to realize a series of SiOC materials with various amounts of segregated carbon. This includes one sample with no segregated carbon phase (denoted as **SiC/SiO_2**), and further samples which contain approximately 1, 12 and 16 vol.% of segregated carbon, respectively (denoted as **C1-SiOC**, **C12-SiOC**, and **C16-SiOC**). **SiC/SiO_2** glass powder was prepared by pyrolysis of polysilsesquioxane in hydrogen atmosphere [22]. **C1-SiOC** was prepared by a sol-gel synthesis of triethoxysilane and methyldiethoxysilane in a 2:1 M ratio, followed by ageing and pyrolysis [9]. **C12-SiOC** was synthesized via cross-linking and pyrolysis of a commercially available polysilsesquioxane (Belsil PMS MK, Wacker GmbH, Burghausen, Germany). **C16-SiOC** was prepared by a catalyzed sol-gel synthesis of a mixture consisting of 80 wt.% polymethylhydrosiloxane (PMHS; average M_n 1700–3200; Merck, Germany) and 20 wt.% 1,3,5,7-tetramethyl-1,3,5,7-tetravinylcyclotetrasiloxane (D_4Vi; 97%, ABCr, Karlsruhe, Germany), followed by ageing and pyrolysis [23]. The synthesized powders were ground and sieved (particle diameter < 40 µm) and were subsequently densified for 30 min at a temperature of 1600 °C and a pressure of 50 MPa using a uniaxial hot press operating in a static argon atmosphere (these samples were used for nanoindentation). Alternatively, the densification was achieved using a Field Assisted Sintering Technique (FAST). Here, the powders were treated at the same temperature and pressure but for only 15 min in argon atmosphere. The samples prepared by the latter routine were used in the Resonant Frequency Damping Analyzer (RFDA). The final monolithic samples are further denoted as **SiC/SiO_2-1600**, **C1-SiOC-1600**, **C12-SiOC-1600** and **C16-SiOC-1600**, respectively.

Additionally, one monolithic SiOC glass (denoted as **C1-SiOC-1100**) was prepared from a sol-gel derived precursor of triethoxysilane and methyldiethoxysilane in a 2:1 M ratio. The precursor was cast in plastic boxes, followed by curing and drying. The resulting monolithic xerogels were pyrolyzed in an alumina tube furnace for 3 h at 1100 °C in argon atmosphere (heating rate of 25 °C/h). Details on the preparation of **C1-SiOC-1100** are reported in [21].

Thermal treatment of the SiOC glass-ceramics were performed for different durations at temperatures of 1100, 1200 and 1300 °C, respectively, in an alumina oven with SiC heating elements using alumina crucibles with a closed lid under air. The applied heating rate was 20 °C/min up to 50 °C below the target temperature, followed by a slower rate of 2 °C/min up to the desired annealing temperature. The subsequent cooling was performed at a rate of 10 °C/min.

2.2. Structural characterization

All samples were cut into smaller pieces using a diamond wire cutter and subsequently ground to co-planar geometry. Their chemical composition was determined using a carbon analyzer Leco-200 (Leco Corporation,USA) and a N/O analyzer Leco TC-436 (Leco Corporation, USA). The silicon elemental content was calculated as the difference to 100 wt.%, assuming no other elements being present in the samples. Archimedean (skeletal) density ρ and open porosity were derived upon water immersion technique. Powder X-ray diffraction (XRD) measurements were performed in flat-sample transmission geometry on a STOE STADI P diffractometer (Stoe, Darmstadt, Germany), equipped with a Mo X-ray tube and a position sensitive detector with a 6° aperture. Raman spectra were recorded on a Horiba HR800 micro-Raman spectrometer (Horiba JobinYvon, Bensheim, Germany), equipped with a He-Ne laser (λ = 633 nm). The measurements were conducted by using a grating of 600 g/mm and a confocal microscope (magnification 50 x NA0.75 – numerical aperture) with a 100 µm aperture, providing a resolution of approximately 1 µm. The laser power of 20 mW was attenuated by using neutral density filters.

2.3. Assessment of the elastic and plastic deformation behavior

Nanoindentation experiments were carried out on co-planar, optically polished samples using a G200 nanoindenter (Agilent Inc.), equipped with a three-sided Berkovich diamond indenter tip (Synton-MDP Inc.). Before the first experiments, both the tip area function and the instrument's frame compliance were calibrated on a Corning 7980 fused silica reference glass sample (Corning Inc.), following the procedure proposed by Oliver and Pharr [24]. Depth profiles of the Young's modulus E and hardness H were obtained by operating in the continuous stiffness measurement mode [25,26]. For statistical relevance, at least ten indentations with a maximum displacement of 2 µm were created at a constant strain-rate of $\dot{\varepsilon} = 0.05\ s^{-1}$ (defined as the loading rate dP/dt divided by the actual load P). The strain-rate sensitivity m was analyzed via a nanoindentation strain-rate jump test as described in detail in Ref. [27]. In total, ten strain-rate jump tests with strain-rates of $\dot{\varepsilon} = 0.05$; 0.007 and 0.001 s^{-1} (in descending order) were performed. Values of m were derived from the slope of the linear regression between the logarithm of hardness and the logarithm of the indentation strain-rate (defined as the displacement rate dh/dt divided by the actual indentation depth h) $m = \partial \ln H / \partial \ln \dot{\varepsilon}_i$ [28], where $\dot{\varepsilon}_i = \dot{\varepsilon}/2$ for materials with a depth-independent hardness [29]. All nanoindentation experiments were carried out in laboratory air at ambient temperatures of around 301 ± 3 K and with thermal drift rates below 0.05 s^{-1}. To avoid interactions between residual stress fields, consecutive indentations were conducted at distances of 50 µm [30]. The same samples were subsequently utilized to study the elastic properties through ultrasonic echography with an Echometer 1077 (Karl Deutsch GmbH & Co. KG, Wuppertal, Germany). Values of the longitudinal c_L and transversal sound wave velocities c_T were calculated from the corresponding sound wave propagation times, as recorded with an accuracy of ± 1 ns by piezoelectric transducers operating at frequencies of 8 to 12 MHz, divided by the exact thickness of the glass plates, which was determined with an accuracy of ± 2 µm using a micrometer screw. On that basis, the shear modulus G, bulk modulus K, and Young's modulus,

as well as the Poisson's ratio ν, were estimated according to the following equations [31]:

$$G = \rho c_T^2 \quad (1)$$

$$K = \rho\left(c_L^2 - \frac{4}{3}c_T^2\right) \quad (2)$$

$$E = \rho\left[\frac{3c_L^2 - 4c_T^2}{(c_L/c_T)^2 - 1}\right] \quad (3)$$

$$\nu = \frac{c_L^2 - 2c_T^2}{2(c_L^2 - c_T^2)} \quad (4)$$

In addition, the temperature dependence of the Young's modulus and shear modulus were evaluated using a RFDA (IMCE NV RFDA HT 1050) on co-planar disk-like samples or rectangular bars with an approximate thickness of 2 mm. Samples were fixed with Pt-Rh wires and heated to 1000 °C at a rate of 10 °C/min in air. The subsequent cooling was carried out at a rate of 10 °C/h.

The investigation of the samples with both, RFDA and Ultrasonic Echography, requires sufficiently large specimens to be reliably fixed in the device or to detect the signal, respectively. The required minimum sample geometries could not be realized for samples **C1-SiOC-1100** (due to the inherent challenges during the polymer-to-ceramic transformation) and **SiC/SiO$_2$-1600** (due to a limited amount of starting material). Consequently, the mentioned two methods were used only for samples meeting the respective requirements (see Table 1 below).

3. Results and discussion

The as-prepared SiOC samples were first analyzed concerning their chemical and phase composition. For a detailed compositional and structural characterization the reader is referred to Refs. [18] and [21]. The monolithic sample pyrolyzed at 1100 °C (i.e., **C1-SiOC-1100**) is fully X-ray amorphous and consists of an SiOC glass matrix with a homogeneously dispersed phase of sp^2-hybridized segregated carbon [5]. The monolithic specimens prepared from hot pressing/FAST at 1600 °C can be regarded as SiOC glass-ceramics composed of a vitreous silica matrix with homogeneously dispersed β-SiC nanoparticles and segregated carbon [5,17,18]. The phase composition in the system SiO$_2$-SiC-C can be estimated from elemental analysis [6]. The chemical and phase compositions of the samples investigated in the present study are summarized in Table 1 and presented in Fig. 1. The volume fractions of SiO$_2$ and SiC for **C1-SiOC-1100** can be regarded as the fraction of Si-O and Si-C bonds, respectively. The volume fraction of SiC is comparable in all samples. This is also evident from Fig. 1, where the compositions investigated in this study lie on a parallel line to the SiO$_2$-C tie-line in the Si-O-C ternary phase diagram. No segregated carbon was noticed in the **SiC/SiO$_2$-1600** sample. By comparing **C1-SiOC-1100** with **C1-SiOC-1600**, it can be concluded that the phase separation has no influence on the overall chemical composition (e.g., through volatilization).

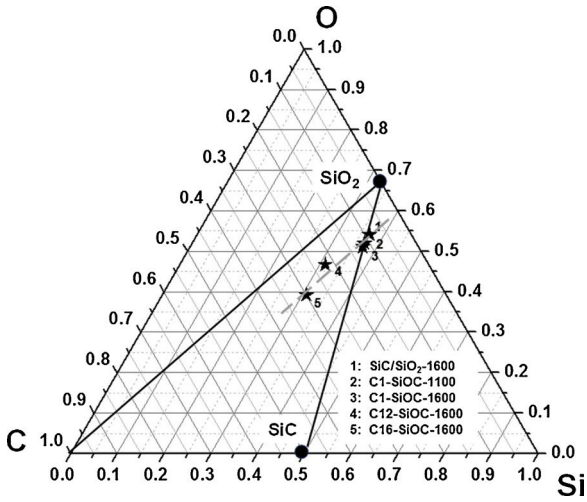

Fig. 1. Ternary phase diagram in the system Si-O-C. The dashed line (parallel to the SiO$_2$-C tie-line) marks that the segregated carbon content increases from **SiC/SiO$_2$-1600** to **C16-SiOC-1600** without large variations in the SiC content.

The skeletal densities of the investigated SiOC samples are summarized in Table 1. Replacing oxygen in the SiO$_2$ network by carbon leads to an increase in density from 2.20 up to 2.28 g/cm^3 in the **C1-SiOC-1100** glass specimen. The further increase in density from 2.28 to 2.36 g/cm^3 is caused by the phase separation in the **C1-SiOC-1600** sample and the accompanied precipitation of β-SiC nanoparticles (with a bulk density of 3.21 g/cm^3 for crystalline β-SiC [32]).

Along with the density, the Young's modulus is significantly enhanced upon the incorporation of carbon into vitreous silica (Table 2). The same trend has already been revealed in previous studies [10,14,33], where it was attributed to the increased degree of cross-linking within the silica glass network [34]. This effect even compensates the significantly lower energy of the Si-C interatomic bonds (U_0 = 447 kJ/mol) compared to the strong Si-O interatomic bonds (U_0 = 800 kJ/mol) in vitreous silica [34]. Besides, phase separation does not seem to significantly alter Young's modulus. Actually, a change in Young's modulus during phase separation might be expected due to the reorganization of the network carbon in β-SiC nanoparticles and the accompanied formation of an oxygen-rich silica matrix. As a result, Young's modulus should decrease during phase separation, getting closer to the value of vitreous silica. However, Young's modulus of glass-ceramics is expected to be an additive function of the constituting phases and their respective volume fractions and properties [35,36]. The comparably high Young's moduli of SiOC glass-ceramics are therefore a consequence of the high Young's modulus of the β-SiC

Table 1
Chemical compositions of the monolithic SiOC samples, their estimated phase compositions and the corresponding skeletal densities ρ. Volume fractions of SiO$_2$, SiC and segregated carbon C$_{segr}$ are calculated by means of the following densities: ρ(SiO$_2$) = 2.20 g/cm^3 [15], ρ(β-SiC) = 3.22 g/cm^3 [32], ρ(C$_{segr}$) = 1.82 g/cm^3 (Graphitized Mesoporous Carbons GMC, Sigma-Aldrich, CAS-# 1333-86-4).

Sample	Empirical Formulae	Phase Composition [mol%]			Phase Composition [vol.%]			Density ρ [g/cm^3]
		SiO$_2$	SiC	C$_{segr}$	SiO$_2$	SiC	C$_{segr}$	
C1-SiOC-1100 [21]	$SiO_{1.38}C_{0.32}$	68.1[1] ± 1.1	30.7[1] ± 2.3	1.2[1] ± 0.5	81.7[2] ± 1.3	17.9[2] ± 1.3	0.4[2] ± 0.9	2.28
SiC/SiO$_2$-1600 [18]	$SiO_{1.47}C_{0.24}$	73.2	26.8	0	85.7	14.3	0	2.36
C1-SiOC-1600 [21]	$SiO_{1.41}C_{0.30}$	70.2 ± 0.5	29.3 ± 2.1	0.5 ± 2.7	83.0 ± 0.6	16.8 ± 1.2	0.2 ± 0.8	2.38
C12-SiOC-1600 [21]	$SiO_{1.50}C_{0.71}$	51.3 ± 0.3	17.2 ± 1.4	31.5 ± 1.7	75.7 ± 0.4	12.3 ± 1.0	11.9 ± 0.7	2.31
C16-SiOC-1600 [21]	$SiO_{1.27}C_{0.97}$	39.6 ± 1.1	22.8 ± 1.7	37.6 ± 1.7	65.7 ± 1.9	18.3 ± 1.3	16.0 ± 0.7	2.34

[1] Molar fractions of SiO$_2$ and SiC can be regarded as the fraction of Si-O and Si-C bonds, respectively.
[2] Volume fractions of SiO$_2$ and SiC can be regarded as the fraction of Si-O and Si-C bonds, respectively. Absolute values are expected to be shifted due to unknown density of the disordered arrangement of SiC$_4$ tetrahedra.

Table 2
Room temperature elastic properties and plasticity of SiOC glasses and glass-ceramics: Young's modulus E, shear modulus G, bulk modulus K, Poisson's ratio υ, hardness H and strain-rate sensitivity m. Literature data for a SiOC glass and Suprasil vitreous silica are added for comparison.

Sample	RFDA			Ultrasonic Echography				Nanoindentation		
	E [GPa]	G [GPa]	ν	E [GPa]	G [GPa]	K [GPa]	ν	E [GPa]	H [GPa]	m
C1-SiOC-1100	–	–	–	–	–	–	–	101.7 ± 0.5	11.4 ± 0.1	0.0059
C12-SiOC-1100 [[14]]	–	–	–	96.1 ± 0.5	–	–	0.110 ± 0.020	101* ± 15	6.4* ± 1	–
SiO_2 (Suprasil) [[31]]	–	–	–	70.0	39.9	35.4	0.170	71.6 ± 0.3	9.3 ± 0.1	0.0068
SiO_2/SiC-1600	–	–	–	–	–	–	–	92.8 ± 1.2	10.6 ± 0.2	0.0060
C1-SiOC-1600	96 ± 1.0	41	0.18	100.2 ± 1.3	42.7 ± 0.2	51.4 ± 0.6	0.175 ± 0.003	101.1 ± 0.8	11.0 ± 0.1	0.0074
C12-SiOC-1600	86 ± 1.0	37	0.17	87.6 ± 1.1	37.6 ± 0.2	43.7 ± 0.6	0.166 ± 0.003	90.4 ± 1.0	10.5 ± 0.1	0.0107
C16-SiOC-1600	99	–	–	92.8 ± 1.0	39.7 ± 0.2	46.5 ± 0.5	0.167 ± 0.002	96.6 ± 1.8	10.6 ± 0.2	–

* Value displays the Vickers microhardness H_V as determined by Vickers microhardness testing.

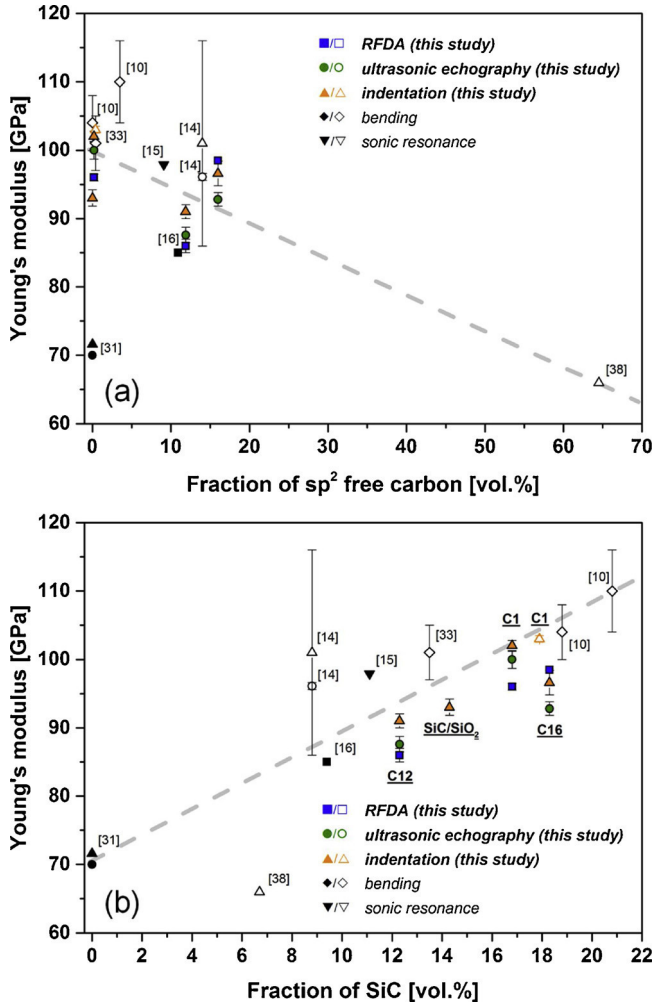

Fig. 2. Room temperature Young's modulus of SiOC glasses (open symbols) and glass-ceramics (filled symbols) as a function of (a) volume fraction of sp^2-hybridized segregated carbon and (b) the volume fraction of Si-C bonds (as for SiOC glasses) or ß-SiC (as for SiOC glass-ceramics). Literature values (black symbols) are added for comparison. Dashed lines were drawn as a guide for the eyes.

nanoparticles (E = 300 GPa [37]), compensating the smaller value of the vitreous silica matrix. The present data of the Young's modulus for the SiOC glass-ceramics are of similar magnitude as previously reported values for SiOC glasses [15,16].

Fig. 2a compares the available literature data for Young's modulus of SiOC materials at ambient temperature to the values determined in this study. Depending on the experimental technique used, Young's modulus of the SiOC samples with identical compositions varies within a range of ± 5 GPa (i.e., ± 5%). Also, some of the literature values derived from bending or indentation experiments display relatively large standard deviations [10,14,33]. However, a rough tendency is discernable in Fig. 2a, that Young's modulus in SiOC glasses and glass-ceramics decreases with increasing content of sp^2-hybridized segregated carbon. While the **C1-SiOC-1100** glass sample with only 1 vol.% of sp^2-hybridized segregated carbon investigated in this study exhibits a Young's modulus of 101.7 GPa, a much lower Young's modulus of only 66 GPa has previously been reported for a SiOC glass with approximately 64 vol.% of segregated carbon [38].

A plot of Young's modulus against the volume fraction of SiC in Fig. 2b (for SiOC glasses, the volume fraction of SiC is thought to be systematically shifted to lower values due to the unknown density of the disordered arrangement of SiC_4 tetrahedra) reveals their direct interrelation. SiOC materials with a larger fraction of SiC typically exhibit a higher Young's modulus as compared to samples containing a smaller fraction of SiC. This result is supposed to be related to the high values of E = 300 GPa of the nano-sized β-SiC precipitates [37]. Thus, sp^2-hybridized segregated carbon and β-SiC nanoparticles have the opposite effect on Young's modulus of SiOC glasses and glass-ceramics. This dependency was already suggested by Soraru et al. for a significantly smaller compositional range of SiOC glasses and for thin films [10,39] and is extended now in this study to bulk SiOC glasses with higher amounts of segregated carbon and monolithic SiOC glass-ceramics.

Fig. 3 illustrates the temperature dependence of Young's modulus of the investigated SiOC glass-ceramics with 1, 12 and 16 vol.% of segregated carbon, respectively. All samples are characterized by an

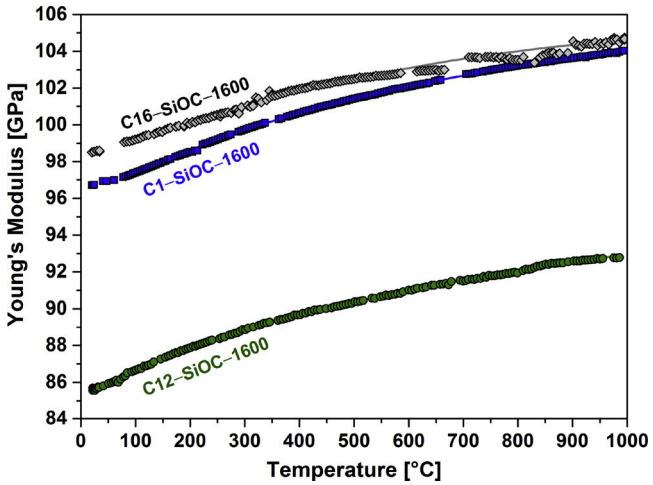

Fig. 3. Temperature dependence of the Young's modulus of the SiOC glass-ceramics investigated in this study. The experimental error is estimated to be ± 1 GPa (i.e., < 2%).

increasing Young's modulus with increasing temperature. It is known from literature that Young's modulus of SiOC glasses and glass-ceramics increases with temperature (i.e. stiffening) analogous to vitreous silica [11,16,40]. In the case of vitreous silica, this behavior has been attributed to continuous atomic displacements during an amorphous-amorphous transformation comparable to the structural rearrangements associated to the α- to β-cristobalite phase transition in crystalline SiO_2 [34,41]. We therefore conclude that the temperature dependence of the Young's modulus in the present SiOC glass-ceramics is dominated by the silica glass matrix. Since the Young's modulus did not show any hysteresis effects during cooling (not shown here), irreversible changes during the measurements can be excluded.

Depending on the respective length scale, several different factors may affect the Young's modulus of glasses, including the atomic bonding energy and packing density, but also the network connectivity [34] and super-structural heterogeneity [42,43]. Consequently, the stability of a glass, e.g., upon exposure to high temperatures can be monitored well by the measurement of Young's modulus, as a change in Young's modulus would be caused by a change in one or more of the above-mentioned structural parameters.

Thus, in the present study, Young's modulus was used to identify possible structural changes (i.e. decomposition or crystallization of the amorphous matrix) occurring in SiOC glass-ceramics (prepared at 1600 °C; i.e., fully phase-separated) which may result from their thermal annealing, for example during high-temperature creep experiments. Annealing temperatures and holding times were chosen according to the time necessary to reach the steady-state regime (secondary creep) in creep experiments, as previously reported [19]. For sample **C1-SiOC-1600**, the chosen annealing conditions were 6 days at 1100 °C and 2 h at 1300 °C, respectively, while for samples **C12-SiOC-1600** and **C16-SiOC-1600** the conditions were 6 days at 1200 °C and 12 h at 1300 °C, respectively. Fig. 4a – c show the temperature evolution of Young's modulus before and after annealing at the chosen conditions. All SiOC glass-ceramics exhibit an increase in Young's modulus after annealing, where the annealing at higher temperature leads to a larger increase. In comparison to the as-prepared sample, **C1-SiOC-1600** shows the lowest total increase of Young's modulus of about 1.4%; whereas **C12-SiOC-1600** exhibits an increase of about 7.3%. **C16-SiOC-1600** shows the highest total increase of the Young's modulus (approximately 8.8% at 1200 °C). Interestingly, **C16-SiOC-1600** shows lower Young's modulus (and its increase) during the thermal annealing at 1300 °C as compared to the features recorded during annealing at 1200 °C (see Fig. 4c). The SiOC glass-ceramics are already fully phase-separated (i.e. the evolution of β-SiC nanoparticles occurred already during synthesis). Consequently, this increase in Young's modulus cannot be attributed to the precipitation of β-SiC nanoparticles.

In order to further rationalize the increase in Young's modulus and to directly compare all investigated samples, Fig. 4d displays the temperature-dependent Young's modulus normalized to the corresponding value at room temperature of the investigated SiOC glass-ceramics (as-prepared and after thermal annealing). The temperature sensitivity of Young's modulus, i.e. the evolution of Young's modulus with temperature, is not affected by thermal annealing, as the curves of the individual glass-ceramics are identical within the estimated accuracy of the measurement ($\pm$ 1 GPa; < 2%). The temperature sensitivity can be correlated to the fragility of glasses [44]. Furthermore, the fragility of glasses is connected to their atomic packing density, where glasses with high atomic packing density are known to be more fragile [45]. Consequently, the stable temperature sensitivity indicates, that the glassy matrix of the investigated SiOC glass-ceramics is not significantly affected by thermal annealing.

In general, two main strategies for improving Young's modulus for specific glass series are discussed in glass science: (i) an increase in the atomic packing density and (ii) an increase in the local bond strength [34]. Both do not apply for our SiOC glass-ceramics. The first is expected to be related to an increase in the skeletal density and the second relies on a change in the elemental composition. For the investigated SiOC samples, the skeletal densities remain constant and consequently the first effect can be ruled out. Moreover, as the samples show only negligible weight loss and changes in their elemental composition (Table 3), also the second effect can be excluded. Consequently, the increase of Young's modulus if SiOC glass-ceramics after thermal annealing should have *other origin* and further supports the stability of the glassy matrix as already discussed considering the temperature sensitivity. One possible effect may arise from crystallization processes of the dispersed phases in SiOC glass-ceramics which take place during thermal annealing.

It is known that Young's moduli of nanocrystalline materials are significantly lower than those of their crystalline counterparts [37]. Consequently, it is expected that an increased ordering /crystallization of the β-SiC nanoparticles or the segregated carbon phase in our SiOC samples might explain the observed increase in their Young's moduli. The evolution of the sp^2-hybridized carbon phase in the SiOC glass-ceramics was studied by Raman spectroscopy, which may provide information on the average crystallite size L_a and the average distance between two defects L_D in the segregated carbon phase. The procedure used for the determination of L_a and L_D from the intensity ratio between D and G band (typical features in Raman spectra of disordered carbons) in silicon oxycarbides is described in detail in [21] and values of the investigated samples are summarized in Table 4. Both L_a and L_D are slightly increased in **C1-SiOC-1600** and **C16-SiOC-1600** after annealing at 1200 °C for 6 days; whereas, they were rather indifferent to the annealing experiment at 1300 °C for 12 h. This indicates some increased ordering of the segregated carbon phase during the long-term annealing at 1200 °C, which may though explain the increase of the Young's modulus in SiOC after annealing.

In addition to the sp^2-hybridized carbon phase, the β-SiC nanoparticles may also be subjected to crystallization during the high-temperature annealing process. Fig. 5 shows the XRD patterns of the SiOC glass-ceramics before and after thermal annealing. There is no indication for the crystallization of cristobalite. The presence of a reflection at $2\theta = 11.5^\circ$ for samples **C16-SiOC-1600** annealed at 1200 °C for 6 days and **C12-SiOC-1600** annealed at 1300 °C for 12 h may be considered as an indication for the presence of the segregated carbon phase [46]. This is in good agreement with the observed increase of L_a and L_D as determined by Raman spectroscopy for C16-SiOC-1600. Differences between XRD and L_a and L_D as determined from Raman spectroscopy for sample C12-SiOC-1600 are due to different volumes accessible for both measurement techniques, where powder XRD gives an averaged picture of the top layer of the whole sample, whereas Raman spectroscopy gives a localized information of low lateral size.

Additionally, slight changes in the shape of the reflections related to β-SiC after thermal annealing can be identified. Rietveld refinement was performed with fixed lattice parameters. Crystallite size and microstrain were refined according to the recommendations given in [47], with both Lorentzian and Gaussian contributions. For **C1-SiOC-1600**, a slight increase in average crystallite size of 2.2 to 3.1 nm and an increase in scale factor of about 20% was determined after thermal annealing, indicating two effects caused by the high-temperature treatment of SiOC glass-ceramics. Firstly, an increase of the crystallite size of β-SiC reflects better ordering thereof. Secondly, an increase in scale factor relates to an increase of the amount of β-SiC, which in the present case can be explained either by the segregation of additional β-SiC during the thermal annealing (which would imply an incomplete phase separation of the SiOC glass during the hot-pressing step while preparing the monolithic glass-ceramics) or by the crystallization (i.e., increase in size) of precipitates that were too small to be reliably distinguished from the background of the XRD patterns (and are consequently not included in the scale factor for β-SiC). In other words, the increase of the scale factor is correlated to the crystallization of x-ray amorphous SiC to nanocrystalline β-SiC.

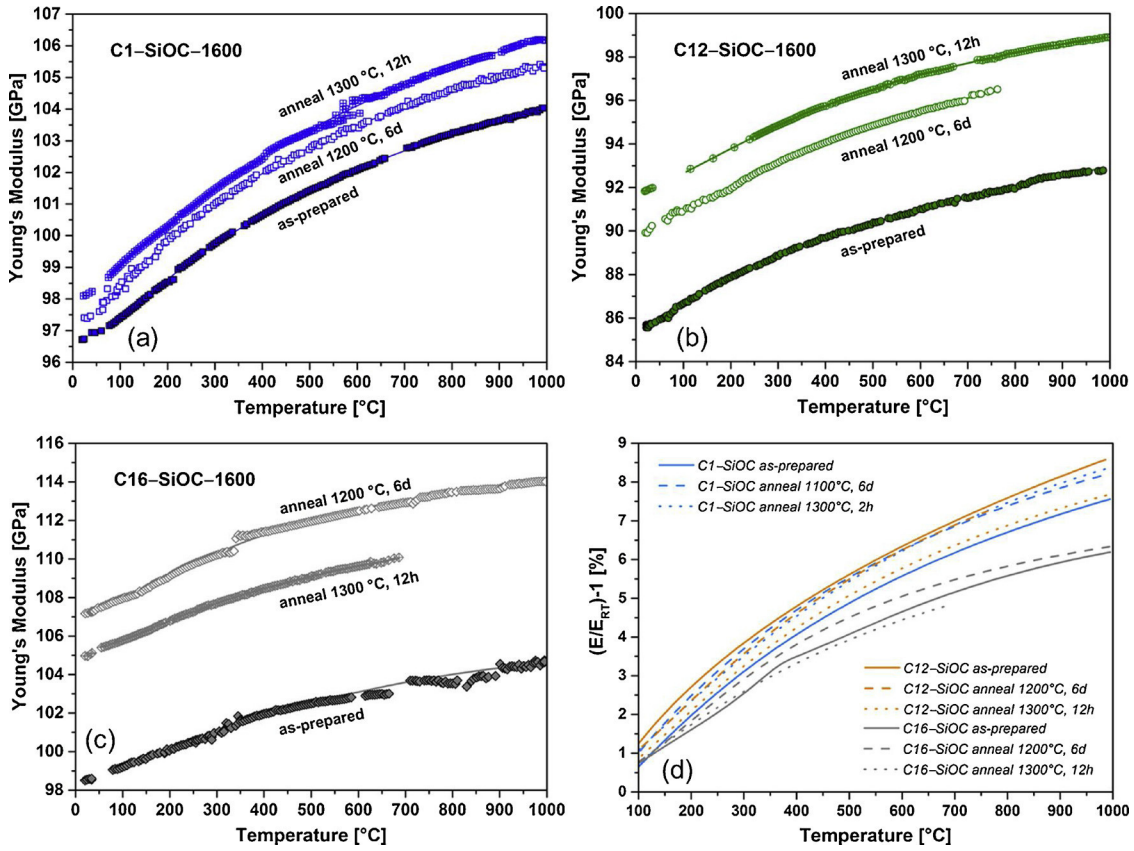

Fig. 4. Temperature dependence of the Young's modulus of the as-prepared (a) **C1-SiOC-1600**, (b) **C12-SiOC-1600** and (c) **C16-SiOC-1600** SiOC glass-ceramics, respectively, and after a thermal treatment at different temperatures and for varying durations. Lines drawn are fits to the experimental data. (d) Temperature dependence of the Young's modulus normalized to its value at room temperature (displayed by trendlines). The experimental error is estimated to be ± 1 GPa (i.e., < 2%).

Table 3
Skeletal density ρ and elemental composition of the investigated as-prepared SiOC glass-ceramics and after a thermal treatment.

Sample	Annealing Conditions	Density ρ [g/cm^3]	Weight loss [%]	Elemental Composition		
				Si [wt.%]	O [wt.%]	C [wt.%]
C1-SiOC-1600	*as-prepared*	2.38*	–	51.78*	41.59*	6.63*
	1100 °C, 6 d	2.38	1.66	52.66	40.57	6.77
	1300 °C, 2 h	2.38	–	52.54	40.59	6.87
C12-SiOC-1600	*as-prepared*	2.31*	–	46.36*	39.52*	14.12*
	1200 °C, 6 d	2.32	0	47.48	38.97	13.55
	1300 °C, 12 h	2.32	0	46.81	39.32	13.87
C16-SiOC-1600	*as-prepared*	2.34*	–	46.79*	33.82*	19.39*
	1200 °C, 6 d	2.37	0.14	47.35	33.56	19.09
	1300 °C, 12 h	2.38	0.19	46.89	33.66	19.45

* Values taken from Ref. [21].

For **C12-SiOC-1600** and **C16-SiOC-1600**, thermal annealing leads to a significant increase of the scale factor (ca. 200% at maximum), accompanied by a slight decrease in the average crystallite sizes from 2.6 to 2.8 to 1.7–2.3 nm. The strong increase of the scale factor implies that there is a significant amount of X-ray amorphous SiC in the as-prepared monolithic SiOC glass-ceramics which crystallizes during the high-temperature annealing. At the same time, nanocrystalline β-SiC nanoparticles increase in size, too. Interestingly, as the amount of X-ray amorphous SiC nanoparticles which crystallizes is significant, there is an overall decrease of the average crystallite size after the thermal annealing.

From the above, it can be concluded that there is an increased ordering of β-SiC in all three samples upon thermal annealing (it is noted that the Rietveld refinement on the available data of such kind of disordered materials has to be regarded as being semi-quantitative and absolute values may be shifted). The most noticeable change is observed in **C16-SiOC-1600** annealed at 1200 °C for 6 days. This is in line with the highest increase in Young's modulus and the highest carbon content. As it is suggested in literature that the presence of segregated carbon slows down β-SiC crystallization [5,48], the as-prepared **C16-SiOC-1600** sample is the least ordered sample with respect to β-SiC nanoparticles, and shows therefore the highest changes during thermal annealing. It is consequently suggested, that this increased ordering of the β-SiC nanoparticles is sufficient for an increase in Young's modulus, however, not high enough to be detectable at the scale of the skeletal density. As crystallization is a thermally activated process, higher temperatures and holding times favor higher degree of ordering and consequently Young's modulus. This can as well explain the relatively

Table 4
Effects of a thermal treatment on the degree of graphitization of the segregated carbon in SiOC glass-ceramics as determined from Raman spectroscopy: Average crystallite size L_a, average distance between two defects L_D. A_D/A_G describes the ratio between the areas assigned to the D and G band, respectively.

Sample	Annealing conditions	A_D/A_G	L_a [nm]	L_D [nm]
C1-SiOC-1600	*as prepared*	3.185 ± 0.233	12.1 ± 0.9	9.5 ± 0.4
	1100 °C, 6 d	2.800 ± 0.142	13.8 ± 0.7	10.2 ± 0.3
	1300 °C, 12 h	2.232 ± 0.356	17.3 ± 2.7	11.4 ± 0.9
C12-SiOC-1600	*as prepared*	4.215 ± 0.251*	9.2 ± 0.6*	8.3 ± 0.3*
	1200 °C, 6 d	4.539 ± 0.422	8.5 ± 0.8	8.0 ± 0.4
	1300 °C, 12 h	4.699 ± 0.036	8.2 ± 0.1	7.8 ± 0.1
C16-SiOC-1600	*as prepared*	4.121 ± 0.521*	9.5 ± 1.3*	8.4 ± 0.6*
	1200 °C, 6 d	3.093 ± 0.203	12.5 ± 0.8	9.7 ± 0.3
	1300 °C, 12 h	4.104 ± 0.075	9.4 ± 0.2	8.4 ± 0.1

* Values are taken from Ref. [21].

large increase in Young's modulus of **C12-SiOC-1600** and **C16-SiOC-1600** in comparison to **C1-SiOC-1600**. Thus, the effect of the β-SiC crystallization in SiOC-based glass-ceramics on their Young's modulus is significantly higher than that of their chemical composition.

The temperature dependencies of shear modulus, G, and Poisson's ratio, determined for **C1-SiOC-1600** prior and post thermal annealing are shown in Fig. 6. In accordance to the evolution of Young's modulus, both shear modulus and Poisson's ratio are increasing with increasing temperature. This indicates that the mechanisms leading to a stiffening during temperature increase are at least partially resulting from an increase of the atomic packing density (as expressed by changes in Poisson's ratio), which is in line with the suggested structural rearrangements in vitreous silica [34,41]. Thermal annealing leads to a slight increase of the shear modulus, however within the estimated experimental error of ± 1 GPa. Poisson's ratio is not significantly impaired by thermal annealing as evidenced by comparing the values of ν before and after annealing at 1100 °C for 6 days. Poisson's ratio correlates to the atomic packing density, as will be addressed in the following, which in turn is expected to be mainly governed by the glassy matrix in a glass-ceramic. As Poisson's ratio of SiOC glass-ceramics is not significantly affected by the thermal treatment protocols, it is concluded that their silica-based amorphous matrix does not change during thermal annealing, indicating a good thermal stability of SiOC glass-ceramics.

Values of the Young's modulus, shear modulus, bulk modulus, Poisson's ratio, hardness and strain-rate sensitivity at room temperature are summarized in Table 2. Poisson's ratio of the SiOC glass-ceramics are virtually independent on their phase composition. The values of ν as determined by ultrasonic echography scatter only slightly within a narrow interval of 0.166 to 0.175, which compares very well with the range of Poisson ratios reported for vitreous silica of 0.15 to 0.18 [27,49–53]. Interestingly, a SiOC glass derived from the same polymeric precursor as the **C12-SiOC-1600** glass-ceramic was found to exhibit an extremely low Poisson's ratio of only 0.11 [14]. Smaller Poisson's ratios in glasses are often correlated to strongly interconnected network structures of low atomic packing density [34,54]. In case of SiOC glass, this is explained by the enhanced degree of cross-linking upon the exchange of two-fold coordinated oxygen atoms with four-fold coordinated carbon. The significantly higher Poisson's ratios of the SiOC glass-ceramics investigated in the present study are linked to the phase separation in SiOC glasses at temperatures exceeding 1250 °C

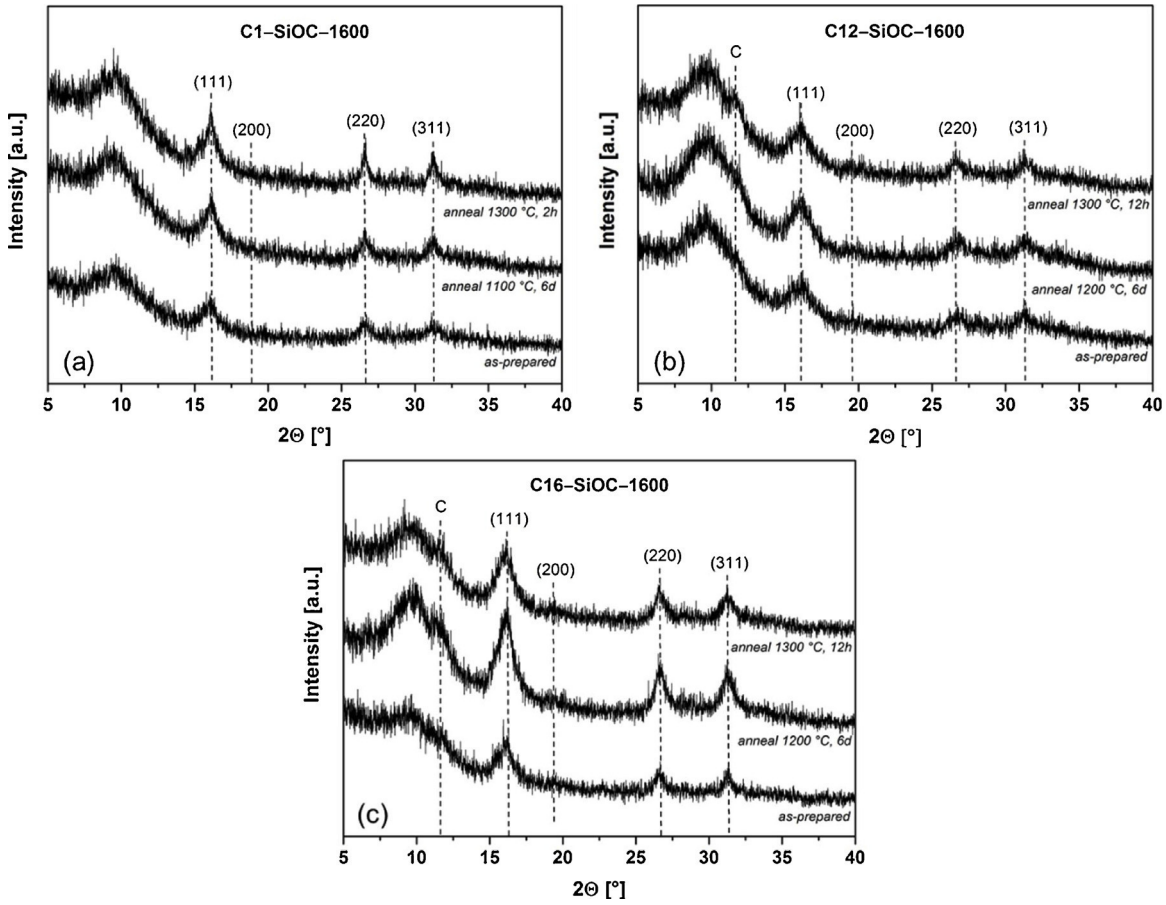

Fig. 5. X-ray diffraction patterns (Mo K_α) of SiOC glass-ceramics prior and after annealing at high temperatures: (a) **C1-SiOC-1600**; (b) **C12-SiOC-1600**; (c) **C16-SiOC-1600**. Indexed reflections relate to β-SiC.

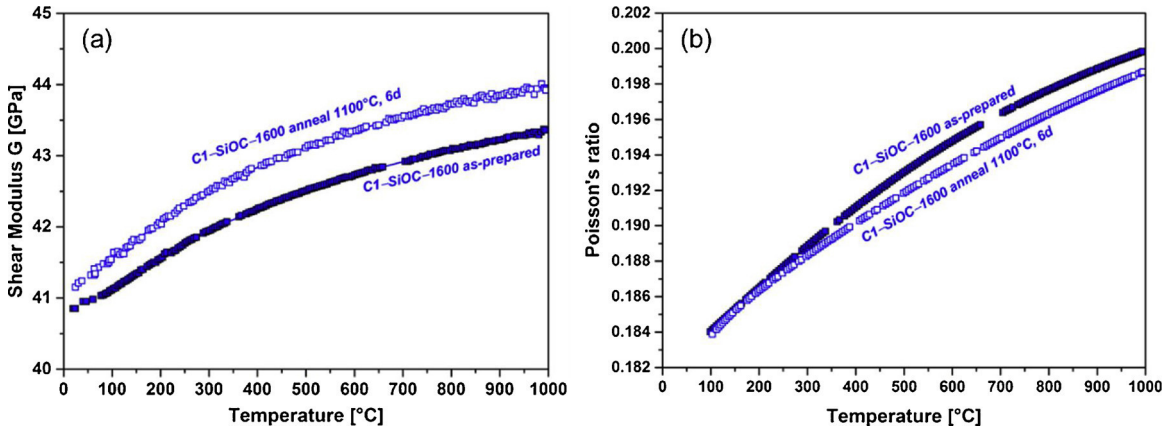

Fig. 6. Temperature dependence of the shear modulus G and Poisson's ratio ν of the (a) as-prepared **C1-SiOC-1600** SiOC glass-ceramic and (b) after a thermal treatment for 6 days at 1100 °C.

[7,9]. We therefore conclude, that the Poisson ratio of our SiOC glass-ceramics are determined by the elastic properties of residual silica glass matrix.

The hardness of the studied SiOC glass and glass-ceramics scatter slightly around 10.5–11.4 GPa. The higher hardness of the **C1-SiOC-1100** glass (H = 11.4 GPa) in comparison to vitreous silica (H = 9.3 GPa [55]) is the direct consequence of the enhanced network connectivity and the accompanied presence of additional network constraints, similarly to silicon oxynitride (SiON) glasses [56]. Before continuing this discussion, we need to note the mismatch in hardness obtained for the **C1-SiOC-1100** glass (H = 11.4 GPa) investigated in the actual study and the previously published Vickers hardness values for SiOC glasses of 8.2–9.3 GPa [10,13]. This discrepancy is attributed to the large contribution of elastic deformation to the indentation response of glasses. This manifests in marked differences between the contact area under load, which determines the hardness H, and the size of the residual hardness imprint after unloading, which is used for evaluating the Vickers hardness H_V [57].

Unlike SiOC glasses, the improved hardness of the SiOC glass-ceramics is governed by a complex interplay between the mechanical stability, volume fraction and distribution of the residual silica glass matrix and the β-SiC nanoparticles as well as the segregated carbon [36]. Here, the β-SiC nanoparticles are supposed to be responsible for the improved hardness of the SiOC glass-ceramics, as polycrystalline β-SiC exhibits a Vickers hardness H_V of 27.1 to 34.1 GPa [58]. Note, that the volume fraction of segregated carbon seems to have only little impact on the hardness. This is evident from the comparison of the **SiC/SiO$_2$-1600** (H = 10.6 GPa) and **C12-SiOC-1600** (H = 10.5 GPa) glass-ceramics, which consist of an almost identical volume fraction of β-SiC nanoparticles, but zero and 12 vol.% segregated carbon, respectively. The same conclusion can be done upon comparing **C1-SiOC-1600** (H = 11.0 GPa) and **C16-SiOC-1600** (H = 10.6 GPa), revealing comparable amounts of β-SiC but 1 and 16 vol.% of segregated carbon, respectively. Interestingly, only marginal differences in hardness are distinguishable between the **C1-SiOC-1100** glass (H = 11.4 GPa) and the **C1-SiOC-1600** glass-ceramic (H = 11.0 GPa). This result is in clear contrast to a previous study, where an increasing hardness was noticed upon phase separation in a SiOC glass [13]. This was related to an increase in density, which is indeed occurring during phase separation (cf. Table 1), though effects related to the elimination of residual porosity in the SiOC glass were also considered.

The brittleness of crystalline metals as well as metallic glasses can be correlated to the ratio between shear and bulk modulus (Pugh ratio G/K) [59]. Metallic glasses show a tough-to-brittle transition at G/K > 0.41-0.43 [60]. In this context, Pugh ratios of 0.83 for **C1-SiOC-1600**, 0.86 for **C12-SiOC-1600** and 0.85 for **C16-SiOC-1600**, would imply a brittle fracture behavior. The chemical composition has no significant influence on the Pugh ratio of SiOC glass-ceramics. Additionally, the index of brittleness B = H/K_{Ic}, which relates the resistance against plastic deformation to the resistance against fracture, was determined for **C1-SiOC-1600** (B = 15 $\mu m^{-0.5}$), **C12-SiOC-1600** (B = 11 $\mu m^{-0.5}$) and vitreous silica (B = 13 $\mu m^{-0.5}$), where higher values correspond to more brittle material [61]. For the calculation the indentation hardness determined in this study was used, whereas values for fracture toughness K_{Ic} were taken from Ref. [62]. As opposed to the Pugh ratio, the index of brittleness displays a notable dependence on the chemical composition. Sample C1-SiOC-1600 with only 1 vol.% of segregated carbon appears to be more brittle than vitreous silica. However, the presence of 12 vol.% segregated carbon in C12-SiOC-1600 has the opposite effect and drastically reduces the brittleness even below the level of vitreous silica. This behavior is in line with the experiences made during grinding of the samples and clearly signifies the importance of both the chemical and phase composition for the mechanical performance of SiOC glasses and glass-ceramics. This argumentation is also supported by previous observations regarding the effects of phase separation on the mechanical stability of alkali-alkaline earth silicate or alkali-borosilicate glasses [55,63–65]. Tuning the volume fraction and structure of the separated phases is therefore supposed as a promising route towards the fabrication of SiOC materials with an enhanced toughness.

For a potential application of SiOC glasses and glass-ceramics at elevated temperatures, a high creep resistance, i.e., low strain-rate sensitivity, is of paramount importance. Using a nanoindentation strain-rate jump test [27], very low strain-rate sensitivities of 0.0059 to 0.0107 were determined for the SiOC glass and glass-ceramics. The results obtained for both the **C1-SiOC-1100** glass (m = 0.0059) and the **SiO$_2$/SiC-1600** (m = 0.0060) glass-ceramic are very close to the values reported for vitreous silica (m = 0.0068 – 0.0150 [66–68]), which displays no significant creep deformation at room temperature [69,70]. With respect to this result, we speculate the creep response of SiOC materials with low amounts of segregated carbon to be determined by the creep resistance of the vitreous silica glass matrix. Nevertheless, regarding the SiOC glass-ceramics a slight but still detectable increase of the strain-rate sensitivity from 0.0060 (**SiO$_2$/SiC-1600**) to 0.0107 (**C12-SiOC-1600**) is seen with increasing amounts of segregated carbon. A higher strain-rate sensitivity in glasses normally signifies a homogenization of the plastic flow [71]. With the presence of a homogeneously dispersed phase of segregated carbon in the vitreous silica glass matrix, fertile sites for a shear-mediated plastic flow are created inside the material.

4. Conclusions

Silicon oxycarbides are known to possess increased mechanical

properties like Young's modulus and hardness. The present study rationalizes the various impacts on their elastic and plastic properties caused by the chemical/phase compositional variability inherent to the SiOC system and gives further insight in the thermal stability of SiOC glass-ceramics.

The elastic properties of silicon oxycarbides are influenced by both phase composition (i.e. volume fraction of β-SiC or fraction of Si-C bonds in Si-O-C glass network and volume fraction of segregated carbon) as well as by their microstructure (i.e. SiOC glass vs. glass-ceramic; phase separation). Whereas Young's modulus is increasing with increasing volume fraction of β-SiC nanoparticles/Si-C bonds and decreasing with increasing amount of segregated carbon, it is not significantly affected upon phase separation. In contrast, Poisson's ratio, and consequently the atomic packing density, is independent of the chemical composition, but is significantly influenced by the phase separation. Both, the development of Young's modulus and Poisson's ratio, can be considered as direct consequences of: (i) the highly cross-linked network architecture of SiOC glasses due to the presence of mixed-bonds $SiO_{4-x}C_x$ tetrahedra; (ii) the decrease of the cross-linking degree of the glassy network during the phase separation and (iii) the high stiffness of crystalline β-SiC.

Thermal annealing of SiOC glass-ceramics leads to an increase in Young's modulus. It is demonstrated that this relies in an increased ordering of the dispersed phases segregated carbon and β-SiC as evidenced by XRD and Raman spectroscopy and not in a change of the glassy silica matrix as testified by an unbiased Poisson's ratio and temperature sensitivity of Young's modulus. This implies, that the silica-rich glassy matrix of SiOC glass-ceramics is stable at high temperatures and longer holding times.

The plastic properties of SiOC glass-ceramics are significantly influenced by the volume fractions of both segregated carbon and β-SiC nanoparticles. The segregated carbon phase reduces brittleness and induces additional sites for sliding during plastic deformation; whereas, the hardness is governed by the volume fraction of β-SiC nanoparticles due to their comparably high hardness. Interestingly, the hardness in SiOC seems to be not affected by phase separation.

Acknowledgements

The authors are grateful for financial support provided from the Deutsche Forschungsgemeinschaft (IO 64/7-1, "High-Temperature Creep in SiOC-Based Glasses and Glass-Ceramics").

References

[1] P. Colombo, G. Mera, R. Riedel, G.D. Soraru, Polymer-derived ceramics: 40 years of research and innovation in advanced ceramics, J. Am. Ceram. Soc. 93 (7) (2010) 1805–1837, https://doi.org/10.1111/j.1551-2916.2010.03876.x.

[2] C. Stabler, E. Ionescu, M. Graczyk-Zajac, I. Gonzalo-Juan, R. Riedel, Silicon oxycarbide glasses and glass-ceramics: "All-Rounder" materials for advanced structural and functional applications, J. Am. Ceram. Soc. 101 (11) (2018) 4817–4856, https://doi.org/10.1111/jace.15932.

[3] Y.D. Blum, D.B. MacQueen, H.-J. Kleebe, Synthesis and characterization of carbon-enriched silicon oxycarbides, J. Eur. Ceram. Soc. 25 (2-3) (2004) 143–149, https://doi.org/10.1016/j.jeurceramsoc.2004.07.019.

[4] H.-J. Kleebe, Y.D. Blum, SiOC ceramic with high excess free carbon, J. Eur. Ceram. Soc. 28 (5) (2008) 1037–1042, https://doi.org/10.1016/j.jeurceramsoc.2007.09.024.

[5] H. Brequel, J. Parmentier, S. Walter, R. Badheka, G. Trimmel, S. Masse, J. Latournerie, P. Dempsey, C. Turquat, A. Desmartin-Chomel, L.L. Neindre-Prum, U.A. Jayasooriya, D. Hourlier, H.J. Kleebe, G.D. Soraru, S. Enzo, F. Babonneau, Systematic structural characterization of the high-temperature behavior of nearly stoichiometric silicon oxycarbide glasses, Chem. Mater. 16 (13) (2004) 2585–2598, https://doi.org/10.1021/cm049847a.

[6] S.J. Widgeon, S. Sen, G. Mera, E. Ionescu, R. Riedel, A. Navrotsky, 29Si and 13C solid-state NMR spectroscopic study of nanometer-scale structure and mass fractal characteristics of amorphous polymer derived silicon oxycarbide ceramics, Chem. Mater. 22 (23) (2010) 6221–6228, https://doi.org/10.1021/cm1021432.

[7] L. Bois, J. Maquet, F. Babonneau, D. Bahloul, Structural characterization of sol-gel derived oxycarbide glasses. 2. Study of the thermal stability of the silicon oxycarbide phase, Chem. Mater. 7 (5) (1995) 975–981, https://doi.org/10.1021/cm00053a025.

[8] F. Rosenburg, E. Ionescu, N. Nicoloso, R. Riedel, High-temperature raman spectroscopy of nano-crystalline carbon in silicon oxycarbide, Materials (Basel) 11 (1) (2018) 1–9, https://doi.org/10.3390/ma11010093.

[9] G.D. Soraru, G. D'Andrea, R. Campostrini, F. Babonneau, G. Mariotto, Structural characterization and high-temperature behavior of silicon oxycarbide glasses prepared from sol-gel precursors containing Si-H bonds, J. Am. Ceram. Soc. 78 (2) (1995) 379–387, https://doi.org/10.1111/j.1151-2916.1995.tb08811.x.

[10] G.D. Soraru, E. Dallapiccola, G. D'Andrea, Mechanical characterization of sol-gel-derived silicon oxycarbide glasses, J. Am. Ceram. Soc. 79 (8) (1996) 2074–2080, https://doi.org/10.1111/j.1151-2916.1996.tb08939.x.

[11] T. Rouxel, G. Massouras, G.-D. Soraru, High temperature behavior of a gel-derived SiOC glass: elasticity and viscosity, J. Solgel Sci. Technol. 14 (1) (1999) 87–94.

[12] T. Rouxel, G.-D. Soraru, J. Vicens, Creep viscosity and stress relaxation of gel-derived silicon oxycarbide glasses, J. Am. Ceram. Soc. 84 (5) (2001) 1052–1058, https://doi.org/10.1111/j.1151-2916.2001.tb00789.x.

[13] H.-J. Kleebe, C. Turquat, G.D. Soraru, Phase separation in an SiCO glass studied by transmission electron microscopy and electron energy-loss spectroscopy, J. Am. Ceram. Soc. 84 (5) (2001) 1073–1080, https://doi.org/10.1111/j.1151-2916.2001.tb00792.x.

[14] C. Moysan, R. Riedel, R. Harshe, T. Rouxel, F. Augereau, Mechanical characterization of a polysiloxane-derived SiOC glass, J. Eur. Ceram. Soc. 27 (1) (2006) 397–403, https://doi.org/10.1016/j.jeurceramsoc.2006.01.016.

[15] G.M. Renlund, S. Prochazka, R.H. Doremus, Silicon oxycarbide glasses. Part II. Structure and properties, J. Mater. Res. 6 (12) (1991) 2723–2734, https://doi.org/10.1557/JMR.1991.2723.

[16] B. Papendorf, E. Ionescu, H.-J. Kleebe, C. Linck, O. Guillon, K. Nonnenmacher, R. Riedel, High-temperature creep behavior of dense SiOC-based ceramic nanocomposites: microstructural and phase composition effects, J. Am. Ceram. Soc. 96 (1) (2013) 272–280, https://doi.org/10.1111/jace.12067.

[17] E. Ionescu, C. Balan, H.-J. Kleebe, M.M. Mueller, O. Guillon, D. Schliephake, M. Heilmaier, R. Riedel, High-temperature creep behavior of SiOC glass-ceramics: influence of network carbon versus segregated carbon, J. Am. Ceram. Soc. 97 (12) (2014) 3935–3942, https://doi.org/10.1111/jace.13206.

[18] C. Stabler, F. Roth, M. Narisawa, D. Schliephake, M. Heilmaier, S. Lauterbach, H.-J. Kleebe, R. Riedel, E. Ionescu, High-temperature creep behavior of a SiOC glass ceramic free of segregated carbon, J. Eur. Ceram. Soc. 36 (15) (2016) 3747–3753, https://doi.org/10.1016/j.jeurceramsoc.2016.04.015.

[19] C. Stabler, D. Schliephake, M. Heilmaier, T. Rouxel, H.-J. Kleebe, M. Narisawa, R. Riedel, E. Ionescu, Influence of SiC/Silica and Carbon/Silica interfaces on the high-temperature creep of silicon oxycarbide-based glass ceramics: a case study, Adv. Eng. Mater. 1800596 (2018) 1–11, https://doi.org/10.1002/adem.201800596.

[20] A. Makishima, J.D. Mackenzie, Direct calculation of Young's modulus of glass, J. Non-Cryst. Solids 12 (1) (1973) 35–45, https://doi.org/10.1016/0022-3093(73)90053-7.

[21] C. Stabler, P. Stein, R. Riedel, E. Ionescu, A. Reitz, B. Albert, Thermal properties of SiOC glasses and glass ceramics at elevated temperatures, Materials (Basel) 11 (279) (2018) 1–18.

[22] M. Narisawa, S. Watase, K. Matsukawa, T. Dohmaru, K. Okamura, White Si-O-C(-H) particles with photoluminescence synthesized by decarbonization reaction on polymer precursor in a hydrogen atmosphere, Bull. Chem. Soc. Jpn. 85 (6) (2012) 724–726, https://doi.org/10.1246/bcsj.20110357.

[23] E. Radovanovic, M.F. Gozzi, M.C. Goncalves, I.V.P. Yoshida, Silicon oxycarbide glasses from silicone networks, J. Non-Cryst. Solids 248 (1) (1999) 37–48, https://doi.org/10.1016/S0022-3093(99)00101-5.

[24] W.C. Oliver, G.M. Pharr, An improved technique for determining hardness and elastic modulus using load and displacement sensing indentation experiments, J. Mater. Res. 7 (6) (1992) 1564–1583, https://doi.org/10.1557/Jmr.1992.1564.

[25] X.D. Li, B. Bhushan, A review of nanoindentation continuous stiffness measurement technique and its applications, Mater. Charact. 48 (1) (2002) 11–36.

[26] G.M. Pharr, J.H. Strader, W.C. Oliver, Critical issues in making small-depth mechanical property measurements by nanoindentation with continuous stiffness measurement, J. Mater. Res. 24 (3) (2009) 653–666, https://doi.org/10.1557/Jmr.2009.0096.

[27] R. Limbach, B.P. Rodrigues, L. Wondraczek, Strain-rate sensitivity of glasses, J. Non-Cryst. Solids 404 (2014) 124–134.

[28] L. Shen, W.C.D. Cheong, Y.L. Foo, Z. Chen, Nanoindentation creep of tin and aluminium: a comparative study between constant load and constant strain rate methods, Mater. Sci. Eng. A (2012) 505–510.

[29] B.N. Lucas, W.C. Oliver, Indentation power-law creep of high-purity indium, Metall. Mater. Trans. A 30 (3) (1999) 601–610, https://doi.org/10.1007/S11661-999-0051-7.

[30] J. Hay, Introduction to instrumented indentation testing, Exp. Techniques 33 (6) (2009) 66–72, https://doi.org/10.1111/J.1747-1567.2009.00541.X.

[31] R. Limbach, A. Winterstein-Beckmann, J. Dellith, D. Möncke, L. Wondraczek, Plasticity, crack initiation and defect resistance in alkali-borosilicate glasses: from normal to anomalous behavior, J. Non-Cryst. Solids 417-418 (2015) 15–27.

[32] J.M. Bind, Phase transformation during hot-pressing of cubic silicon carbide, Mater. Res. Bull. 13 (2) (1978) 91–96, https://doi.org/10.1016/0025-5408(78)90071-5.

[33] S. Walter, G.D. Soraru, H. Brequel, S. Enzo, Microstructural and mechanical characterization of sol gel-derived Si-O-C glasses, J. Eur. Ceram. Soc. 22 (13) (2002) 2389–2400, https://doi.org/10.1016/S0955-2219(01)00537-4.

[34] T. Rouxel, Elastic properties and short-to medium-range order in glasses, J. Am. Ceram. Soc. 90 (10) (2007) 3019–3039, https://doi.org/10.1111/j.1551-2916.2007.01945.x.

[35] A.J. Stryjak, P.W. McMillan, Microstructure and properties of transparent glass-

ceramics. Part 2. The physical properties of spinel transparent glass-ceramics, J. Mater. Sci. 13 (8) (1978) 1794–1804, https://doi.org/10.1007/BF00548743.
[36] N. Miyata, H. Jinno, Discussion of the indentation hardness of a glass-ceramic with participate microstructure, J. Mater. Sci. 17 (9) (1982) 2693–2699, https://doi.org/10.1007/BF00543906.
[37] G.D. Soraru, V.M. Sglavo, S. Dirè, G. D'Andrea, F. Babonneau, High-strength, high-modulus silicon-oxycarbide glasses, in: P. Durán, J.F. Fernández (Eds.), Third EURO-CERAMICS, Faenza Editrice Ibérica S.L., 1993, pp. 1157–1162.
[38] S. Martinez-Crespiera, E. Ionescu, H.-J. Kleebe, R. Riedel, Pressureless synthesis of fully dense and crack-free SiOC bulk ceramics via photo-crosslinking and pyrolysis of a polysiloxane, J. Eur. Ceram. Soc. 31 (5) (2011) 913–919, https://doi.org/10.1016/j.jeurceramsoc.2010.11.019.
[39] G.D. Sorarù, L. Kundanati, B. Santhosh, N. Pugno, Influence of free carbon on the Young's modulus and hardness of polymer-derived silicon oxycarbide glasses, J. Am. Ceram. Soc. 0 (0) (2018) 1–7, https://doi.org/10.1111/jace.16131.
[40] S. Spinner, G.W. Cleek, Temperature dependence of Young's modulus of vitreous germania and silica, J. Appl. Phys. 31 (1960) 1407–1410, https://doi.org/10.1063/1.1735852.
[41] D.J. Lacks, First-order amorphous-Amorphous transformation in silica, Phys. Rev. Lett. 84 (20) (2000) 4629–4632, https://doi.org/10.1103/PhysRevLett.84.4629.
[42] O. Benzine, S. Bruns, Z. Pan, K. Durst, L. Wondraczek, Local deformation of glasses is mediated by rigidity fluctuation and granularity, Adv. Sci. 5 (2018), https://doi.org/10.1002/advs.201800916 1800916/1-1800916/9.
[43] S. Sawamura, L. Wondraczek, Scratch hardness of glass, Phys. Rev. Mater. (2018) (in press).
[44] M. Idriss, F. Celarie, Y. Yokoyama, F. Tessier, T. Rouxel, Evolution of the elastic modulus of Zr-Cu-Al BMGs during annealing treatment and crystallization: role of Zr/Cu ratio, J. Non-Cryst. Solids 421 (2015) 35–40, https://doi.org/10.1016/j.jnoncrysol.2015.04.028.
[45] C.A. Angell, Perspective on the glass transition, J. Phys. Chem. Solids 49 (8) (1988) 863–871, https://doi.org/10.1016/0022-3697(88)90002-9.
[46] M.A. Mazo, A. Tamayo, J. Rubio, Advanced silicon oxycarbide-carbon composites for high temperature resistant friction systems, J. Eur. Ceram. Soc. 36 (10) (2016) 2443–2452, https://doi.org/10.1016/j.jeurceramsoc.2016.03.012.
[47] D. Balzar, N. Audebrand, M.R. Daymond, A. Fitch, A. Hewat, J.I. Langford, A. Le Bail, D. Louer, O. Masson, C.N. McCowan, N.C. Popa, P.W. Stephens, B.H. Toby, Size-strain line-broadening analysis of the ceria round-robin sample, J. Appl. Crystallogr. 37 (6) (2004) 911–924, https://doi.org/10.1107/S0021889804022551.
[48] H. Brequel, J. Parmentier, G.D. Sorar, L. Schiffini, S. Enzo, Study of the phase separation in amorphous silicon oxycarbide glasses under heat treatment, Nanostruct. Mater. 11 (6) (1999) 721–731, https://doi.org/10.1016/S0965-9773(99)00360-8.
[49] R. Brueckner, Mechanical Properties of Glasses, VCH, 1991, pp. 665–713.
[50] A. Pedone, G. Malavasi, A.N. Cormack, U. Segre, M.C. Menziani, Insight into elastic properties of binary alkali silicate glasses; prediction and interpretation through atomistic simulation techniques, Chem. Mater. 19 (13) (2007) 3144–3154, https://doi.org/10.1021/cm062619r.
[51] Q. Zhao, M. Guerette, L. Huang, Nanoindentation and Brillouin light scattering studies of elastic moduli of sodium silicate glasses, J. Non-Cryst. Solids 358 (3) (2012) 652–657, https://doi.org/10.1016/j.jnoncrysol.2011.10.034.
[52] P. Sellappan, T. Rouxel, F. Celarie, E. Becker, P. Houizot, R. Conradt, Composition dependence of indentation deformation and indentation cracking in glass, Acta Mater. 61 (16) (2013) 5949–5965, https://doi.org/10.1016/j.actamat.2013.06.034.
[53] S. Sawamura, R. Limbach, H. Behrens, L. Wondraczek, Lateral deformation and defect resistance of compacted silica glass: quantification of the scratching hardness of brittle glasses, J. Non-Cryst. Solids 481 (2018) 503–511, https://doi.org/10.1016/j.jnoncrysol.2017.11.035.
[54] G.N. Greaves, A.L. Greer, R.S. Lakes, T. Rouxel, Poisson's ratio and modern materials, Nat. Mater. 10 (11) (2011) 823–837, https://doi.org/10.1038/nmat3134.
[55] R. Limbach, A. Winterstein-Beckmann, J. Dellith, D. Moencke, L. Wondraczek, Plasticity, crack initiation and defect resistance in alkali-borosilicate glasses: from normal to anomalous behavior, J. Non-Cryst. Solids 417-418 (2015) 15–27, https://doi.org/10.1016/j.jnoncrysol.2015.02.019.
[56] G.L. Paraschiv, S. Gomez, J.C. Mauro, L. Wondraczek, Y. Yue, M.M. Smedskjaer, Hardness of oxynitride glasses: topological origin, J. Phys. Chem. B 119 (10) (2015) 4109–4115, https://doi.org/10.1021/jp512235t.
[57] W.C. Oliver, G.M. Pharr, Measurement of hardness and elastic modulus by instrumented indentation: advances in understanding and refinements to methodology, J. Mater. Res. 19 (1) (2004) 3–20, https://doi.org/10.1557/jmr.2004.19.1.3.
[58] Y.C. Cha, G. Kim, H.J. Doerr, R.F. Bunshah, Effects of activated reactive evaporation process parameters on the microhardness of polycrystalline silicon carbide thin films, Thin Solid Films 253 (1) (1994) 212–217, https://doi.org/10.1016/0040-6090(94)90322-0.
[59] S.F. Pugh, XCII. Relations between the elastic moduli and the plastic properties of polycrystalline pure metals, The London, Edinburgh, and Dublin Philosophical Magazine and Journal of Science 45 (367) (1954) 823–843, https://doi.org/10.1080/14786440808520496.
[60] J.J. Lewandowski, W.H. Wang, A.L. Greer, Intrinsic plasticity or brittleness of metallic glasses, Philos. Mag. Lett. 85 (2) (2005) 77–87, https://doi.org/10.1080/09500830500080474.
[61] B.R. Lawn, D.B. Marshall, Hardness, toughness, and brittleness: an indentation analysis, J. Am. Ceram. Soc. 62 (7-8) (1979) 347–350, https://doi.org/10.1111/j.1151-2916.1979.tb19075.x.
[62] T. To, C. Stabler, E. Ionescu, R. Riedel, F. Célarié, T. Rouxel, Fracture toughness and crack behavior of dense SiOC glass ceramics, J. Eur. Ceram. Soc. (2019) (submitted).
[63] A.K. Seal, P. Chakraborti, N.R. Roy, S. Mukherjee, M.K. Mitra, G.C. Das, Effect of phase separation on the fracture toughness of SiO2-B2O3-Na2O glass, Bull. Mater. Sci. 28 (5) (2005) 457–460, https://doi.org/10.1007/BF02711236.
[64] S. Deriano, T. Rouxel, M. LeFloch, B. Beuneu, Structure and mechanical properties of alkali-alkaline earth-silicate glasses, Phys. Chem. Glasses 45 (1) (2004) 37–44.
[65] S. Cheng, C. Song, P. Ercius, Indentation cracking behaviour and structures of nanophase separation of glasses, Eur. J. Glass Sci. Technol. Part B 58 (6) (2017) 237–242, https://doi.org/10.13036/17533562.58.6.040.
[66] R. Limbach, B.P. Rodrigues, L. Wondraczek, Strain-rate sensitivity of glasses, J. Non-Cryst. Solids 404 (2014) 124–134, https://doi.org/10.1016/j.jnoncrysol.2014.08.023.
[67] D. Peykov, E. Martin, R.R. Chromik, R. Gauvin, M. Trudeau, Evaluation of strain rate sensitivity by constant load nanoindentation, J. Mater. Sci. 47 (20) (2012) 7189–7200, https://doi.org/10.1007/s10853-012-6665-y.
[68] A.A. Elmustafa, D.S. Stone, Strain rate sensitivity in nanoindentation creep of hard materials, J. Mater. Res. 22 (10) (2007) 2912–2916, https://doi.org/10.1557/JMR.2007.0374.
[69] T. Chudoba, F. Richter, Investigation of creep behaviour under load during indentation experiments and its influence on hardness and modulus results, Surf. Coat. Technol. 148 (2-3) (2001) 191–198, https://doi.org/10.1016/S0257-8972(01)01340-8.
[70] A.C. Fischer-Cripps, A simple phenomenological approach to nanoindentation creep, Mater. Sci. Eng., A A385 (1-2) (2004) 74–82, https://doi.org/10.1016/j.msea.2004.04.070.
[71] H. Meinhard, P. Grau, G. Berg, S. Mosch, Hardness and flow behavior of glass in the nanometer range. An interpretation of the load dependence of the hardness, Glass Sci. Technol. (Frankfurt/Main) 70 (11) (1997) 333–339.

Journal of the European Ceramic Society 36 (2016) 3747–3753

Contents lists available at www.sciencedirect.com

Journal of the European Ceramic Society

journal homepage: www.elsevier.com/locate/jeurceramsoc

High-temperature creep behavior of a SiOC glass ceramic free of segregated carbon

Christina Stabler[a], Felix Roth[a], Masaki Narisawa[b], Daniel Schliephake[c], Martin Heilmaier[c], Stefan Lauterbach[d], Hans-Joachim Kleebe[d], Ralf Riedel[a], Emanuel Ionescu[a,*]

[a] Technische Universität Darmstadt, Institut für Materialwissenschaft, Jovanka-Bontschits-Strasse 2, D-64287 Darmstadt, Germany,
[b] Osaka Prefecture University, Graduate School of Engineering, 1-1, Gakuen-Cho, Sakai 599-8531, Japan
[c] Karlsruher Institut für Technologie, Institut for Applied Materials, Engelbert-Arnold-Strasse 4, D-76131 Karlsruhe
[d] Technische Universität Darmstadt, Institut für Angewandte Geowissenschaften, Schnittspahnstrasse 9, D-64287 Darmstadt, Germany

ARTICLE INFO

Article history:
Received 1 December 2015
Received in revised form 18 March 2016
Accepted 11 April 2016
Available online 28 April 2016

Keywords:
Silicon oxycarbide
High-temperature creep
Segregated carbon
Glass ceramic

ABSTRACT

In this study we present the high-temperature creep behavior of a dense SiOC glass ceramic free of segregated carbon. Solid-state NMR spectroscopy, XRD and TEM investigations indicate that the sample consists of β-SiC nanoparticles homogeneously dispersed in an amorphous silica matrix. Compression creep experiments were performed at 1100–1300 °C and stresses of 50–100 MPa. The calculated creep viscosity of SiOC is two orders of magnitude higher than that of pure silica. Whereas the activation energy for creep (696 kJ/mol) is close to that determined in pure silica glass. However, a stress exponent of 1.7 was calculated, suggesting that other mechanisms might contribute to the creep in addition to the Newtonian viscous flow. The strong difference in the creep rates and creep mechanism of the SiOC glass ceramic and amorphous silica is discussed in terms of possible contributions of the interface between the silica matrix and the β-SiC nanoparticles.

1. Introduction

Silicon oxycarbides are referred to as black glasses and can be described as consisting of an amorphous network of corner-connected SiO_xC_{4-x} (x = 0–4) tetrahedra. Despite some few reports on other techniques (*e.g.*, [1]), the main synthetic approach to incorporate significant amount of carbon within a silica network still relies on the thermal conversion of sol–gel precursors based on organo-substituted alkoxysilanes (*e.g.*, $R_xSi(OR')_4$ with R and R' being H, alkyl or aryl groups) as well as of polyorganosiloxanes in inert gas atmosphere [2]. Both types of precursors exhibit Si–C and Si–O bonds within their backbone, which are preserved upon their transformation into silicon oxycarbide glass. The composition of SiOC-based glasses can be controlled upon choosing suitable organic substituents and cross-linking degrees of the precursor gel and has been shown to have a strong influence on their properties. Typically, organo-substituted polysiloxane-based precursors convert into silicon oxycarbides consisting of a glassy SiOC matrix and a finely dispersed segregated carbon phase. Depending on the amount and nature of the organic substituents in the precursor, carbon-rich silicon oxycarbides can be provided, which exhibit large amounts of segregated carbon [2–4].

Silicon oxycarbides have been shown to keep their amorphous nature up to temperatures beyond 1000 °C [5], and exhibit excellent behavior in oxidative and corrosive environments [2]. At temperatures of *ca.* 1200–1300 °C, the single-phase glassy SiOC network starts to partition [5,6]. Thus, NMR studies show that in SiOC glasses annealed at temperatures up to 1400 °C only SiO_4 and SiC_4 tetrahedra and no mixed-bonds $SiO_{4-x}C_x$ tetrahedra are detectable [6,7]. The phase-separated SiOC materials can therefore be considered as consisting of an amorphous silica-rich matrix in which silicon carbide nanoparticles and segregated carbon are dispersed. Interestingly, the silica matrix keeps its amorphous nature up to very high temperatures (*i.e.*, 1500 °C), whereas β-SiC nanoparticles crystallize [6,8,9]. Subsequently, the segregated carbon can undergo a carbothermal reaction with the silica matrix upon formation of β-SiC and release of gaseous CO.

In addition to their unique crystallization behavior, silicon oxycarbide glasses exhibit outstanding creep resistance up to high temperatures [10–14], which makes this class of materials highly

* Corresponding author.
E-mail address: ionescu@materials.tu-darmstadt.de (E. Ionescu).

http://dx.doi.org/10.1016/j.jeurceramsoc.2016.04.015
0955-2219/

Table 1
Chemical composition obtained from elemental analysis of the hot-pressed SiOC sample and calculated volume fraction of the assumed phases present. Volume fractions are calculated assuming the following densities: $\rho(SiO_2) = 2.2\ g/cm^3$ [20], $\rho(\beta\text{-}SiC) = 3.22\ g/cm^3$ (ICSD-# 164974), $\rho(C) = 1.82\ g/cm^3$ (Graphitized Mesoporous Carbons GMC, Sigma-Aldrich, CAS-# 1333-86-4), $\rho(Si) = 2.33\ g/cm^3$ (PDF-# 00-027-1402).

	Si [wt.%]	O [wt.%]	C [wt.%]	SiO_2 [vol.%]	SiC [vol.%]	C [vol.%]	Si [vol.%]
Hot-pressedSiOC monolith	51.59[a]	43.03	5.38	83.9	14.9	0	1.3
Standard Deviation	±1.03[b]	±0.22	±0.32	±1.1	±1.2	±1.3	

[a] Not measured; calculated as the difference to 100 wt.%.
[b] Assumed standard deviation = relative standard deviation.

Table 2
Chemical composition obtained from elemental analysis of the hot-pressed SiOC sample compared to the SiOC starting powder and calculated volume fraction of the assumed phases present.

Sample	Chemical composition	SiO_2 [vol.%]	SiC [vol.%]	C [vol.%]
SiOC powder [21]	$SiO_{1.54}C_{0.26}(H_{0.12})$	87.3	11.9	0.8[a]
Hot-pressed SiOC monolith	$SiO_{1.46}C_{0.24}$	85.7	14.3	0

[a] The volume fraction of segregated carbon was formally calculated upon neglecting the presence of hydrogen in the white SiOC powder. However, as the materials contains significant amounts of hydrogen, it is considered that no segregated carbon is present and that $SiO_{1.54}C_{0.26}H_{0.12}$ is single-phasic.

interesting for high and ultrahigh temperature applications. Thus, the glass transition temperature of silicon oxycarbide glasses was shown to lie in the range of 1350–1400 °C [10,13,14], thus far beyond the glass transition temperature of vitreous silica (*i.e.*, 1170 °C [15]). This is considered to be a consequence of the incorporation of carbon into the silica network. In a recent study, also the effect of the segregated carbon on the high-temperature creep behavior of SiOC was considered and discussed [14].

In the present study we used a SiOC glass free of segregated carbon, which was obtained upon pyrolysis of polysilsesquioxane particles in hydrogen atmosphere [16,17], and subsequent densification by means of hot-pressing at high temperature. The compression creep experiments of the phase-separated sample indicate that at temperatures beyond 1000 °C its shear viscosity is *ca.* 2 orders of magnitude higher than that known for vitreous silica. The analyzed phenomenon is briefly discussed with respect to the presence of mixed-bonds located at the interface between silica and SiC precipitates (*i.e.*, consisting of corner-connected SiO_xC_{4-x} tetrahedra) causing the outstanding creep resistance of the synthesized phase-separated SiOC.

2. Experimental procedure

For the present study white SiOC powder obtained by pyrolysis in hydrogen atmosphere [17] has been used. The SiOC powder was hot-pressed in a graphite mold at 1600 °C with a constant pressure of 50 MPa and a dwell time of 30 min in Argon atmosphere. Monolithic samples were cut from the obtained pellets with a diamond wire cutter and subsequently used for all experiments.

The chemical composition of the hot-pressed samples was determined using a carbon analyzer Leco-200 (Leco Corporation, USA) and a N/O analyzer Leco TC-436 (Leco Corporation, USA). The silicon weight fraction was considered to be the difference to 100 wt.%, assuming no other elements being present in the sample.

Powder XRD measurements were performed in flat-sample transmission geometry on a STOE STADI P diffractometer equipped with a Molybdenum X-ray tube and a position sensitive detector with a 6° aperture.

TEM examinations were performed with a field emission gun (Modell JEM2100F, JEOL, Tokyo, Japan) operating at an acceleration voltage of 200 kV. Specimen preparation followed standard routines: cutting, dimpling and argon-ion thinning to perforation in a Gatan Duomill 600 (Gatan Inc., Pleasanton, USA), followed by thin carbon coating (Bal-Tec RES100, Bal-Tec AG, Liechtenstein), to minimize charging under the electron beam.

MAS NMR experiments were performed on a Bruker Avance II+ spectrometer at 400 MHz proton resonance frequency. Micro-Raman spectra were recorded with a Horiba HR800 micro-Raman spectrometer (Horiba JobinYvon, Bensheim, Germany) equipped with an Ar laser (514.5 nm). The measurements were performed by using a grating of 600 gm m^{-1} and a confocal microscope (magnification 100× NA 0.9) with a 100 μm aperture, giving a resolution of 2–4 μm. The laser power (20 mW) was attenuated by using neutral density filters; thus the power on the sample was in the range from 6 μW to 2 mW.

The high temperature creep experiments where performed on a Zwick universal testing device equipped with a Maytec vacuum furnace (<10^{-4} Pa). The samples were ground and polished to be plane parallel with respect to the creep loaded surface and rectangular in shape with the chosen dimensions of $3 \times 3 \times 5\ mm^3$. For the compression creep tests the samples were coated with hexagonal BN in order to reduce friction between the loading punches and the sample surfaces. The creep behavior was studied in the temperature range between 1100 °C and 1300 °C with an applied constant true stress of 75 MPa. Additionally, measurements were performed at a constant temperature of 1200 °C but with different true stresses between 50 and 100 MPa. True strain and true stress were calculated according to the procedure described in [18] and [19]. The strain rates were computed after reaching the steady-state creep stage, which has been defined as the stage a constant strain rate which does not change after at least 2% plastic strain (*i.e.*, here deformation under load) was observed.

3. Results and discussion

An as-prepared hot-pressed silicon oxycarbide monolith was investigated with respect to its chemical composition, shown in Table 1. As the weight fraction of silicon was not measured but calculated as the difference to 100 wt.%, a relative standard deviation of 2% was assumed in order to perform a propagation of uncertainty. The actual composition indicates the presence of 1.3 vol.% elemental silicon which is however in the size of the uncertainty and can therefore be excluded. This is supported by visible Raman spectroscopy, as neither free carbon nor elemental silicon were detected. The values for the phase composition in Table 2 were obtained by assuming that neither free carbon nor elemental silicon is present.

As shown in Table 2, the chemical composition of the hot-pressed sample does not differ significantly from the composition of the SiOC powder [21]. The main difference here relies on the presence of a significant amount of hydrogen in the starting SiOC

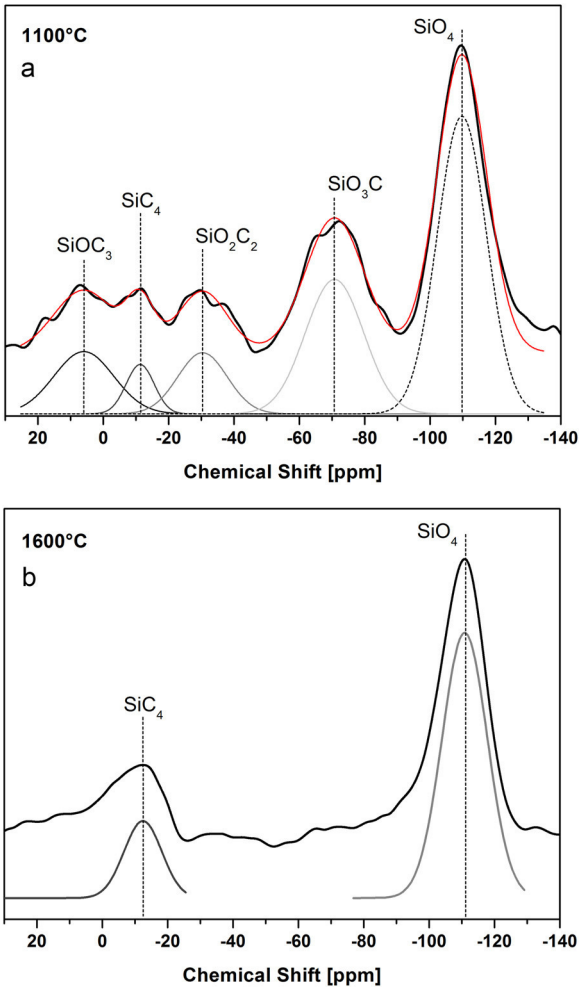

Fig. 1. ^{29}Si MAS NMR of (a) the SiOC powder as-prepared at 1100 °C and (b) of the SiOC sample hot-pressed at 1600 °C.

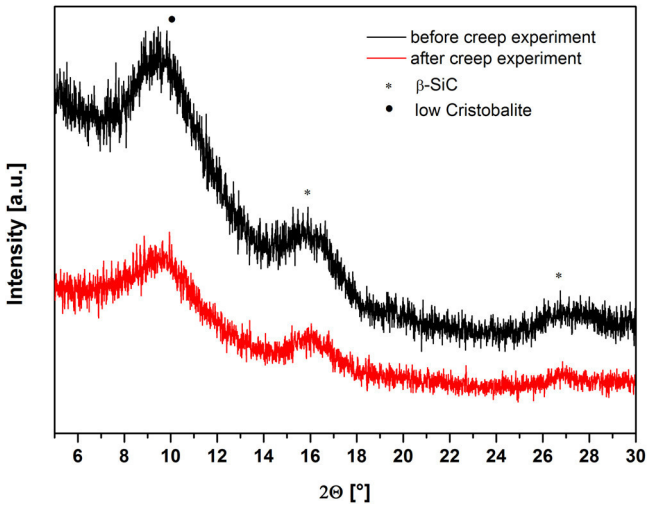

Fig. 2. XRD pattern of the hot-pressed SiOC before and after creep experiments. The XRD pattern was taken from a sample subjected to creep experiments at 1200 °C and varying true stresses between 50 and 100 MPa (elapsed creep measurement time was 42 h; *cf.* Fig. 5b).

powder (Table 1), which was not present in the hot-pressed sample. The chemical composition of the monolithic SiOC indicates that there is no segregated carbon present in the material.

The ^{29}Si MAS NMR spectrum of the starting white SiOC powder used for the preparation of the monolithic specimens (Fig. 1a) reveals as expected the presence of $SiO_{4-x}C_x$ tetrahedra. Thus, the deconvolution of the spectrum indicates the presence of five signals with chemical shifts at +6, −11, −30, −70 and −110 ppm corresponding to $SiOC_3$, SiC_4, SiO_2C_2, SiO_3C and SiO_4 respectively [22] and is in agreement with recent NMR studies of Tavakoli et al. [23]. The NMR spectrum of the hot-pressed monolithic sample (Fig. 1b) reveals that there are no mixed-bonds $SiO_{4-x}C_x$ tetrahedra detectable anymore; instead, only the signals corresponding to SiC_4 and SiO_4 tetrahedra were observed, indicating that the monolithic sample is phase-separated, consisting of a SiC phase dispersed in a silica matrix.

In Fig. 2, the X-ray diffraction pattern of the hot-pressed SiOC sample before and after the compression creep experiments are shown and indicate that the sample is mainly amorphous. The broad reflections at 2θ values of 15.9, 27.3 and 31.3° correspond to β-SiC. There is no indication for the crystallization of low cristobalite in the sample even during thermal-mechanical exposure at 1200 °C.

TEM images of the hot-pressed SiOC sample support the findings of elemental analysis and XRD and are shown in Fig. 3. Spherical β-SiC particles with an average size of 5 nm are homogeneously dispersed in an amorphous matrix. No free carbon phase can be detected. The sample is dense without cracks or pores. In comparison, Fig. 4 shows the TEM micrographs of a crept monolithic SiOC sample, supporting that the high-temperature creep experiments did not induce a crystallization of the silica-rich matrix. The β-SiC crystallites remained constant in particle size during the creep experiment but show an increased crystallinity. No individual SiO_2 precipitates can be identified however the lower °2θ range seems to be slightly organized which might indicate a starting SiO_2 phase crystallization (most probably low Cristobalite).

As shown in Table 2, the phase-separated SiOC sample considered in the present study for the investigation of the high temperature creep behavior can be regarded as consisting of a SiO_2 matrix in which β-SiC particles are homogeneously dispersed. Therefore pure silica will be used in this section as an appropriate reference material for plastic deformation. The compression creep experiments are shown in Fig. 5 and Table 3 summarizes the steady-state creep rates of the SiOC sample.

Interestingly, long loading times (up to more than 6 days, depending on the used temperature and pressure) were needed in order to achieve steady-state conditions.

Using the obtained steady-state strain rates, it is possible to determine the apparent activation energy for creep and the stress exponent using the Norton's power law (Eq. (1)), where $\dot{\varepsilon}$ is the steady-state strain rate, B is a material dependent constant, σ is the applied stress and Q is the activation energy. In a plot $\log(\dot{\varepsilon})$ *vs.* $\log(\sigma)$ (Fig. 6a) the slope gives the stress exponent, whereas the apparent activation energy can be obtained from a $\ln(\dot{\varepsilon})$ *vs.* 1/T plot (Fig. 6b).

$$\dot{\varepsilon} = B\sigma^n e^{-\frac{Q}{RT}} \quad (1)$$

The stress exponent is indicative for the mechanism of plastic deformation. If the dependence of the strain rate on the stress is linear (*i.e.*, the stress exponent n = 1), the materials exhibit a so-called Newtonian viscous flow behavior. This is generally expected for glasses loaded at lower stresses [24]. Higher values for the stress exponent are observed in crystalline solids (n = 3–5) and relate to dislocation climb controlled creep. The creep of superplastic materials shows a stress exponent of n = 2 which rely on grain boundary sliding as creep mechanism. The stress exponent in our material was found to be 1.7, indicating that probably more than one mechanism is active in the creep of our SiOC sample. This is a rather

Table 3
True strain rates measured at different stresses and temperatures during the steady-state creep of the hot-pressed SiOC sample.

Temperature [°C]	True strain rates [s^{-1}]		
	For 50 MPa applied stress	For 75 MPa applied stress	For 100 MPa applied stress
1100	–	1.93×10^{-8} s^{-1}	–
1150	–	1.27×10^{-7} s^{-1}	–
1200	4.67×10^{-7} s^{-1}	1.02×10^{-6} s^{-1}	1.50×10^{-6} s^{-1}
1250	–	8.27×10^{-6} s^{-1}	–
1300	–	3.86×10^{-5} s^{-1}	–

unexpected finding, as recently stress exponents close to unity were reported for phase-separated SiOC glasses [13]. The difference between the SiOC materials reported in the literature and our system is related to the fact that our material is free of segregated carbon (as compared to the samples reported in the literature containing 13 vol.% of segregated carbon [14]).

There are only few publications in the literature reporting on glasses showing stress exponent values of 2. For instance, fiber elongation experiments performed with Rb_2O-containing silica glass [25] and a soda-lime glass [26] led to stress exponent values close to 2. Moreover, Nieh et al. reported on a reciprocal stress exponent of 0.5 (corresponding to n = 2) for a $Zr_{10}Al_5Ti_{17.9}Cu_{14.6}Ni$ metallic glass in the supercooled liquid region. As their metallic glass probably showed some crystallization upon the tensile test, it was suggested that the creep is determined by both grain boundary sliding of the nano-crystalline part and viscous flow of the amorphous part [27]. This consideration might be also applied on the creep behavior of our SiOC sample, as it consists of an amorphous matrix (which will creep by viscous flow) as well as of a nano-crystalline part (β-SiC).

Reger-Leonhard et al. suggested that these findings might also be interpreted as indicating a transition from linear to non-linear flow characteristics upon higher stresses (>100 MPa), as deduced from the transition state theory [28]. Thus, their study of the creep behavior of a $Zr_{55}Cu_{30}Al_{10}Ni_5$ metallic glass both in an amorphous as well as in a partially crystallized state (crystalline content of *ca.* 8 vol%) revealed only minor differences [28]. Also in our case, the possibility of a transition in the mechanism from linear to non-linear at *e.g.*, 100 MPa in our SiOC sample cannot be ruled out. However, more detailed investigation on the high-temperature creep behavior of our single-phase SiOC system is needed in order to clarify the dependence between the stress exponent n and the applied stress.

The apparent activation energy for creep of SiOC in the present study was determined to be 696 kJ/mol. This is significantly higher than the apparent activation energy determined for a SiOC sample containing *ca.* 0.5 vol.% segregated carbon (*i.e.*, 296 kJ/mol [10] for the single-phase materials and 463 kJ/mol for the phase-separated sample [14]) although it is similar to values reported for vitreous silica. Thus, Doremus critically compared the viscosity data of pure silica glass [15] and considered the work of Hetherington et al. [29] on a type I silica (0.0003 wt.% hydroxyl content) to be the most accurate in the temperature range between 1000 °C up to 1400 °C, with an activation energy for viscous flow of 712 kJ/mol.

The similar values of the activation energy for vitreous silica and for our SiOC sample suggest that probably the same process is responsible for the plastic deformation in both the phase-separated SiOC as well as in pure silica glass. It is still questionable whether there are several parallel processes occurring during the creep of our sample, yielding the apparent activation energy.

The shear viscosity can be calculated from creep rates using Eq. (2) assuming a Newtonian behavior during the steady-state creep stage [10]. As our sample has a stress exponent of 1.7 the calculated shear viscosity has to be considered with a larger error. In eq. (2) η is the effective viscosity, σ is the applied stress, ν is the Poisson ratio and $\dot{\varepsilon}$ is the steady-state creep rate. The Poisson ratio of SiOC was measured to be 0.11 by Moysan et al. [30].

$$\eta = \frac{\sigma}{2(1+\nu)\dot{\varepsilon}} \tag{2}$$

It must be taken into account that the Poisson ratio stated in literature was measured on a SiOC sample with 13 vol.% segregated carbon. Though the Poisson ratio might be slightly different for the present sample, the value for vitreous silica is regarded as the upper

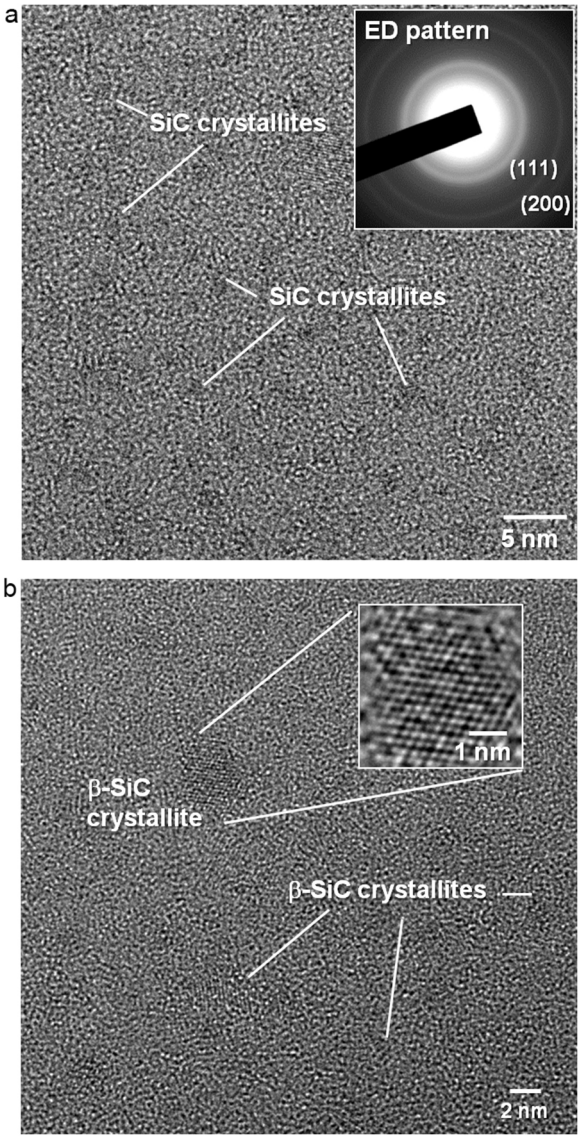

Fig. 3. TEM micrographs of the hot-pressed monolithic SiOC sample showing: (a) SiC nanoparticles homogeneously dispersed within a silica-rich matrix; the ED pattern in the inset shows diffraction rings which were assigned to (111) and (200) planes of β-SiC. (b) the inset shows the filtered iFFT from HRTEM of a β-SiC nanocrystallite.

Table 4
Shear viscosity calculated from Eq. (2) using the Poisson ratio of SiOC (0.11) [30] and of vitreous silica (0.17) [31].

Poisson ratio	Viscosity [Pa s]				
	At 1100 °C	At 1150 °C	At 1200 °C	At 1250 °C	At 1300 °C
0.11	1.75×10^{-15}	2.65×10^{-14}	3.31×10^{-13}	4.09×10^{-12}	8.75×10^{-11}
0.17	1.66×10^{-15}	2.52×10^{-14}	3.14×10^{-13}	3.88×10^{-12}	8.30×10^{-11}

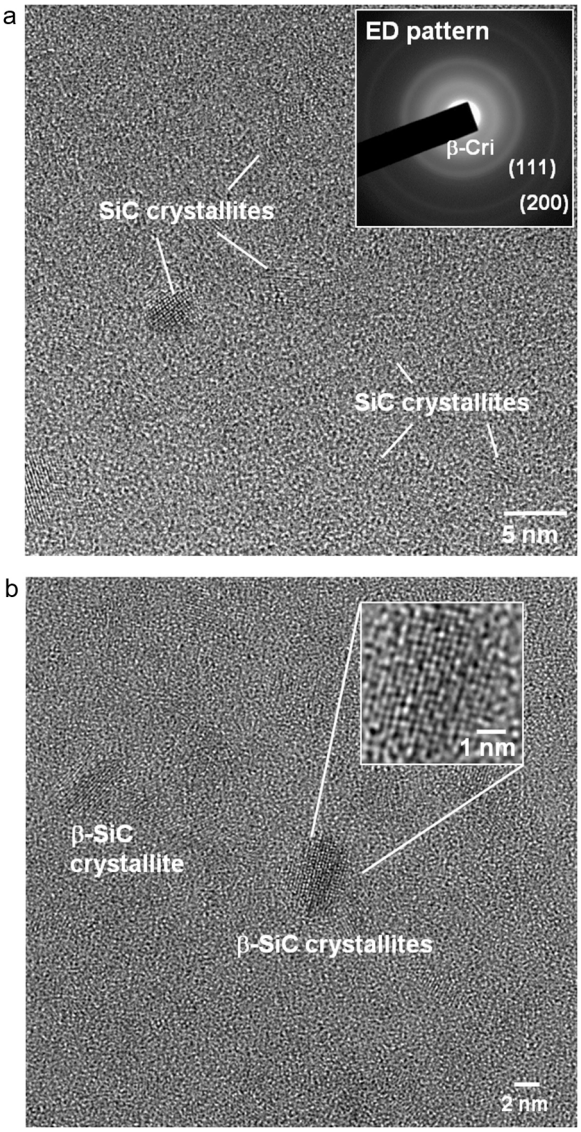

Fig. 4. TEM micrographs hot-pressed monolithic SiOC sample after creep experiments at 1200 °C and varying true stresses between 50 and 100 MPa (elapsed creep measurement time was 42 h; *cf.* Fig. 5b) showing: (a) SiC nanoparticles homogeneously dispersed within a silica-rich matrix; the ED pattern in the inset shows diffraction rings which were assigned to (111) and (200) planes of β-SiC. The inner ring in the ED pattern can be interpreted as the starting crystallization of a SiO_2-phase (low Cristobalite; β-Cri). (b) the inset shows the filtered iFFT from HRTEM of a β-SiC nanocrystallite.

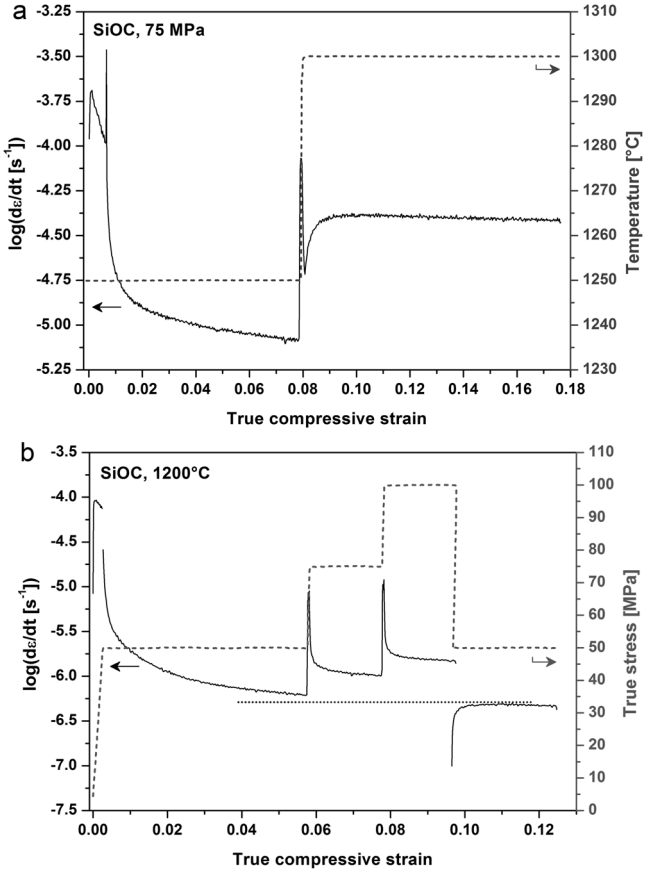

Fig. 5. Logarithmic steady-state creep rates of the monolithic SiOC sample *vs.* true compressive strain at (a) 1250 and 1300 °C and a constant true stress of 75 MPa. The dashed line corresponds to the *y*-axis on the right side showing the actual temperature. (b) constant temperature of 1200 °C and variing stresses of 50, 75 and 100 MPa. The red dashed line corresponds to the *y*-axis on the right side showing actual true stress. The black dotted line is a guide to the eye for comparisson of the staedy-state creep rates at the beginning and at the end of the measurement.

limit for the actual Poisson ratio of the investigated SiOC sample. Table 4 compares the calculated viscosity values obtained by using a Poisson ratio of 0.11 (as for SiOC [30]) and 0.17 (as for vitreous silica [31]). As it is clear from the values shown in Table 4, there are only minor differences resulting from the use of the different Poisson ratios. Hence, the glass transition temperature T_g was estimated to be between 1254 °C (as for $\nu = 0.17$) and 1255 °C (as for $\nu = 0.11$), assuming a viscosity of $10^{12.6}$ Pa at the glass transition.

The calculated shear viscosity of the SiOC sample at different temperatures and a constant true stress of 75 MPa are depicted in Fig. 7. As reference, the measured viscosity of vitreous silica taken from [29] is also depicted.

The calculated viscosity values of the hot-pressed SiOC free of segregated carbon are in good agreement with those obtained from beam bending experiments of an SiOC sample containing low amount of segregated carbon (*i.e.*, *ca.* 0.5 vol%) [10] and are significantly higher (nearly two orders of magnitude) than those reported for vitreous silica.

As mentioned above, the microstructure of our hot-pressed SiOC sample can be regarded as consisting of a glassy SiO_2 matrix in which β-SiC nanoparticles are dispersed. The presence of the nanoparticles is expected to increase the viscosity of the silica matrix by particle hardening. Consequently, it was interesting to understand whether the difference in the viscosity of our phase-separated SiOC and vitreous silica can be explained by the presence of the silicon carbide nanoparticles within the silica rich-matrix. Boccaccini et al. describe the effective viscosity of glasses with rigid

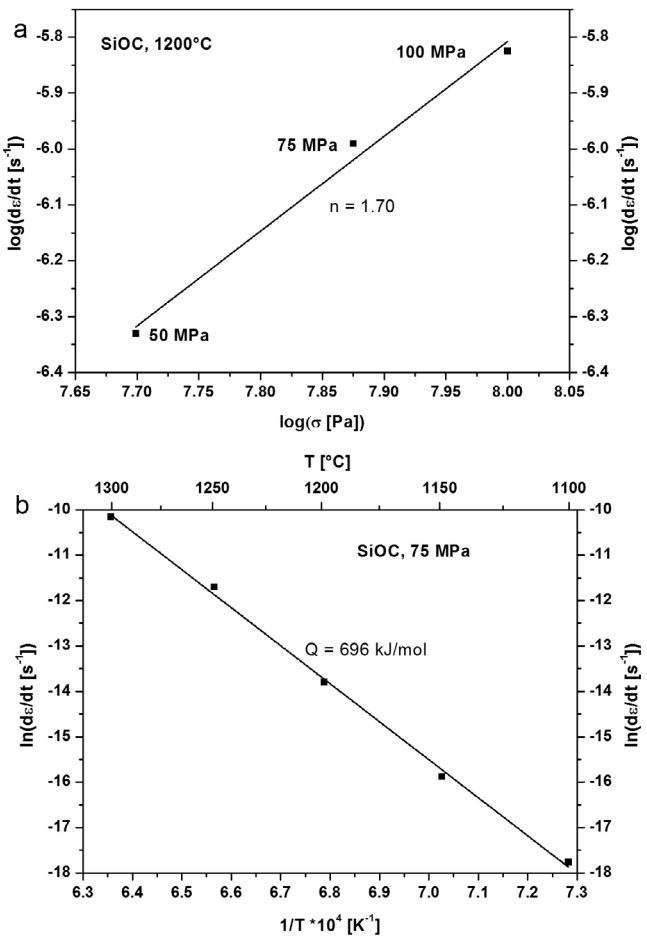

Fig. 6. (a) Steady-state creep rates of SiOC at 1200 °C and varying applied stresses. The slope gives the stress exponent n; (b) steady-state creep rates of SiOC at a constant applied stress (75 MPa) and varying temperatures. The slope gives the apparent activation energy for creep Q.

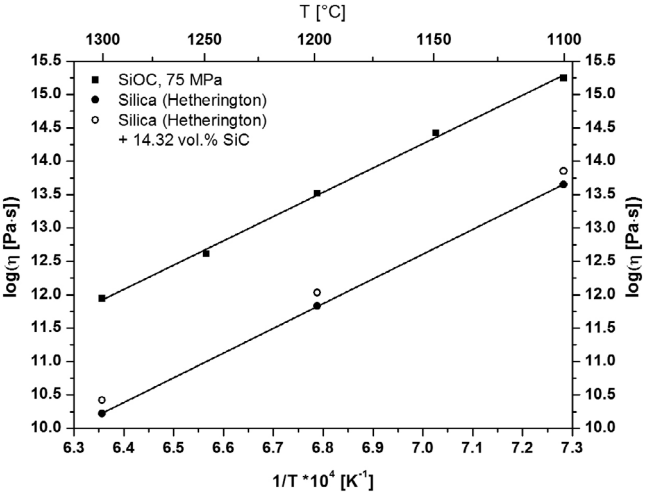

Fig. 7. Viscosity data of SiOC, pure silica and SiC particle-hardened silica calculated from Eqs. (2) and (3).

inclusions with a size between 150 and 300 μm *cf.* the Eq. (3), with $\eta_{matrix}(T)$ being the viscosity of the matrix, f the volume fraction of the dispersed particles and m a function describing the habit of the dispersed particles (*cf.* Eq. (4), F being a so-called shape factor, with the value 1/3 for spherical particle shape) [32].

$$\eta = \eta_{matrix}(1-f)^m \tag{3}$$

$$m = \frac{3F-2}{3F(1-2F)} \tag{4}$$

We have applied the mentioned equations in order to estimate the effect of the presence of SiC nanoparticles in our hot-pressed SiOC sample on its viscosity. Thus, the reported viscosity of pure vitreous silica [29] was used for $\eta_{matrix}(T)$. The volume fraction of SiC particles was taken from Table 2. The effective viscosity values of such a SiO_2/SiC nanocomposite at different temperatures is shown in Fig. 7 (empty circles). Obviously, the particle-hardening due to the presence of the dispersed β-SiC nanoparticles is not sufficient to explain the significantly improved viscosity values of the studied SiOC material as compared to vitreous silica. However, it must be emphasized that Eq. (3) does take into account the amount and shape but not the size of the dispersed particles. Rouxel et al. showed in a series of SiON amorphous glasses mixed in different ratios with SiC particles with varying size (3 μm to 150 μm) that the size of the dispersed particles has a significant influence on the resulting viscosity [33]. Thus, it was shown that for a particle volume fraction of 28 vol.% the relative viscosity of the SiC/SiON composites increases with decreasing the particle size, with a more rapid increase at particle sizes smaller than 16 μm [33]. However, from their data it can be estimated that as long as the volume fraction of the dispersed particles is low (*i.e.*, 10–15 vol.%) the particle size effect on the relative viscosity is not as pronounced as at higher volume fractions (*cf.* 28 vol.% as mentioned above). This estimation is also supported by experiments done on nanofluids (nanocomposites comprised of nanoparticles homogeneously dispersed within a liquid matrix), which indicate that at moderate volume fractions of the nanoparticles (10–15 vol.%), the viscosity of the base fluid increases only moderately with the size of the nanoparticles, *i.e.*, by less than a factor of 10 [34–36].

Indeed, there should be an additional effect contributing to the increase of the viscosity of the hot-pressed (*i.e.*, phase separated) SiOC sample as compared to vitreous silica (nearly 100 times higher). Currently, we consider that $SiO_{4-x}C_x$ tetrahedra present at the interface between the silicon carbide nanoparticles and the glassy silica matrix strongly influence the viscosity of the material. The fact that fully phase-separated SiOC glass might still contain mixed-bonds $SiO_{4-x}C_x$ tetrahedra at the interface between the SiC nanoparticles and the silica matrix was proposed in the past in the literature [37]. However, this assumption was not supported by ^{29}Si NMR data (*i.e.*, neither in the literature, nor in the present study). Thus, more detailed investigation concerning this aspect is needed.

4. Conclusion

High-temperature creep experiments on a hot-pressed SiOC material revealed significantly lower creep rates as compared to vitreous silica. The activation energy for creep (696 kJ/mol) however was found to be similar to that of vitreous silica (712 kJ/mol); whereas the stress exponent was 1.7, indicating some deviation from a truly Newtonian behavior. This has not been clarified yet. The shear viscosity of SiOC is two orders of magnitude higher as compared to that of vitreous silica. This outstanding creep resistance of SiOC cannot be explained solely by particle hardening. Also crystallization processes during the creep experiments can be excluded. Currently, we assume that the interface between the silicon carbide nanoparticles and the glassy silica matrix might have a significant contribution to the unique creep resistance of the SiOC samples free of segregated carbon investigated in this study.

Acknowledgements

The authors thank Prof. Buntkowsky and Dr. H. Breitzke from the TU Darmstadt for recording the MAS NMR spectra and M.Sc. Anke Böttcher for the support with the assessment of the elemental analysis data. Financial support from the Deutsche Forschungsgemeinschaft (IO 64/7-1, "High-Temperature Creep in SiOC-Based Glasses and Glass-Ceramics") as well as from the R&D Convergence Program of MSIP (Ministry of Science, ICT and Future Planning) and NST (National Research Council of Science & Technology) of Republic of Korea (Grant: CMIP-13-4-KIMS) is gratefully acknowledged.

References

[1] A.H. Tavakoli, M.M. Armentrout, S. Sen, A. Navrotsky, Hydrogenated Si-O-C nanoparticles: Synthesis, structure, and thermodynamic stability, J. Mater. Res. 30 (2) (2015) 295–303.
[2] P. Colombo, G. Mera, R. Riedel, G.D. Soraru, Polymer-derived ceramics: 40 years of research and innovation in advanced ceramics, J. Am. Ceram. Soc. 93 (7) (2010) 1805–1837.
[3] H.J. Kleebe, Y.D. Blum, SiOC ceramic with high excess free carbon, J. Eur. Ceram. Soc. 28 (5) (2008) 1037–1042.
[4] Y.D. Blum, D.B. MacQueen, H.J. Kleebe, Synthesis and characterization of carbon-enriched silicon oxycarbides, J. Eur. Ceram. Soc. 25 (2–3) (2005) 143–149.
[5] A. Saha, R. Raj, Crystallization maps for SiCO amorphous ceramics, J. Am. Ceram. Soc. 90 (2) (2007) 578–583.
[6] L. Bois, J. Maquet, F. Babonneau, D. Bahloul, Structural characterization of sol-gel derived oxycarbide glasses. 2. Study of the thermal stability of the silicon oxycarbide phase, Chem. Mater. 7 (5) (1995) 975–981.
[7] H. Brequel, J. Parmentier, S. Walter, R. Badheka, G. Trimmel, S. Masse, J. Latournerie, P. Dempsey, C. Turquat, A. Desmartin-Chomel, L.L. Neindre-Prum, U.A. Jayasooriya, D. Hourlier, H.J. Kleebe, G.D. Soraru, S. Enzo, F. Babonneau, Systematic structural characterization of the high-temperature behavior of nearly stoichiometric silicon oxycarbide glasses, Chem. Mater. 16 (13) (2004) 2585–2598.
[8] P. Dibandjo, S. Dire, F. Babonneau, G.D. Soraru, Influence of the polymer architecture on the high temperature behavior of SiCO glasses: a comparison between linear- and cyclic-derived precursors, J. Non-Cryst. Solids 356 (3) (2010) 132–140.
[9] M. Esfehanian, R. Oberacker, T. Fett, M.J. Hoffmann, Development of dense filler-free polymer-derived SiOC ceramics by field-assisted sintering, J. Am. Ceram. Soc. 91 (11) (2008) 3803–3805.
[10] T. Rouxel, G.-D. Soraru, J. Vicens, Creep viscosity and stress relaxation of gel-derived silicon oxycarbide glasses, J. Am. Ceram. Soc. 84 (5) (2001) 1052–1058.
[11] T. Rouxel, G. Massouras, G.D. Soraru, High temperature behavior of a gel-derived SiOC glass: elasticity and viscosity, J. Sol-Gel Sci. Technol. 14 (1) (1999) 87–94.
[12] A. Scarmi, G.D. Soraru, R. Raj, The role of carbon in unexpected visco(an)elastic behavior of amorphous silicon oxycarbide above 1273 K, J. Non-Cryst. Solids 351 (27–29) (2005) 2238–2243.
[13] B. Papendorf, E. Ionescu, H.-J. Kleebe, C. Linck, O. Guillon, K. Nonnenmacher, R. Riedel, High-temperature creep behavior of dense SiOC-based ceramic nanocomposites: microstructural and phase composition effects, J. Am. Ceram. Soc. 96 (1) (2013) 272–280.
[14] E. Ionescu, C. Balan, H.-J. Kleebe, M.M. Mueller, O. Guillon, D. Schliephake, M. Heilmaier, R. Riedel, High-temperature creep behavior of SiOC glass-ceramics: influence of network carbon versus segregated carbon, J. Am. Ceram. Soc. 97 (12) (2014) 3935–3942.
[15] R.H. Doremus, Viscosity of silica, J. Appl. Phys. 92 (12) (2002) 7619–7629.
[16] M. Narisawa, T. Kawai, S. Watase, K. Matsukawa, T. Dohmaru, K. Okamura, A. Iwase, Long-lived photoluminescence in amorphous Si-O-C(-H) ceramics derived from polysiloxanes, J. Am. Ceram. Soc. 95 (12) (2012) 3935–3940.
[17] M. Narisawa, S. Watase, K. Matsukawa, T. Dohmaru, K. Okamura, White Si-O-C(-H) particles with photoluminescence synthesized by decarbonization reaction on polymer precursor in a hydrogen atmosphere, Bull. Chem. Soc. Jpn. 85 (6) (2012) 724–726.
[18] D. Schliephake, M. Azim, K. von Klinski-Wetzel, B. Gorr, H.-J. Christ, H. Bei, E.P. George, M. Heilmaier, High-temperature creep and oxidation behavior of Mo-Si-B alloys with high Ti contents metall, Mater. Trans. A 45 (3) (2014) 1102–1111.
[19] J.R. Davis, Tensile Testing, 2 ed., ASM International, 283, 2004.
[20] G.M. Renlund, S. Prochazka, R.H. Doremus, Silicon oxycarbide glasses: part II. Structure and properties, J. Mater. Res. 6 (12) (1991) 2723–2734.
[21] M. Narisawa, K. Terauds, G. Ma, H. Hokazono, R. Raj, A. Iwase, Evaluation of high temperature resistance of white Si-O-C(-H) ceramics in an inert atmosphere, J. Non-Cryst. Solids 410 (2015) 106–111.
[22] S.J. Widgeon, S. Sen, G. Mera, E. Ionescu, R. Riedel, A. Navrotsky, 29Si and 13C solid-state NMR spectroscopic study of nanometer-scale structure and mass fractal characteristics of amorphous polymer derived silicon oxycarbide ceramics, Chem. Mater. 22 (23) (2010) 6221–6228.
[23] A.H. Tavakoli, M.M. Armentrout, M. Narisawa, S. Sen, A. Navrotsky, White Si-O-C ceramic: structure and thermodynamic stability, J. Am. Ceram. Soc. 98 (1) (2015) 242–246.
[24] J.H. Simmons, R.K. Mohr, C.J. Montrose, Non-Newtonian viscous flow in glass, J. Appl. Phys. 53 (6) (1982) 4075–4080.
[25] J.H. Li, D.R. Uhlmann, Flow of glass at high stress levels: i. Non-Newtonian behavior of homogeneous 0.08 Rb20.0.92 SiO2 glasses, J. Non-Cryst. Solids 3 (1) (1969) 127–147.
[26] J.H. Simmons, R. Ochoa, K.D. Simmons, J.J. Mills, Non-Newtonian viscous flow in soda-lime-silica glass at forming and annealing temperatures, J. Non-Cryst. Solids 105 (3) (1988) 313–322.
[27] T.G. Nieh, T. Mukai, C.T. Liu, J. Wadsworth, Superplastic behavior of a Zr-10Al-5Ti-17.9Cu-14.6Ni metallic glass in the supercooled liquid region, Scr. Mater. 40 (9) (1999) 1021–1027.
[28] A. Reger-Leonhard, M. Heilmaier, J. Eckert, Newtonian flow of Zr55Cu30Al10Ni5 bulk metallic glassy alloys, Scr. Mater. 43 (5) (2000) 459–464.
[29] G. Hetherington, K.H. Jack, J.C. Kennedy, Viscosity of vitreous SiO2, Phys. Chem. Glasses 5 (5) (1964) 130–136.
[30] C. Moysan, R. Riedel, R. Harshe, T. Rouxel, F. Augereau, Mechanical characterization of a polysiloxane-derived SiOC glass, J. Eur. Ceram. Soc. 27 (1) (2006) 397–403.
[31] R. Brueckner, Mechanical Properties of Glasses, VCH, 1991.
[32] A.R. Boccaccini, On the viscosity of glass composites containing rigid inclusions, Mater. Lett. 34 (3–6) (1998) 285–289.
[33] T. Rouxel, B. Baron, P. Verdier, T. Sakuma, SiC particle reinforced oxynitride glass: stress relaxation, creep and strain-rate imposed experiments, Acta Mater. 46 (17) (1998) 6115–6130.
[34] S.K. Verma, A.K. Tiwari, Progress of nanofluid application in solar collectors: a review, Energy Convers. Manage. 100 (2015) 324–346.
[35] C.T. Nguyen, F. Desgranges, G. Roy, N. Galanis, T. Mare, S. Boucher, H. Angue Mintsa, Temperature and particle-size dependent viscosity data for water-based nanofluids—hysteresis phenomenon, Int. J. Heat Fluid Flow 28 (6) (2007) 1492–1506.
[36] A.T. Utomo, H. Poth, P.T. Robbins, A.W. Pacek, Experimental and theoretical studies of thermal conductivity, viscosity and heat transfer coefficient of titania and alumina nanofluids, Int. J. Heat Mass Transfer 55 (25–26) (2012) 7772–7781.
[37] H.-J. Kleebe, C. Turquat, G.D. Soraru, Phase separation in an SiCO glass studied by transmission electron microscopy and electron energy-loss spectroscopy, J. Am. Ceram. Soc. 84 (5) (2001) 1073–1080.

ADVANCED ENGINEERING MATERIALS
www.aem-journal.com

Influence of SiC/Silica and Carbon/Silica Interfaces on the High-Temperature Creep of Silicon Oxycarbide-Based Glass Ceramics: A Case Study

*Christina Stabler, Daniel Schliephake, Martin Heilmaier, Tanguy Rouxel, Hans-Joachim Kleebe, Masaki Narisawa, Ralf Riedel, and Emanuel Ionescu**

In the present study, the high-temperature creep behavior of three SiOC glass ceramics with different phase compositions are compared by the authors. All three SiOC glass ceramics have a vitreous silica matrix in common, but comprise different homogeneously dispersed phases: 1) only spherical β-SiC nanoparticles (sample denoted hereafter SiC/SiO_2), 2) only high-aspect ratio sp^2-hybridized carbon (i.e., C/SiO_2), and 3) both phases (SiC and segregated carbon, i.e., C/SiC/SiO_2). Compression creep experiments are performed at temperatures in the range between 1100 and 1300 °C and true stresses of 50 to 200 MPa. The determined activation energy for creep of the SiOC glass ceramics of around 700 kJ mol^{-1} is independent of the phase composition. A stress exponent value of approximately 2 indicates an interface-controlled deformation mechanism. All SiOC glass ceramics exhibit significantly higher creep viscosities than that of vitreous silica. Surprisingly, the spherical β-SiC nanoparticles have a higher impact on the effective creep viscosities of SiOC as compared to that of the high-aspect ratio segregated carbon phase. It is concluded that this originates from the β-SiC/silica and C/silica interfaces, which have different effects on the creep behavior of silicon oxycarbide-based glass ceramics.

Dr. E. Ionescu, C. Stabler, Prof. R. Riedel
Technical University of Darmstadt
Institute of Materials Science
Jovanka-Bontschits-Strasse 2, D-64287 Darmstadt, Germany
E-mail: ionescu@materials.tu-darmstadt.de

Dr. D. Schliephake, Prof. M. Heilmaier
Karlsruher Institut für Technologie
Institut for Applied Materials
Engelbert-Arnold-Strasse 4, D-76131 Karlsruhe, Germany

Prof. T. Rouxel
University of Rennes 1
Physics Institute
IPR UMR UR1-CNRS 6251, Campus Beaulieu, 35042 Rennes cedex, France

Prof. H.-J. Kleebe
Technische Universität Darmstadt
Institute of Applied Geoscience
Schnittspahnstrasse 9, D-64287 Darmstadt, Germany

Prof. M. Narisawa
Osaka Prefecture University
Graduate School of Engineering
1-1, Gakuen-Cho, Sakai 599-8531, Japan

DOI: 10.1002/adem.201800596

Dedicated to Prof. Peter Greil on the occasion of his 65th Birthday

1. Introduction

Silicon oxycarbides (SiOCs)[1–4] are promising materials for high temperature application due to their high stability in harsh environments. They are mainly synthesized via the pyrolysis of preceramic polymeric precursors such as polyorganosiloxanes or precursors that are derived from sol-gel synthesis of alkoxysilanes.[1,4,5] During the pyrolysis in inert atmosphere, Si-O and Si-C bonds of the precursors are preserved to yield X-ray amorphous silicon oxycarbides at 1000 °C. The glassy network of SiOC consists of tetrahedrally coordinated silicon atoms that are connected to oxygen and carbon. The special distribution of these corner-shared so-called mixed-bonds $SiO_{4-x}C_x$ tetrahedra is still a matter of debate in literature.[6,7] At higher temperatures, that is, 1150–1200 °C, the onset of the phase separation of the glassy matrix occurs to yield SiOC glass ceramics that consist of a vitreous silica matrix in which SiC nanoparticles are homogeneously dispersed.[8–10] The phase separation can be followed by ^{29}Si MAS NMR spectroscopy, revealing the increase of SiO_4 and SiC_4 tetrahedra at the expense of the mixed-bonds tetrahedra.[8,11] The phase separation is a continuous process and is not finished before 1400 °C.[8,11] Interestingly, the silica matrix keeps its amorphous nature up to temperatures of 1500 °C. Beyond that temperature the SiOC glass ceramics start to decompose.[8–10] SiOC glasses and glass ceramics have no fixed stoichiometric composition and are usually divided into carbon-rich and low carbon containing SiOC glasses. Depending on the chemical composition, a secondary phase consisting of sp^2-hybridized carbon, the so-called segregated or "free" carbon phase, is homogeneously dispersed in the glassy SiOC matrix.

On the atomistic level, the SiOC glassy network can be formally regarded as vitreous silica with bivalent oxygen being partly replaced by tetravalent carbon. The exchange leads to an increase in the glass network connectivity and is consequently considered to significantly improve the (thermo)mechanical properties of silicon oxycarbides in comparison to those of

vitreous silica, for example, SiOC glasses exhibits higher Young's modulus, hardness, flexural strength and glass transition temperature T_g as well as crystallization resistance.[12–14] Furthermore, also SiOC-based glass ceramics, that is, phase-separated silicon oxycarbides, exhibit an increase in Young's modulus, hardness, and T_g as compared to vitreous silica.[15,16] Additionally, SiOC glasses and glass ceramics show excellent creep resistance at high temperatures.[13,16–18] This is considered to rely on the "reinforcing" effect of the dispersed carbon and SiC precipitates in the silica matrix.[13,16,17,19,20]

In a previous case study,[17] we tried to rationalize the influence of the phase composition of SiOC glass ceramics on their creep behavior, namely to assess the effect of the segregated carbon versus the network carbon on the high-temperature creep of SiOC glass ceramics. Thus, a series of SiOC glass ceramics with varying degree of segregated carbon (from ca. 1 to ca. 11 vol %) was analyzed. It was found that the creep resistance and strain recovery in SiOC glass ceramics increase with increasing amount of segregated carbon. However, there is a lack of information on the effect of the amount of SiC nano particles on the HT creep behavior of SiOC glass ceramics.

Recently, it was found that upon the proper choice of the pyrolysis atmosphere, two special SiOC compositions can be accessed[21]: The pyrolysis of a polysilsesquioxane under hydrogen atmosphere leads to the selective elimination of the segregated carbon phase, whereas the pyrolysis of the same precursor under CO_2 atmosphere leads to the selective elimination of the network carbon.[21] Thus, the thermal conversion of the precursor in H_2 atmosphere delivers an SiOC glass with negligible amount of segregated carbon[18,21,22]; whereas its conversion in CO_2 delivers a nanocomposite consisting of vitreous silica and segregated carbon, that is, C/SiO_2.[21]

In the present study, the creep behavior of these two unique compositions of SiOC glass ceramics (i.e., SiC/SiO_2 and C/SiO_2) is studied and compared to that of a glass ceramic consisting of vitreous silica matrix and both disperse phases, that is, SiC and carbon (i.e., C/SiC/SiO_2). The influence of the segregated carbon phase and the influence of SiC nanoparticles on the creep behavior of SiOC glass ceramics is addressed and possible implications of the SiC/silica and C/silica interfaces are discussed.

2. Experimental Section

2.1. Materials Synthesis

Monolithic specimens were obtained using uniaxial hot-pressing of SiOC glass powders at 1600 °C in a cylindrical graphite die at a constant pressure of 50 MPa (duration of pressing 30 min) in static argon atmosphere. Suitable monolithic coupons were cut from the obtained monolithic samples with a diamond wire cutter and used for the experiments.

The synthesis procedure of the SiOC glass powders used as starting materials for the two glass ceramic compositions investigated in the present study, that is, SiC/SiO_2 and C/SiO_2, is described in detail in ref. [21]. Both SiOC glass powders were synthesized from the same polymeric precursor but were pyrolyzed under different atmospheres. For SiC/SiO_2, the polymeric precursor was pyrolyzed in hydrogen atmosphere, whereas for sample C/SiO_2, the precursor was pyrolyzed in CO_2 and subsequently in Argon atmosphere. Afterwards, both glass powders were consolidated by hot-pressing. The third sample, that is, C/SiC/SiO_2, was prepared from the commercially available polymethylsilsequioxane Belsil PMS MK (Wacker GmbH, Burghausen, Germany). The polymer was crosslinked in an alumina tube furnace at 250 °C for 2 h under flowing argon atmosphere and subsequently heat-treated at 1000 °C for 2 h. The heating and cooling rates were 100 °C h^{-1}. The obtained glassy chunks were crushed and sieved using a mesh size of 40 μm to obtain the glass powder.

2.2. Materials Characterization

The chemical composition of the samples was determined using a carbon analyzer Leco-200 (Leco Corporation, USA) and a N/O analyzer Leco TC-436 (Leco Corporation, USA). Archimedean (skeletal) density and open porosity was measured utilizing water immersion technique. Precise density measurements were performed by the flotation method in a density gradient column.[23] The chosen heavy liquids were iodobenzene ($\rho = 1.83\,g\,cm^{-3}$) and methylene iodide ($\rho = 3.32\,g\,cm^{-3}$). Details are described in ref. [24]. The accuracy of the used setup is estimated to be $0.001\,g\,cm^{-3}$. As reference materials, two different window glasses (with $\rho = 2.161$ and $2.514\,g\,cm^{-3}$) as well as crystalline silicon ($\rho = 2.333\,g\,cm^{-3}$) were used. MAS NMR experiments were performed on a Bruker AvanceII+ spectrometer at 400 MHz proton resonance frequency. TEM examinations were performed with a field emission gun (Modell JEM2100F, JEOL, Tokyo, Japan) operating at an acceleration voltage of 200 kV. Specimen preparation followed standard routines, that is, cutting, dimpling and argon-ion thinning to perforation in a Gatan Duomill 600 (Gatan Inc., Pleasanton, USA), followed by thin carbon coating (Bal-Tec RES100, Bal-Tec AG, Liechtenstein), in order to minimize charging under the electron beam.

Powder XRD measurements were performed in flat-sample transmission geometry on a STOE STADI P diffractometer (Stoe, Darmstadt, Germany) equipped with a Molybdenum X-ray tube and a position sensitive detector with a 6° aperture. Raman spectra were recorded on a Horiba HR800 micro-Raman spectrometer (Horiba JobinYvon, Bensheim, Germany) equipped with a He-Ne laser (633 nm). The measurements were performed by using a grating of $600\,g\,mm^{-1}$ and a confocal microscope (magnification 50 × NA0.75–numerical aperture) with a 100 μm aperture, giving a resolution of approximately 1 μm. The laser power (20 mW) was attenuated by using neutral density filters.

2.3. High-Temperature Creep Measurements

The high temperature creep experiments where performed in compression using a Zwick universal testing device equipped with a Maytec vacuum furnace ($<10^{-4}$ Pa). The rectangular samples (dimensions of $3 \times 3 \times 5\,mm^3$) were ground and polished to be plane parallel with respect to the mechanically loaded surface. For the high-temperature compression creep

tests, the samples were coated with hexagonal BN in order to reduce friction between the loading punches and the sample surfaces. The experiments were performed at temperatures between 1100 and 1300 °C and applied true stresses between 50 and 200 MPa. Creep recovery measurements were conducted at 1200 °C and 100 MPa true stress. After reaching the steady-state regime, that is, a constant strain rate at constant true stress over a notable compressive strain, the stress was released and the elastic recovery was recorded. True strain and true stress were calculated according to the procedure described in refs. [25] and [26]. The strain rates were computed after reaching the steady-state creep stage.

3. Results and Discussion

3.1. Material Characterization

The elemental compositions of the investigated monoliths are summarized in **Table 1**. All three samples reveal substantial differences regarding the molar fractions of oxygen and carbon. This can be further rationalized by calculating the volume fractions of the phases assumed to be present in SiOC glass ceramics, that is, amorphous silica matrix with homogeneously dispersed nano-sized β-SiC particles and sp^2-hybridized carbon.[18,27] Considering the absence of C-O bonds in SiOC materials as evidenced by ^{13}C MAS NMR spectroscopy,[7] the phase composition in the system SiO_2–SiC–C can be calculated for each sample. The results are displayed in Table 1. Sample SiC/SiO_2 reveals the presence of 14.3 vol% SiC nanoparticles dispersed within amorphous silica; there is no sp^2-hybridized carbon in SiC/SiO_2.[18] In contrast, sample C/SiO_2 is a composite containing ca. 11.5 vol% segregated carbon homogeneously dispersed within vitreous silica, with a negligible amount of SiC nanoparticles. Sample $C/SiC/SiO_2$ reveals the presence of all three phases (vitreous silica, 12.3 vol% SiC and 11.9 vol% segregated carbon, see Table 1). It should be noted that the volume fraction of silica in $C/SiC/SiO_2$ is significantly lower than that in SiC/SiO_2 and C/SiO_2 (ca. 76 vol % vs. ca. 86 and 87 vol%, respectively). This has been considered accordingly during the evaluation of the creep behavior of the samples, as will be discussed below.

^{29}Si MAS NMR spectroscopy, TEM imaging, XRD, and Raman spectroscopy were performed in order to evaluate the phase compositions of the investigated samples. **Figure 1** compares the ^{29}Si MAS NMR spectra of the investigated glass ceramics, that is, SiC/SiO_2, C/SiO_2, and $C/SiC/SiO_2$. The main signal in C/SiO_2 exhibits a chemical shift of ca. −111 ppm related to SiO_4 tetrahedra, indicating that in C/SiO_2 no SiC nanoparticles are present; whereas the ^{29}Si MAS NMR spectra of SiC/SiO_2 and $C/SiC/SiO_2$ show in addition to the signal at −111 ppm a signal with a chemical shift of ca. −11 ppm and −18 ppm, respectively, which was assigned to SiC_4.[17,18] Despite the resolution of the spectra is not very high and thus it does not allow any unambiguous statement about the presence of $SiO_{4-x}C_x$ mixed-bond tetrahedra (see discussion below), it can be concluded that SiC nanoparticles are present in both samples, that is, SiC/SiO_2 and $C/SiC/SiO_2$, as also supported by TEM imaging (see **Figure 2**) and X-ray diffraction (see **Figure 3**a).

This finding has been substantiated by TEM imaging. As shown in Figure 2, sample C/SiO_2 reveals only the presence of nanoscaled sp^2-hybridized carbon dispersed within an amorphous silica matrix. The segregated carbon phase has a high aspect ratio (i.e., ratio between length and lateral size/width) of 10 to 20 in accordance to previous studies on SiOC.[16] In comparison, in SiC/SiO_2 only nano-sized SiC particles are present; whereas in $C/SiC/SiO_2$ both disperse phases are present in the silica matrix.

X-ray diffraction patterns of SiC/SiO_2 and $C/SiC/SiO_2$ show the presence of broad, but noticeable reflections related to nano-sized β-SiC (as it was also revealed by selected area diffraction SAED during the HR TEM investigation); those are absent in the diffractogram of C/SiO_2 (*cf.* Figure 3a). The broad hump centered at a 2θ value of approximately 10° is caused by the presence of amorphous silica. No indications for the crystallization of cristobalite are visible.

Figure 3b displays the Raman spectra of C/SiO_2 and $C/SiC/SiO_2$. Both samples reveal the typical features of disordered carbon materials, namely the G band at 1575–1595 cm^{-1}, the D band at ca. 1350 cm^{-1} (for an excitation wavelength of 514.5 nm), a band related to C-C sp^3 vibrations at ca. 1150–1200 cm^{-1} and the D' band at ca. 1620 cm^{-1}. Additionally, the overtone of the D band, namely 2D band, at 2500–2800 cm^{-1} and the combinational mode D + G band at ca. 2900 cm^{-1} are visible.[29] The Raman spectrum of SiC/SiO_2 (not shown) lacks any bands and confirm the fact that there is no sp^2 hybridized excess carbon in SiC/SiO_2.

The degree of graphitization in C/SiO_2 and $C/SiC/SiO_2$ does not show significant differences as rationalized by some calculated graphitization indicators L_a, L_D, and L_{eq}.[30–32] L_a describes the lateral crystal size of individual domains of the

Table 1. Chemical composition obtained from elemental analysis, estimated phase composition and density of the prepared SiOC glass ceramics.

Sample	Elemental composition	Phase composition			Density [g cm^{-3}]
		SiO_2 [vol%]	SiC [vol%]	C_{free} [vol%]	
SiC/SiO_2	$SiO_{1.47}C_{0.24}$	85.7	14.3	0	2.36
C/SiO_2	$SiO_{1.94}C_{0.53}$	87.2 ± 1.0	1.3 ± 1.0	11.5 ± 0.6	2.20
$C/SiC/SiO_2$	$SiO_{1.50}C_{0.71}$	75.7 ± 0.4	12.3 ± 1.0	11.9 ± 0.7	2.31

Volume fractions of the phases are calculated assuming the following densities: $\rho(SiO_2) = 2.20\,g\,cm^{-3}$,[20] $\rho(\beta\text{-SiC}) = 3.22\,g\,cm^{-3}$,[28], $\rho(C) = 1.82\,g\,cm^{-3}$ (Graphitized Mesoporous Carbons GMC, Sigma-Aldrich, CAS-# 1333-86-4)

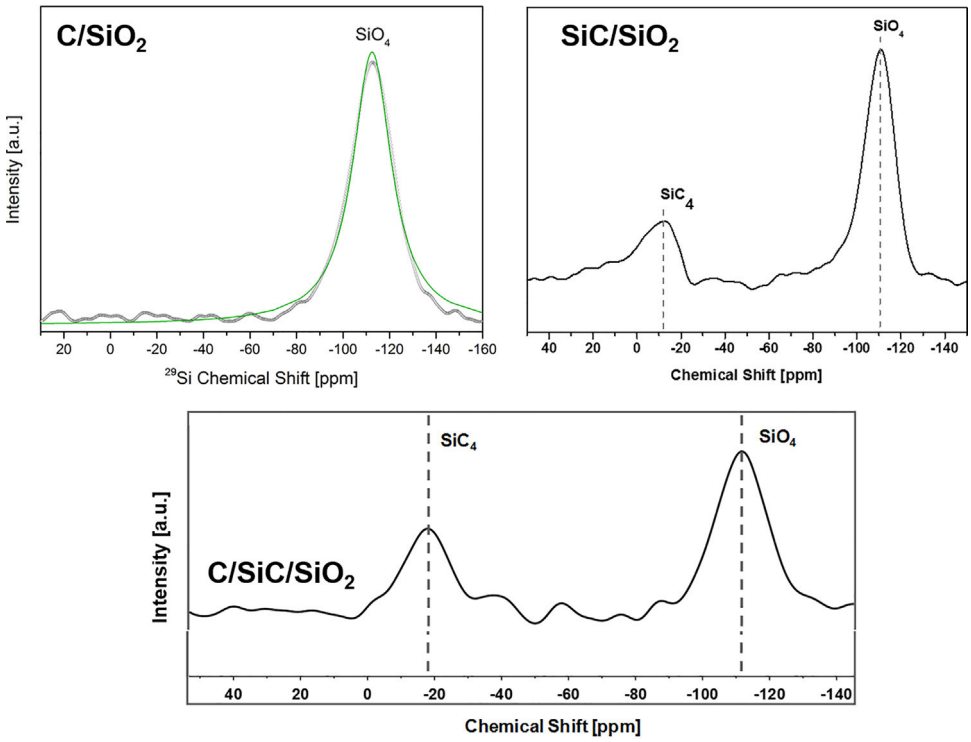

Figure 1. ^{29}Si MAS NMR of the a) C/SiO_2, b) SiC/SiO_2, and c) $C/SiC/SiO_2$ glass ceramics.

segregated carbon phase, whereas L_{eq} considers as well the tortuosity of the domains. L_D measures the average inter-defect distance. The average lateral crystal size L_a of the studied samples is in the same range as the mean inter-defect distance (Figure 3b). The equivalent size L_{eq} is only slightly larger than L_a, indicating that the carbon precipitates are nano-scaled.[27] Moreover, the width of the D and G bands ranges between 40 and 50 cm^{-1} which is close to the values known for glassy carbon ($w_D = 52.7\ cm^{-1}$; $w_G = 56.1\ cm^{-1}$).[33] Thus, we can consider the segregated carbon phase in the studied SiOC glass ceramics as being nano-scaled and poorly ordered.

As a consequence of the results above, all three investigated samples can be regarded as SiOC glass ceramics that have a vitreous silica matrix in common, but different kinds and/or amounts of dispersed phases, namely β-SiC and segregated carbon.

The different phase compositions have a direct impact on the skeletal density of the investigated SiOC samples as evidenced in Table 1. Samples containing SiC particles, that is, SiC/SiO_2 and $C/SiC/SiO_2$, have higher densities of 2.36 and 2.31 $g\,cm^{-3}$, respectively; whereas the density of C/SiO_2 (2.20 $g\,cm^{-3}$) is similar to that of vitreous silica. All hot-pressed SiOC monoliths are dense and crack-free, hence being suitable to investigate the intrinsic creep behavior of SiOC materials.

As discussed already in ref. [18], SiC/SiO_2 does not crystallize during the creep experiments. This is important to verify, as crystallization would lead to a decrease of the creep rates due to strain hardening caused by the crystalline particles,[13] hindering the precise assessment of the creep behavior. Moreover, the post-creep samples did not show evidence of any changes in their microstructure, as also reported previously.[18]

A further fundamental concept of creep is the conservation of the volume during the (plastic) deformation. This requirement is clearly fulfilled in our samples. For instance, a significant densification is known to start in vitreous silica only at pressures beyond several GPa.[34] It is reasonable to expect that a densification of SiOC glass ceramics may occur in a similar range of pressure, as the matrix consists of vitreous silica. As a proof of concept, the precise density of $C/SiC/SiO_2$ was assessed before and after the different creep experiments using the flotation method in a density gradient column.[23,24] The results for $C/SiC/SiO_2$ are shown in **Figure 4**. As expected, the density of the samples does not change during the creep experiment, independently of the used temperature and mechanical load. Moreover, the results indicate that there is no micro-cracking occurring during the creep. Thus, any non-negligible change in the volume of the studied samples during the HT creep experiments can be ruled out.

3.2. High-Temperature Creep Experiments

All SiOC samples developed a steady-state regime, that is, a constant strain rate over a minimum range of 2% plastic strain at constant true stress, during the creep experiments. This required relatively long holding times (up to 14 days, depending on the phase composition, measurement temperature, and applied pressure). **Table 2** summarizes the steady-state creep rates of the three different SiOC samples. In order to analyze the creep behavior of the SiOC glass ceramics, the activation energy for creep Q and the stress exponent n were determined. Both are

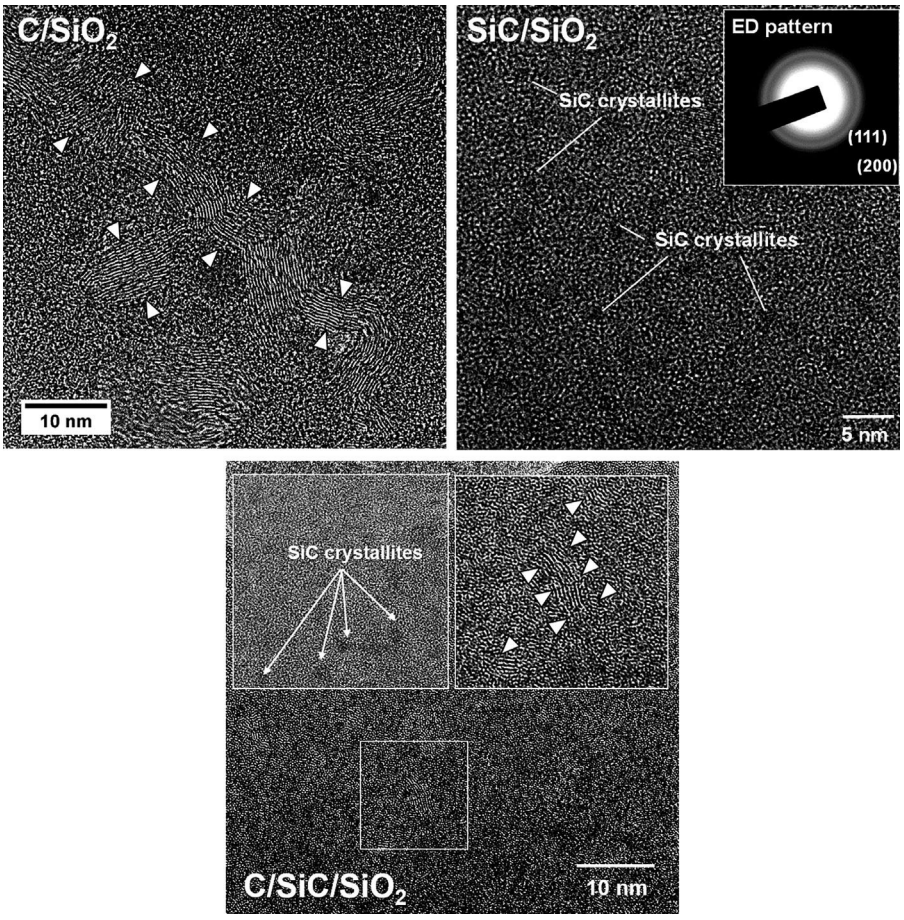

Figure 2. HR TEM micrographs of C/SiO_2, SiC/SiO_2 and $C/SiC/SiO_2$.

connected via the temperature dependent (Arrhenius type) Norton's power law (*cf.* Equation (1)), with $\dot{\varepsilon}$ being the steady-state strain rate, B a material-dependent constant, σ being the applied stress, and Q the activation energy for creep. The activation energy Q characterizes the activation volume or the species carrying the plastic deformation, whereas the stress exponent n is indicative for the actual creep mechanism.

$$\dot{\varepsilon} = B\sigma^n e^{-\frac{Q}{RT}} \tag{1}$$

The activation energy Q for creep of sample $C/SiC/SiO_2$ was investigated at two different applied true stresses, namely 50 and 75 MPa. **Figure 5**a shows the Arrhenius plot of the steady-state creep rates of $C/SiC/SiO_2$ at these stresses with the corresponding Q values of 740 and 730 kJ mol^{-1}, respectively. Consequently, it can be concluded that the activation energy for creep does not change significantly with the applied loading. It should be mentioned that these values are rather different from the values in the range of ca. 300 kJ mol^{-1} determined under similar experimental conditions for SiOC glass ceramics showing similar phase compositions to that of $C/SiC/SiO_2$,[16,17] though similar to the value of 712 kJ mol^{-1} reported by Hetherington et al. for vitreosil, that is, a fused silica containing some metallic impurities (interestingly, hydroxyl-group containing sol-gel-based silica, that is, spectrosil, was found in the same study to exhibit an activation energy of only 510 kJ mol^{-1}).[35]

The creep viscosity can be calculated using Equation (2) in the case of a steady-state behavior, where η is the apparent viscosity, σ is the applied stress, ν is Poisson's ratio, and $\dot{\varepsilon}$ is the steady-state creep rate. Poisson's ratio of the investigated SiOC glass ceramics has been estimated to range between 0.11 (as determined for a single-phase SiOC glass[36]) and 0.17 as determined for vitreous silica.[37] For the present assessment, Poisson's ratio of 0.17 has been taken for all three samples, considering their large volume fractions of silica. It should be noted also that the creep viscosity values do not change significantly if ν is varied from 0.11 to 0.17. For instance, the calculated creep viscosity of $C/SiC/SiO_2$ at 1200 °C and 75 MPa true stress changes is 1.65×10^{14} Pa s and 1.56×10^{14} Pa s for ν being 0.11 and 0.17, respectively. Hence, the influence of Poisson's ratio on the calculated creep viscosity is rather small and Poisson's ratio of 0.17 has been exclusively used in the following discussion.

$$\eta = \frac{\sigma}{2(1+\nu)\dot{\varepsilon}} \tag{2}$$

Figure 5b summarizes the calculated creep viscosities of sample $C/SiC/SiO_2$ at different applied true stresses and measurement temperatures. The calculated creep viscosities of $C/SiC/SiO_2$ obtained with 50 MPa (2.5×10^{14} Pa s), 75 MPa (1.6×10^{14} Pa s)

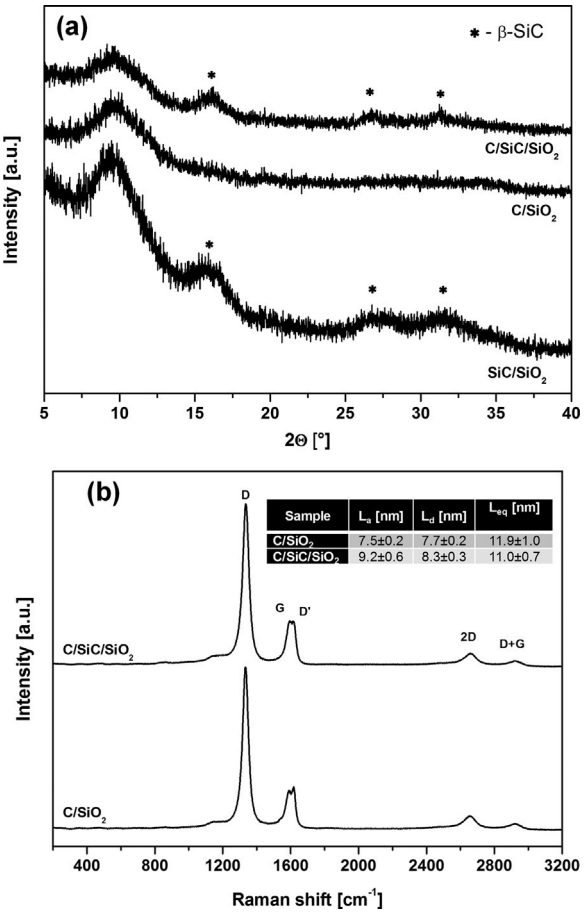

Figure 3. a) X-ray diffraction patterns (Mo K_α radiation) of the investigated samples. All samples are predominantly amorphous – SiC/SiO_2 and $C/SiC/SiO_2$ reveal the presence of weak and broad reflections of β-SiC; b) Raman spectra of C/SiO_2 and $C/SiC/SiO_2$ revealing the presence of sp^2-hybridized disordered segregated carbon; the calculated graphitization parameters L_a (lateral cluster size), L_{eq} (cluster size considering tortuosity), and L_D (inter-defect distance)[30–32] are similar, indicating that the degree of ordering of carbon in the studied samples is comparable.

and 100 MPa (1.2×10^{14} Pa s, data not shown) are similar to each other though indicate a non-Newtonian behavior (shear thinning), however one should note that the differences in the viscosity values at 1150 and 1200 °C at 50 and 75 MPa are comparable with the estimated resolution/accuracy of the device (the estimated resolution of the device for strain rates is 1.0×10^{-8} s^{-1}). However, the calculated creep viscosity at 200 MPa (data not shown) is 4.0×10^{13} Pa s and, thus, significantly smaller than the values recorded at lower applied stress. Therefore, it is assumed that between 100 and 200 MPa a change in the creep behavior of SiOC glass ceramics may occur. Consequently, for the comparison of the three SiOC glass ceramics investigated in this study, the data obtained from the creep experiments performed at temperatures between 1100 and 1300 °C as well as at applied stress between 50 and 100 MPa were chosen.

The activation energies for creep of all three investigated SiOC glass ceramics are summarized in the Arrhenius plots of the steady-state creep rates in Figure 5c (true stress 75 MPa). All three SiOC glass ceramics show an activation energy of about 700–730 kJ mol^{-1} independent of the phase composition (see also the discussion above to Figure 5a). The discrepancy between the Q values of the samples studied in the present study and that reported in literature may relate to the different holding times used during the creep experiments, respectively. It is known that longer holding time during creep experiments is beneficial for the assessment of the behavior of materials which achieve the steady-state regime of the creep (secondary creep) very slowly.[38] Thus, it is considered that the values determined in the present study of around 700 kJ mol^{-1} may be more accurate than the reported values of about 300 kJ mol^{-1} reported so far in literature. However, the difference found between the value of 730–750 kJ mol^{-1} in the present study and, for example, the value of 510 kJ mol^{-1} for sol-gel based silica[35] and the probably accidental coincidence with the value of 712 kJ mol^{-1} found for fused silica containing metallic impurities[35] makes clear that further investigations are needed to clarify which species is carrying the deformation in SiOC glass ceramics.

Despite the similar values of the activation energy, there are obvious differences in the creep behavior of the three different SiOC glass ceramics investigated in the present study. Sample C/SiO_2 exhibits the highest creep rates, followed by SiC/SiO_2. By contrast, sample $C/SiC/SiO_2$, which comprises both segregated carbon and the β-SiC nanoparticles dispersed within vitreous silica, shows the lowest creep rate values (Figure 5c).

The stress exponent n is indicative for the mechanism underlying the creep. **Figure 6** shows the Norton plots of the investigated SiOC glass ceramics, yielding n values of 2.0, 1.70, and 2.1 for C/SiO_2, SiC/SiO_2, and $C/SiC/SiO_2$, respectively. As the difference between the measured values is considered to be small, it is concluded that the creep mechanism is independent of the phase composition in SiOC glass ceramics. Thus, the nature of the dispersed phases, that is, β-SiC in SiC/SiO_2 or carbon in C/SiO_2, does not seem to affect the underlying

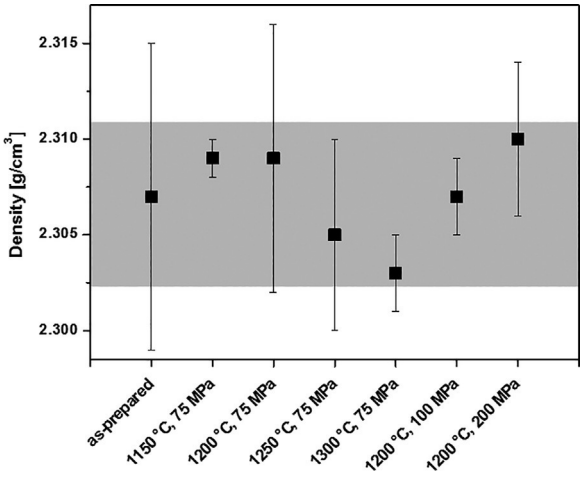

Figure 4. Density values of $C/SiC/SiO_2$ determined before (as-prepared monolith) and after performing creep experiments (temperature and pressure are indicated at the x-axis). No densification was observed during creep experiments.

Table 2. True strain rates measured at different true stresses and temperatures during the steady-state creep of the hot-pressed SiOC samples as well as values of the activation energy of creep Q and stress exponent n.

		True strain rates [10^{-8} s^{-1}] at various applied stresses						
Sample	Temperature [°C]	50 MPa	65 MPa	75 MPa	85 MPa	100 MPa	$Q^{a)}$ [kJ mol^{-1}]	$n^{b)}$
SiC/SiO_2[18]	1100	–	–	1.93	–	–	696 ± 17	1.7 ± 0.2
	1150	–	–	12.7	–	–		
	1200	46.7	–	102	–	150		
	1250	–	–	827	–	–		
	1300	–	–	3860	–	–		
C/SiO_2	1100	–	–	–	–	–	731 ± 15	2.0 ± 0.1
	1150	–	–	61.8	–	–		
	1200	355	649	514	957	1440		
	1250	–	–	4070	–	–		
	1300	–	–	21500	–	–		
$C/SiC/SiO_2$	1100	–	–	–	–	–	730 ± 14	2.1 ± 0.10
	1150	1.29	–	2.95	–	–		
	1200	8.48	–	20.5	–	35.0		
	1250	68.1	–	167	–	–		
	1300	490	–	1020	–	–		

[a)] at 75 MPa true stress; [b)]at 1200 °C measurement temperature

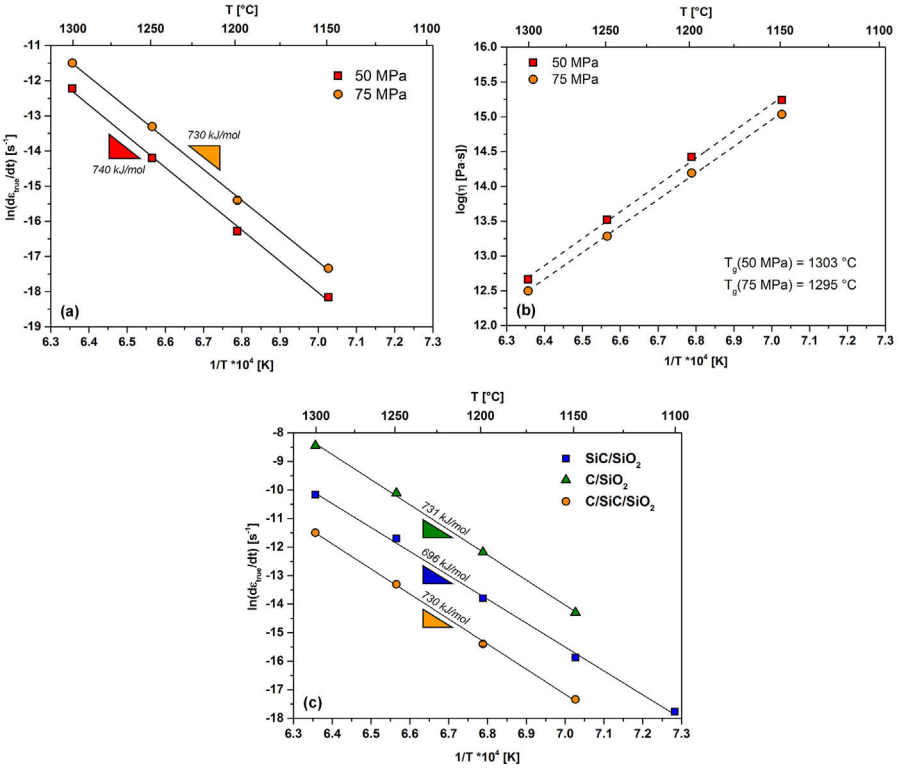

Figure 5. a) Comparison of the activation energies Q for creep of sample $C/SiC/SiO_2$ at 50 and 75 MPa applied true stress; b) Creep viscosities η of $C/SiC/SiO_2$ as function of temperature at a constant true stress of 50 (squares) and 75 MPa (circles); c) Activation energies Q for creep of samples C/SiO_2, SiC/SiO_2,[18] and $C/SiC/SiO_2$ (constant true stress 75 MPa).

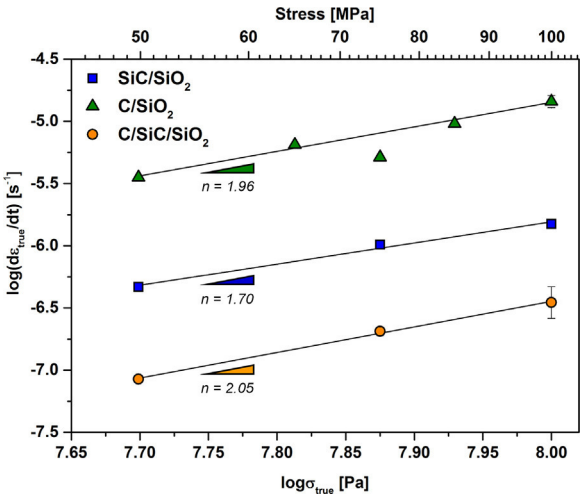

Figure 6. Stress exponent of the investigated SiOC glass ceramics. Data for SiC/SiO2 are taken from ref. [18].

mechanism. However, a stress exponent of approximately 2 is rather unusual, as glasses are expected to plastically deform via Newtonian viscous flow ($n = 1$) and suggests an interface-controlled process. Stress exponent values close to 2 are also reported for polycrystalline ceramics possessing a continuous glassy grain boundary phase being prone to grain boundary sliding.[39–41] A similar finding, that is, $n = 2$, was reported for a $Zr_{10}Al_5Ti_{17.9}Cu_{14.6}$ metallic glass in the supercooled liquid region in which partial crystallization occurred and was assigned to a combination of viscous flow of the glass and phase boundary sliding of the nano-crystalline precipitates.[42] Thus, it is considered that the creep in our SiOC glass ceramics is an interface-controlled process; moreover, a value of 2 for n agrees well with the shear-thinning behavior observed in the samples investigated in the present study.

It can be concluded that the phase composition of SiOC glass ceramics does neither affect the activation energy for creep nor the stress exponent, but it has an obvious impact on the creep rate levels. This can be clearly seen in **Figure 7**a, showing the creep viscosities of C/SiO_2, SiC/SiO_2, and $C/SiC/SiO_2$ as functions of temperature, with $C/SiC/SiO_2$ exhibiting the highest and C/SiO_2 the lowest viscosities among the studied samples. The corresponding T_g values were determined to be 1212 °C for C/SiO_2, 1255 °C for SiC/SiO_2, and 1295 °C for $C/SiC/SiO_2$. In the following, we try to rationalize the effect of the two types of precipitates (i.e., carbon and SiC) on the creep rates of the silica matrix.

Generally, the homogeneous dispersion of particles within a (mainly) viscous matrix leads to an increase of its effective viscosity (particle hardening). Three aspects have an important influence on the effective viscosity of those composite materials: 1) the volume fraction of the particles (i.e., viscosity increases with increasing the volume fraction of the particles[19]), 2) the particle shape (high aspect ratios typically lead to a larger increase in viscosity as spherical particles[43,44]), and 3) the particle size or vice versa particle spacing (the threshold itself scales with the particle volume fraction[19]). Considering those aspects, it is expected that all three SiOC glass ceramics investigated in the present study should show higher effective viscosities in comparison to that of vitreous silica. This is indeed clearly proven in Figure 7a.

As expected, $C/SiC/SiO_2$ reveals the highest viscosity values and consequently highest creep resistance, as it possesses the highest fractions of dispersed particles of comparable size (12.0 vol% β-SiC and 11.9 vol% segregated carbon).

Sample C/SiO_2 has viscosities being about one order of magnitude higher than those of vitreous silica; whereas SiC/SiO_2 shows values ca. two orders of magnitude higher in comparison to those of vitreous silica. This is an unexpected finding, as the volume fraction of the disperse phase in both samples is similar (i.e., 11.5 vol% carbon and 14.3 vol% SiC, respectively), though

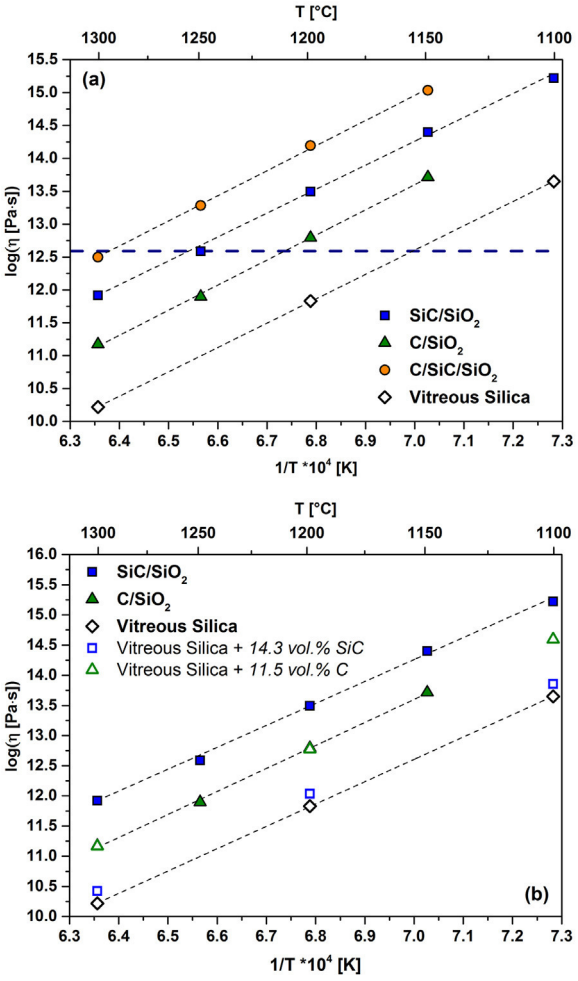

Figure 7. a) Creep viscosities of the investigated SiOC glass ceramics. The values for vitreous silica[35] are included as reference; b) Comparison of the experimentally determined creep viscosities (filled symbols) for SiC/SiO_2 and C/SiO_2 with the calculated effective viscosities of composites with similar composition, that is, silica containing SiC (SiO_2 + 14.3 vol% SiC) and carbon (SiO_2 + 11.5 vol% C), respectively, (empty symbols). For C/SiO_2, the experimental data at 1200 and 1300 °C are fully overlapping with the calculated data points. The viscosities of the composites were estimated according to Equation (3) and (40, using the phase compositions given in **Table 1**.

the aspect ratio of the carbon phase is significantly higher than that of the spherical SiC nanoparticles. As mentioned above, high-aspect-ratio particles (here segregated carbon) are expected to induce a larger increase in viscosity as compared to spherical particles (here β-SiC). However, the opposite trend is observed in our SiOC glass ceramics. This has been further substantiated upon estimating the effective viscosity in glass ceramics based on the Equation (3) and (4) using the model of a glassy matrix reinforced with rigid inclusions, as reported by Boccaccini et al.[45] The effective viscosity η can be calculated from the viscosity of the glass matrix η_{matrix}, the volume fraction of the dispersed particles f, and a shape-related parameter m which is calculated from the shape factor F according to Equation (4), with F having, for example, a value of 1/3 for spherical inclusions and of 0.48986 for particles with an aspect ratio of 10.[45]

For the SiOC glass ceramics investigated in the present study, the effective viscosities were calculated using the viscosity values for vitreous silica[35] as representative for their matrix. The volume fractions of spherical β-SiC and segregated carbon were taken from Table 1 and the aspect ratio of segregated carbon was set to be 10 based on TEM observation.

$$\eta = \eta_{matrix}(1-f)^m \tag{3}$$

$$m = \frac{3F-2}{3F(1-2F)} \tag{4}$$

Figure 7b shows the experimental values of the creep viscosities for SiC/SiO_2 and C/SiO_2 and the calculated effective viscosities of composites consisting of vitreous silica reinforced with the same volume fractions of SiC and carbon, respectively.[35] The calculated effective viscosity of a composite consisting of vitreous silica and 11.2 vol% segregated carbon (i.e., same phase composition as in C/SiO_2) was found to be approximately one order of magnitude higher as compared to that of vitreous silica and matches very well with the experimentally determined creep viscosity of C/SiO_2 (Figure 7b).

Interestingly, there is a strong discrepancy between the experimental and the calculated values in the case of sample SiC/SiO_2, as also reported in ref. [18]. Thus, the effective viscosity of a composite consisting of vitreous silica reinforced with 14.3 vol% SiC (i.e., same phase composition as in SiC/SiO_2) was calculated to be only about three times higher as compared to that of vitreous silica (Figure 7b); however, the measured viscosities of SiC/SiO_2 were found to be as high as two orders of magnitude larger than that of silica (Figure 7b). This severe discrepancy is proposed to originate from a strong interface between the SiC particles and the glassy matrix. This interface may consist of $SiO_{4-x}C_x$ mixed bonds tetrahedra and, thus, a covalent bonding between the SiC particles and the vitreous silica matrix may be present and significantly increase the creep resistance of SiC/SiO_2 as compared to pure vitreous silica. The possible impact of the nano-size of the β-SiC particles (and consequently lower particle percolation threshold[19]) has been assumed to be less important due to the relatively low volume fraction of the spherical particles, as also reported in several studies related to the effect of nanofillers on the viscosity of nanofluid-based composites.[46–48]

The results shown in Figure 7b demonstrate that the effective viscosity in the investigated SiOC glass ceramics is not necessarily (and exclusively) dominated by the shape of the dispersed particles (spherical SiC vs. high aspect ratio segregated carbon) but strongly affected by the nature of the interface between the disperse particles and the matrix. Thus, the SiC/SiO_2 interface seems to be strong and significantly influences the viscosity; whereas in the case of C/SiO_2, the increase of the viscosity relies only on the particle hardening effect. This is in agreement with reports from recent DFT simulations showing that the segregated carbon phase is rather weakly bonded to the glassy matrix.[49,50] For SiC/SiO_2 and $C/SiC/SiO_2$, covalent bonding consisting of mixed-bonds $SiO_{4-x}C_x$ tetrahedra has been postulated between the SiC nanoparticles and the silica matrix,[51] as discussed before; however, to our best knowledge, no experimental proof for the presence of the mixed-bond tetrahedra at the SiC/silica interface has been available so far. Moreover, as proposed in a recent study,[52] the presence of mixed-bonds $SiO_{4-x}C_x$ tetrahedra also at the sp^2-C/silica interface for $C/SiOC/SiO_2$ cannot be ruled out, however are thought to be less abundant in comparison to the SiC/SiO_2 interface.

It seems that in SiOC glass ceramics the viscosity is determined by particle hardening effect if weak interfaces are present (as for C/SiO_2); whereas it is interface-dominated for inclusions which have strong interface to the matrix (as probably for SiC/SiO_2).

Recently, it was shown in a study related to the creep behavior of nanocomposites consisting of a $Cu_{64}Zr_{36}$ metallic glass matrix and dispersed B2 CuZr precipitates that an amorphous interface between the dispersed B2 CuZr (nano)particles and the $C_{64}Zr_{36}$ glass matrix induces a significant increase of the creep rates of the nanocomposite.[53] This is a rather unexpected finding, as typically the introduction of rigid inclusions into a mainly viscous matrix is expected to induce a decrease of the creep rates, that is, particle hardening.[19,45] Furthermore, it was shown that in the studied compositions the interface orientation has a strong contribution and thus controls the creep behavior of the B2-CuZr/MG-$Cu_{64}Zr_{36}$ nanocomposite.[53]

However, if the interface between matrix and dispersed precipitates is of crystalline nature, a reinforcing effect of the inclusion of rigid precipitates in the metallic glass matrix may be expected. This effect was reported for, for example, a $Cu_{64}Zr_{36}$ nano-glass possessing crystalline grain boundaries (e.g., B2 CuZr or fcc Cu-based grain boundaries).[54] Concluding the studies on the creep behavior of bulk metallic glasses and nanocomposites thereof, it seems that a weak interface between glass and rigid inclusions (or an amorphous, weak interface at the grain boundaries of nano-glasses) leads to an increase of the creep rates of the nanocomposites; whereas strong, crystalline interfaces significantly improve the creep resistance of the metallic glass nanocomposites or of nano-glasses.

As the value of 2 for the stress exponent indicates, interface sliding has a significant contribution to creep in our SiOC glass ceramics. It seems that free carbon having a weak interface with silica promotes shear at the border (i.e., carbon/silica interface); whereas the sliding process becomes geometrically constrained when SiC particles are present. Both types of interface, that is, that between carbon and matrix as well as that between SiC and matrix, lead to an increase of the creep resistance. The difference

relies on the origin and the extent of the "reinforcing" effect: in the case of glass ceramics possessing weak interfaces, the improvement of the creep resistance is relatively moderate (i.e., one order of magnitude increase of the creep viscosity) and can be rationalized by the particle hardening effect.[19,45] Whereas in the case of the glass ceramics having strong interface between matrix and dispersed particles, the creep resistance is significantly improved and mainly determined/controlled by the interface contribution.

3.3. Creep Recovery

A further peculiar and known feature of SiOC materials is their visco(an)elastic behavior. This was firstly described by Scarmi et al.[55] and later rationalized upon applying the Jeffreys viscoelastic model in ref. [17]. It was suggested that the elastic behavior is caused by the incorporation of the segregated carbon phase.[6,17,55] **Figure 8** shows the creep experiments of the investigated SiOC glass ceramics at 1200 °C under 100 MPa true stress and subsequent creep recovery.

It is observed that the recovered strain correlates to the volume fraction of segregated carbon present in the ceramic, in agreement with a previously reported study.[17] Thus, the (an) elastic recovery in C/SiO_2 and $C/SiC/SiO_2$ was 19.22 and 20.82%, respectively, and correlated to the volume fraction of carbon in the samples, which was 11.5 and 11.9 vol%, respectively. Interestingly, both samples show nearly the same (an)elastic recovery despite the presence of additional β-SiC nanoparticles in $C/SiC/SiO_2$, thus indicating that the β-SiC nanoparticles do not contribute significantly to the (an)elastic recovery. Consequently, it is reasonable to assume that the (an)elastic recovery in SiC/SiO_2 represents the contribution of the vitreous silica matrix. Thus, SiC/SiO_2 exhibits a recovery value of 8.8%, being smaller for instance than that reported for soda lime silica glass at temperatures above T_g (16–22%[56]).

From above, it is clear that the effect of segregated carbon on the (an)elastic recovery is significant and that the SiC phase barely contributes to it. In a previous study, three SiOC glass ceramic samples with the compositions ≈17 vol% SiC + 83 vol% SiO_2, 5.9 vol% C + 16.6 vol% SiC + 77.5 vol% SiO_2 and 14.2 vol% C + 8.3 vol% SiC + 77.5 vol% SiO_2 were shown in an experiment performed at 1300 °C and 50 MPa to exhibit creep recovery values of ≈3%, 53%, and ≈50%, respectively. This is in agreement with the finding from the present study, that is, the carbon phase has a strong contribution to the creep recovery in SiOC-based glass ceramics.

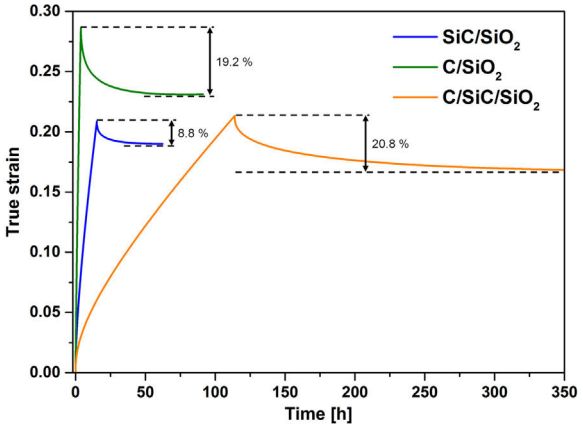

Figure 8. Creep recovery of the investigated SiOC-based glass ceramics (at 1200 °C and 100 MPa true stress).

4. Conclusions

The present study discusses the high temperature behavior of silicon oxycarbide glass ceramics within the context of the contributions of their C-SiO_2 and SiC-SiO_2 interfaces. It is shown that the incorporation of rigid inclusions into silica contributes to a decrease of its creep rates and a concomitant increase of viscosity, independently whether the interface between the precipitates and matrix is weak (as for C/SiO_2) or strong (as probably for SiC/SiO_2). However, it is concluded that the main parameter which affects the extent of the improvement of the creep resistance is not the aspect ratio of the inclusions, but the nature (bond strength) of their interface with the matrix. Disperse particles with weak interface to the matrix contribute to a significant decrease of the steady state creep rates; however, strong/covalent interfaces have much stronger effect on the creep strength, reducing the steady state creep rates by several orders of magnitudes as compared to those of the pure matrix. Concerning the (an)elastic creep recovery of the studied SiOC glass ceramic samples, it is shown that the carbon phase has a strong contribution; whereas the incorporation of SiC particles seems to not significantly affect the (an)elastic recovery behavior of the matrix.

Acknowledgements

Dr. Hergen Breitzke (TU Darmstadt) is acknowledged for recording the ^{29}Si MAS NMR spectra. The authors would like to thank Hans Chen (Karlsruhe Institute of Technology) for the support regarding the creep experiments. Financial support was provided from the Deutsche Forschungsgemeinschaft (IO 64/7-1 and HE 1872/30-1, "High-Temperature Creep in SiOC-Based Glasses and Glass-Ceramics").

Conflict of Interest

The authors declare no conflict of interest.

Keywords

glass ceramics, high-temperature creep, interface-controlled creep, interfaces, silicon oxycarbide

Received: June 1, 2018
Revised: July 16, 2018
Published online:

[1] P. Colombo, G. Mera, R. Riedel, G. D. Soraru, *J. Am. Ceram. Soc.* **2010**, *93*, 1805.
[2] K. Lu, *Mater. Sci. Eng. R.* **2015**, *97*, 23.

[3] K. Lu, D. Erb, *Int. Mater. Rev.* **2018**, *63*, 139.
[4] C. Stabler, E. Ionescu, M. Graczyk-Zajac, I. Gonzalo, R. Riedel, *J. Am. Ceram. Soc.* **2018**, https://doi.org/10.1111/jace.15932
[5] R. Riedel, G. Mera, R. Hauser, A. Klonczynski, *J. Ceram. Soc. Jpn.* **2006**, *114*, 425.
[6] A. Saha, R. Raj, D. L. Williamson, *J. Am. Ceram. Soc.* **2006**, *89*, 2188.
[7] S. J. Widgeon, S. Sen, G. Mera, E. Ionescu, R. Riedel, A. Navrotsky, *Chem. Mater.* **2010**, *22*, 6221.
[8] L. Bois, J. Maquet, F. Babonneau, D. Bahloul, *Chem. Mater.* **1995**, *7*, 975.
[9] P. Dibandjo, S. Dire, F. Babonneau, G. D. Soraru, *J. Non-Cryst. Solids* **2010**, *356*, 132.
[10] M. Esfehanian, R. Oberacker, T. Fett, M. J. Hoffmann, *J. Am. Ceram. Soc.* **2008**, *91*, 3803.
[11] H. Brequel, J. Parmentier, S. Walter, R. Badheka, G. Trimmel, S. Masse, J. Latournerie, P. Dempsey, C. Turquat, A. Desmartin-Chomel, L. L. Neindre-Prum, U. A. Jayasooriya, D. Hourlier, H. J. Kleebe, G. D. Soraru, S. Enzo, F. Babonneau, *Chem. Mater.* **2004**, *16*, 2585.
[12] G. D. Soraru, E. Dallapiccola, *G. D'Andrea, J. Am. Ceram. Soc.* **1996**, *79*, 2074.
[13] T. Rouxel, G.-D. Soraru, J. Vicens, *J. Am. Ceram. Soc.* **2001**, *84*, 1052.
[14] E. Ionescu, S. Sen, G. Mera, A. Navrotsky, *J. Eur. Ceram. Soc.* **2018**, *38*, 1311.
[15] G. M. Renlund, S. Prochazka, R. H. Doremus, *J. Mater. Res.* **1991**, *6*, 2723.
[16] B. Papendorf, E. Ionescu, H.-J. Kleebe, C. Linck, O. Guillon, K. Nonnenmacher, R. Riedel, *J. Am. Ceram. Soc.* **2013**, *96*, 272.
[17] E. Ionescu, C. Balan, H.-J. Kleebe, M. M. Mueller, O. Guillon, D. Schliephake, M. Heilmaier, R. Riedel, *J. Am. Ceram. Soc.* **2014**, *97*, 3935.
[18] C. Stabler, F. Roth, M. Narisawa, D. Schliephake, M. Heilmaier, S. Lauterbach, H.-J. Kleebe, R. Riedel, E. Ionescu, *J. Eur. Ceram. Soc.* **2016**, *36*, 3747.
[19] T. Rouxel, B. Baron, P. Verdier, T. Sakuma, *Acta Mater.* **1998**, *46*, 6115.
[20] T. Rouxel, G. Massouras, G.-D. Soraru, *J. Sol-Gel Sci. Technol.* **1999**, *14*, 87.
[21] M. Narisawa, F. Funabiki, A. Iwase, F. Wakai, H. Hosono, *J. Am. Ceram. Soc.* **2015**, *98*, 3373.
[22] F. Rosenburg, E. Ionescu, N. Nicoloso, R. Riedel, *Materials* **2018**, *11*, 93.
[23] F. H. Horn, *Phys. Rev.* **1955**, *97*, 1521.
[24] T. Rouxel, H. Ji, V. Keryvin, T. Hammouda, S. Yoshida, *Adv. Mater. Res. (Zuerich, Switz.)* **2008**, *39–40*, 137.
[25] D. Schliephake, M. Azim, K. von Klinski-Wetzel, B. Gorr, H.-J. Christ, H. Bei, E. P. George, M. Heilmaier, *Metall. Mater. Trans. A* **2014**, *45*, 1102.
[26] J. R. Davis, *Tensile Testing*, ASM International, Russell, OH, USA **2004**.
[27] C. Stabler, A. Reitz, P. Stein, B. Albert, R. Riedel, E. Ionescu, *Materials (Basel)* **2018**, *11*, 279.
[28] J. M. Bind, *Mater. Res. Bull.* **1978**, *13*, 91.
[29] A. C. Ferrari, J. Robertson, *Phys. Rev. B: Condens. Matter Mater. Phys.* **2000**, *61*, 14095.
[30] L. G. Cancado, K. Takai, T. Enoki, M. Endo, Y. A. Kim, H. Mizusaki, A. Jorio, L. N. Coelho, R. Magalhaes-Paniago, M. A. Pimenta, *Appl. Phys. Lett.* **2006**, *88*, 163106/163101.
[31] L. G. Cancado, A. Jorio, E. H. M. Ferreira, F. Stavale, C. A. Achete, R. B. Capaz, M. V. O. Moutinho, A. Lombardo, T. S. Kulmala, A. C. Ferrari, *Nano Lett.* **2011**, *11*, 3190.
[32] N. Larouche, B. L. Stansfield, *Carbon* **2010**, *48*, 620.
[33] A. Cuesta, P. Dhamelincourt, J. Laureyns, A. Martinez-Alonso, J. M. D. Tascon, *Carbon* **1994**, *32*, 1523.
[34] T. Rouxel, H. Ji, T. Hammouda, A. Moreac, *Phys. Rev. Lett.* **2008**, *100*, 225501/225501.
[35] G. Hetherington, K. H. Jack, J. C. Kennedy, *Phys. Chem. Glasses* **1964**, *5*, 130.
[36] C. Moysan, R. Riedel, R. Harshe, T. Rouxel, F. Augereau, *J. Eur. Ceram. Soc.* **2007**, *27*, 397.
[37] R. Brueckner, *Mechanical Properties of Flasses*, VCH, New York, USA **1991**.
[38] M. Hammond, E. Breval, C. G. Pantano, *Ceram. Eng. Sci. Proc.* **1993**, *14*, 947.
[39] R. Raj, M. F. Ashby, *Metall. Trans.* **1971**, *2*, 1113.
[40] A. G. Evans, *Am. Ceram. Soc. Bull.* **1981**, *60*, 850.
[41] A. G. Evans, A. Rana, *Acta Metall. Mater.* **1980**, *28*, 129.
[42] T. G. Nieh, T. Mukai, C. T. Liu, J. Wadsworth, *Scr. Mater.* **1999**, *40*, 1021.
[43] B. A. Wilcox, A. H. Clauer, *Acta Metall.* **1972**, *20*, 743.
[44] A. Mortensen, *Concise Encyclopedia of Composite Materials*, Elsevier Science, Amsterdam, Netherlands **2006**.
[45] A. R. Boccaccini, *Mater. Lett.* **1998**, *34*, 285.
[46] S. K. Verma, A. K. Tiwari, *Energy Convers. Manage* **2015**, *100*, 324.
[47] C. T. Nguyen, F. Desgranges, G. Roy, N. Galanis, T. Mare, S. Boucher, H. Angue Mintsa, *Int. J. Heat Fluid Flow* **2007**, *28*, 1492.
[48] A. T. Utomo, H. Poth, P. T. Robbins, A. W. Pacek, *Int. J. Heat Mass Transfer* **2012**, *55*, 7772.
[49] J. P. Nimmo, P. Kroll, *J. Phys. Chem. C* **2014**, *118*, 29952.
[50] P. Kroll, *J. Mater. Chem.* **2010**, *20*, 10528.
[51] H.-J. Kleebe, C. Turquat, G. D. Soraru, *J. Am. Ceram. Soc.* **2001**, *84*, 1073.
[52] M. Graczyk-Zajac, D. Vrankovic, P. Waleska, C. Hess, P. V. Sasikumar, S. Lauterbach, H.-J. Kleebe, G. D. Sorarù, *J. Mater. Chem. A* **2018**, *6*, 93.
[53] C. Kalcher, T. Brink, J. Rohrer, A. Stukowski, K. Albe, *Acta Mater.* **2017**, *141*, 251.
[54] C. Kalcher, O. Adjaoud, J. Rohrer, A. Stukowski, K. Albe, *Scr. Mater.* **2017**, *141*, 115.
[55] A. Scarmi, G. D. Soraru, R. Raj, *J. Non-Cryst. Solids* **2005**, *351*, 2238.
[56] L. Duffrene, R. Gy, H. Burlet, R. Piques, *J. Non-Cryst. Solids* **1997**, *215*, 208.

Journal of the Ceramic Society of Japan 124 [10] 1006-1012 2016 Full paper

Synthesis and high-temperature creep behavior of a SiLuOC-based glass-ceramic

Christina STABLER, Christoph SEEMÜLLER,* Ahmad CHOUDHARY, Martin HEILMAIER,* Stefan LAUTERBACH, Hans-Joachim KLEEBE** and Emanuel IONESCU†**

Technische Universität Darmstadt, Institut für Materialwissenschaft, Jovanka-Bontschits-Strasse 2, D-64287 Darmstadt, Germany
***Karlsruher Institut für Technologie, Institut for Applied Materials, Engelbert-Arnold-Strasse 4, D-76131 Karlsruhe**
****Technische Universität Darmstadt, Institut für Angewandte Geowissenschaften, Schnittspahnstrasse 9, D-64287 Darmstadt, Germany**

In this work, a lutetium-modified silicon oxycarbide (SiOC) glass ceramic was prepared from a single-source precursor via pyrolysis and subsequent hot pressing. It is shown that the main crystalline phase in the hot-pressed SiLuOC is $Lu_2Si_2O_7$. The high-temperature (HT) creep behavior of SiLuOC was assessed by compression creep experiments performed between 1100 and 1300°C at constant true stresses between 25 and 75 MPa. The calculated viscosity values of SiLuOC were found to be significantly higher as compared to those of SiRE(Al,Mg)ON glasses (RE = rare earth elements). Thus, the presented SiLuOC-based glasses might be used as alternative sintering aids for the liquid-phase sintering of HT creep resistant Si_3N_4 monolithic samples.

Key-words : Silicon oxycarbides, SiLuOC glass ceramics, High-temperature creep behavior, Polymer-derived ceramics

[Received April 26, 2016; Accepted June 13, 2016]

1. Introduction

The fabrication of dense Si_3N_4 is typically realized by liquid-phase sintering upon the use of sintering additives. Common sintering additives for Si_3N_4 are MgO, Y_2O_3, Al_2O_3, rare-earth oxides (i.e., RE_2O_3) and combinations thereof.[1] During the sintering process, they form a liquid phase with the SiO_2 phase being present on the surface of the Si_3N_4 grains, wetting the Si_3N_4 grains and thus facilitating the compaction via particle rearrangement. α-Si_3N_4 grains subsequently dissolve in the formed melt and re-precipitate as β-Si_3N_4 whiskers which are responsible for the high fracture toughness of the liquid-phase sintered Si_3N_4 monoliths. Upon cooling, the melt usually forms an amorphous or partially crystallized grain-boundary phase. The viscosity of the glassy phase at the sintering temperature determines on the one hand the densification of Si_3N_4 during sintering; however, it limits on the other hand its high-temperature (HT) mechanical properties.[1] Therefore, grain-boundary glassy phases with improved creep resistance or transient grain-boundary phases which crystallize during the sintering process are necessary in order to provide Si_3N_4-based monoliths with improved HT creep behavior. If compared to silicate-based glasses, polymer-derived SiOC glasses and glass ceramics exhibit improved HT creep resistance.[2] Moreover, SiOC-based materials exhibit improved mechanical properties such as higher hardness and Young's Moduli (E) as compared to vitreous silica.[3),4] SiOC glasses and glass ceramics are typically prepared via pyrolysis of polysiloxanes at temperatures of 1000–1200°C. The as-prepared silicon oxycarbides are X-ray amorphous[5] and consist of a glassy single-phasic SiOC matrix in which segregated carbon is finely dispersed.[6),7] At temperatures exceeding 1250°C, silicon oxycarbides phase-separate and convert into multi-phasic amorphous systems comprising of β-SiC nanoparticles homogeneously dispersed within an amorphous SiO_2 matrix.[8),9]

There is rather scarce information available in the literature concerning the use of silicon oxycarbide-based sintering aids for the preparation of dense Si_3N_4 monoliths. In a case study, Plachký et al.[10] successfully prepared dense Si_3N_4 ceramics via hot-pressing using aluminum-modified SiOC glass (SiAlOC) as sintering additive. First creep tests showed a promising creep resistance of the obtained Si_3N_4 sample. Moreover, it has been demonstrated that in this case dense monolithic Si_3N_4 samples can be obtained at shorter sintering times and lower temperatures (i.e., 30 min at 1600°C) as compared to the conditions commonly used to prepare dense Si_3N_4 using alumina as sintering additive (1–2 h at 1750–1800°C).[10] In the SiAlOC/Si_3N_4 system, the densification was shown to be promoted via liquid-phase sintering, whereas at higher temperatures the melt reacts with Si_3N_4 upon the formation of O'-SiAlON, the latter being responsible for the improved HT creep behavior of the samples.

The goal of the present study was to investigate the potential of lutetium-modified SiOC (SiLuOC) as a sintering additive for the preparation of dense and HT creep resistant Si_3N_4 monoliths. It is known that lutetium provides among the rare-earth metal ions the highest viscosity in Si–RE–Me oxynitride grain-boundary melts.[11),12] Moreover, lutetium is known to promote the α-Si_3N_4-to-β-Si_3N_4 phase transformation rate, as RE ions with small ionic radius show the fastest transformation rate;[11),13),14] thus, the use of SiLuOC might contribute to an improved fracture toughness of the resulting Si_3N_4 samples with elongated β-Si_3N_4 grains.

In this study, Lu-containing silicon oxycarbide glasses were prepared upon pyrolysis of a suitable single-source precursor and the evolution of their chemical and phase composition with temperature was carefully analyzed. Furthermore, SiLuOC-based monoliths were prepared via hot-pressing of SiLuOC glass powders and their HT creep behavior was studied. The results

† Corresponding author: E. Ionescu; E-mail: ionescu@materials.tu-darmstadt.de
‡ Preface for this article: DOI http://dx.doi.org/10.2109/jcersj2.124.P10-1

DOI http://dx.doi.org/10.2109/jcersj2.16101

obtained within the present study indicate that SiLuOC glass powder is a suitable sintering aid for the preparation of dense Si_3N_4 monoliths with improved HT creep resistance.

2. Experimental procedure

A commercially available polymethylsilsesquioxane (PMS Belsil MK, Wacker) was mixed with lutetium acetate hydrate (15 wt.%) at room temperature. Thus, lutetium acetate hydrate [Lu(III)AcHy] was added upon stirring to PMS MK which was previously dissolved in acetone. After 2 h of stirring, a milky white suspension was obtained and subsequently dried in a rotary evaporator. The resulting polysilsesquioxane-based powder was pyrolyzed in argon or nitrogen atmosphere at 1100°C. The thermal conversion of the single-source precursor into SiLuOC glass was investigated using thermogravimetric analysis (TGA) coupled with evolved gas analysis (EGA; i.e. in situ mass spectrometry). TGA/EGA was carried out with a thermal analysis device (STA 449C Jupiter, Netzsch, Germany) coupled with a quadrupole mass spectrometer (QMS 403C Aëolos, Netzsch, Germany). The TGA/EGA experiment was performed upon heating under flowing argon up to 1450°C by using a heating rate of 5°C/min. FTIR spectra were collected using a Bruker Vertex 70 FT-IR instrument (Bruker, USA) in attenuated total reflectance (ATR) geometry. For the elemental analysis, a carbon analyzer Leco-200 (Leco Corporation, USA) was used to determine the carbon content and an N/O analyzer Leco TC-436 (Leco Corporation, USA) to determine the oxygen content. The Lutetium and silicon content was estimated under the assumption that no lutetium is released during pyrolysis. The silicon fraction was calculated as the difference to 100 wt.% of the sum of the wt.% values of carbon, oxygen, nitrogen and lutetium, assuming no other elements being present in the samples.

The HT evolution of the amorphous SiLuOC glass synthesized upon pyrolysis at 1100°C in argon atmosphere was studied by annealing for 5 h at different temperatures in argon or nitrogen atmosphere using a HT graphite furnace (GT Advanced Technologies, USA). Additionally, pressure-assisted annealing was performed at 1500 and 1600°C in a hot press in argon or nitrogen atmosphere. In all cases the heating rate was set to 20°C/min.

The microstructural evolution of the samples annealed at 1100°C and upon hot pressing at 1600°C in argon was studied by transmission electron microscopy (TEM), utilizing a Jeol 2100F instrument (Jeol, Tokyo, Japan) operated at 200 keV. The received powder samples were finely dispersed on a lacy carbon grit and mildly carbon coated to minimize charging under the incident electron beam.

For the investigation of the HT creep behavior of the SiLuOC-based glass-ceramic, monolithic samples were prepared via hot-pressing of SiLuOC glass powder in nitrogen atmosphere at 1600°C for 30 min, using a uniaxial pressure of 30 MPa.

Powder XRD measurements of the annealed samples were performed in flat-sample transmission geometry on a difractometer from STOE company (STOE STADI P) equipped with a Mo X-ray tube, a Germanium (111) monochromator and a position sensitive detector with a 6° aperture. XRD measurements of the hot-pressed pellet used for creep experiments were performed on a Bruker D8 diffractometer equipped with a Cu X-ray tube and a Sol-X detector [Si(Li) solid-state detector; Bruker AXS].

The HT creep experiments where performed on a Zwick universal testing device equipped with a Maytec vacuum furnace ($<10^{-4}$ Pa). The samples were ground to be plane parallel with respect to the creep loaded surfaces and rectangular in shape with dimensions of $3 \times 3 \times 5\,mm^3$. The creep behavior was studied in the temperature range between 1100 and 1300°C using a constant true stress of 75 MPa. Additionally, measurements were performed at a constant temperature of 1200°C but with true stresses ranging between 25 and 75 MPa. True strain and true stress were calculated from the continuously monitored compression and load, respectively, according to the procedure described in Ref. 15 and 16. At the beginning of each experiment the zero-point of strain was determined inductively via the extensometer. During the experiment, the difference between the piston and extensometer was continuously followed. The strain rates were computed after reaching the steady-state creep stage being defined when a constant strain rate was observed after a minimum of 2% plastic true strain.

3. Results and discussion

Figure 1 shows the IR spectra of the unmodified PMS MK polymer and the Lu-modified PMS MK in comparison. The bands assignment (Fig. 1) was done according to Ref. 17 and 18. As can be seen in Fig. 1, there are no major differences between the FTIR spectra of the PMS MK and the Lu-modified sample. However bands between 1550 and 1450 cm^{-1} corresponding to asymmetric stretching vibrations of acetate COO^-, and to asymmetric deformation vibrations of O–CO–CH_3 bonds respectively,[17] are only present in the Lu-modified sample. Additionally, the FTIR spectrum of the Lu-modified precursor shows the presence of an absorption band at ca. 950 cm^{-1} [Fig. 1(b)], which

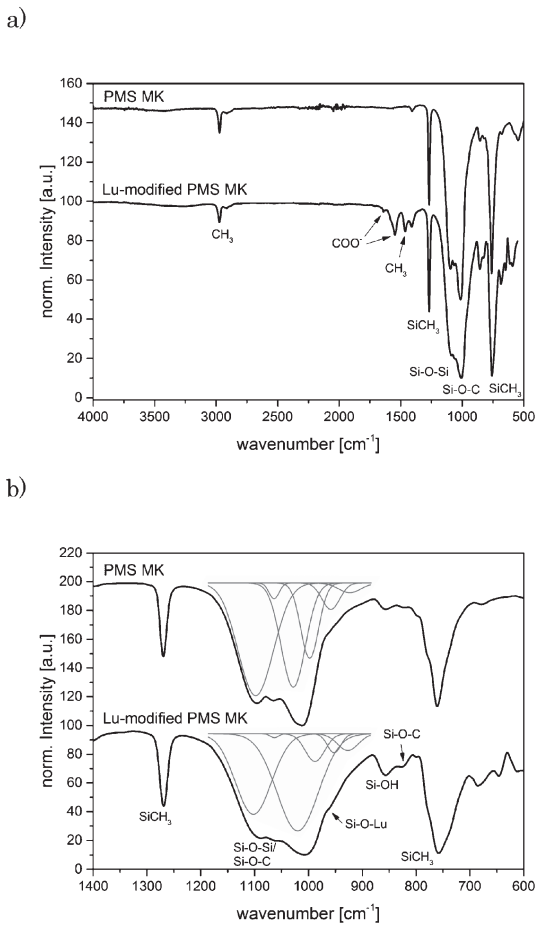

Fig. 1. (a) ATR FTIR spectra for pure PMS MK and for Lu-modified PMS MK; (b) represents the magnification of the spectra from (a) in the range from 500 to 1400 cm^{-1}. Gray lines represent a qualitative fit of the underlying bands.

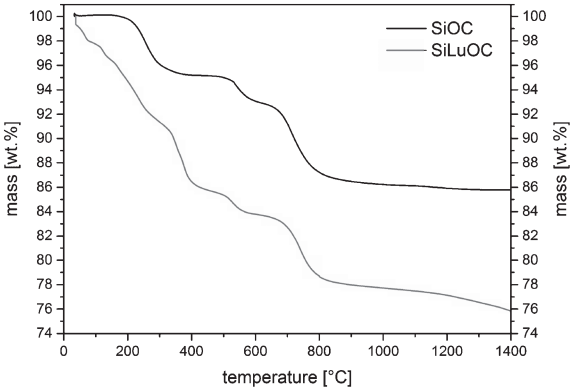

Fig. 2. Thermogravimetric analysis of PMS MK and of the Lu-modified PMS MK sample.

has been assigned to Si–O–Lu and thus indicates that the Lu(III) acetate hydrate reacts with the polysilsesquioxane.

The conversion of the single-source precursor into SiLuOC glass was followed by thermogravimetric analysis coupled with mass spectrometry given in **Fig. 2**. Selected mass spectra of the Lutetium-modified PMS MK are depicted in **Fig. 3**. PMS MK decomposes showing three main weight losses up to 800°C; whereas the pyrolysis of the Lutetium-modified PMS MK can be divided into 4 stages: (i) from room temperature to 150°C, (ii) from 150 to 450°C, (iii) from 480 to 650°C and (iv) from 650 to 800°C. In the first stage, mainly the used solvent (acetone) and water evaporate. During the second stage the outgassing of ethanol and hydrogen can be identified, indicating that cross-linking of the polymeric precursor is occurring. Additionally, the outgassing of acetate ions can be observed. The stages (iii) and (iv) correspond to the second and third weight loss of the unmodified PMS MK and are mainly identical. At 480°C, remaining acetate but mainly ethanol or ethylene and hydrogen are evaporated marking the beginning of the ceramization process. The last stage is mainly due to the evaporation of methane and hydrogen marking the end of the ceramization process. The modification with lutetium leads to an increased weight loss of about 10 wt.% up to 800°C in comparison to the unmodified PMS MK due to the evaporation of acetate. From 800 to 1200°C no further weight loss can be detected. At 1200°C a small weight loss was detected for both precursors where the lutetium-modified precursor exhibits a slightly higher weight loss.

The SiLuOC glass material obtained upon pyrolysis of the Lu-modified polysilsesquioxane precursor was annealed at high temperature in order to assess its crystallization behavior. SiLuOC glass samples were annealed in argon or nitrogen atmosphere at temperatures ranging from 1100 to 1600°C. As can be seen in **Fig. 4** the annealing atmosphere has no significant influence on the crystallization behavior and the phase composition of the SiLuOC-based samples. At 1100°C, the only detectable crystalline phase is monoclinic $Lu_2Si_2O_7$. However, the samples prepared at 1100°C were mainly amorphous. The presence of $Lu_2Si_2O_7$ was already reported in highly creep-resistant Si_3N_4 with Lu_2O_3 as sintering additive[19] and is reported to have a beneficial impact on the oxidation resistance.[20] The XRD patterns of the samples annealed at 1300°C show the presence of nano-sized β-SiC in addition to monoclinic $Lu_2Si_2O_7$. The samples annealed at 1500 and 1600°C show both phases, i.e. β-SiC and $Lu_2Si_2O_7$, with enhanced crystallization. No additional crystalline phase was detected. Even at 1600°C after 5 h of annealing both samples show an amorphous hump with its maximum at a 2θ value of 10° corresponding to amorphous silica, proving that the sample is still partially amorphous. However, it can be clearly seen that an increase in temperature leads to an enhanced crystallization, which will be beneficial for the mechanical prop-

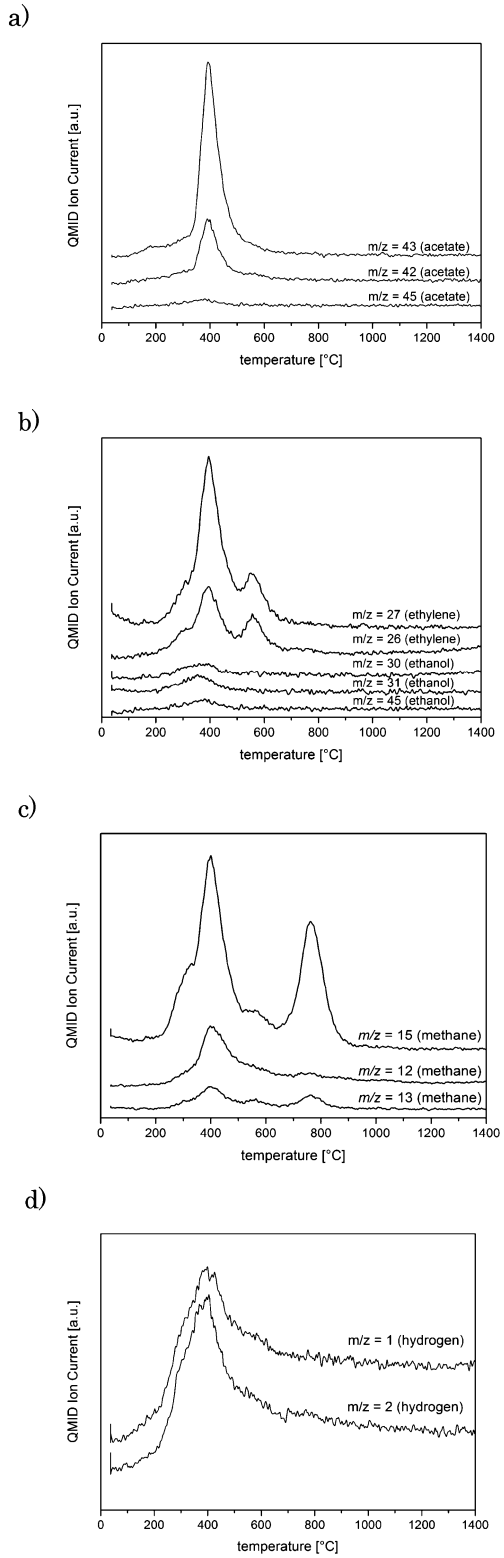

Fig. 3. QMID ion current curves of the lutetium-modified PMS MK during pyrolysis indicating the outgassing of species such as acetate (a), ethanol/ethylene (b), methane (c) and hydrogen (d).

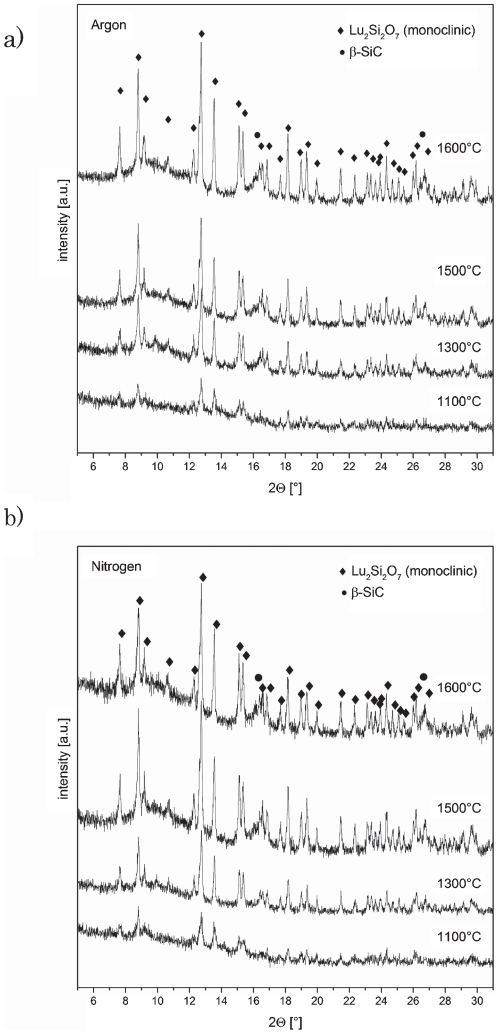

Fig. 4. XRD patterns of SiLuOC as prepared at 1100°C and annealed at temperatures of 1300, 1500 and 1600°C in (a) argon and (b) nitrogen atmosphere.

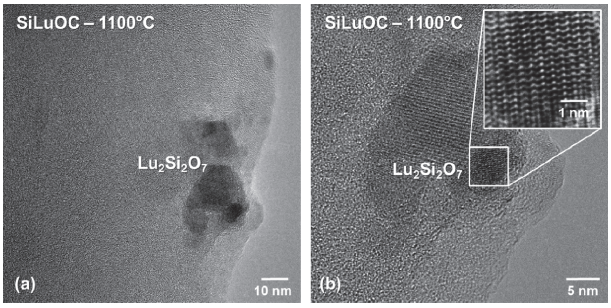

Fig. 5. TEM bright field imaging of the SiLuOC sample pyrolyzed at 1100°C. Small $Lu_2Si_2O_7$ crystallites in the range of 5–20 nm in size are embedded in a homogeneous amorphous SiOC matrix.

erties of Si_3N_4 if SiLuOC will be used as a sintering additive.

TEM analysis of the microstructural evolution of the samples revealed in both samples, (i) annealed at 1100°C (**Fig. 5**) and (ii) upon hot pressing at 1600°C (**Fig. 6**), the crystallization of small $Lu_2Si_2O_7$ particles, identified by energy-dispersive X-ray spectroscopy (EDS) in addition to electron-diffraction data analysis, embedded in the SiOC-based matrix. This finding is consistent with the XRD results given in Fig. 4. While the sample processed at low temperature showed a homogeneous amorphous SiOC matrix with $Lu_2Si_2O_7$ crystallites ranging from 5–20 nm in size (Fig. 5), the HT sample revealed a marked change in microstructure.

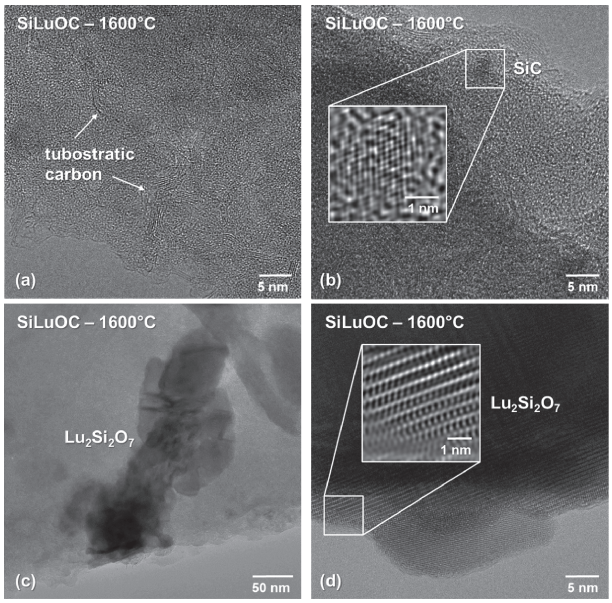

Fig. 6. TEM bright field images of the SiLuOC material upon hot pressing at 1600°C. The formerly amorphous matrix now revealed a high volume fraction of turbostratic carbon, shown in (a), in addition to the crystallization of nanosized SiC crystallites (b). The inset in (b) reveals an enlarged Fourier-filtered image of a SiC crystallite. Moreover, this sample showed a coarsening of the $Lu_2Si_2O_7$ crystallites, ranging from 20–300 nm. The inset in (d) depicts an enlarged Fourier-filtered image of the well crystallized region of the $Lu_2Si_2O_7$ (boxed area).

Here, a coarsening of the well crystallized $Lu_2Si_2O_7$ particles was observed. In this case, the crystal size varied between 20 and 300 nm (Fig. 6). Moreover, the initially fully amorphous SiOC matrix now showed a high volume fraction of turbostratic carbon [Fig. 6(a)] in addition to the crystallization of nanosized SiC particles of approximately 2–5 nm in diameter embedded on a still partially amorphous matrix [Fig. 6(b)]. This homogeneous microstructural evolution is based on the phase partitioning and carbothermal reduction process occurring at temperatures exceeding 1250°C, in addition to the transformation of the excess free carbon phase into turbostratic carbon.[21),22)]

For the assessment of the HT creep behavior, SiLuOC-based monoliths were prepared upon hot-pressing of glassy SiLuOC powders at 1600°C in nitrogen atmosphere. Its estimated elemental analysis is shown in **Table 1**. As the amount of incorporated lutetium is low, only 3.8 vol.% $Lu_2Si_2O_7$ is present and the chemical and phase composition is changed only slightly in comparison to the ternary system.

The XRD pattern of the hot-pressed monolithic SiLuOC sample used for the creep experiments is shown in **Fig. 7**. The main crystalline phase is monoclinic $Lu_2Si_2O_7$.

In order to assess the deformation behavior of SiLuOC, HT creep experiments at constant applied compressive stress between 25 and 75 MPa were performed and the steady-state creep rates at different temperatures between 1100 and 1300°C and pressures were evaluated from the recorded plastic strain (**Table 2**). The corresponding creep curves in true compressive strain vs. time are shown in **Fig. 8**. It has to be noted that long loading

Table 1. Chemical composition of hot-pressed SiOC and SiLuOC samples and calculated phase composition of the assumed phases present. Volume fractions are calculated assuming the following densities: $\rho(SiO_2) = 2.2\,g/cm^3$,[23] $\rho(\beta\text{-SiC}) = 3.22\,g/cm^3$ (ICSD-# 164974), $\rho(C) = 1.82\,g/cm^3$ (Graphitized Mesoporous Carbons GMC, Sigma-Aldrich, CAS-# 1333-86-4), $\rho(Lu_2Si_2O_7\ mon.) = 6.21\,g/cm^3$ (PDF 00-034-0509)

Sample	Chemical composition	SiO_2 [vol.%]	SiC [vol.%]	free C [vol.%]	$Lu_2Si_2O_7$ [vol.%]
SiOC	$SiO_{1.44}C_{0.28}+C_{0.42}$	75.9	13.4	10.8	—
SiLuOC	$SiO_{1.46}C_{0.29}Lu_{0.02}+C_{0.36}$	72.8	14.1	9.3	3.8

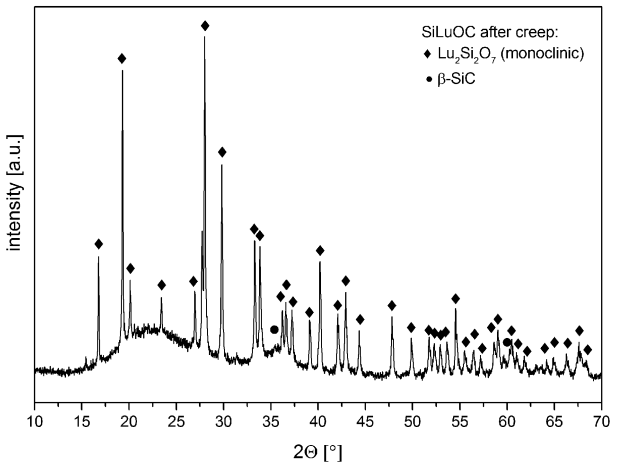

Fig. 7. XRD pattern of the hot-pressed SiLuOC sample used for the creep experiments.

Table 2. As-determined steady-state creep rates of hot-pressed SiLuOC at different temperatures and stresses

Temperature [°C]	True strain rates [s^{-1}]		
	25 MPa applied stress	50 MPa applied stress	75 MPa applied stress
1100	—	—	$3.5\cdot10^{-8}\,s^{-1}$
1200	$5.9\cdot10^{-8}\,s^{-1}$	$2.5\cdot10^{-7}\,s^{-1}$	$6.2\cdot10^{-7}\,s^{-1}$
1300	—	—	$1.2\cdot10^{-5}\,s^{-1}$

times of nearly up to 100 h were necessary to obtain steady-state conditions.

In the steady-state creep regime Norton's power law equation is valid [Eq. (1)], where $\dot{\varepsilon}$ is the steady-state strain rate, B is a material-dependent constant, σ is the applied stress and Q is the activation energy. Hence, the apparent activation energy for creep can be obtained from the slope of an Arrhenius plot [**Fig. 9**(a)] whereas the stress exponent n can be evaluated from the slope of a Norton plot ($\log(\dot{\varepsilon})$ vs. $\log(\sigma)$ [Fig. 9(b)].

$$\dot{\varepsilon} = B\sigma^n e^{-\frac{Q}{RT}} \quad (1)$$

An apparent activation energy of 520 kJ/mol was determined for SiLuOC. This is significantly lower in comparison to the value of 712 kJ/mol reported for vitreous silica.[24] It is however considerably higher than the value of a SiOC sample containing approximately 0.5 vol.% segregated carbon (i.e., 296 kJ/mol^2). These SiOC samples were however prepared at 1100°C and can therefore be regarded as single-phase materials in comparison to the phase-separated sample investigated in this study.

The stress exponent n is indicative for the mechanism responsible for the creep. In the present study, a value of 2.1 was determined for SiLuOC. It is generally expected that glasses loaded at lower stresses exhibit a linear dependence of the strain rate on the stress (i.e., the stress exponent n = 1),[25] which correlates to a Newtonian viscous flow behavior. The rather unexpected stress exponent of approximately 2 determined for SiLuOC, is not yet fully understood, however, similar values were already observed in a glassy SiOC system without segregated carbon.[26] As a stress exponent of 2 correlates to grain-boundary sliding in superplastic materials, a viscous contribution of the silica matrix and a sliding contribution from the nano-crystalline part, [Fig. 6(a)], is proposed here. However, it was already reported for bulk metallic glasses that stress exponents > 1 can be as well regarded as a transition from linear to non-linear behavior according to transition state theory.[27),28] Additionally, it was observed that this transition occurs at lower stresses with decreasing temperature below T_g. As the creep tests in this study were performed below and close to T_g of SiLuOC, the possibility of a transition cannot be ruled out.

The shear viscosity of SiLuOC was calculated from the steady-state creep rates using [Eq. (2)], where η is the actual viscosity, σ is the applied stress, ν is the Poisson ratio and $\dot{\varepsilon}$ is the steady-state creep rate. This equation is only valid in the measured temperature and pressure regime as it implies Newtonian viscous flow behavior. The Poisson ratio of SiOC was determined to be 0.11 by Moysan et al.;[3] this value was used also for the SiLuOC system.

a)

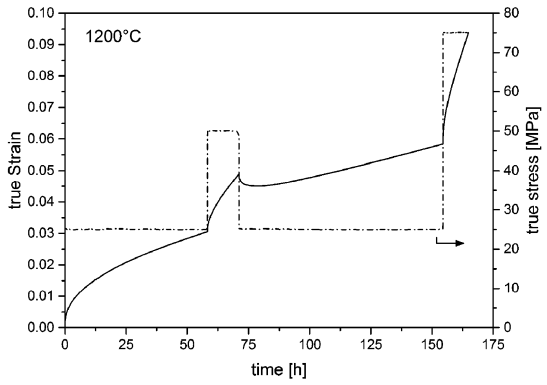

b)

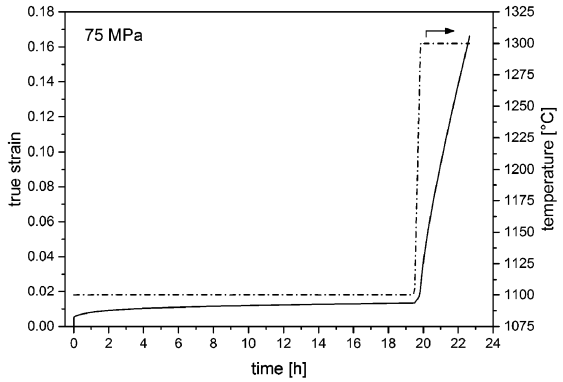

Fig. 8. True creep strain plotted vs. time of SiLuOC (continuous curves) (a) at constant temperature of 1200°C and true stresses of 25, 50 and 75 MPa (dashed); (b) at a true stress of 75 MPa and two temperatures, i.e. 1100 and 1300°C (dashed).

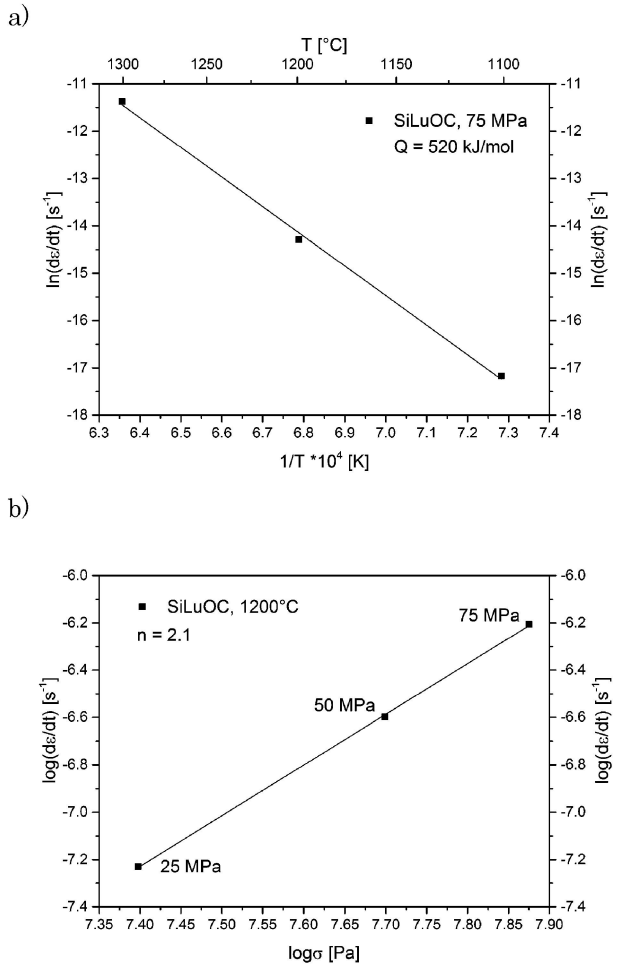

Fig. 9. (a) Steady-state creep rates of SiLuOC at a constant applied stress (75 MPa) and varying temperatures; (b) Steady-state creep rates of SiLuOC at 1200°C and varying applied stresses.

$$\eta = \frac{\sigma}{2(1+\nu)\dot{\varepsilon}} \tag{2}$$

From the calculated viscosity data the glass-transition temperature T_g of SiLuOC (defined as the temperature at which the viscosity is $10^{12.6}$ Pa·s) is estimated to 1291°C. The viscosity of SiLuOC was found to be higher than for the single-phasic ternary system with 0.5 wt.% segregated carbon[2] and even higher than that of SiAlOC,[29] which was already used by Plachký et al. as sintering additive for Si_3N_4.[10]

As already mentioned, common sintering additives for Si_3N_4 are MgO, Y_2O_3, Al_2O_3, RE_2O_3 and combinations thereof.[1] Consequently, depending on the type of additive, SiYAlON or SiRE(Al,Mg)ON glasses can be expected to be present as grain-boundary phases in common Si_3N_4 materials produced by liquid-phase sintering. The viscosity of this glassy phase at the sintering temperature determines on the one hand the densification during sintering and on the other hand the HT performance of the resulting ceramic. Becher et al. investigated the viscosity of silicon-based oxynitride glasses. From their results, the glass-transition temperature of SiYAlON glasses (56Si28Y16Al oxynitride glasses) was found to be in the range of 870 to 950°C, depending on their nitrogen content.[30] In the system 56.5Si44La0.5Y20N80O a maximum glass-transition temperature of around 1020°C was determined.[30] This is significantly lower than the glass-transition temperature for SiLuOC (1291°C) determined here, which will have an impact on the densification behavior of Si_3N_4 powders and consequently an external pressure during the sintering process should be necessary. A high viscosity of the liquid melt during sintering however provides β-Si_3N_4 particles with high aspect-ratio and improved fracture toughness of the resulting ceramic.[1]

4. Conclusion

SiLuOC glass ceramics exhibit promising behavior for the use as sintering additive for Si_3N_4. The phase composition is independent of the processing atmosphere yielding mainly amorphous materials containing low volume fractions of $Lu_2Si_2O_7$ as main crystalline phase in all cases. The calculated viscosity of SiLuOC is significantly higher as compared to SiRE(Al,Mg)ON glasses used in typical liquid-phase sintering of Si_3N_4. Furthermore, SiLuOC can partially be crystallized with increasing temperature due to the intrinsic phase-separation common for to all SiOC systems starting at around 1250°C and due to an enhanced crystallization of the $Lu_2Si_2O_7$ secondary phase.

Acknowledgements The German Science Foundation (Deutsche Forschungsgemeinschaft, Bonn, Germany) is gratefully acknowledged for financial support (HE 1872/30-1 and IO 64/7-1). The authors thank Prof. Riedel for valuable discussions and continuous support. Claudia Fasel is acknowledged for recording the TGA/EGA data and for valuable discussions.

References

1) G. Ziegler, J. Heinrich and G. Woetting, *J. Mater. Sci.*, 22, 3041–3086 (1987).
2) T. Rouxel, G.-D. Soraru and J. Vicens, *J. Am. Ceram. Soc.*, 84, 1052–1058 (2001).
3) C. Moysan, R. Riedel, R. Harshe, T. Rouxel and F. Augereau, *J. Eur. Ceram. Soc.*, 27, 397–403 (2006).
4) G. D. Soraru, E. Dallapiccola and G. D'Andrea, *J. Am. Ceram. Soc.*, 79, 2074–2080 (1996).
5) M. Esfehanian, R. Oberacker, T. Fett and M. J. Hoffmann, *J. Am. Ceram. Soc.*, 91, 3803–3805 (2008).
6) A. Saha, R. Raj and D. L. Williamson, *J. Am. Ceram. Soc.*, 89, 2188–2195 (2006).
7) S. J. Widgeon, S. Sen, G. Mera, E. Ionescu, R. Riedel and A. Navrotsky, *Chem. Mater.*, 22, 6221–6228 (2010).
8) A. Saha and R. Raj, *J. Am. Ceram. Soc.*, 90, 578–583 (2007).
9) L. Bois, J. Maquet, F. Babonneau and D. Bahloul, *Chem. Mater.*, 7, 975–981 (1995).
10) T. Plachky, Z. Lences, L. Hric, P. Sajgalik, P. Balaz, R. Riedel and H. J. Kleebe, *J. Eur. Ceram. Soc.*, 30, 759–767 (2010).
11) P. F. Becher, N. Shibata, G. S. Painter, F. Averill, K. van Benthem, H.-T. Lin and S. B. Waters, *J. Am. Ceram. Soc.*, 93, 570–580 (2010).
12) P. F. Becher and M. K. Ferber, *J. Am. Ceram. Soc.*, 87, 1274–1279 (2004).
13) N. Saito, D. Nakata, K. Nakashima, and A. Umemoto, Grain growth of β-silicon nitride in RE-Mg-Si-O-N liquid, "Ceram. Trans.", 192(Developments and Applications of Advanced Engineering Ceramics and Composites) (2006) pp. 73–80.
14) M. J. Hoffmann, H. Gu and R. M. Cannon, Influence of the interfacial properties on the microstructural development and properties of silicon nitride ceramics, "Mater. Res. Soc. Symp. Proc.", 586(Interfacial Engineering for Optimized Properties II) (2000) pp. 65–74.
15) D. Schliephake, M. Azim, K. von Klinski-Wetzel, B. Gorr, H.-J. Christ, H. Bei, E. P. George and M. Heilmaier, *Metall. Mater. Trans., A Phys. Metall. Mater. Sci.*, 45, 1102–1111 (2014).
16) J. R. Davis, "Tensile Testing", 2 ed., ASM International (2004)

p. 283.
17) G. Socrates, "Infrared and Raman Characteristic Group Frequencies - Tables and Charts", Third Edition ed., Chichester: John Wiley & Sons Ltd (2004).
18) R. Al-Oweini and H. El-Rassy, *J. Mol. Struct.*, **919**, 140–145 (2009).
19) S. M. Wiederhorn, R. F. Krause, Jr., F. Lofaj and U. Taeffner, Creep behavior of improved high temperature silicon nitride, "Key Eng. Mater.", 287(Advanced Si-Based Ceramics and Composites) (2005) pp. 381–392.
20) M. K. Cinibulk, G. Thomas and S. M. Johnson, *J. Am. Ceram. Soc.*, **75**, 2037–2043 (1992).
21) H. J. Kleebe, *Phys. Status Solidi A*, **166**, 297–313 (1998).
22) S. Martinez-Crespiera, E. Ionescu, H. J. Kleebe and R. Riedel, *J. Eur. Ceram. Soc.*, **31**, 913–919 (2011).
23) G. M. Renlund, S. Prochazka and R. H. Doremus, *J. Mater. Res.*, **6**, 2723–2734 (1991).
24) G. Hetherington, K. H. Jack and J. C. Kennedy, *Phys. Chem. Glasses*, **5**, 130–136 (1964).
25) J. H. Simmons, R. K. Mohr and C. J. Montrose, *J. Appl. Phys.*, **53**, 4075–4080 (1982).
26) C. Stabler, F. Roth, M. Narisawa, D. Schliephake, M. Heilmaier, S. Lauterbach, H.-J. Kleebe, R. Riedel and E. Ionescu, *J. Eur. Ceram. Soc.*, **36**, 3747–3753 (2016).
27) A. Reger-Leonhard, M. Heilmaier and J. Eckert, *Scr. Mater.*, **43**, 459–464 (2000).
28) B. S. S. Daniel, A. Reger-Leonhard, M. Heilmaier, J. Eckert and L. Schultz, *Mech. Time-Depend. Mater.*, **6**, 193–206 (2002).
29) R. R. Harshe, "Synthesis and Processing of Amorphous Si(Al)OC Bulk Ceramics: High Temperature Properties and Applications", in Department of Materials Science, Technical University of Darmstadt (2004) p. 222.
30) P. F. Becher, S. Hampshire, M. J. Pomeroy, M. J. Hoffmann, M. J. Lance and R. L. Satet, *Int. J. Appl. Glass Sci.*, **2**, 63–83 (2011).

materials

MDPI

Article

Thermal Properties of SiOC Glasses and Glass Ceramics at Elevated Temperatures

Christina Stabler [1], Andreas Reitz [2], Peter Stein [1], Barbara Albert [2], Ralf Riedel [1] and Emanuel Ionescu [1,*]

[1] Institut für Materialwissenschaft, Technische Universität Darmstadt, Otto-Berndt-Straße 3, D-64287 Darmstadt, Germany; stabler@materials.tu-darmstadt.de (C.S.); p.stein@mfm.tu-darmstadt.de (P.S.); riedel@materials.tu-darmstadt.de (R.R.)

[2] Eduard-Zintl-Institut für Anorganische und Physikalische Chemie, Technische Universität Darmstadt, Alarich-Weiss-Straße 12, D-64287 Darmstadt, Germany; reitz@ac.chemie.tu-darmstadt.de (A.R.); albert@ac.chemie.tu-darmstadt.de (B.A.)

* Correspondence: ionescu@materials.tu-darmstadt.de

Received: 30 January 2018; Accepted: 8 February 2018; Published: 10 February 2018

Abstract: In the present study, the effect of the chemical and phase composition on the thermal properties of silicon oxide carbides (SiOC) has been investigated. Dense monolithic SiOC materials with various carbon contents were prepared and characterized with respect to their thermal expansion, as well as thermal conductivity. SiOC glass has been shown to exhibit low thermal expansion (e.g., ca. 3.2×10^{-6} K^{-1} for a SiOC sample free of segregated carbon) and thermal conductivity (ca. 1.5 W/(m·K)). Furthermore, it has been observed that the phase separation, which typically occurs in SiOC exposed to temperatures beyond 1000–1200 °C, leads to a decrease of the thermal expansion (i.e., to 1.83×10^{-6} K^{-1} for the sample above); whereas the thermal conductivity increases upon phase separation (i.e., to ca. 1.7 W/(m·K) for the sample mentioned above). Upon adjusting the amount of segregated carbon content in SiOC, its thermal expansion can be tuned; thus, SiOC glass ceramics with carbon contents larger than 10–15 vol % exhibit similar coefficients of thermal expansion to that of the SiOC glass. Increasing the carbon and SiC content in the studied SiOC glass ceramics leads to an increase in their thermal conductivity: SiOC with relatively large carbon and silicon carbides (SiC) volume fractions (i.e., 12–15 and 20–30 vol %, respectively) were shown to possess thermal conductivities in the range from 1.8 to 2.7 W/(m·K).

Keywords: silicon oxycarbide; silicon oxide carbide; thermal transport; thermal conductivity; thermal expansion

1. Introduction

Silicon oxide carbide (or silicon oxycarbide, SiOC) glasses and glass ceramics belong to the group of polymer-derived ceramics (PDCs). They consist of corner-sharing $SiO_{4-x}C_x$ tetrahedra (x = 0–4) [1], and can be described as vitreous silica glasses, with oxygen being partly replaced by carbon within the glass network. The main synthesis approach, which incorporates significant amounts of carbon into silica, relies on the thermal conversion of sol–gel derived precursors based on organo-substituted alkoxysilanes or of polyorganosiloxanes [2]. A significant amount of Si–O and Si–C bonds were preserved upon the thermal treatment, yielding X-ray amorphous SiOC at 1000 °C. The carbon was present as network carbon, i.e., bonded to silicon (sp^3-hybridized; $SiO_{4-x}C_x$ tetrahedra) as well as in form of disordered segregated carbon phase (sp^2-hybridized) [3] homogeneously dispersed inside the glassy matrix. The final composition of the SiOC glasses can be tuned upon choosing appropriate preceramic precursors [2,4,5].

Silicon oxide carbide glasses were shown in various studies to undergo phase separation at temperatures beyond 1200 °C. As evidenced by solid-state Magic Angle Spinning ^{29}Si NMR (MAS NMR) measurements, the glassy matrix of SiOC glasses is continuously evolving in the temperature range between 1200–1600 °C [6]. At temperatures between 1000–1200 °C, the SiOC glass matrix consists of $SiO_{4-x}C_x$ (x = 0 to 4) mixed-bonds silicon tetrahedra [1]. These materials are fully X-ray amorphous [7,8], and can consequently be addressed as SiOC glasses. At temperatures exceeding 1200 °C, the phase separation of the glassy matrix starts, and the mixed bonds containing SiO_3C, SiO_2C_2, and $SiOC_3$ tetrahedra disappear [6]. Thus, in SiOC samples exposed to high temperatures, e.g., 1600 °C, no mixed-bonds tetrahedra are detectable by ^{29}Si MAS NMR spectroscopy. At the same time, β-SiC nanoparticles become visible in XRD upon phase separation and crystallization [9]. However, there are no indications of the crystallization of cristobalite up to temperatures of even beyond 1500 °C [10]. Consequently, these samples can be regarded as glass ceramics consisting of a silica matrix in which homogeneously dispersed nanoparticles of β-SiC and a sp^2-hybridized segregated carbon phase are present.

The concept of phase separation is especially important, as for instance SiOC materials prepared at around 1000 °C will be different if they are exposed to working temperatures exceeding 1200 °C. Therefore, it is necessary to know the thermal properties of both SiOC glasses and glass ceramics. Moreover, the chemical composition is known to govern various properties of SiOC materials, e.g., oxidation [11,12] and crystallization resistance [8]. Consequently, for an optimal design of SiOC suitable for applications at high temperatures and in harsh environments, the impact of the chemical composition on the thermal properties must be known.

SiOC glasses exhibit high stability with respect to decomposition and crystallization up to temperatures beyond 1000 °C, and furthermore show excellent behavior in oxidative and corrosive environments [2]. Thus, SiOC glasses are potential high-temperature materials for application in internal combustion engines, high-temperature reactors, heat exchangers, etc. For such applications, knowledge of the thermal properties of SiOC glasses and glass ceramics is of great interest.

Several studies report on the thermal expansion of SiOC-based materials. Typically, values for the coefficient of thermal expansion (hereafter CTE) are reported to be close to 3 ppm/K for pure SiOC systems [13–15]. Some studies show the possibility of tailoring the CTE of SiOC-based materials. The CTE can be increased up to 6.6 ppm/K upon the incorporation of additional phases, either by the pyrolysis of metal-modified preceramic precursors yielding Si(M)OC nanocomposites [16], or by the use of highly conductive fillers [15]. In a similar manner, the CTE can as well be reduced. Very recently, Fedorova et al. reported on the synthesis of SiOC materials containing β-eucryptite that exhibit a near-zero CTE [17].

Less information is available in the literature on the thermal transport of SiOC materials. Mazo et al. and Eom et al. reported thermal conductivities of silicon oxide carbides ranging from ca. 1.3 to ca. 1.8 W/(m·K) at room temperature [18–20]. Gurlo et al. measured the temperature-dependent thermal conductivity of a SiOC glass and glass ceramic with the same chemical composition [21]. The SiOC glass showed a very low thermal conductivity of about 0.5 W/(m·K). However, the investigated monolith exhibited a significant porosity of ca. 12 vol %. Consequently, in the mentioned study, no clear distinction between the impact of phase separation and porosity on the thermal properties of silicon oxide carbide was possible. Upon increasing the porosity in SiOC to approximately 80 vol %, the thermal conductivity can be decreased to values of about 0.041–0.078 W/(m·K) [22]. Despite the mentioned studies in the literature reporting on the low intrinsic thermal conductivity of SiOC-based materials, there is no systematic assessment of the thermal transport in silicon oxide carbides available, which tries to rationalize, for instance, the effect of the composition and nano/microstructure of SiOC on its thermal conductivity. Thus, in the present study, we evaluate the effect of the composition of SiOC on its thermal properties, i.e., thermal expansion as well as thermal transport. Moreover, we address the aspect of whether, and to which extent, the phase separation that occurs at high temperatures in silicon oxide carbide glasses affects their thermal conductivity.

2. Experimental Procedure

Materials Synthesis. SiOC glasses and glass ceramic samples with four different compositions, mainly with varying contents of segregated carbon (C1–SiOC, C12–SiOC, C16–SiOC, and C17–SiOC; C1, C12, C16, and C17 indicate the approximate volume fraction of segregated carbon in the prepared samples), were synthesized for this study. Monolithic specimens were obtained by uniaxial hot pressing silicon oxide carbide powders at 1600 °C (monolithic samples were denoted as C1–SiOC–1600, C12–SiOC–1600, C16–SiOC–1600, and C17–SiOC–1600). Additionally, monolithic samples of C1–SiOC were prepared in a pressureless pyrolysis process at 1100 °C (monolithic sample denoted as C1–SiOC–1100). Suitable monolithic coupons were cut from the obtained monolithic samples with a diamond wire cutter, and used for the experiments.

C12–SiOC and C17–SiOC were prepared from the commercially available polymethylsilsesquioxane Belsil PMS MK (Wacker GmbH, Burghausen, Germany), and polysiloxane SPR–212 (Starfire Systems Inc., NY, USA), respectively. Both polymers were cross-linked in an alumina tube furnace at 250 °C for two hours under flowing argon atmosphere. Subsequently, the cross-linked samples were heated at 1000 °C, with a holding time of two hours. The heating and cooling rates were 100 °C/h. The obtained glassy chunks were crushed and sieved to a grain size of < 40 μm. Hot pressing of C12–SiOC was performed at 1600 °C in a cylindrical graphite die at a constant pressure of 50 MPa in static argon atmosphere. The temperature was held at 1600 °C for 30 min before cooling down. C17–SiOC was densified upon spark plasma sintering (SPS) at 1600 °C for 15 min in a cylindrical graphite die.

C16–SiOC was prepared according to Radovanovic et al. [23] upon the sol–gel processing using 80 wt % polymethylhydrosiloxane (PMHS; average M_n 1700–3200; Merck, Germany) and 20 wt % 1,3,5,7-tetramethyl-1,3,5,7-tetravinylcyclotetrasiloxane (D_4Vi; 97%, ABCr, Karlsruhe, Germany). After 30 min stirring at 0 °C, 1 wt % platinum catalyst (Platinum(0)-1,3-divinyl-1,1,3,3-tetramethyl-disiloxane complex solution; 0.1 M in poly(dimethylsiloxane) vinyl terminated; Merck, Germany) was added and homogenized for five minutes. The mixture was subsequently filled in polystyrene boxes with a closed lid. After 30 min at 0 °C, the samples were stored for 24 h at −15 °C. The xerogels obtained were pyrolyzed at 1000 °C, crushed, sieved to < 40 μm, and densified in the hot press using the same parameters as those mentioned for C12–SiOC.

C1–SiOC was derived from a sol–gel process established by Soraru et al. [3]. Triethoxysilane (97%, ABCr, Karlsruhe, Germany) and methyldiethoxysilane (97%, ABCr, Karlsruhe, Germany) were mixed under vigorous stirring in a molar ratio of 2:1. Polymerization was started at neutral pH with an equimolar amount of deionized water with respect to the molar amount of ethoxy groups present in the two alkoxysilanes. The sol was vigorously stirred for 15 min at ambient conditions, and subsequently filled in rectangular polystyrene boxes (50 × 50 × 190 mm^3) with a closed lid. The lid was additionally sealed with parafilm to allow a slow and steady progress of the sol–gel reaction, as a fast reaction resulted in cracking of the monolithic pieces. The samples were aged for four weeks. The obtained monolithic xerogels had an approximate thickness of 1.15 mm. The samples were dried in temperature steps of 20 °C per day until 120 °C. One part of the samples was pyrolyzed in an alumina tube furnace at 1100 °C for three hours under flowing argon atmosphere using a slow heating rate of 25 °C/h. Faster heating resulted in cracking of the monolithic pieces. The second part of the samples was used to prepare SiOC powder for densification in a uniaxial hot press. The experimental parameters of the hot-pressing procedure were the same as for sample C12–SiOC.

Materials characterization. The chemical composition of the samples was determined using a carbon analyzer Leco-200 (Leco Corporation, St. Joseph, MI, USA) and a N/O analyzer Leco TC-436 (Leco Corporation, St. Joseph, Michigan, USA). The silicon weight fraction was calculated as the difference to 100 wt %, assuming that no other elements were present in the samples. Archimedean (skeletal) density and open porosity was measured with the water immersion technique. The closed porosity was measured via He pycnometry on a Pycnomatic ATC pycnometer (Porotec, Hofheim am Taunus., Germany) on finely ground powders in order to ensure full access to the total surface. Powders were ground for 2 × 60 min in a horizontal mixer mill in ZrO_2 grinding containers.

The relative density was averaged from three individual measurement cycles. Each measurement cycle consisted of several individual measurements (full evacuation and subsequent purging of the chamber). A cycle was finished when five individual values were detected within a standard deviation of 0.2%. The closed porosity was calculated from the percental deviation from the skeletal density determined by the water immersion technique. Powder XRD measurements were performed in flat-sample transmission geometry on a STOE STADI P diffractometer (Stoe, Darmstadt, Germany) equipped with a Molybdenum X-ray tube and a position sensitive detector with a 6° aperture. Raman spectra were recorded on a Horiba HR800 micro-Raman spectrometer (Horiba JobinYvon, Bensheim, Germany) equipped with a He–Ne laser (633 nm). The measurements were performed by using a grating of 600 g/mm and a confocal microscope (magnification 50 × NA 0.75–numerical aperture) with a 100-µm aperture, giving a resolution of approximately 1 µm. The laser power (20 mW) was attenuated by using neutral density filters.

Measurement of the thermal properties. The coefficient of thermal expansion (CTE) was measured using a dilatometer (DIL 402 E, NETZSCH Gerätebau GmbH, Selb, Germany) and an Al_2O_3 standard with a contact force of approximately 0.25 N. Samples prepared at 1600 °C were cut in pieces with the approximate dimension of 3 mm × 4 mm × 25 mm. Sample C1–SiOC–1100 could only be prepared in the dimensions of 0.7 mm × 4 mm × 15 mm. The measurements were performed under constant argon flow, and with heating and cooling rates of 5 K/min. The CTE was determined from the slope of the linear part of the dilatometric curves, i.e., between room temperature and 1000 °C. The specific heat capacity (C_p) was determined from differential scanning calorimetry (DSC) measurements. All of the DSC experiments were realized in a STA 449 F3 Jupiter (Netzsch Gerätebau GmbH, Selb, Germany), equipped with a type-S thermocouple. DSC measurements were performed in Pt crucibles with alumina inliners from room temperature to 1000 °C under argon atmosphere with a heating rate of 20 K/min. C_p values were calculated relating to sapphire samples following DIN standard 51007. The thermal diffusivity was determined using a Laser Flash LFA 1600 instrument (Linseis Messgeräte GmbH, Selb, Germany) equipped with a type-S thermocouple. The measurements were conducted in vacuum using graphite sample holders. A graphite sample was measured in parallel as reference material.

3. Results and Discussion

3.1. Chemical and Microstructural Characterization of SiOC Samples

The XRD patterns of the samples investigated in this study are shown in Figure 1. Sample C1–SiOC–1100 was fully X-ray amorphous; whereas all of the other samples revealed the presence of broad reflections related to nanocrystalline β-SiC [24]. The broad hump centered at a 2θ value of approximately 9.5° is related to the presence of amorphous silica.

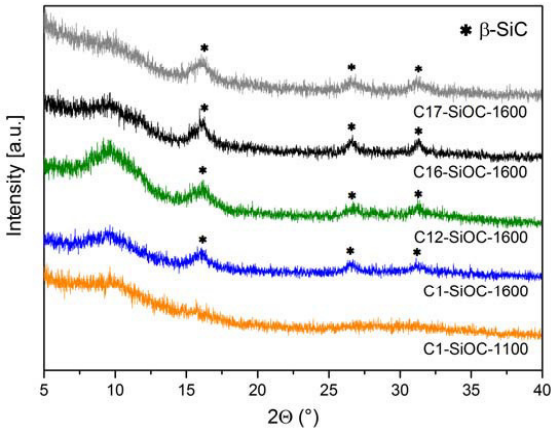

Figure 1. XRD patterns (λ = Mo K_α) of the investigated silicon oxide carbides (SiOC) materials [24].

The chemical composition of the investigated SiOC samples is summarized in Table 1. It is evident that the phase separation has no significant influence on the chemical composition (compare sample C1–SiOC–1100 and C1–SiOC–1600). As previously proven by the ^{29}Si MAS NMR spectra of samples C1–SiOC and C12–SiOC, which were prepared at 1600 °C [25,26], and the XRD patterns and Raman spectra of the studied samples shown in Figures 1 and 2, the hot-pressed samples can be considered as glass ceramics consisting of an amorphous silica matrix in which nano-sized β-SiC particles and a segregated carbon phase are dispersed. On the other hand, samples prepared at 1100 °C show a different microstructure. They are fully X-ray amorphous SiOC glasses, and exhibit $SiO_{4-x}C_x$ mixed-bonds tetrahedra [3]. Consequently, the phase composition of SiOC glasses and glass ceramics can be estimated by considering the absence of C–O bonds in SiOC materials [1]. In the case of SiOC glasses, molar fractions of SiC and SiO_2 can be regarded as the amount of Si–C and Si–O bonds, respectively. The segregated carbon content increased from a very limited amount in C1–SiOC–1600 (i.e., ca. 0.1 vol %) to a rather large fraction in C17–SiOC–1600 (i.e., ca. 17.4 vol %). The volume fraction of SiC was comparable in C1–SiOC–1600 and C16–SiOC–1600 (16.8 and 18.3 vol %, respectively), and only slightly lower in C12–SiOC–1600 (i.e., 12.3 vol %). Sample C17–SiOC–1600 has a significantly higher amount of SiC in comparison to the other samples, i.e., 29.1 vol %.

Table 1. Empirical formulae and phase compositions of the silicon oxide carbide (SiOC) samples used in this study [1].

Sample	Composition	SiO_2 (mol %)	SiC (mol %)	C_{free} (mol %)	SiO_2 (vol %)	SiC (vol %)	C_{free} (vol %)
C1–SiOC–1100	$SiO_{1.38}C_{0.32}$	68.1 [1] ± 1.1	30.7 [1] ± 2.3	1.2 [1] ± 2.9	-	-	-
C1–SiOC–1600	$SiO_{1.41}C_{0.30}$	70.2 ± 0.5	29.3 ± 2.1	0.5 ± 2.7	83.1 ± 0.4	16.8 ± 1.2	0.1 ± 0.7
C12–SiOC–1600	$SiO_{1.50}C_{0.71}$	51.3 ± 0.3	17.2 ± 1.4	31.5 ± 1.7	75.7 ± 0.4	12.3 ± 1.0	11.9 ± 0.7
C16–SiOC–1600	$SiO_{1.27}C_{0.97}$	39.6 ± 1.1	22.8 ± 1.7	37.6 ± 1.7	65.7 ± 1.9	18.3 ± 1.3	16.0 ± 0.7
C17–SiOC–1600	$SiO_{0.94}C_{1.13}$	29.5 ± 0.5	33.1 ± 1.4	37.4 ± 1.5	53.5 ± 0.9	29.1 ± 1.2	17.4 ± 0.7

[1] Molar fractions of silicon carbides (SiC) and SiO_2 can be regarded as the amount of Si–C and Si–O bonds, respectively.

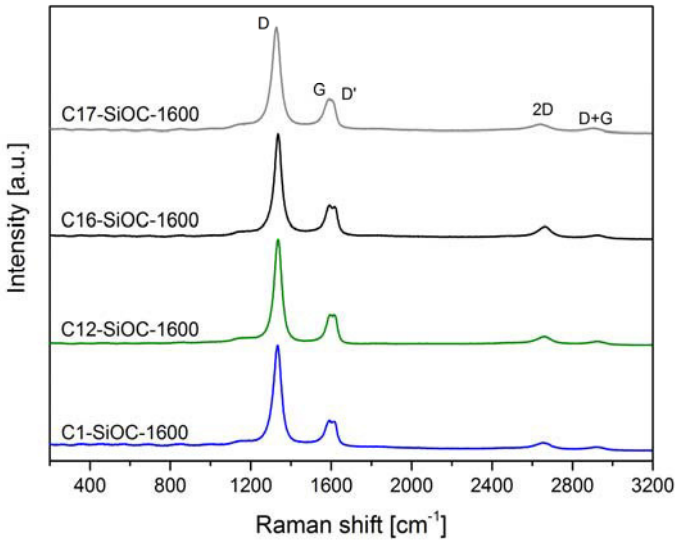

Figure 2. Raman spectra of the hot-pressed SiOC glass ceramics.

Raman spectroscopy is a powerful tool to investigate carbon-containing materials. The first order Raman spectrum of sp^2 carbon exhibits a band of E_{2g} symmetry that relates to the bond stretching of sp^2 carbon pairs that are contained in rings or chains. This band is called G band, and appears at around 1575–1595 cm^{-1}. Disordered or nanostructured carbon-based materials exhibit additional bands in their first order Raman spectrum, such as: a band of A_{1g} symmetry, which relates to the breathing modes of sp^2 carbon atoms within rings (the so-called D band; its position depends on the laser

wavelength; ca. 1350 cm^{-1} at 514.5 nm); a band related to C–C sp^3 vibrations (ca. 1150–1200 cm^{-1}; can be observed upon UV laser excitation); a D'' band (ca. 1500 cm^{-1}), which relates to amorphous carbon; and a D' band (ca. 1620 cm^{-1}). Further important features in the Raman spectrum of disordered carbon materials are the two-dimensional (2D) band ($\lambda \approx$ 2500–2800 cm^{-1}) and the D + G band ($\lambda \approx$ 2900 cm^{-1}), representing overtone and combinational modes, respectively [27].

Besides C1–SiOC–1100, which is lacking any bands in the Raman spectrum (not shown), and is suffering from large fluorescence, all of the samples that were hot-pressed at 1600 °C showed rather similar Raman spectra, and revealed the typical features of a disordered sp^2-hybridized segregated carbon phase, as shown in Figure 2.

This can be further illustrated by the comparison of some calculated graphitization indicators. The ratio between the D and the G bands gives information about the lateral crystal size L_a of the individual domains of the segregated carbon phase, which can be estimated by using the equation given in Cançado et al. [28] (Equation (1)). Similarly, the average inter-defect distance, L_D, can be calculated from Equation (2) [29].

$$L_a(nm) = 2.4 \cdot 10^{-10} \cdot {\lambda_L}^4 \cdot \left(\frac{A_D}{A_G}\right)^{-1} \quad (1)$$

$${L_D}^2\left(nm^2\right) = 1.8 \cdot 10^{-9} \cdot {\lambda_L}^4 \cdot \left(\frac{A_D}{A_G}\right)^{-1} \quad (2)$$

with λ_L being the laser wavelength in nm, as well as A_D and A_G representing the integrated area of the D band and the G band, respectively. Larouche et al. defined the value L_{eq}, which describes the average continuous carbon precipitate size, including tortuosity [30], and can be calculated from the ratio A_{2D}/A_D, as shown in Equation (3).

$$L_{eq}(nm) = 77.0648 \cdot \left(\frac{A_{2D}}{A_D}\right) \quad (3)$$

The values for L_a, L_D, and L_{eq} are listed in Table 2. No significant difference is observed for the investigated SiOC glass ceramics. Thus, it is concluded that the segregated carbon phase has a comparable degree of graphitization for all of the SiOC glass ceramics, independently of their chemical composition, as already shown by Roth et al. for SiOC samples prepared at 1600 °C with an intermediate amount of segregated carbon [31]. The average lateral crystal size is in the same range as the mean inter-defect distance. The equivalent size L_{eq} is only slightly larger than L_a, indicating that the carbon precipitates are nanoscaled. Moreover, the width of the D and G bands ranges between 40 and 50 cm^{-1}, which is close to the values known for glassy carbon (wD = 52.7 cm^{-1}; wG = 56.1 cm^{-1}) [32].

Table 2. Indicators for the degree of graphitization of the segregated carbon phase in the prepared SiOC glass ceramics.

Sample	$C_{segregated}$ (vol %)	A_D/A_G	L_a (nm)	L_d (nm)	L_{eq} (nm)
C1–SiOC–1600	0.1 ± 0.7	4.868 ± 1.074	7.9 ± 1.7	7.7 ± 0.8	10.0 ± 0.5
C12–SiOC–1600	11.9 ± 0.8	4.215 ± 0.251	9.2 ± 0.6	8.3 ± 0.3	11.0 ± 0.7
C16–SiOC–1600	16.0 ± 0.7	4.121 ± 0.521	9.5 ± 1.3	8.4 ± 0.6	11.6 ± 3.3
C17–SiOC–1600	17.4 ± 0.7	4.998 ± 0.340	7.5 ± 0.5	7.5 ± 0.2	10.1 ± 0.6

The skeletal density of SiOC increased upon phase separation, as shown in Table 3 by the comparison of the values for C1–SiOC–1100 and C1–SiOC–1600, whereas the chemical composition does not strongly affect the density of SiOC glass ceramics.

Table 3. Skeletal density and volume fractions of porosity in the SiOC samples investigated in this study. The density of silica is taken from Renlund et al. [13] and indicated for the sake of comparison.

Sample	Composition	Skeletal Density (g/cm^3)	Open Porosity (vol %)	Closed Porosity (vol %)
Vitreous Silica	SiO_2	2.20	-	-
C1–SiOC–1100	$SiO_{1.38}C_{0.32}$	2.28	0.3	-
C1–SiOC–1600	$SiO_{1.41}C_{0.30}$	2.38	0	-
C12–SiOC–1600	$SiO_{1.50}C_{0.71}$	2.31	0	-
C16–SiOC–1600	$SiO_{1.27}C_{0.97}$	2.34	0	-
C17–SiOC–1600	$SiO_{0.94}C_{1.13}$	2.33	1.6	7.0

All of the monolithic samples prepared in this study, except C17–SiOC–1600, are fully dense and crack-free, as evidenced by the measurements of the open and closed porosity (*cf.* Table 3), as well as scanning electron microscopy (SEM). C17–SiOC–1600 reveals only little open porosity (i.e., 1.6 vol %), but comprises ca. 7 vol % closed porosity, as determined by helium pycnometry. Thus, apart from C17–SiOC–1600, the samples are suitable for measuring the intrinsic thermal properties of SiOC glasses and glass ceramics. For C17–SiOC–1600, values are expected to be underdetermined due to the presence of closed porosity [33].

3.2. Thermal Properties of SiOC Glasses and Glass Ceramics

The thermal expansion and specific heat capacity of SiOC glass and glass ceramics were assessed. Moreover, the thermal diffusivity was measured, and used to rationalize the thermal conductivity in the studied samples. The temperature-dependent thermal conductivity $\lambda(T)$ can be calculated according to Equation (4):

$$\lambda(T) = \alpha(T) \cdot C_p(T) \cdot \rho(T) \quad (4)$$

where $\alpha(T)$ is the temperature-dependent thermal diffusivity, $C_p(T)$ is the temperature-dependent specific heat capacity, and $\rho(T)$ is the temperature-dependent density. At temperatures exceeding 900 °C, values for the specific heat capacity and thermal diffusivity were extrapolated (neglecting possible glass transitions). For the sample C1–SiOC–1100, the phase separation starting at approximately 1200 °C [7] was neglected upon extrapolation. In the following, the results of the multimethod approach used for the rationalization of the thermal transport in silicon oxide carbide are described and discussed.

The coefficient of thermal expansion (CTE) values determined for the SiOC glass ceramics between 100–1000 °C (Figure 3 and Table 4) are nearly one order of magnitude higher in comparison to that of vitreous silica (CTE = 5.7 × 10^{-7} K^{-1}, [14]), but are still very low. They are close to the values reported by Renlund et al. [13] (CTE = 3.14 × 10^{-6} K^{-1}) for a SiOC glass ceramic with a composition similar to that of C12–SiOC–1600. For SiOC glass ceramics, the thermal expansion increased as the carbon content increased. This is in agreement with pyrolytic carbon and β-SiC having larger CTE values of 4–6 × 10^{-6} K^{-1} [34] and 4.3–4.9 × 10^{-6} K^{-1} [35], respectively. The thermal expansion of C1–SiOC–1100 was already investigated by Rouxel et al. [14], and determined to be 3.12 × 10^{-6} K^{-1}. This is very close to the value of 3.23 × 10^{-6} K^{-1} determined in this study, and consequently higher in comparison to that of C1–SiOC–1600. Thus, the phase separation of silicon oxide carbides leads to a decrease in their thermal expansion, following the lower value for vitreous silica. Upon the incorporation of additional carbon, the CTE of the silicon oxide carbide glass ceramics can be raised again to the values of the SiOC glass (*cf.* C1–SiOC–1100 vs. C17–SiOC–1600, both with a CTE value of 3.23 × 10^{-6} K^{-1}). This proves the possibility of adjusting/tailoring the thermal properties of SiOC materials by altering the content of their segregated carbon phase.

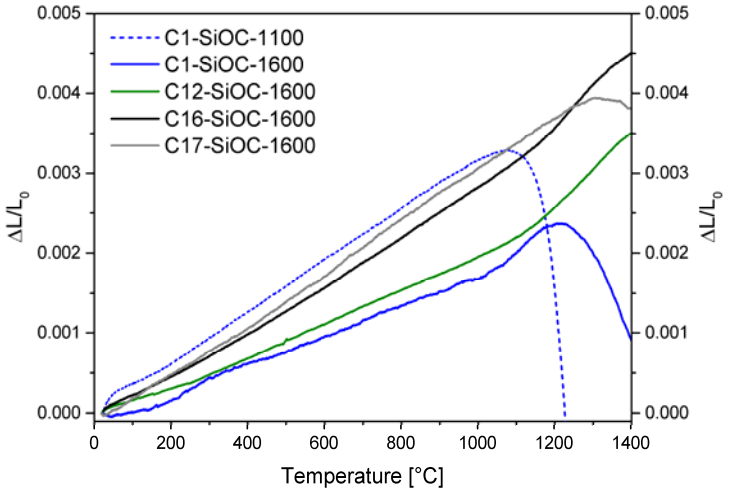

Figure 3. Thermal expansion of a SiOC glass and SiOC glass ceramics. The heating rate during the dilatometric experiments was 5 K/min.

Table 4. Coefficient of thermal expansion (CTE) values of SiOC glass and glass ceramics in the temperature range between 100–1000 °C. CTE_{HT} represents the thermal expansion coefficient between T_g and 1300 °C.

Sample	Composition	CTE (10^{-6} K^{-1})	CTE_{HT} (10^{-6} K^{-1})
C1–SiOC–1100	$SiO_{1.38}C_{0.32}$	3.23	-
C1–SiOC–1600	$SiO_{1.41}C_{0.30}$	1.84	4.41
C12–SiOC–1600	$SiO_{1.50}C_{0.71}$	2.02	4.87
C16–SiOC–1600	$SiO_{1.27}C_{0.97}$	3.09	5.29
C17–SiOC–1600	$SiO_{0.94}C_{1.13}$	3.23	-

At higher temperatures, samples C1–SiOC–1600, C12–SiOC–1600, and C16–SiOC–1600 reveal an increase in the values for CTE (*cf.* CTE_{HT} in Table 4). This behavior is also known in the literature for other glass systems [36,37]. The values for CTE_{HT} of SiOC glass ceramics are higher than the CTE values at 100–1000 °C by a factor of ca. 2. This increase in the CTE values has to be considered when anticipating applications of SiOC materials at temperatures beyond 1000 °C.

For the calculation of the temperature-dependent thermal conductivity, knowledge of the temperature-dependent densities of the SiOC materials is necessary. These can be calculated from the CTEs under the assumption of isotropic expansion, as expected for amorphous materials. Furthermore, it has to be noted that the influence of the temperature on the density of SiOC is small due to the low thermal expansion.

All of the SiOC glass ceramics except C17–SiOC–1600 showed a monotonic expansion, followed by an increase in the slope at higher temperatures. From this kink, the glass transition temperature T_g can be estimated by the intersection of the linear slopes to the left and right of the kink. They were determined to be 1060 °C for C1–SiOC–1600, 1157 °C for C12–SiOC–1600, and 1171 °C for C16–SiOC–1600. The values for T_g were approximately 140–170 °C lower than those derived from the temperature dependence of the shear viscosity obtained via compression creep measurements (data not shown), and even lower than those reported for vitreous silica (i.e., ~1190 °C depending on the amount of impurities [38]). Within this context, it should be mentioned that in various studies, the impact of the applied pressure in the dilatometer on the determined T_g value has been considered to be significant, and thus, a high mechanical load during the dilatometry experiments was shown to lead to relatively low T_g values (as with respect to values determined by other methods), while the values of the CTE remain unbiased [39]. As the focus of the present study was the accurate determination of the thermal expansion, the specimens were thoroughly fixed in the dilatometer (load of 0.25 N, corresponding to

0.02 MPa). Consequently, the determined T_g values were considered as being altered by the mechanical load used, and were thus less accurate than those determined from creep experiments [25,26,40].

An additional parameter that can be determined from the thermal expansion curve is the dilatometric softening point corresponding to the maximum of the dilatometric curve, and to a viscosity of ca. 10^{10} Pa·s. Among the SiOC glass ceramics studied, such a maximum is visible for samples C1–SiOC–1600 at 1220 °C, and for C17–SiOC–1600 at 1300 °C, which is again significantly lower than those derived from the shear viscosities. Similar to T_g, the dilatometric softening point was dependent on the applied pressure for fixing the samples inside the dilatometer [39]. With increasing pressure, the dilatometric softening point was shifted to lower temperatures. Moreover, the value determined for sample C17–SiOC–1600 was considered as being biased by a slight densification due the elimination of the residual porosity.

C1–SiOC–1100 showed a monotonic increase in the thermal expansion up to 1070 °C. At higher temperatures, a rapid shrinkage was observed, as already described by Rouxel et al. [14] for the same SiOC glass composition. The C1–SiOC–1100 specimen investigated in this study was slightly bent after the measurement, most probably due to viscous flow. However, the measured specimen was very thin (0.7 mm), and the softening point was considered as being biased, as Euler's critical load is dependent on the second moment of area [41]. Consequently, neither the glass transition temperature nor the softening point could be evaluated for sample C1–SiOC–1100.

The evolution of the specific heat capacity with the increasing temperature of the SiOC materials and glassy carbon is shown in Figure 4. The values were in the range as expected for ceramics, and rather similar to those known for vitreous silica [42] and β-SiC [43]. The temperature dependence of the specific heat capacity of samples with low contents of carbidic carbon (C1–SiOC and C12–SiOC) resembled that of vitreous silica, whereas that of the samples with a higher carbidic carbon content (C16–SiOC and C17–SiOC) resembled that of β-SiC, revealing a steeper slope in their linear range. C1–SiOC–1100 showed a nearly identical behavior to vitreous silica, up to ca. 700 °C. The phase separation lead to a decrease in the specific heat capacity, probably due to the increase in density during this process (*cf.* Table 3), as evidenced by the comparison of C1–SiOC–1100 and C1–SiOC–1600. On the other hand, an increase in the specific heat capacity could be observed for C12–SiOC–1600, C16–SiOC–1600, and C17–SiOC–1600, with no significant differences at 1000 °C. The similar molar masses and densities of the three investigated SiOC glass ceramics was considered to be the main reason for the nearly identical specific heat capacities at 1000 °C.

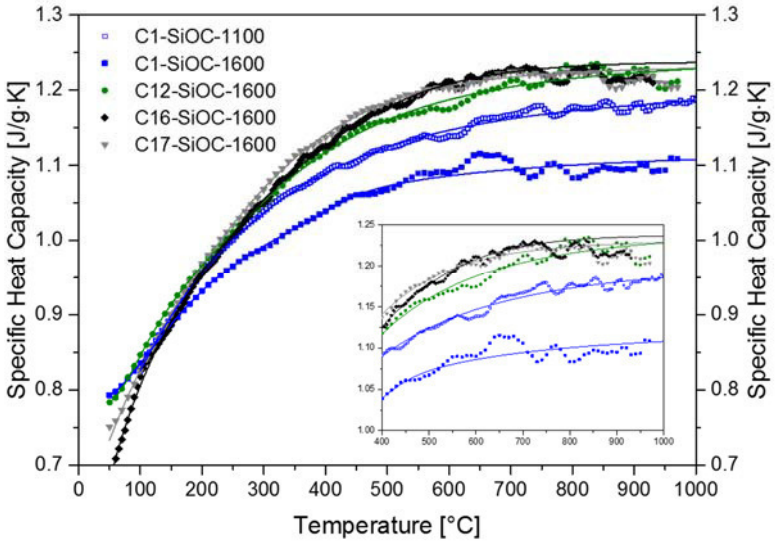

(**a**)

Figure 4. *Cont.*

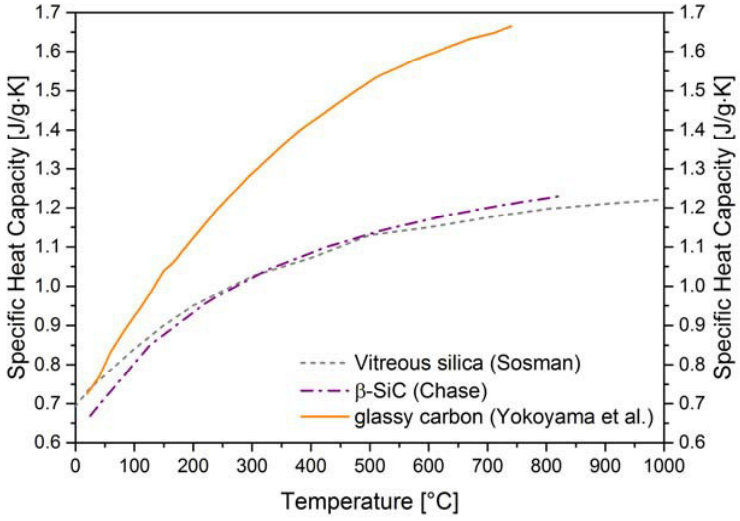

(**b**)

Figure 4. Temperature-dependent specific heat capacities of SiOC glasses and glass ceramics (**a**). Points represent the measured values; the solid lines represent eye guidelines. The inset details the specific heat capacities in the temperature range of 400 °C to 1000 °C. The values for glassy carbon [44], vitreous silica [42], and β-SiC [43] are plotted for comparison (**b**).

Figure 5 summarizes the thermal diffusivity of the investigated SiOC glass and glass ceramics. The low carbon-containing SiOC glass ceramics revealed comparable values to fused silica [45]. The thermal diffusivity in SiOC increased as the amounts of segregated carbon increased. This observation matched the higher thermal diffusivity values for glassy carbon of 0.05 cm^2/s to 0.044 cm^2/s in the temperature range between 20–700 °C [44]. However, the amount of carbidic carbon (i.e., volume fraction of β-SiC) additionally seemed to have an important influence. This is expressed by the comparison of C16–SiOC–1600 and C17–SiOC–1600, as their amount of segregated carbon was comparable; however, their thermal diffusivities were significantly different. It is conceivable that the comparably high values of C17–SiOC–1600 were resulting from the higher amount of β-SiC (*cf.* Table 1), which showed significantly higher thermal diffusivity values of 0.809 cm^2/s at room temperature [46].

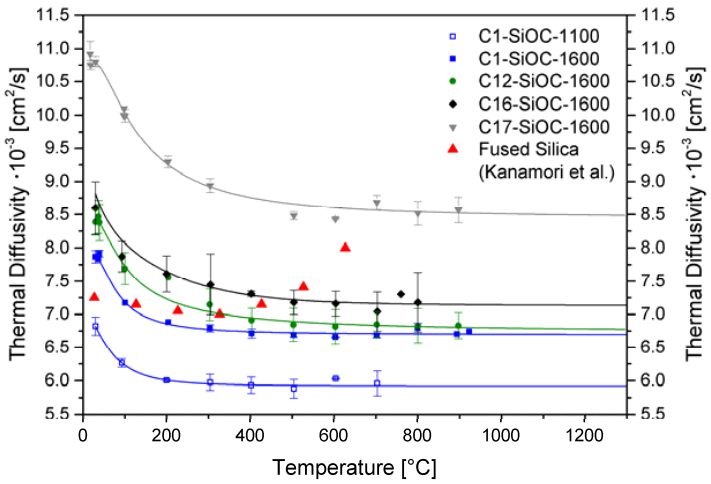

Figure 5. Thermal diffusivity of SiOC glass and glass ceramics. The data points represent the values measured, while the solid lines represent guidelines for the eyes. The data for fused silica are taken from Kanamori et al. [45].

Interestingly, sample C1–SiOC–1100 showed lower values for the thermal diffusivity in comparison to the phase-separated SiOC glass ceramics, as well as to fused silica (see Figure 5). Two aspects are considered here: (i) SiOC glasses prepared at 1000–1100 °C are known to possess a significant amount of hydrogen [10], and most probably a significant content of dangling bonds. These are expected to act as phonon scatterers; (ii) the unique network architecture of the SiOC glass, which was shown to be characterized by a low mass fractal dimension (~2.5) [1], was also considered to be an important reason for the reduced thermal diffusivity in SiOC glass. It was shown in numerous papers that fractal networks (such as silicate-based or vitreous silica) show anomalous behavior with respect to heat transport, and that this is correlated to their fractal architecture [47–49]. However, it is still not clear whether and to which extent the mass fractal dimension of a network alters its thermal transport. Thus, additional and more detailed theoretical and experimental investigations are needed for our silicon oxide carbide glasses and glass ceramics in order to elucidate this aspect.

Based on the thermal diffusivity data determined for glassy SiOC (C1–SiOC–1100), as well as the comparison with its phase-separated analogous material (C1–SiOC–1600), it can be concluded that the phase separation in SiOC leads to higher values of thermal diffusivity. This is an obvious effect, if we assume that the network architecture of the silica matrix in SiOC glass ceramics is comparable to vitreous silica. Furthermore, at a synthesis temperature of 1600 °C, significantly lower values of hydrogen in the resulting SiOC glass ceramics were present, as evidenced by Soraru et al. and Brequel et al. [3,10].

The thermal conductivity was calculated according to Equation (1) using the thermal properties presented above. Figure 6 summarizes the thermal conductivities obtained for the SiOC glass and glass ceramics. The values for C17–SiOC–1600 were corrected with respect to their open and closed porosity, as porosity reduced the thermal transport [33]. The impact of the open porosity was corrected in a first step. For materials with small fractions of open porosity (<10 vol %), the relation developed by Loeb [50] (*cf.* Equation (5)) was reported to yield appropriate values for their effective thermal conductivity [33]. As a second step, the impact of the closed porosity was corrected using the Maxwell–Eucken equation [51] (*cf.* Equation (6)). This equation was reported to appropriately taking into account fractions of < 15 vol % of closed porosity that are homogeneously dispersed in a solid matrix [33].

$$\lambda_{eff} = \lambda_s(1 - v_p) \tag{5}$$

$$\lambda_{eff} = \lambda_s \frac{\lambda_p + 2\lambda_s + 2v_p(\lambda_p - \lambda_s)}{\lambda_p + 2\lambda_s - v_p(\lambda_p - \lambda_s)} \tag{6}$$

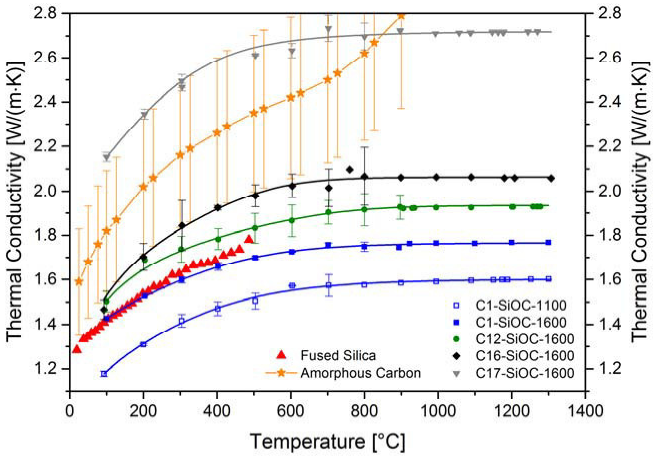

Figure 6. Thermal conductivity of SiOC glasses and glass ceramics. The data points represent the values measured; the solid lines are a guide for the eyes. The standard deviation is taken as the relative standard deviation according to the thermal diffusivity measurements. Data for fused silica and for amorphous carbon are taken from Cahill [52] and Ho et al. [53], respectively.

In the above equations, λ_{eff} is the effective thermal conductivity of the porous sample, λ_s is the thermal conductivity of the solid pore-free sample, λ_p is the thermal conductivity through the pores, and v_p is the volume fraction of the pores. λ_p is expected to be negligible.

Among all of the studied samples, the glassy SiOC material (C1–SiOC–1100) showed the lowest thermal conductivity, whereas the phase-separated low carbon-containing SiOC glass ceramic sample (C1–SiOC–1600) showed values very similar to vitreous silica [52] (Figure 6). As the content of segregated carbon increased in the SiOC glass ceramics, the thermal conductivity was observed to increase. This is probably due to the higher thermal conductivity value of the segregated carbon present in the materials. For instance, amorphous carbon [53] exhibited values in the range of the high carbon-containing SiOC glass ceramics up to 800 °C (C16–SiOC–1600 and C17–SiOC–1600), and reached values of ca. 3.18 W/(m·K) at 1000 °C. Interestingly, the thermal conductivity of C17–SiOC–1600 was significantly higher than that of C16–SiOC–1600, despite there being a comparable content of segregated carbon present in both samples (i.e., 16 vs. 17 vol %). The reason for this remarkable difference is considered to rely on the different content of the nanoscaled silicon carbide phase present in the mentioned samples. As crystalline β-SiC exhibited comparatively large thermal conductivities of 178.2 W/(m·K) [46], the increased volume fraction of silicon carbide in C17–SiOC–1600 may indeed be the reason for its higher thermal conductivity, as compared to C16–SiOC–1600.

The only available data on the temperature-dependent thermal transport in SiOC-based materials in the literature has been shown and discussed in Gurlo et al. [21]. It was stated that the thermal transport in multiphasic SiOC materials (i.e., glassy SiOC with additional segregated carbon or SiOC glass ceramics containing segregated carbon and additional disperse phases such as silicon carbide) should be governed by the percolating phases [21] present in their microstructures. In the case study mentioned [21], and for our sample C1–SiOC–1600, the only percolating phase was the glassy silica matrix. Sample C12–SiOC was close to the percolation threshold of segregated carbon, as recently evidenced by Roth et al. via electrical conductivity measurements [31]. For C16–SiOC–1600 and C17–SiOC–1600, a percolating path of the segregated carbon phase was expected to be present due to its higher volume fraction. Indeed, samples C12–SiOC–1600 to C17–SiOC–1600 exhibited an increase of the thermal conductivity as the segregated carbon content increased, getting closer to the typical values for amorphous carbon. However, this increase did not scale linearly with the amount of segregated carbon. A varying degree of ordering (i.e., graphitization) of the segregated carbon phase in the different SiOC glass ceramics can be ruled out, as evidenced by the Raman spectroscopy data presented above (Table 2). Sample C17–SiOC–1600 revealed a significantly higher thermal conductivity, which was most probably due to the higher content of β-SiC nanoparticles, as discussed already for the thermal diffusivity. Consequently, a simple Maxwell–Garnett model [54,55] for the description of its thermal conductivity, where a thermal interaction of dispersed particles is ignored, may be not suitable for sample C17–SiOC–1600.

There are several models proposed in the literature for the calculation of the effective thermal conductivity of composite materials at different border conditions. As already pointed out, a percolating phase is expected to behave differently than an isolated phase, and for our samples, both situations have to be considered. Kingery pointed out that for a two-phase system, the effective thermal conductivity depends on the conductivity of both phases (regardless whether they are continuous or not), and on their distribution [56]. However, a continuous phase dominates the effective thermal conductivity of the composite [56]. For composites with more than one continuous phase, i.e., interpenetrating phase composites (IPC), the description of the effective thermal conductivity is more complex. However, upon the comparison of a model developed for liquid-phase sintered Cu/W IPCs, a linear dependence of the effective thermal conductivity on the volume fractions of the interpenetrating phases may be expected [57]. This model seems to fit our samples well, as in the model, copper as the high conducting phase (and in our samples, the segregated carbon phase) has lower volume fractions than the lower conducting phase tungsten (in our samples, glassy SiO_2). This is especially important, as the different

models for the effective thermal conductivity of composites yield different results depending on which phase (isolated, continuous, etc.) is the higher or lower conducting phase [58].

Sample C1–SiOC–1600 consisted of ca. 83 vol % glassy SiO_2 and ca. 17 vol % dispersed particles (β-SiC). The continuous phase was the glassy SiO_2 matrix. For sample C12–SiOC–1600, the glassy SiO_2 matrix was forming a continuous phase, and the segregated carbon was expected to form at least partially percolating paths. The effective thermal conductivities of both of these material mixtures (C1–SiOC–1600, C12–SiOC–1600) have been computed by means of a first-order computational homogenization scheme. The SiC inclusions and the segregated carbon phase have been approximated by spherical particles with a diameter of 5 nm, and by rods with dimensions of $10 \times 2 \times 2$ nm^3, respectively. These particles were randomly placed in a sample volume of fused silica with dimensions $100 \times 100 \times 100$ nm^3. Insertion continued until reaching the desired volume fractions of 12.3 vol % for SiC, and 11.9 vol % for carbon for C12–SiOC–1600. Figure 7a shows a view of the particle distribution in sample C12–SiOC–1600. A cross-section of sample C12–SiOC–1600 is given in Figure 7b, and exhibits good agreement with the sample microstructure as observed by TEM [26,40], particularly with respect to the interparticle spacing.

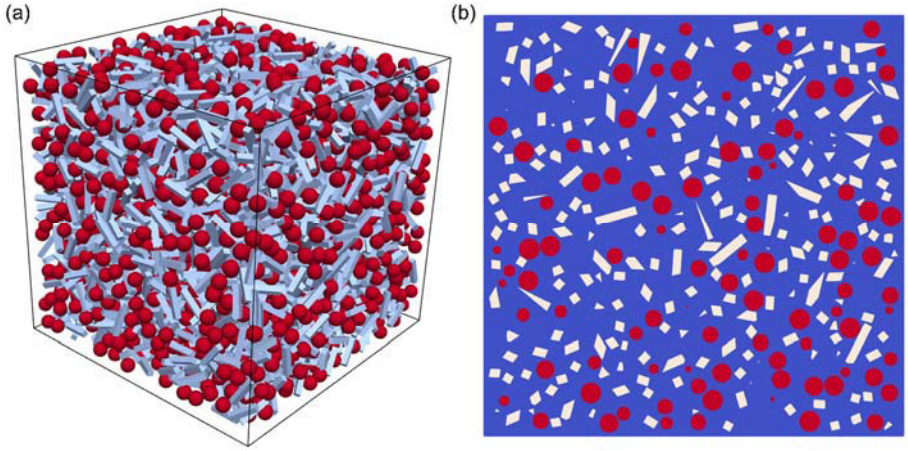

Figure 7. Modeled microstructure of sample C12–SiOC–1600: (**a**) three-dimensional representation of a $100 \times 100 \times 100$ nm^3 volume and (**b**) two-dimensional cross-section of (**a**). Red spheres represent β-SiC nanoparticles (5 nm diameter), and white rods represent the segregated carbon phase.

The effective thermal conductivity tensor was determined from the solution of a Laplace problem with three sets of linear temperature boundary conditions, each with respect to one of the spatial directions. The employed thermal conductivities for fused silica, SiC, and segregated carbon read 1.75 W/(m·K) [52], 5 W/(m·K) [59,60], and 2.5 W/(m·K) [53], respectively. The trace of the conductivity tensor yielded the desired isotropic thermal conductivity of the material mixture. For sample C12–SiOC–1600, the thermal conductivity was found to exceed that of fused silica by a factor of 1.22, possessing a value of approximately 2.14 W/(m·K). This is significantly higher than the experimental determined values. However, the numerical simulations were performed upon neglecting the thermal contact resistance at the interface between the particles and the matrix. We assume that this was due to the high total surface area of the nano-sized β-SiC particles, which summed up to a significant total thermal contact resistance between the β-SiC particles and the matrix. As a consequence, the values of the thermal conductivity were lowered. If the segregated carbon phase was present as a percolating phase, its thermal conductivity had a linear impact on the effective thermal conductivity relative to its volume fraction [57]. This concept is depicted in Figure 8 for thermal conductivity values at 800 °C as a function of the volumetric amount of segregated carbon phase and β-SiC. A linear trend line was drawn between the first percolating phase (fused silica) and the second percolating phase

(amorphous carbon). Samples C1–SiOC–1600 and C12–SiOC–1600 both fell on this line, supporting the linear relation between the interpenetrating phases.

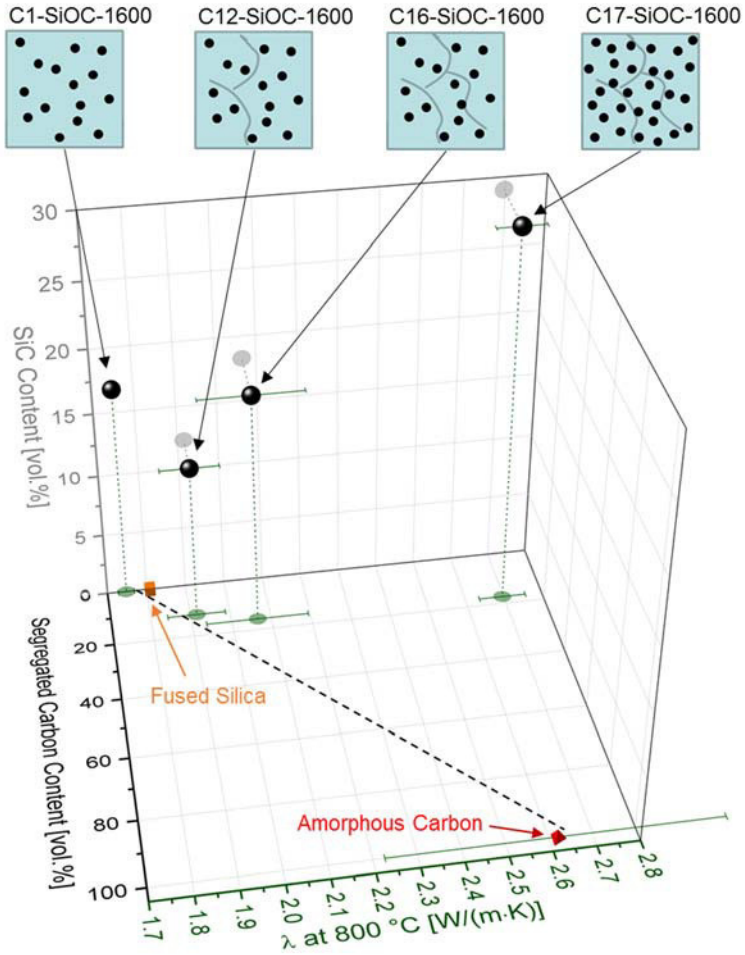

Figure 8. Thermal conductivity λ of the SiOC glass ceramics investigated in this work, and of reference materials at 800 °C, as a function of the segregated carbon content and the SiC content. Data for fused silica was extrapolated from Cahill [52], and data for amorphous carbon was taken from Ho et al. [53]. Two-dimensional (2D) projections of the individual values on the xy plane and on the yz plane are included as green and grey transparent dots, respectively. Sample C1–SiOC–1600 and sample C12–SiOC–1600 can be effectively described as a linear mixture between the two percolating phases (*cf.* trend line), namely, the glassy SiO_2 matrix and the segregated carbon phase. The β-SiC particles possibly show a slight impact for C16–SiOC–1600, and a significant impact for C17–SiOC–1600. They are expected to have a strong contribution to the thermal transport as part of a high-λ percolating phase consisting of segregated carbon and β-SiC. The highly schematic images of the respective microstructures are indicated for SiOC glass ceramics at the top insets, in which the black dots represent β-SiC, and the grey lines represent the segregated carbon phase.

C16–SiOC–1600 fell slightly off the linear trend line. However, a clear statement is difficult, as the rather high standard deviation of the thermal conductivity of amorphous carbon hampered the conclusions. Most probably, C16–SiOC–1600 had two percolating phases, namely, the glassy SiO_2 matrix, and the segregated carbon phase. A contribution of the β-SiC nanoparticles to the percolating carbon phase cannot be excluded. However, as the thermal conductivity of C17–SiOC–1600 is by far higher than that expected from a linear mixture between the two percolating phases (glassy SiO_2 matrix and segregated carbon phase), a contribution of the SiC nanoparticles is most probable. As already discussed for the thermal diffusivity, the β-SiC particles are expected to be the reason for

this steep increase, as C17–SiOC–1600 possessed almost 30 vol % β-SiC nanoparticles. Consequently, for C17–SiOC–1600, two percolating phases were expected to be present, namely the low thermal conductivity (low-λ) glassy SiO_2 matrix, and a high-λ percolating path consisting of β-SiC and segregated carbon (dominated by the contribution of SiC).

Gurlo et al. [21] investigated a hot-pressed material, which was synthesized from the same polymer as sample C12–SiOC–1600 in this study, and additionally, the same chemical composition prepared at 1100 °C. It is important to note that the latter sample was obtained from a self-filler process, and the final monolith showed a considerable porosity of 12 vol %. Additionally, the self-filler technique introduces additional grain boundaries, and consequently increases the overall interfacial thermal resistance. The sample with the composition equivalent to C12–SiOC–1600 showed slightly lower thermal conductivities, comparable to those reported here for C1–SiOC–1600. The sample prepared at 1100 °C possessed considerably lower values of about 0.5 to 0.7 W/(m·K). Upon comparison with samples C1–SiOC–1100 and C1–SiOC–1600 in this study, it can be concluded that the low values from Gurlo et al. [21] are probably related to the porosity, as indicated in the study, as well as additional grain boundaries originating from the self-filler-assisted synthesis [21].

The thermal conductivity of sample C1–SiOC–1100 from our study can be considered as being representative of the intrinsic thermal transport of the glass matrix in SiOC glasses, as it possesses only a very limited amount of segregated carbon and no porosity.

4. Conclusions

In the present study, the effect of the chemical/phase composition and the microstructure of SiOC materials on their thermal properties was investigated. Values of the heat capacity, thermal diffusivity, and thermal conductivity of glassy SiOC with no segregated carbon are similar to those reported for vitreous silica, whereas the thermal expansion in SiOC was slightly larger than that of silica. It is shown that the phase separation of SiOC glass leads to a rather significant decrease of the coefficient of thermal expansion (i.e., from 3.2×10^{-6} K^{-1} in the glass to 1.8×10^{-6} K^{-1} in the phase-separated state), and a slight increase of the thermal conductivity (i.e., from 1.5 to 1.7 W/(m·K)). The changes in thermal expansion and thermal conductivity, which were associated with the phase separation of the SiOC glass network, could be adjusted by tuning the content of segregated carbon (which may be present in the glassy, as well as the phase-separated state), and of SiC nanoparticles, which were in situ generated upon the phase separation of the SiOC glass network. Thus, fractions of ca. 10 vol % of segregated carbon are sufficient to modify the thermal expansion of phase-separated SiOC from 1.8×10^{-6} K^{-1} back to its value from the single-phase glassy state. Increasing the content of segregated carbon (i.e., up to 12–15 vol %) and SiC nanoparticles (up to 29 vol %) in the evaluated phase-separated SiOC glass ceramics lead to thermal conductivity values in the rage from 1.18 and 2.7 W/(m·K). It is considered that tailoring the chemical/phase composition in silicon oxide carbides via suitable polymeric precursors and processing parameters enabled tuning their thermal properties.

Acknowledgments: The authors thank Claudia Fasel for the assessment of the thermal expansion of SiOC as well as Lothar Bischoff and Maren Lepple for the DSC measurements. Fruitful discussions with Felix Rosenburg are gratefully acknowledged. Financial support was provided from the Deutsche Forschungsgemeinschaft (IO 64/7-1, "High-Temperature Creep in SiOC-Based Glasses and Glass-Ceramics"). EI furthermore acknowledges support from the EU COST Action CM1302 (European network "Smart Inorganic Polymers", SIPs).

Author Contributions: C.S. and E.I. conceived and designed the experiments; C.S. synthesized the samples and performed elemental analysis, SEM imaging and density, XRD and Raman measurements. A.R. performed the laser flash measurements. P.S. performed the computational modeling; C.S., A.R., P.S., B.A., R.R., E.I. contributed reagents/materials/analysis tools; C.S. and E.I. analyzed the data. C.S. wrote the paper. All authors read the paper and provided input and corrections on the text.

Conflicts of Interest: The authors declare no conflict of interest.

References

1. Widgeon, S.J.; Sen, S.; Mera, G.; Ionescu, E.; Riedel, R.; Navrotsky, A. ^{29}Si and ^{13}C solid-state NMR spectroscopic study of nanometer-scale structure and mass fractal characteristics of amorphous polymer-derived silicon oxycarbide ceramics. *Chem. Mater.* **2010**, *22*, 6221–6228. [CrossRef]
2. Colombo, P.; Mera, G.; Riedel, R.; Sorarù, G.D. Polymer-derived ceramics: 40 Years of research and innovation in advanced ceramics. *J. Am. Ceram. Soc.* **2010**, *93*, 1805–1837. [CrossRef]
3. Soraru, G.D.; D'Andrea, G.; Campostrini, R.; Babonneau, F.; Mariotto, G. Structural characterization and high-temperature behavior of silicon oxycarbide glasses prepared from sol-gel precursors containing Si-H bonds. *J. Am. Ceram. Soc.* **1995**, *78*, 379–387. [CrossRef]
4. Pantano, C.G.; Singh, A.K.; Zhang, H. Silicon oxycarbide glasses. *J. Sol-Gel Sci. Technol.* **1999**, *14*, 7–25. [CrossRef]
5. Soraru, G.D. Silicon oxycarbide glasses from gels. *J. Sol-Gel Sci. Technol.* **1994**, *2*, 843–848. [CrossRef]
6. Bois, L.; Maquet, J.; Babonneau, F.; Bahloul, D. Structural Characterization of Sol-Gel Derived Oxycarbide Glasses. 2. Study of the Thermal Stability of the Silicon Oxycarbide Phase. *Chem. Mater.* **1995**, *7*, 975–981. [CrossRef]
7. Soraru, G.D.; Modena, S.; Guadagnino, E.; Colombo, P.; Egan, J.; Pantano, C. Chemical durability of silicon oxycarbide glasses. *J. Am. Ceram. Soc.* **2002**, *85*, 1529–1536. [CrossRef]
8. Gregori, G.; Kleebe, H.-J.; Blum, Y.D.; Babonneau, F. Evolution of C-rich SiOC ceramics: Part II. Characterization by high lateral resolution techniques: Electron energy-loss spectroscopy, high-resolution TEM and energy-filtered TEM. *Int. J. Mater. Res.* **2006**, *97*, 710–720. [CrossRef]
9. Saha, A.; Raj, R. Crystallization maps for SiCO amorphous ceramics. *J. Am. Ceram. Soc.* **2007**, *90*, 578–583. [CrossRef]
10. Brequel, H.; Parmentier, J.; Walter, S.; Badheka, R.; Trimmel, G.; Masse, S.; Latournerie, J.; Dempsey, P.; Turquat, C.; Desmartin-Chomel, A.; et al. Systematic Structural Characterization of the High-Temperature Behavior of Nearly Stoichiometric Silicon Oxycarbide Glasses. *Chem. Mater.* **2004**, *16*, 2585–2598. [CrossRef]
11. Hurwitz, F.I.; Heimann, P.; Farmer, S.C.; Hembree, D.M., Jr. Characterization of the pyrolytic conversion of polysilsesquioxanes to silicon oxycarbides. *J. Mater. Sci.* **1993**, *28*, 6622–6630. [CrossRef]
12. Brewer, C.M.; Bujalski, D.R.; Parent, V.E.; Su, K.; Zank, G.A. Insights into the oxidation chemistry of SiOC ceramics derived from silsesquioxanes. *J. Sol-Gel Sci. Technol.* **1999**, *14*, 49–68. [CrossRef]
13. Renlund, G.M.; Prochazka, S.; Doremus, R.H. Silicon oxycarbide glasses. Part II. Structure and properties. *J. Mater. Res.* **1991**, *6*, 2723–2734. [CrossRef]
14. Rouxel, T.; Massouras, G.; Soraru, G.-D. High temperature behavior of a gel-derived SiOC glass: Elasticity and viscosity. *J. Sol-Gel Sci. Technol.* **1999**, *14*, 87–94. [CrossRef]
15. Reitz, E.; Schell, K.G.; Bucharsky, E.C.; Oberacker, R.; Hoffmann, M.J. Precursor derived SiOC/$MoSi_2$-composites for diesel glow plugs: Preparation and high temperature properties. *J. Ceram. Soc. Jpn.* **2016**, *124*, 1017–1022. [CrossRef]
16. Harshe, R.; Balan, C.; Riedel, R. Amorphous Si(Al)OC ceramic from polysiloxanes: Bulk ceramic processing, crystallization behavior and applications. *J. Eur. Ceram. Soc.* **2004**, *24*, 3471–3482. [CrossRef]
17. Fedorova, A.; Michelsen, L.; Scheffler, M. Polymer-derived ceramic tapes with small and negative thermal expansion coefficients. *J. Eur. Ceram. Soc.* **2018**, *38*, 719–725. [CrossRef]
18. Mazo, M.A.; Palencia, C.; Nistal, A.; Rubio, F.; Rubio, J.; Oteo, J.L. Dense bulk silicon oxycarbide glasses obtained by spark plasma sintering. *J. Eur. Ceram. Soc.* **2012**, *32*, 3369–3378. [CrossRef]
19. Mazo, M.A.; Tamayo, A.; Caballero, A.C.; Rubio, J. Electrical and thermal response of silicon oxycarbide materials obtained by spark plasma sintering. *J. Eur. Ceram. Soc.* **2017**, *37*, 2011–2020. [CrossRef]
20. Eom, J.-H.; Kim, Y.-W.; Kim, K.J.; Seo, W.-S. Improved electrical and thermal conductivities of polysiloxane-derived silicon oxycarbide ceramics by barium addition. *J. Eur. Ceram. Soc.* **2018**, *38*, 487–493. [CrossRef]
21. Gurlo, A.; Ionescu, E.; Riedel, R.; Clarke, D.R. The Thermal Conductivity of Polymer-Derived Amorphous Si-O-C Compounds and Nano-Composites. *J. Am. Ceram. Soc.* **2016**, *99*, 281–285. [CrossRef]
22. Qiu, L.; Li, Y.M.; Zheng, X.H.; Zhu, J.; Tang, D.W.; Wu, J.Q.; Xu, C.H. Thermal-Conductivity Studies of Macro-porous Polymer-Derived SiOC Ceramics. *Int. J. Thermophys.* **2014**, *35*, 76–89. [CrossRef]

23. Radovanovic, E.; Gozzi, M.F.; Goncalves, M.C.; Yoshida, I.V.P. Silicon oxycarbide glasses from silicone networks. *J. Non-Cryst. Solids* **1999**, *248*, 37–48. [CrossRef]
24. Thibault, N.W. Morphological and structural crystallography and optical properties of SiC. *Am. Mineral.* **1944**, *29*, 249–278.
25. Papendorf, B.; Ionescu, E.; Kleebe, H.-J.; Linck, C.; Guillon, O.; Nonnenmacher, K.; Riedel, R. High-temperature creep behavior of dense SiOC-based ceramic nanocomposites: Microstructural and phase composition effects. *J. Am. Ceram. Soc.* **2013**, *96*, 272–280. [CrossRef]
26. Ionescu, E.; Balan, C.; Kleebe, H.-J.; Mueller, M.M.; Guillon, O.; Schliephake, D.; Heilmaier, M.; Riedel, R. High-temperature creep behavior of SiOC glass-ceramics: Influence of network carbon versus segregated carbon. *J. Am. Ceram. Soc.* **2014**, *97*, 3935–3942. [CrossRef]
27. Ferrari, A.C.; Robertson, J. Interpretation of Raman spectra of disordered and amorphous carbon. *Phys. Rev. B* **2000**, *61*, 14095–14107. [CrossRef]
28. Cancado, L.G.; Takai, K.; Enoki, T.; Endo, M.; Kim, Y.A.; Mizusaki, H.; Jorio, A.; Coelho, L.N.; Magalhães-Paniago, R.; Pimenta, M.A. General equation for the determination of the crystallite size L_a of nanographite by Raman spectroscopy. *Appl. Phys. Lett.* **2006**, *88*, 163106. [CrossRef]
29. Cancado, L.G.; Jorio, A.; Ferreira, E.H.M.; Stavale, F.; Achete, C.A.; Capaz, R.B.; Moutinho, M.V.O.; Lombardo, A.; Kulmala, T.S.; Ferrari, A.C. Quantifying Defects in Graphene via Raman Spectroscopy at Different Excitation Energies. *Nano Lett.* **2011**, *11*, 3190–3196. [CrossRef] [PubMed]
30. Larouche, N.; Stansfield, B.L. Classifying nanostructured carbons using graphitic indices derived from Raman spectra. *Carbon* **2010**, *48*, 620–629. [CrossRef]
31. Roth, F.; Waleska, P.; Hess, C.; Ionescu, E.; Nicoloso, N. UV Raman spectroscopy of segregated carbon in silicon oxycarbides. *J. Ceram. Soc. Jpn.* **2016**, *124*, 1042–1045. [CrossRef]
32. Cuesta, A.; Dhamelincourt, P.; Laureyns, J.; Martinez-Alonso, A.; Tascon, J.M.D. Raman microprobe studies on carbon materials. *Carbon* **1994**, *32*, 1523–1532. [CrossRef]
33. Smith, D.S.; Alzina, A.; Bourret, J.; Nait-Ali, B.; Pennec, F.; Tessier-Doyen, N.; Otsu, K.; Matsubara, H.; Elser, P.; Gonzenbach, U.T. Thermal conductivity of porous materials. *J. Mater. Res.* **2013**, *28*, 2260–2272. [CrossRef]
34. Piat, R.; Schnack, E. Identification of coefficients of thermal expansion of pyrolytic carbon with different texture degrees. *Key Eng. Mater.* **2003**, *251–252*, 333–338. [CrossRef]
35. Li, Z.; Bradt, R.C. Thermal expansion of the cubic (3C) polytype of silicon carbide. *J. Mater. Sci.* **1986**, *21*, 4366–4368. [CrossRef]
36. Debenedetti, P.G.; Truskett, T.M.; Lewis, C.P.; Stillinger, F.H. Theory of supercooled liquids and glasses: Energy landscape and statistical geometry perspectives. In *Advances in Chemical Engineering*; Academic Press: Cambridge, MA, USA, 2001; pp. 21–79.
37. Mattern, N.; Hermann, H.; Roth, S.; Sakowski, J.; Macht, M.-P.; Jovari, P.; Jiang, J. Structural behavior of $Pd_{40}Cu_{30}Ni_{10}P_{20}$ bulk metallic glass below and above the glass transition. *Appl. Phys. Lett.* **2003**, *82*, 2589–2591. [CrossRef]
38. Doremus, R.H. Viscosity of silica. *J. Appl. Phys.* **2002**, *92*, 7619–7629. [CrossRef]
39. Mazurin, O.V. Problems of compatibility of the values of glass transition temperatures published in the world literature. *Glass Phys. Chem.* **2007**, *33*, 22–36. [CrossRef]
40. Stabler, C.; Roth, F.; Narisawa, M.; Schliephake, D.; Heilmaier, M.; Lauterbach, S.; Kleebe, H.-J.; Riedel, R.; Lonescu, E. High-temperature creep behavior of a SiOC glass ceramic free of segregated carbon. *J. Eur. Ceram. Soc.* **2016**, *36*, 3747–3753. [CrossRef]
41. MacLeod, I.A. *Modern Structural Analysis: Modelling Process and Guidance*; Thomas Telford Ltd.: London, UK, 2005.
42. Sosman, R.B. *The Properties of Silica: An Introduction to the Properties of Substances in the Solid Non-Conducting State*; The Chemical Catalog Company, Inc.: New York, NY, USA, 1927.
43. Chase, M.W.J. *NIST-JANAF Thermochemical Tables*; American Institute of Physics: College Park, MA, USA, 1998.
44. Yokoyama, J.; Murabayashi, M.; Takahashi, Y.; Mukaibo, T. Measurement of high-temperature thermal properties of glassy carbon by laser flash method. *Tanso* **1971**, *65*, 44–47. [CrossRef]
45. Kanamori, H.; Fujii, N.; Mizutani, H. Thermal diffusivity measurement of rock-forming minerals from 300° to 1100° K. *J. Geophys. Res.* **1968**, *73*, 595–605. [CrossRef]

46. Kim, K.J.; Lim, K.-Y.; Kim, Y.-W. Electrical and Thermal Properties of SiC Ceramics Sintered with Yttria and Nitrides. *J. Am. Ceram. Soc.* **2014**, *97*, 2943–2949. [CrossRef]
47. Posselt, D.; Kjems, J.K.; Bernasconi, A.; Sleator, T.; Ott, H.R. The Thermal-Conductivity of Silica Aerogel in the Phonon, the Fracton and the Particle-Mode Regime. *Europhys. Lett.* **1991**, *16*, 59–65. [CrossRef]
48. Nakayama, T. Boson peak and terahertz frequency dynamics of vitreous silica. *Rep. Prog. Phys.* **2002**, *65*, 1195–1242. [CrossRef]
49. Alexander, S.; Laermans, C.; Orbach, R.; Rosenberg, H.M. Fracton interpretation of vibrational properties of cross-linked polymers, glasses, and irradiated quartz. *Phys. Rev. B* **1983**, *28*, 4615–4619. [CrossRef]
50. Loeb, A.L. Thermal conductivity. VIII. A theory of thermal conductivity of porous materials. *J. Am. Ceram. Soc.* **1954**, *37*, 96–99. [CrossRef]
51. Eucken, A. The heat conductivities of ceramic refractory materials. Calculations of heat conductivity from the constituents. *Forsch. Geb. Ingenieurwesen* **1932**, *16*, 353–360.
52. Cahill, D.G. Thermal Conductivity Data. 2014. Available online: http://users.mrl.illinois.edu/cahill/tcdata/tcdata.html (accessed on 14 December 2017).
53. Ho, C.Y.; Powell, R.W.; Liley, P.E. Thermal conductivity of the elements. *J. Phys. Chem. Ref. Data* **1972**, *1*, 279–421. [CrossRef]
54. Maxwell, J. *A Treatise on Electricity and Magnetism*; Clarendon Press: Oxford, UK, 1892.
55. Garnett, J.C.M. Colours in metal glasses and in metallic films. *Philos. Trans. R. Soc. Lond. Ser. A* **1904**, *203*, 385–420. [CrossRef]
56. Kingery, W.D. Thermal conductivity. XIV. Conductivity of multicomponent systems. *J. Am. Ceram. Soc.* **1959**, *42*, 617–627. [CrossRef]
57. German, R.M. A model for the thermal properties of liquid-phase sintered composites. *Metall. Trans. A* **1993**, *24*, 1745–1752. [CrossRef]
58. Wang, J.; Carson, J.K.; North, M.F.; Cleland, D.J. A new structural model of effective thermal conductivity for heterogeneous materials with co-continuous phases. *Int. J. Heat Mass Transf.* **2008**, *51*, 2389–2397. [CrossRef]
59. Jeong, T.; Zhu, J.-G.; Mao, S.; Pan, T.; Tang, Y.J. Thermal Characterization of SiC Amorphous Thin Films. *Int. J. Thermophys.* **2012**, *33*, 1000–1012. [CrossRef]
60. Li, M.; Yue, Y. Molecular dynamics study of thermal transport in amorphous silicon carbide thin film. *RSC Adv.* **2014**, *4*, 23010–23016. [CrossRef]